

**DEVELOPMENT AND APPLICATION OF AN ION
MOBILITY SPECTROMETER – QUADRUPOLE MASS
SPECTROMETER INSTRUMENT**

by

DAVID CHRISTOPHER HOWSE

A thesis submitted to the University of Birmingham

for the degree of

DOCTOR OF PHILOSOPHY

School of Physics and Astronomy

University of Birmingham

April 2014

UNIVERSITY OF
BIRMINGHAM

University of Birmingham Research Archive

e-theses repository

This unpublished thesis/dissertation is copyright of the author and/or third parties. The intellectual property rights of the author or third parties in respect of this work are as defined by The Copyright Designs and Patents Act 1988 or as modified by any successor legislation.

Any use made of information contained in this thesis/dissertation must be in accordance with that legislation and must be properly acknowledged. Further distribution or reproduction in any format is prohibited without the permission of the copyright holder.

Abstract

The aim of the project described in this thesis was to develop a system in house that would be capable of providing a technique to enhance the reliability of detection of threat agents such as compounds used for chemical warfare and explosives. This was to be done by using a combination of an ion mobility spectrometer (IMS) in tandem with a quadrupole mass spectrometer (QMS). When meeting these requirements, the latest electronics and software were incorporated in the instrumentation to maximise sensitivity and flexibility.

By attaching a QMS to an IMS, an extra dimension in specificity is gained whereby a more positive identification of a compound is made based on m/z values, thereby providing further information on the ion-molecule processes taking place in the IMS. Flexibility in operation was achieved by using the graphical programming language LabVIEW for the software aspects, allowing program development and modification to be made more quickly than would be the case than if a procedural language such as C++ had been used.

A special 'pulse to analogue' converter developed during the project provided increased sensitivity and resolution over earlier systems in regard to obtaining selected mass mobility spectra.

Proof-of-principle measurements are provided that demonstrate the capabilities of the newly developed IMS-QMS system in both positive and negative ion modes of operation, with some results obtained that are consistent with those from previous investigations.

Data obtained for various chemicals not previously investigated are also provided. The reduced mobilities, mobility and mass spectra are presented for all compounds investigated including acetone, methyl salicylate and various nitroaromatic compounds.

Dedication

Dedicated in loving memory to my mother.

Acknowledgements

I wish to express gratitude and thanks to my supervisor, Dr. Chris Mayhew for his unfailing support and guidance during the process of system development, application and writing up culminating in this thesis submission. His friendly manner and approach coupled with a quick wit have all helped to make my time in the department an enjoyable and rewarding experience.

Chapter 1 INTRODUCTION TO THE IMS-QMS SYSTEM

1.1	Overview	1
1.2	Combining Ion mobility spectrometry with mass spectrometry	3
1.3	Comparison of the IMS technique with other methodologies	3
1.4	IMS – MS Systems	4
1.5	An introduction to Ion Mobility Spectrometry (IMS)	5
1.6	Operating principles of the drift tube	7
1.7	Ion Mobility Spectrum	9
1.8	IMS Components	10
1.9	IMS Performance and limiting factors	17
1.10	Theoretical considerations of IMS Operation	18
1.11	Determining K theoretically	20
1.12	Determining K practically	20
1.13	Effect of errors in measurement of K_0	21
1.14	Ion-molecule reactions in the positive ions mode.....	23
1.15	Ion-molecule reactions in the negative ions mode.....	26
1.16	Concluding remarks.....	28

Chapter 2 DEVELOPMENT OF THE IMS-QMS INSTRUMENTATION

2.1	Practical system arrangement.....	29
2.2	Measurement of relative humidity in the gas flows.....	31
2.3	Carrier gas considerations.....	32
2.4	Calculating reduced mobilities.....	33
2.5	Electronics Development.....	34

2.6	Trigger and Gate Pulse Generator	35
2.7	The gate interface unit.....	40
2.8	Raw dc Power Supply for the variable gate voltage regulator	41
2.9	Variable Gate Voltage Regulator	43
2.10	Opto-isolated input and regenerative output stage	44
2.11	Circuit development of the output circuit for the gate pulse interface.....	45
2.12	Operation of the gate control circuit	49
2.13	Time response of the gate control circuit.....	50
2.14	An alternative bipolar version of the gate control circuit	53
2.15	The Electrometer	56
2.15.1	The complete electrometer	59
2.15.2	Optimising the frequency response of the I – V converter	63
2.15.3	Faraday plate switch	65
2.16	IMS drift tube heater controller	66
2.16.1	Circuit operation of the heater controller.....	67
2.16.2	Thermal Switch Monitoring.....	69
2.17	Acquisition of channeltron pulses and processing for tuned mass mobility...75	
2.17.1	Hardware solution for converting ion counts from the channeltron into an analogue of the ion current.....	76
2.17.2	Hardware considerations.....	77
2.17.3	Circuit diagrams and descriptions of the pulse converter stages.....	79
2.17.4	Sync pulses generator.....	80
2.17.5	Pulse count considerations.....	83
2.17.6	Data acquisition considerations.....	84

2.17.7 Determining the relationship between the count reading given by LabVIEW and the frequency of the ion pulses.....	86
2.18 Testing and verifying the operation of the pulse converter.....	87
2.18.1 Characterisation Measurements.....	89
2.19 Comments and discussion of the results obtained.....	92
2.20 Theoretical considerations on the response of the pulse count converter to a steady input frequency.....	97
2.20.1 The pulse counting window.....	99
2.20.2 The effect of increasing the number of accumulations n on uncertainty ϵ	102
2.20.3 The relationship between measured frequency and actual input frequency.....	103
2.20.4 Plotting the error curve.....	104
2.21 Reconstruction filter.....	110
2.22 Ion Pulse Simulator.....	112
2.23 Concluding Remarks.....	114

Chapter 3 SOFTWARE DEVELOPMENT FOR THE IMS-QMS SYSTEM

3.1 A short description of the LabVIEW programming environment	115
3.2 Program development	116
3.3 Hardware considerations	117
3.4 Program operation	120
3.4.1 IMS program functionality	122
3.4.2 Saving results in a spreadsheet	126
3.5 Descriptions of the programs making up the suite	129
3.5.1 Ion Mobility Spectra - IMS.vi	129
3.5.2 Total Ions Mass Mobility Spectra - TIMMS.vi	129
3.5.3 Operating the TIMMS program	130
3.5.4 Selected Ions Mass Mobility Spectra - SIMMS.vi	133

3.5.5 Mass Spectra - MS.vi	135
----------------------------------	-----

Chapter 4 CHARACTERISING THE IMS-QMS SYSTEM

4.1 System tests	142
4.2 Testing rationale	143
4.3 List of Tests Performed	143

Tests

Test 4.1 The effect of varying the drift tube voltage on ion current (dc).....	144
Test 4.2 The effect of varying the screen grid voltage on ion current (dc).....	146
Test 4.3 The effect of varying the gate pulse width on the RIP.....	147
Test 4.4 The effect of averaging on the quality of the ion mobility spectrum.....	150
Test 4.5 Investigating the microphony effect of the screen grid to FP voltage.....	154
Test 4.6 The effect of varying voltage difference between screen grid and FP on RIP..	156
Test 4.7 Effects on the RIP with varying drift tube voltage.....	158
Test 4.8 Investigating the change in ion mobility over time.....	161
Test 4.9 Investigating the change in ion mass mobility over time.....	163
Test 4.10 The effect of varying FP to cone voltage on RIP mass spectra.....	164

Chapter 5 CHARACTERISATION OF THE IMS-QMS SYSTEM IN POSITIVE ION MODE

5.1 Introduction.....	170
5.1.1 Analyte sample preparation.....	171
5.2 Investigation using tertiary butanol in an undoped system.....	172
5.2.1 Determining the flow rate for a given concentration.....	173

5.2.2 Resultant spectra for tertiary butanol.....	174
5.2.3 Reduced mobilities.....	181
5.3 Investigation using acetone in an undoped system.....	182
5.3.1 Determining the flow rate of the syringe drive.....	182
5.3.2 Resultant spectra for acetone.....	183
5.4 Investigation using di-acetone in an undoped system	188
5.5 Investigation using DPGME in an undoped system.....	192
5.6 Summary and review	199

Chapter 6 CHARACTERISATION OF THE IMS-QMS SYSTEM IN NEGATIVE ION MODE

6.1 Introduction.....	200
6.2 Ion spectra observed in clean air using the present system.....	201
6.3 Investigations using analytes.....	204
6.4 Investigation using methyl silicilate.....	204
6.5 Investigation using 1,3 DNB.....	208
6.6 Investigation using 2,4 DNT.....	211
6.7 Investigation using 2,6 DNT.....	213
6.8 Investigation using 1,3,5 TNB.....	218
6.9 Investigation using 2,4,6 TNT.....	221
6.10 Investigating the use of the dopant hexachloroethane in nitrogen.....	225
6.11 Investigating TNT in pure nitrogen with no dopant present.....	228
6.12 Summary and review.....	230

Chapter 7 REVIEW AND DISCUSSION OF FURTHER WORK

7.1 Review of achievements made with the IMS-QMS system	232
7.2 Factors that have arisen since the design and use of the system.....	233
Consideration of Reduced Mobility and Correction Factor in its calculation.....	233
7.3 Future improvements.....	235
Incorporation of a calibration factor	235
Direct display of K_0 on mobility spectra.....	236
Generation of carrier gas (pure air)	237
Monitoring drift voltage.....	238
Software implementation of the pulse converter using a microcontroller.....	238
Improvements on pumping to eliminate the microphony effect in IMS spectra.....	238
Accurate incorporation of transit time of ions through the quadrupole.....	239
Further signal processing of spectral data.....	239
Simplified drift tube.....	239
Alternative ionisation source.....	239
7.4 Newly emerging applications	240
7.5 Potential applications for the newly developed IMS-QMS system	240
7.6 Final comments.....	241

Appendix 1

A1.1 – Estimation of ion density and current	242
A1.2 – Calculation of E/N within the drift tube	244
A1.3 – Comparing thermal and drift kinetic energies of an ion	245

Appendix 2

Determining the component values for the trigger and gate pulse generator

A2.1 The astable section	246
A2.2 The monostable section	247
A2.3 Lens power supply unit.....	249

Appendix 3

A3.1 LabVIEW program IMS.vi – first section	253
LabVIEW program IMS.vi – second section	254
A3.2 LabVIEW program TIMMS.vi – first section	255
LabVIEW program TIMMS – second section	256
A3.3 LabVIEW program SIMMS.vi – first section	257
LabVIEW program SIMMS.vi – second section	258
A3.4 LabVIEW program MS.vi – first section	259
LabVIEW program MS.vi – second section	260
LabVIEW program MS.vi – third section	261
A3.5 Averaging over several spectral scans with the MS program	262

Appendix 4

A4.1 Bringing the tube up to atmospheric pressure using lab air (with the drift tube pumped down, rotary and turbo pumps working)	263
---	-----

A4.2	Bringing the IMS-MS system up to atmosphere and shutting down	264
A4.3	Changing the set point on the mass flow controllers	265
A4.4	Wiring changes for selecting the ion polarity	266
A4.5	IMS-QMS Settings – Positive ion mode	267
A4.6	IMS-QMS Settings – Negative ion mode	268
A4.7	Calibrating the SXP unit. (0 to 600 amu)	269
A4.8	Removing the IMS drift tube from the system	270
A4.9	IMS to Quad pressure chart	272
A4.10	Important points to observe when shutting the system down	273
A4.11	IMS temperature comparison/calibration	274
A4.12	Parameter values relative to a normally working system	277
A4.13	Modification to ring connections to eliminate the drift problem.....	278

Appendix 5

A5.1	Determining the syringe flow rate required to give a final concentration in the gas flow to the drift tube	279
A5.2	- Program to calculate syringe flow rate for a required sample concentration in the drift flow gas	280
A5.3	Program to calculate reduced ion mobility	281
A5.4	Sample Dilution using a Pressure Vessel	282
A5.5	Sample Concentration using a Diffusion tube	285
A5.6	Dilution Chart	286
A5.7	Calculation of vapour pressure using the Antoine equation	287

Appendix 6

A6.1	Quadrupole connections for ion modes – A pictorial summary	288
------	--	-----

Appendix 7

A7.1 High input impedance kilovoltmeter289

Appendix 8

Publications in preparation290

REFERENCES291

List of Figures

Chapter 1

Figure 1.1 Basic layout of an IMS-QMS system	5
Figure 1.2 Basic components of the drift tube used in the molecular physics group	6
Figure 1.3 Ring connections to the resistor chain	7
Figure 1.4 An example obtained from our system of a typical ion mobility spectrum	10
Figure 1.5 Alignment of the grids forming the ion gate	14

Chapter 2

Figure 2.1 Schematic layout of the IMS-QMS system showing the IMS-QMS interface and flow of carrier gas.....	29
Figure 2.2 The functional blocks of the gate pulse generator	35
Figure 2.3 Circuit diagram showing the main operating sections of the pulse generator	36
Figure 2.4 Astable timing component connections	37
Figure 2.5 Monostable timing component connections	37
Figure 2.6 Pulse width range extension	38
Figure 2.7 Control of gate operating mode	39
Figure 2.8 External/internal trigger selection	39
Figure 2.9 Principal sections inside the gate pulse interface unit	41
Figure 2.10 Raw dc power supply for the gate interface	42
Figure 2.11 Adjustable voltage regulator for the gate pulses	43
Figure 2.12 Basic operation of the opto-isolated input and regenerative output stage	46
Figure 2.13 Basic Schmitt trigger using complementary MOS devices	47
Figure 2.14 Interfacing requirements to prevent over-voltage of the gate drive circuitry	48
Figure 2.15 Input and output stages of the gate control circuit	49

Figure 2.16 Simplified version of the gate control circuit	52
Figure 2.17 Switching waveforms for the gate circuit shown in Figure 2.15	53
Figure 2.18 Gate pulse interface using bipolar transistors	54
Figure 2.19 Switching waveforms for the bipolar output circuit shown in Figure 2.18	57
Figure 2.20 Representation of the equivalent circuit of the FP connected to the current to voltage converter	59
Figure 2.21 Block diagram of the electrometer stages	56
Figure 2.22 Circuit diagram of the Electrometer Amplifier for the IMS-QMS system	61
Figure 2.23 Operation of the gain control switch	62
Figure 2.24 Frequency response of the current-to-voltage converter	63
Figure 2.25 Switching the Faraday plate between the electrometer amplifier input and electrostatic lens operation	65
Figure 2.26 Overall circuit diagram of the heater controller	67
Figure 2.27 Series connection of thermal switches for flashover prevention	69
Figure 2.28 Circuit to monitor the state of the thermal switches	70
Figure 2.29 showing the physical layout of the thermal switches on the heater, and the monitoring led's on the monitor box	72
Figure 2.30 Optimised switch monitoring circuit – part A	73
Figure 2.31 Optimised switch monitoring circuit – part B	74
Figure 2.32 Flashover prevention circuit	75
Figure 2.33 Ion count signal from the pulse converter	78
Figure 2.34 Block diagram of Pulse Count to Voltage Converter	79
Figure 2.35 1 MHz time-base generator	79
Figure 2.36 Divider ($\div 100$)	80

Figure 2.37 Sync pulses generator – timing diagram	81
Figure 2.38 Sync pulse generator waveforms.....	82
Figure 2.39 P1, P2 sync pulses generator	83
Figure 2.40 8-bit Counter and D to A Converter	84
Figure 2.41 Plot of input frequency to output count with 500 accumulations	93
Figure 2.42 Percentage variation (error) in count with pulse frequency	94
Figure 2.43 Representing a channeltron pulse arriving within the counting widow	99
Figure 2.44 showing how uncertainty in measurement of f_p increases towards 20 kHz.....	100
Figure 2.45 showing variation of uncertainty over the range 10 to 70 kHz.....	100
Figure 2.46 showing a more correct representation of variation in uncertainty over the range 10 to 70 kHz.....	101
Figure 2.47 Representing channeltron pulses at $f_p > 20$ kHz	101
Figure 2.48 showing effect of $n=2$ on the uncertainty ϵ	103
Figure 2.49 showing effect of $n=4$ on the uncertainty in measurement of f_p	103
Figure 2.50 finding the minimum n at a particular value of f_p	104
Figure 2.51 User form for calculation of least no. of accumulations to resolve f_p	105
Figure 2.52 showing the effect of f_p on n at $\epsilon = 0$	106
Figure 2.53 Variation of error in measured pulse frequency f_m with $n=1$	107
Figure 2.54 Variation of error in measured pulse frequency f_m with $n=2$	108
Figure 2.55 Variation of error in measured pulse frequency f_m with $n=3$	108
Figure 2.56 Phase relationship of the pulses between frames.....	106
Figure 2.57 Basic single pole low-pass filter	111
Figure 2.58 Final version used for the reconstruction filter.....	111
Figure 2.59 Circuit diagram of the ion pulse simulator	112

Figure 2.60 Pulse converter and simulator system connection	113
---	-----

Chapter 3

Figure 3.1 Pin assignment for the PCI 6014 DAQ card connector box	118
Figure 3.2 IMS Front Panel	120
Figure 3.3 Block diagram showing the data acquisition and signal averaging sections of the program IMS	123
Figure 3.4 showing the false case that is selected when $i = 0$	126
Figure 3.5 Writing sets of data strings to a spreadsheet	128
Figure 3.6 TIMMS Front Panel	130
Figure 3.7 SIMMS Front Panel	133
Figure 3.8 Mass selection in the SIMMS program	134
Figure 3.9 A screenshot of the spectrum provided by the SIMMS program showing the RIP for water clusters of m/z 55	135
Figure 3.10 The MS Front Panel	136
Figure 3.11 A screen shot of the mass spectra program showing water clusters and contaminants before baking out	137
Figure 3.12 Setting up the mass range over which the mass spectrum is plotted	139
Figure 3.13 Obtaining the ion count over a pre-determined dwell time	140

Chapter 4

Figure 4.1 Plot of ion current vs drift voltage	145
Figure 4.2 Plot of ion current vs screen voltage	146
Figure 4.3 Plot of RIP vs gate pulse width	148
Figure 4.4 Magnified section of Figure 4.3	149
Figure 4.5 IMS spectrum with two averages	151

Figure 4.6 IMS spectrum with ten averages	152
Figure 4.7 IMS spectrum with one hundred averages	153
Figure 4.8 IMS spectrum with five hundred averages	153
Figure 4.9 Effect of drift tube voltage on drift time	159
Figure 4.10 Effect of drift voltage on RIP Current	160
Figure 4.11 Variation of RIP current with elapsed time	162
Figure 4.12 Variation of drift time with elapsed time	162
Figure 4.13 Counts over $V_{FP-CONE} = 1$ to 14 V	167
Figure 4.14 Branching Ratios for $V_{FP-CONE} = 1$ to 14 V	167
Figure 4.15 Total Ion transmission	168

Chapter 5

Figure 5.2.1 Mass spectrum for the water RIP	174
Figure 5.2.2 Total ions mass mobility spectrum for the protonated water clusters shown in Figure 5.2.1	175
Figure 5.2.3 Mass spectrum with tertiary butanol injected at a rate of 15 ml/hour	175
Figure 5.2.4 Mass spectrum with tertiary butanol injected at a rate of 20 ml/hour	176
Figure 5.2.5 Total ions mass mobility spectrum with syringe rate set at 20 ml/hour	176
Figure 5.2.6 Total ions mass mobility spectrum with syringe rate set at 15 ml/hour	177
Figure 5.2.7 Selected mass ion mobility spectrum for m/z 55, $H^+(H_2O)_3$	177
Figure 5.3.8 Selected mass ion mobility spectrum for m/z 69, (impurity)	178
Figure 5.2.9 Selected mass ion mobility spectrum for m/z 73, $H^+(H_2O)_4$	175
Figure 5.2.10 Selected mass ion mobility spectrum for m/z 93, $MH^+(H_2O)$	179
Figure 5.2.11 Selected mass ion mobility spectrum for m/z 111, $MH^+(H_2O)_2$	179

Figure 5.2.12 Selected mass ion mobility spectrum for m/z 149, M_2H^+	180
Figure 5.2.13 Selected mass ion mobility spectrum for m/z 167, $M_2H^+(H_2O)$	180
Figure 5.2.14 IMS spectra for T.B. from previous workers	181
Figure 5.2.15 Tuned mass ion mobility spectra from previous workers	181
Figure 5.3.1 Mass spectrum for acetone sample at 85 ppbv in pure air	183
Figure 5.3.2 Total ions mass mobility spectrum at a syringe rate of 15 ml/hour	184
Figure 5.3.3 Selected ion mass mobility spectrum at m/z 59 with dimer present	185
Figure 5.3.4 Mass spectrum obtained at a higher concentration of acetone	186
Figure 5.3.5 Total ions mass mobility spectrum showing presence of the dimer only with high sample concentration	187
Figure 5.3.6 showing dissociation of the dimer at m/z 59, no monomer is seen	187
Figure 5.3.7 showing the majority of the dimer at m/z 117	188
Figure 5.4.1 Mass spectrum at low concentration	189
Figure 5.4.2 Mass spectrum at higher concentration producing a dimer	189
Figure 5.4.3 TIMMS spectrum at lower sample concentration with absence of dimer	190
Figure 5.4.4 TIMMS spectrum at higher concentration showing predominance of dimer ...	190
Figure 5.5.1 Molecular structure of DPM(A)	192
Figure 5.5.2 Molecular structure of DPM(B)	192
Figure 5.5.3 TIMMS spectrum at high concentration of DPGME	193
Figure 5.5.4 showing that dimer is dominant	194
Figure 5.5.5 SIMMS showing drift time at m/z 297	194
Figure 5.5.6 SIMMS showing drift time at m/z 149	194
Figure 5.5.7 TIMMS spectrum at a lower analyte concentration of DPGME.....	195

Figure 5.5.8 Mass spectrum of DPGME at a lower concentration	195
Figure 5.5.9 Total Ions Mass mobility spectrum at diminishing concentration	196
Figure 5.5.10 Mass spectrum at diminishing concentration of DPGME.....	196
Figure 5.5.11 TIMMS showing dominant RIP at 23.1 ms	197
Figure 5.5.12 SIMMS for DPGME at m/z 149	197
Figure 5.5.13 SIMMS at m/z 279	198

Chapter 6

Figure 6.2.1 TIMMS spectrum showing RIP in clean air in negative ion mode	202
Figure 6.2.2 <i>m/z</i> of the RIP components in the negative ion mode	203
Figure 6.4.1 Mass spectrum for a low concentration of methyl salicylate	205
Figure 6.4.2 SIMMS spectrum at m/z 151 for MS	205
Figure 6.4.3 TIMMS spectrum of MS.....	206
Figure 6.4.4 Mass spectrum at higher concentration of M.S. analyte showing the occurrence of a dimer	207
Figure 6.4.5 Mass spectrum at higher concentrations showing dominance of m/z 212 and a strong dimer	207
Figure 6.5.1 Mass spectrum of 1,3 DNB	209
Figure 6.5.2 Total ion mobility spectrum of 1,3 DNB	210
Figure 6.5.3 Selected ion mass mobility spectrum at m/z 168 for 1,3 DNB	210
Figure 6.5.4 TIMMS showing reversion to RIP after 2½ hours	211
Figure 6.6.1 Mass scan for 2,6 DNT	212
Figure 6.6.2 Expanded view of the mass peak around 181 amu for 2,6 DNT	212
Figure 6.6.3 TIMMS scan for 2,6 DNT	213

Figure 6.7.1	TIMMS for 2,4 DNT	214
Figure 6.7.2	Expanded view of TIMMS for 2,4 DNT	214
Figure 6.7.3	Mass scan for 2,4 DNT	215
Figure 6.7.4	Exploded view of the peaks obtained around 181 amu for 2,4 DNT	215
Figure 6.7.5	Exploded view of the peaks obtained around 196 amu for 2,4 DNT	216
Figure 6.7.6	SIMMS scan at m/z 181 for 2,4 DNT	216
Figure 6.7.7	SIMMS scan at m/z 196 for 2,4 DNT	217
Figure 6.8.1	TIMMS scan for TNB	218
Figure 6.8.2	MS scan for TNB	219
Figure 6.8.3	SIMMS scan at m/z 213 for TNB	219
Figure 6.8.4	SIMMS scan at m/z 274 for TNB	220
Figure 6.8.5	MS scan for TNB	220
Figure 6.8.6	IMS scan for TNB	221
Figure 6.9.1	MS scan of 2,4,6 TNT in air	222
Figure 6.9.2	TIMMMS scan of 2,4,6 TNT in air	223
Figure 6.9.3	SIMMS scan at m/z 226 in air	223
Figure 6.9.4	MS scan for 2,4,6, TNT in air at 70°C source gas temperature	224
Figure 6.9.5	TIMMS scan for 2,4,6 TNT in air at 86°C	225
Figure 6.10.1	TIMMS scan for N ₂ with C ₂ Cl ₆ dopant	226
Figure 6.10.2	Low resolution MS scan for N ₂ with C ₂ Cl ₆ dopant	226
Figure 6.10.3	MS scan around m/z 35 for N ₂ with C ₂ Cl ₆ dopant	227
Figure 6.10.4	MS scan around m/z 53 for N ₂ with C ₂ Cl ₆ dopant	227
Figure 6.10.5	MS scan around m/z 72 for N ₂ with C ₂ Cl ₆ dopant	228

Figure 6.11.1 Mass scan around m/z 211 to 230 for N ₂ (no dopant present)	229
Figure 6.11.2 Mass scan around m/z 225 to 229 for N ₂ (no dopant present)	229
Figure 6.11.3 Mass scan around m/z 224 to 228 for N ₂ with Cl ⁻ dopant	230

Appendices

Figure A2.3.1 Schematic diagram of the lens PSU	249
Figure A2.3.2 Showing composition of REG.....	249
Figure A2.3.3 Circuit for lens voltage adjustment.....	250
Figure A2.3.4 Showing circuit for F2 boost.....	250
Figure A2.3.5 Showing 50 Hz noise filter to the screen grid.....	251
Figure A2.3.6 Showing the layout of the front panel of the lens PSU.....	251
Figure A2.3.7 Showing the pin arrangement of the PSU output socket.....	252
Figure A2.3.8 Showing the pin arrangement of the connecting lead plug.....	252
Figure A4.1 Showing the screen grid to FP order of assembly.....	271
Figure A4.2 IMS to Quad pressure chart.....	272
Figure A4.3 Relationship between indicated temperature on the controller and actual drift gas temperature.....	276
Figure A4.4 Modification to ring circuit.....	278
Figure A5.1 - Flows relating to concentration in the inlet system.....	279
Figure A5.2 Layout of the dilution rig.....	284
Figure A6.1 Quadrupole connections for ion modes	288
Figure A7.1 Circuit diagram for a high input impedance kilovoltmeter.....	289

List of Tables

Chapter 1

Table 1.1 Proton affinity of water clusters (H ₂ O) _n as stated by Cheng.....	25
Table 1.2 Reactant anions observed in previous studies by Carr and Spangler.....	27

Chapter 2

Table 2.1 Summary of gate control circuit operation	49
Table 2.2 Operation of the thermal switches	69
Table 2.3 Switch failure diagnosis	71
Table 2.4 Thermal switch fault diagnosis	73
Table 2.5 Relationship between pulse count and D/A output voltage	86
Table 2.6 Count variations with frequency using 500 accumulations.....	89
Table 2.7 Count variations with frequency using 1000 accumulations.....	90
Table 2.8 Count variations at low frequencies using 500 accumulations.....	90
Table 2.9 Count variations at low frequencies using 1000 accumulations.....	90
Table 2.10 Count variation around transition freq. range using 500 accumulations.....	91
Table 2.11 Count variation around the transition point using 500 accumulations.....	91
Table 2.12 Resistance values required to produce various test frequencies	113

Chapter 4

Table 4.1 Listing the test parameters.....	144
Table 4.2 Optimising SNR	155
Table 4.3 RIP characteristics for various screen-to Faraday plate voltages	157
Table 4.4 Variation of drift time and RIP count over time	163

Chapter 5

Table 5.3.1 Mass assignments for the peaks seen in Figure 5.3.1	183
Table 5.3.2 Ion assignments for the peaks shown in Figure 5.3.2	184
Table 5.3.3 Temporal values of the masses shown in Figure 5.3.1	185
Table 5.3.4 Results from an acetone study made by Watts	186
Table 5.4.1 Ion mass assignments	190
Table 5.4.2 Drift times for selected ion masses	191
Table 5.4.3 Ion mass assignments for the peaks shown in the TIMMS spectra of Figures 5.4.3 and 5.4.4	191
Table 5.5.1 Ion mass assignments	196
Table 5.5.2 Ion assignment table summarizing the DPGME investigation	198

Chapter 6

Table 1.2 Reactant anions observed in previous studies by Carr and Spangler	203
Table 6.2.1 Reactant anions observed in the present IMS-QMS system	204
Table 6.4.2 Ion m/z , drift times, relative intensities and calculated K_0 values at low concentration of MS.....	208
Table 6.10.1 Identification of m/z ions for N_2 with C_2Cl_6 dopant at the masses seen in figure 6.10.6	228
Table 6.12.1 Listing of analytes used in the negative ion mode with their results	231

Appendices

Table A2.3.1 Assignment of PSU output socket pins.....	252
Table A2.3.2 Assignment of connecting cable plug.....	252

Table A4.1 Controller temperature readings against actual drift tube and heating jacket temperatures	275
Table A4.2 Variation of indicated temperature with actual drift tube temperature	275

List of Abbreviations

IMS	Ion Mobility Spectrometer
QMS	Quadrupole Mass Spectrometer
CWA	Chemical Warfare Agent
CAM	Chemical Agent Monitor
K	Ion mobility
K_0	Reduced ion mobility
t_d	Drift time
V_{HT}	High tension voltage (as applied to the drift tube)
RIP	Reactant Ion Peak
APCI	Atmospheric Pressure Chemical Ionisation
FP	Faraday Plate
R_p	Resolving power
led	light emitting diode

Software programs:

IMS	Ion Mobility Spectrum
SIMMS	Selected Ions Mass Mobility Spectrum
TIMMS	Total Ions Mass Mobility Spectrum
MS	Mass Spectrum

CHAPTER 1 INTRODUCTION TO THE IMS-QMS SYSTEM

1.1 Overview

Within the Molecular Physics Group, the tandem Ion Mobility Spectrometer – Quadrupole Mass Spectrometer (IMS-QMS) system described in this thesis was developed in order to aid in fundamental studies of the chemical processes occurring in an ion mobility spectrometer [1, 2-4] with regard to the detection of trace gases arising from the presence of chemical warfare agents (CWAs) [5-9], explosive compounds [10-17] and drugs [18-28]. Examples of other growing areas of application with IMS are:

- Monitoring industrial processes [29] to check that levels of particular substances given off are within permissible limits such as in semiconductor manufacture [30-33], electrical circuit breakers [34-36] and in printing [37,38].
- Monitoring food quality [39-41] and pesticide levels [42-45].
- Biological applications in areas such as breath analysis [46-52], detecting bacteria [53,54] and pharmaceutical cleanliness [55-58].
- Monitoring the environment [59-63].

These wide- ranging applications of IMS are due to its constructional simplicity and readiness to allow miniaturisation and transportation (where all the necessary systems are self contained). A particular advantage of IMS over other types of analytical instruments is that it operates at atmospheric pressure, hence avoiding the need for a bulky and expensive vacuum system. The technique is very sensitive and is capable of detecting trace amounts of chemical compounds in

the parts per billion by volume (ppbv) concentration range within a few seconds and therefore provides real time analysis.

The present research and development described in this thesis forms part of a collaborative project with Smiths Detection Ltd, who are based in Watford, U.K. Smiths Detection is considered to be world leader in the design and manufacture of IMS equipment. They produced the CAM (Chemical Agent Monitor) [64,65] in the 1980s that was used extensively during combat in the 1991 Persian Gulf War. Since then, over 60,000 CAMS have been introduced into military establishments' worldwide today [66].

Although IMS systems are very sensitive they are however, not very specific with regard to the identity of a particular chemical owing to their relatively poor temporal resolution. It is possible for several different ions to appear to, or even have, the same drift time and so there is a clear requirement to improve their performance in this aspect. The limited temporal resolution inherent in IMS systems makes them prone to giving false alarms known as false positives and these occur when a chemical of similar mass and molecular cross-section, i.e. of similar ion mobility to a given threat agent, is detected [67]. False negatives can also happen when any molecules present, having a high proton affinity, are more easily ionised than the target chemical. This can saturate the system and cause the target response to be suppressed. These effects may be reduced by using chemical dopants. The term dopant (or reagent gas) is used to describe a chemical such as acetone or ammonia that is introduced into the reaction region of the drift tube in order to modify the ionisation chemistry in the instrument such that it suppresses any response from background interferents. [68]

The electronic systems for the present IMS and the data acquisition software (using ‘LabVIEW’ [69]) for the overall IMS-QMS system were designed and constructed in the laboratory and are described in detail in chapters 2 and 3. Characterisation of the system is described in chapter 4. The intended use of the system for investigating ion-molecule chemical reactions and the results obtained from these experiments are discussed in chapters 5 (positive ion mode) and 6 (negative ion mode).

1.2 Combining Ion Mobility Spectrometry with Mass Spectrometry

The combination of IMS-QMS enables certain limitations of IMS-technique-only systems to be overcome [70,71]. In order to be more selective, the identification of the m/z of the ions may be detected and interpreted resulting in a mass spectrum that can then be related to the compounds of interest thus improving the range of characterisation capability. This then promotes a better understanding of the chemical processes involved in IMS systems used for the detection of threat agents.

1.3 Comparison of the IMS technique with other methodologies

Other comparable techniques that may be used for the detection of volatiles at low concentrations are the Selected Ion Flow Tube Mass Spectrometer (SIFT-MS) and Proton Transfer Reaction Mass Spectrometer (PTR-MS).

SIFT [72] (and its predecessor the Flowing Afterglow (FA) [73] method) is generally used as a means for measuring kinetics such as absolute rate coefficients. However, the PTR-MS and IMS methods are mainly used as analytical techniques for identifying compounds from their ion-molecule reactions.

With the SIFT method (an improvement on the earlier flowing afterglow method) an electron impact ionisation source is used to produce 70 eV [74] electrons that bombard the molecules of a reagent gas to produce a soup of parent and fragment ions in the ionisation region. A particular reactant ion is chosen with the use of a quadrupole mass filter before being admitted into the reaction (flow tube) region for reaction with the analyte. The product and reactant ions are then sampled into a mass analyser for identification. The whole system operates at a low pressure of around 5 - 10 mBar.

In recent years SIFT-MS has been developed into an analytical tool, predominantly using H_3O^+ , O_2^+ and NO^+ as reactant ions. However, owing to its lower sensitivity and more complicated operation compared to PTR-MS, few groups use it for chemical analysis.

PTR-MS [75] is simpler to operate because a mass filter is not required. Furthermore, an electric field is used to transport the ions in a low pressure drift tube, which eliminates the need for the relatively large flow rates of buffer gas encountered with SIFT.

IMS-MS is similar to PTR-MS in that it is based on drift tube technology. However, unlike PTR-MS the drift tube operates at atmospheric pressure. Whilst this makes the instrument simpler in design compared to PTR-MS, the ion-molecule chemistry is more complicated and restricted (e.g. positive ion mode cannot be used for detecting explosives). Nevertheless, it is the dominant analytical technique in current use for threat agent detection and therefore it is crucial that the ion-molecule chemistry is explored in detail.

A further advantage is gained over SIFT and PTR-MS in that isomers can be distinguished due to their differing cross sections. [76-78]

1.4 IMS – MS Systems

The first IMS-MS system was developed by McDaniel in 1960 at Georgia Tech. [79]. A magnetic sector mass analyser was used in this instrument to characterise the ion peaks in the ion mobility spectrum of pure hydrogen. Since then, instruments have been developed in research institutions covering a variety of mass analysers and IMS pressures [80-85]. Figure 1.1 shows a schematic representation of a basic layout for an IMS interfaced to a QMS. The heating jacket around the IMS is necessary to maintain a constant elevated operating temperature.

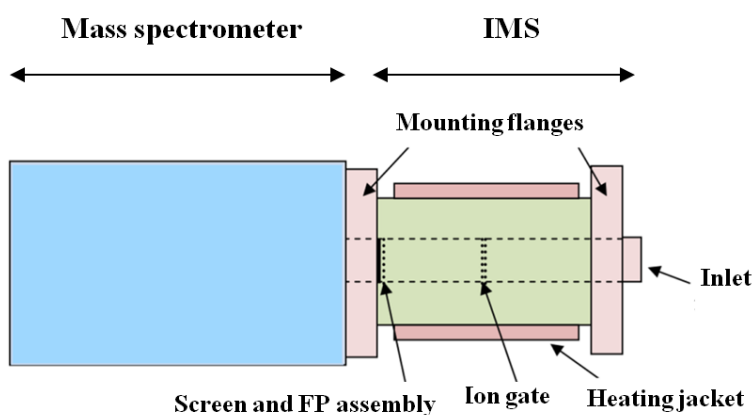


Figure 1.1 Basic layout of an IMS-QMS system. The screen is placed close to the faraday plate (FP) to shield against unwanted signal due to the electric field from the approaching ion swarm. The ion gate is placed midway along the drift tube.

Quadrupole mass spectrometers are widely used in many areas of science and their principles of operation are well documented. The use of IMS systems has however, mainly been confined to military and security applications and so for this reason most of the research details on the development of modern commercial IMS systems are not available. An introductory explanation of the operation of an IMS system is therefore given in the following sections to provide an understanding of the basic principles.

1.5 An introduction to Ion Mobility Spectrometry (IMS)

IMS is a technique used to identify low concentrations of particular ions arising from chemical compounds introduced in the gas phase into the spectrometer according to their mobility K . Mobility is a property that determines the time (known as the ‘drift time’, t_d) that it takes for the ions to travel along the drift region under the influence of a uniform electric field through a buffer gas at a given temperature. The buffer gas commonly used is purified air at slightly above atmospheric pressure. Figure 1.2 represents a typical drift tube design comprising of a cylindrical glass or ceramic tube having circular metallic drift rings clamped along its periphery.

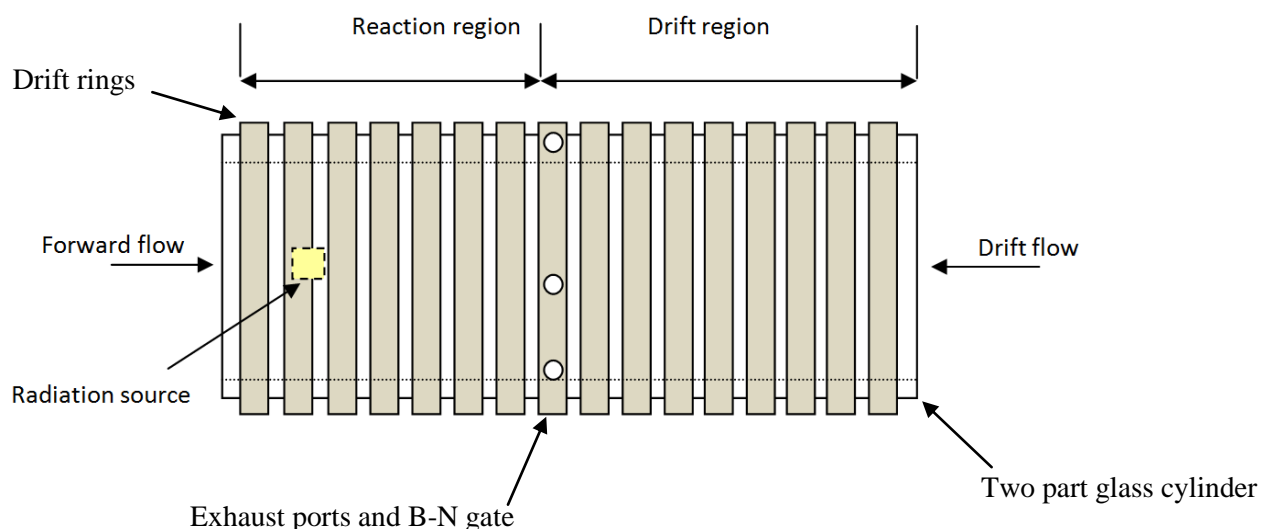


Figure 1.2 Basic components of a drift tube. The drift rings provide a linear electric field along the axis of the drift tube to impart a drift velocity on the ion swarm. The Bradbury-Nielson (B-N) gate allows a pulse of ions to be introduced into the drift region.

The electric field is set up by connecting a voltage divider resistor chain across the series of drift rings, as indicated in figure 1.3. By making all the resistors of equal value (10 M Ω in our instrument), a uniform field is set up along the reaction and drift regions. Further features of the drift tube are discussed in more detail in the next section.

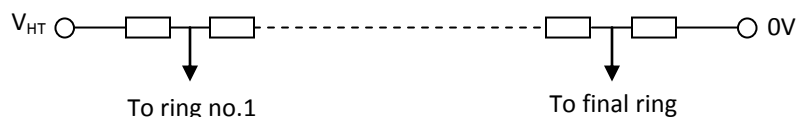


Figure 1.3 Ring connections to the resistor chain. All resistors are of equal value.

1.6 Operating principles of the drift tube

This section provides a brief overview of the operation of drift tubes typically used in ion mobility systems with the main emphasis on the equipment used by the Molecular Physics group.

Within the drift tube typically used in ion mobility systems, the following processes will occur:

- a) The sample analyte representing threat agents to be detected is introduced into the forward flow direction of the buffer gas which is normally air that has been passed through a molecular sieve to limit the moisture content in the air. It then flows into the IMS reaction region.
- b) Ionisation of predominantly the buffer gas takes place within the reaction region of the drift tube causing a series of ion-molecule chemical reactions to occur resulting in the production of reactant ions. Any trace threat molecules that are present under the investigation (e.g. DMMP used to simulate nerve agents) will interact with the reactant ions to form product ions (ionised sample molecules.) As they travel along the drift tube, ions of different mass, size and shape due to chemical structure (“cross-section”) reach different drift (terminal) velocities v_d (cm/s). In a vacuum, the drift time for a drift tube length of typically 10 cm through a gradient of 250 V/cm would be in the order of microseconds. However, in an IMS system, the drift pressure is

around one atmosphere, and so the ion drift time is actually in the order of milliseconds since the ions are slowed down by collisions with the buffer gas molecules. Note, a restriction must be met regarding the ratio of electric field strength E to gas number density N , to enable the mobility to be independent of E/N for allowing comparison of mobility values between different instruments. The restriction is that E/N is to be less than two Townsends (where 1 Townsend (Td) = 10^{-17} V cm²). This was first noticed during investigations made by Rutherford and Roentgen in the late 19th century when making measurements of the ion mobility of air molecules ionised by radiation.

- c) At an appropriate time an ion gate is quickly pulsed open to allow a small pulse of the resultant reactant ions and product ions to pass through into the drift region where they drift towards a Faraday plate (FP) (shown in figure 1.1) under the influence of the electric field applied by the drift rings. In this region separation of different species of ions occurs according to their mobility. The flow of buffer gas in this region is in the opposite direction to that in the reaction region in order to limit neutral threat agents from entering the drift region where they would continue to react with the ions. If this occurs, the mobility spectrum shows an ion signal between the peaks thereby degrading the temporal resolution and possibly masking any smaller peaks.
- d) As the ions discharge at the Faraday plate, various current pulses are produced as a function of time according to a given ion(s) mobility. Signal conditioning of the pulses is then used to enable subsequent display of the mobility spectrum.

The times taken for the various ions to travel down the tube gives an indication of what the particular chemical may be when the mobility spectrum is observed. This allows chemicals to be characterised by their ion mobility K which is determined from the drift velocity v_d attained by ions in the weak electric field E in the drift tube (typically 200 to 300 V/cm), according to the equation,

$$v_d = K \times E \quad (1.1)$$

1.7 Ion Mobility Spectrum

A mobility spectrum shows the arrival times of the ions as current peaks at various drift times. The arrival time t_d of a particular ion peak at the Faraday plate is obtained from the ion mobility spectrum, which may contain several peaks and can be said to give the chemicals signature or fingerprint. An example of a positive polarity mobility spectrum is seen in figure 1.4 (obtained using our instrument with tertiary butanol at 16 ppbv concentration in pure air) showing the reactant ion peak (RIP) $H^+(H_2O)_n$, the protonated monomer $MH^+(H_2O)_n$ and the proton bound dimer $M_2 H^+(H_2O)_n$, where M represents tertiary butanol. The intensity of each peak is related to the abundance of the corresponding ion.

One advantage of ion mobility spectra over conventional mass spectra is that it can be used to distinguish different isomers due to their differing geometries in chemical structure and hence collisional cross section.

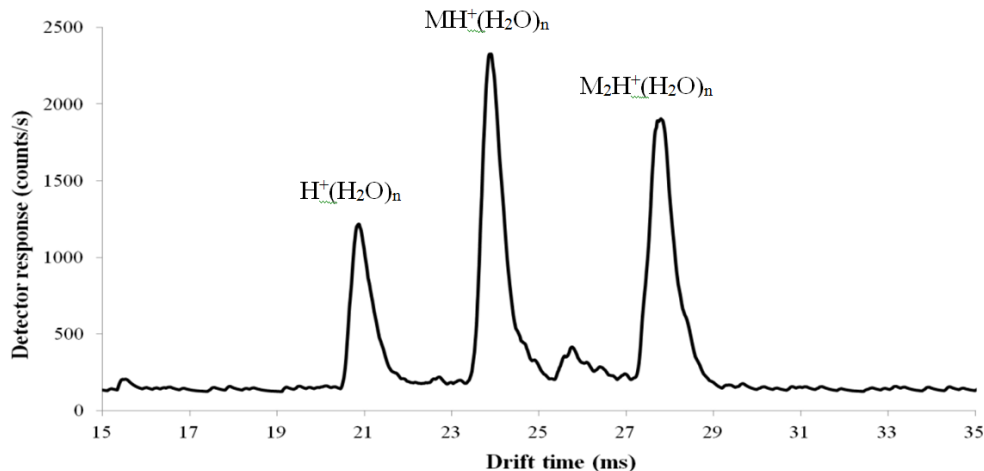


Figure 1.4 An example obtained from our system of a typical ion mobility spectrum. M represents the analyte, being tertiary butanol in this case.

1.8 IMS Components.

As previously mentioned, a typical ion mobility spectrometer is formed from the following components: An ionization source, ion gate, drift tube, a collector and corresponding electronics for signal acquisition.

Ionisation source

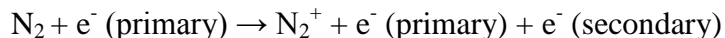
Various methods are used to provide a source of ionising radiation such as a corona discharge or by the use of radioactive materials. Corona discharge sources suffer from sputtering which requires them to be frequently cleaned or replaced. A better solution that is commonly used is a weak radioactive source (activity around 10mCi) consisting of a ^{63}Ni coated cylinder having a half life of 100.1 years and emits a constant stream of beta particles (electrons). [86] Through spontaneous disintegration of the radioactive source ($^{63}_{28}\text{Ni} \rightarrow ^{63}_{29}\text{Cu} + e^{-}$), the electrons are ejected with a range of very high kinetic energies up to a maximum energy of approximately 67

keV with a mean energy of 17 keV. Through electron impact ionisation and a series of chemical reactions (described later) this produces both positive and negative ions in the reaction region.

Since a 10 mCi radioactive source is relatively weak (for safety reasons) this sets a limit on the amount of ions produced. Therefore, at high sample concentrations, the number of sample molecules may exceed the ionisation capacity after which the detector becomes insensitive to higher concentrations. For example, in positive ion mode, when several compounds are introduced having similar proton affinities to the target compound, they are ionised in accordance with their respective concentrations. A problem may arise if the target compound has a lower proton affinity than those of the interference compounds since they may be more easily ionised leaving a depletion of ions for target recognition. This may cause a false negative response such as that mentioned in section 1.1. In this situation, molecules with a high charge affinity are more easily ionised than the target chemical, M which causes the response to the target to be suppressed. This effect can be reduced by adding a chemical dopant (reagent gas) such as acetone or ammonia into the reaction region allowing the final form of the reactant ions to be optimised for selective sample ionisation.

IMS systems can operate in either positive or negative ion mode depending on the sample for detection. In order to do this, the direction of the electric field is arranged to suit (e.g. in positive mode to detect cations, the ion source is at a high positive potential (several kV) and the detector is virtually at 0V potential). Nerve agents react efficiently with positive ions in an IMS environment whereas for the detection of explosives the IMS must be operated in negative ion mode. This method of ionisation of the sample molecules is known as “Atmospheric Pressure Chemical Ionisation” APCI. In the reaction region where the ions are formed, the high energy

electrons from the ionisation source predominantly ionise the nitrogen and oxygen gas molecules in the buffer gas (air). Cations and secondary electrons are formed. For example;

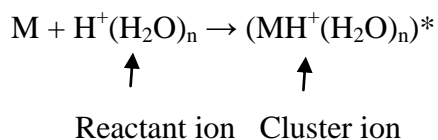


During this process, a steady state of approximately 10^7 ions per cm^3 is produced by the 10 mCi radiation source. (See Appendix A1.1)

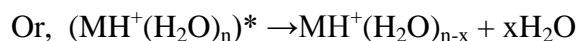
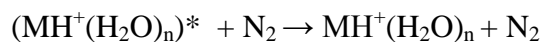
Positive ion mode

In the reaction region, the N_2^+ ions are short lived because they rapidly react with other species (predominantly O_2) and water vapour present in the purified air carrier gas and consequently do not appear in the mobility spectrum. Through a series of ion-molecule reactions the reactant (terminal) ions are ultimately produced being predominantly $\text{H}^+(\text{H}_2\text{O})_n$ (hydrated protons) where n typically is 1 to 4. The actual size of the water clusters produced is dependent on the humidity in the drift tube.

If M represents the trace molecule to be detected, and providing that M has a higher proton affinity than the water cluster, then the formation of cations follows the route: [66]

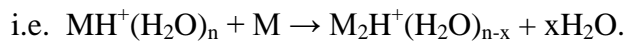


The cluster ion complex may be stabilised by collisions with N_2 or another air molecule or through a loss of water molecules to form the product ion as follows:



The product ion is called a protonated monomer.

As the concentration of the threat agent M increases, there is a possibility of the formation of a proton-bound dimer product ion whereby another sample neutral molecule attaches to the protonated monomer,



↑ ↑ ↑

cluster ion neutral sample protonated dimer

The dimer produces another peak in the IMS spectra. This observation can reduce the incidence of false alarms, since the chance of two different chemicals producing both a monomer and a dimer at the same corresponding drift times is less likely than if the monomer drift time only was considered.

Ion Gate

Once product ions have been formed they enter the drift region in short pulses. This is achieved by using an electronically pulsed ion gate. The pulse that triggers the gate operation also triggers the data acquisition program to start the timing of the ions from the gate to the Faraday plate.

A design based on the Bradbury-Neilson gate invented in 1936 is commonly used [87-90] which consists of a grid of interdigitated wires as shown in Figure 1.5. When a potential difference is applied across the wires (typically 100 V), the ions are deflected through 90° and collide with the wires thereby dissipating their charge. The neutrals are then passed through the exhaust port along with the contra flowing drift gas. By setting the wires to the same potential (as that of the adjacent ring) the ions will pass through the gate and will be carried by the electric field into the drift region. Typically, the gate pulse width is 0.2 ms wide, and operates at a pulse frequency of

25 Hz (corresponding to a sampling time of 40 ms). The time that the gate is ‘open’ is kept short to improve ion separation and hence resolution as the ion swarm travels down the drift region. (We have found that with gate pulse widths of up to 0.3 ms the full width half maximum (FWHM) of the ion peak in the mobility spectrum is relatively independent of pulse width. At pulse widths lower than 0.3 ms, there is a rapid fall off in the amplitude of the peak).

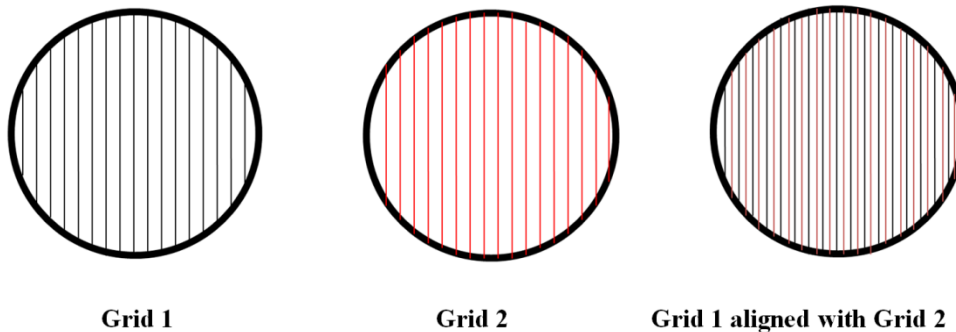


Figure 1.5 Alignment of the grids forming the ion gate to allow interdigitation of the wires.

The ion gate is formed from two etched grids where the wires are offset relative to each other by half a grid spacing. The grids are then aligned one on top of the other (with an intervening insulating ring to provide isolation). One side of the grid is connected to its adjacent ring, the other side then being connected to the gate pulse circuit.

Drift Tube

In the drift region, the ions travel along the electric field lines from the gate to the collector, separating out along the way according to their mobilities. When the ions reach the collector, they are discharged and produce an electric current which is then amplified by the corresponding circuitry.

If the drift tube is too short, this could result in overlapping peaks because ion-separation may be insufficient, resulting in poor resolution. By using long drift tubes better separation of the ions can be achieved. However, as the ions pass down the drift tube, they gradually spread out axially and disperse radially due to diffusion and coulombic repulsion [91] from their similarly charged neighbours. The overall effect is the loss of ions and broadening of the mobility peaks with a subsequent loss in peak intensity. These constraints therefore impose practical limits on the dimensional size of the drift region. [92-94]

The issues of diffusion and resolution are outlined in more detail in section 1.9.

In our instrument, the construction of the drift tube used (referring to figure 1.2) is such that there are 16 rings in total, each 9 mm wide and equally spaced apart at 2 mm separation. The length of the drift region (from gate to FP) is 10.36 cm and with 4.5 kV applied to the high voltage connection on the first ring, the electric field gradient is produced along the axis of the drift tube is 217 V/cm.

The temperature of the drift tube is controlled, and set to a temperature of 30 °C to avoid the need to compensate for changes in ambient temperature. (Miniaturised portable systems such as the CAM do not have temperature control in order to conserve power. Instead, they monitor the tube temperature with a thermistor and take this into account at the signal processing stage when calculating ion mobility).

Pressure changes will also affect the signal response times and so must also be taken into account when obtaining a reduced mobility.

Screen grid

Just prior to reaching the Faraday plate (FP), the ion swarm pulse passes through a screen electrode (a perforated piece of stiff gold plated foil) placed approximately 1.5 mm in front of the FP). The purpose of this is to shield the FP from the electric field produced by the oncoming ion swarm, which would otherwise induce an unwanted signal (an image current) that would degrade the sharpness of the peaks. In our instrument, the optimum potential applied to the screen to allow maximum ion transmission was found to be around +25 V. A side issue from introducing the screen grid is that it forms a microphonic effect with the Faraday plate introducing noise interference from any vibrations due to the turbomolecular pumps used on the mass spectrometer (see later), which is then superimposed onto the ion response signal. This can be minimised by averaging the data obtained over a number of mobility spectra in order to have an acceptable signal to noise ratio (typically taking approximately 20 s to do 500 averages).

Faraday plate (FP)

This is the final destination for most of the ions and is located at the end of the drift tube. As the ions strike the FP they release their charge. The number of ions hitting the FP gives a proportional signal strength and hence the height of a peak is an indication of the relative concentration of the representative chemical.

The FP is simply a circular metal disk with a laser etched hole of diameter 0.07 mm in the centre to produce an orifice that allows a sample of the ions to pass from the drift tube (at atmospheric pressure) into the vacuum of the mass spectrometer to enable them to be mass analysed. Only about 0.1% of the total ions get through due to the requirement of such a small orifice to maintain the pressure differential.

(Prior to the ions entering the mass spectrometer, the Faraday plate and screen grid are mounted on the inlet to the mass spectrometer chamber, and are supplied from separate voltage sources.)

The current pulse flowing from the FP is in the order of about 0.1 nA and so must be suitably amplified prior to it being digitised to facilitate processing for display of the ion mobility spectrum. [95] The amplification process is achieved by converting the current to a proportional voltage which is then amplified to produce an output of 1V when the input current is 10 nA. The digitisation involves conversion from the analogue voltage into its equivalent binary form using a data acquisition card (the type used is the PCI-6014 manufactured by National Instruments).

[96]

A mobility spectrum is obtained by averaging over several hundred scans in order to reduce unwanted background noise picked up from the turbo molecular pumps such that an acceptable signal-to-noise ratio is reached.

The amplifier and all of the other associated electronics required to operate the IMS were designed and built in the laboratory, the details of which are described fully in chapter 2.

Displaying of mass spectra and ion mobility spectra was accomplished by using a suite of programs developed using LabVIEW version 7.1 (© National Instruments). A description of the programs and the associated hardware connections is provided in Chapter 3.

1.9 IMS Performance and limiting factors

There are two aspects critical to IMS performance which are outlined below:

Resolving power – the ability of the instrument to distinguish between different ion peaks.

Sensitivity – this is a measure of the instruments capability to detect low concentrations (ppmv to ppbv) of a threat agent as an observable signal above background noise.

A definition of the resolving power of an IMS instrument usually quoted [97] is:

$$R_p = \frac{t_d}{t_w} \quad (1.2)$$

Where t_d = drift time of the ion peak and t_w = width of the ion peak at half its maximum height (also called ‘full width at half maximum’ FWHM.)

For commercial instruments, the value of R_p is typically 30 to 50 and around 150 for high resolution systems [66]. For our system, it was found that t_w was 0.3 ms when the RIP for water clusters arrived at a t_d of 20.6 ms giving a value for R_p of approximately 69. Since resolution is also dependent on gate pulse width and field strength, these parameters need to be taken into consideration to optimise the RIP without losing too much signal peak intensity [98].

1.10 Theoretical Considerations of IMS Operation

Within a short time interval an ion may collide with a neutral drift gas molecule which could slow or even stop its motion. It then accelerates again until another collision occurs. The average distance that an ion travels between collisions is reflected by its mean free path. As a result of this continuous acceleration and deceleration of individual ions, the ion swarm will eventually reach an average terminal speed known as the drift velocity v_d . Thus, the velocity is dependent on the collision frequency (ions with larger cross-sections will collide with molecules in the drift flow more frequently than ions having smaller cross-sections). Owing to the large number of collisions, the total distance an ion travels through its ‘random walk’ is roughly 50 times that of

the gate to the collector [66]. In our instrument, we found that t_d for H_3O^+ is about 20.6 ms (at $E = 217 \text{ V/cm}$, $T = 30 \text{ }^\circ\text{C}$ and $P = 1006 \text{ mbar}$). The length of the drift region is 10.36 cm and so the velocity v_d is approximately 5 m/s.

The mobility constant K has a specific value for a particular ion under a given set of conditions of temperature, pressure and drift gas. It has been found from early experiments on ions in gases (around 1934), that the mobility K is independent of the ratio of E/N up to about two Townsends (Td) (where $1 \text{ Td} = 10^{-17} \text{ Vcm}^2$). N is the number density of the ions. However, at values of E/N greater than about 2 Td, mobility does become dependent on E/N [66]. For our instrument, E/N is set at approximately 0.94 Td (see calculation in Appendix A1.2).

The weak field relationship between K and the diffusion coefficient D is given by the Einstein relationship $K = \frac{eD}{kT}$ where e is the charge on the ion, and k is Boltzmann's constant. This equation is valid only when the electric field does not cause heating of the ions. To satisfy this condition, the energy gained by the ions from the electric field between collisions should be much less than their thermal energy. When this is not the case, the ions are no longer thermalised, the diffusive forces are not spherically symmetrical and the Einstein equation becomes invalid. K then becomes dependant on the ratio E/N .

Thus, E must be a relatively weak field in order for K to be independent of field strength. At high field strengths, the drift velocity and hence K becomes unpredictable.

In our instrument, the energy gained by the ions from the electric field is only about 0.013% of their thermal energy (see appendix A1.3).

1.11 Determining K theoretically

From the theoretical modelling by Revercomb and Mason [99] and McDaniel [100] of ion behaviour in an electric field, a fundamental relationship between ion mobility and collision at the molecular level is commonly quoted when considering the effect on K of various parameters.

Namely:

$$K = \frac{3q}{16N} \left(\frac{2\pi}{\mu kT} \right)^{\frac{1}{2}} \left(\frac{1}{\Omega} \right) \quad (1.3)$$

where:

$\mu = \frac{Mm}{M+m}$ is the “reduced mass” of the ion, m is the mass of the ion, M is the mass of

the drift gas, q is the charge on the ion, N is the number density of the drift gas, k is

Boltzmann’s constant, T is the absolute temperature, and Ω is the collision cross section of the ion in the drift gas.

When $m \gg M$, μ approximates to m and so K varies only in inverse proportion to Ω . (The cross section Ω is determined from the ions size, shape and polarisability.)

It is the variation of mobility with ion cross-section that causes the separation of different ion species and forms the basis of IMS. Conversely, when K is known, the cross-section of the ion can be found from a re-arrangement of equation 1.3.

1.12 Determining K Practically

If V is the voltage on the drift ring at the start of the drift region relative to ground (at the end of

the drift region), and L is the length of the drift region, then $E = \frac{V}{L}$, but $K = \frac{v_d}{E}$ and so

$$K = \frac{Lv_d}{V}, \text{ but } v_d = \frac{L}{t_d} \text{ which finally gives } K = \frac{L^2}{Vt_d} \quad (1.4)$$

With L and V fixed, we can set a constant $b = \frac{L^2}{V}$ and so $K = \frac{b}{t_d}$

Thus K for a particular ion is easily calculated from its arrival time.

For given operating conditions of pressure and temperature, the ion mass and cross section fundamentally determine the mobility of an ionised compound. The normalised operating conditions agreed on within the IMS community are at standard temperature and pressure (STP) which can be approximated by converting the measured mobility into a ‘reduced mobility’ so allowing comparison to be made with K_0 values obtained by other workers in the field where different operating conditions may exist. Temperature and pressure changes will affect signal response times and so must be compensated for during signal processing. The measured mobility K is then expressed as a reduced mobility K_0 where:

$$K_0 = K \frac{273}{T} \frac{P}{1013} \quad (1.5).$$

T represents the temperature of the drift gas in degrees Kelvin and P is the pressure inside the tube in mbar. By doing this, comparisons can be made between systems having different operating conditions.

1.13 Effect of errors in measurement of K_0

Errors in measuring the parameters E, L, T and P are due to various factors which will influence the final value obtained for K_0 , these being:

E – Apart from error in the direct measurement of the applied voltage V_{HT} , the linearity of the electric field depends on the tolerance in value of the series of resistors forming the divider chain. Since high value resistors are difficult to obtain with tolerances $< 5\%$, this will affect the homogeneity of the electric field.

L – It is not straightforward to directly measure the distance between the gate and the FP and so it must be inferred from design drawings. The distance is also influenced in operation by thermal expansion and clamping pressure on the ‘O-ring’ seals.

T – Ideally, this represents the actual temperature of the drift gas. It is not however possible to measure this directly using a thermocouple since any additional connections involve dissimilar metal-metal contact introducing errors in the overall equivalent thermal voltage presented by the thermocouple. The temperature is therefore measured at the body of the drift tube and so a deviation from the actual drift gas temperature may be present.

P – The pressure of the drift gas may be determined with reasonable accuracy from monitoring the pressure of the carrier gas supply as it enters the drift region (the ‘contra flow’).

Errors in measurement of the parameters are in the order of $\pm 1\%$ for *L*, $\pm 2\%$ for V_{HT} , $\pm 1\%$ for t_d , $\pm 2\%$ for *P* and $\pm 1\%$ for *T*. The overall error can therefore be calculated and is around $\pm 5\%$ to a first approximation. This figure is in agreement with that given in a paper by Vautz et.al. [101].

The drift time for water clusters in air mentioned in section 1.2.3 for our system was 20.6 ms, and using equation 1.3 gives $K = (10.36)^2 / (2194 \times 0.0206) = 2.38 \text{ cm}^2/\text{Vs}$ (*V* was measured as 2194 V when the applied voltage V_{HT} was 4500 V.)

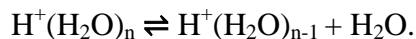
At 30 °C ($T = 273 + 30 = 303\text{ K}$) and $P = 1006\text{ mbar}$, then from equation 1.5,

$$K_o = 2.38 \left(\frac{273}{303} \right) \left(\frac{1006}{1013} \right) = 2.12 \pm 5\% \text{ cm}^2 \text{ V}^{-1} \text{ s}^{-1} \text{ which is only about 2.8\% larger than}$$

that quoted by Vautz et. al, although their operating temperature was less than that of the present study. Within experimental error, the values of K_o can be considered to be in agreement. Values of K_o will to a certain extent be machine specific. This is because it is a characteristic of the instrument which varies with humidity and temperature of the carrier gas, in turn affecting the concentration and size of the water clusters surrounding the ion and hence its mobility.

1.14 Ion-molecule reactions in the positive ions mode

In an undoped system, ion mobility peaks seen in the absence of analyte are generally due to protonated water clusters being $\text{H}^+(\text{H}_2\text{O})_n$ where $n = 1$ to 4 as discussed in chapter 4. The water clusters $\text{H}^+(\text{H}_2\text{O})_n$ signifying the RIP appear in the mobility spectrum as a single peak representing the weighted average of their drift times. This is due to the clusters continually switching in size due to break up from collisions with carrier gas molecules and then recluster according to the relationship



The use of chemical dopants

It was mentioned in section 1.1 that one of the main problems associated with detection of chemical warfare agents (CWAs) using ion mobility spectrometry is that it is prone to giving “false positives” from environmental compounds having mobilities similar to that of a CWA. A reduction in response to these interfering background chemicals may be gained by using a

chemical dopant in the ionising region. This is the approach taken with IMS systems for military and security use.

With the system undoped and operating in positive mode, the reactant ion peak is formed from the protonated water cluster ions $H^+(H_2O)_n$ where $n = 1$ to 4 clusters are dominant. The proton affinity (PA) of water quoted by NIST is 165.2 kcal/mol [102] and any chemical molecule with a higher PA will spontaneously react with the protonated water to form a product ion. In the case of higher order water clusters, a proton transfer reaction will take place providing that the PA of the neutral cluster is less than that of the analyte molecule [103,104]. This condition can be stated as

$H^+(H_2O)_n + M \rightarrow MH^+ + (H_2O)_n$ occurring spontaneously when $PA(H_2O)_n < PA(M)$, whereby the change in enthalpy of reaction $\Delta H = PA(M) - PA(H_2O)_n > 0$, with $n = 1, 2, 3 \dots$ is exothermic.

The level of hydration may thus place a limit on the ability to detect certain analytes. For example, the PA of water clusters increases with cluster size as seen in table 1.1 given by Cheng [105]. (PA values for water clusters differ slightly between various authors by about 3%.) Thus, in a dry system, it may be possible to protonate vapours of say, isopropyl alcohol which has a PA of 189.5 kcal/mol when only single water molecules ($PA = 173.4$ kcal/mol) are present. For higher order water clusters however, their PA is >189.5 kcal/mol and so protonation would then not be possible. In most IMS systems particularly those operating at ambient temperatures (as is the case with portable military systems where clustering is also inevitable), certain vapours such as those arising from explosives are not generally detectable in positive ion mode. In such cases,

the negative ion mode of operation is used where it is found that the electron affinity of the analyte provides a more energetically favourable route for a reaction to occur.

Table 1.1 Proton affinity of water clusters $(\text{H}_2\text{O})_n$ as stated by Cheng [105]

$\text{H}^+(\text{H}_2\text{O})_n, n$	1	2	3	4	5
PA (kcal/mol)	173.4	206.6	213.5	223.7	231

By adding a dopant to the carrier gas, a change in ionization selectivity is achieved. For example, by doping with ammonia (NH_3) vapour, the reactant ion will change to $(\text{H}_2\text{O})_n\text{NH}_4^+$, which selectively ionizes compounds with a higher PA than NH_3 (204.0 kcal/mol). Thus any interferences with $\text{PA} > \text{H}_2\text{O}$ and $< \text{NH}_3$ that may have been seen in a water chemistry based system will now be suppressed in an ammonia based system, hence the incidence of false positives due to these interferences will be reduced.

Dopants currently in use with military IMS systems are monomers of ammonia (PA = 204.0 kcal/mol) and acetone (PA = 194.1 kcal/mol). These dopants therefore provide a system that is less susceptible to background interferences. CWAs which are mostly organophosphates having a PA > 210 kcal/mol will thus form product ions from a doped system. Using a dopant affects the ion drift velocity since it will change the size of the cluster ion, i.e. if M represents the sample molecule, then in an undoped system, the product ion would be the protonated monomer $\text{MH}^+(\text{H}_2\text{O})_n$. But for the same system with say, acetone doping, there would be instead, the protonated acetone associated monomer $\text{MAcH}^+(\text{H}_2\text{O})_m$ where $m < n$. [66] Therefore since $\text{MH}^+(\text{H}_2\text{O})_n$ will have a smaller cross sectional area than $\text{MAcH}^+(\text{H}_2\text{O})_m$ (H_2O has a mass of 18 amu whereas Ac being $\text{OC}(\text{CH}_3)_2$ has a mass of 58 amu) it will have a higher drift velocity and

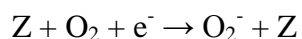
hence mobility. Note, ammonia NH_3 has a mass of 17 amu and so ions formed from using this dopant will have a higher drift velocity than in the undoped case. This effect would be advantageous for separating out peaks that may otherwise have overlapped in an undoped system. For example, it can also be used to shift the RIP to a position away from that of the target chemical in cases where they otherwise may overlap (causing false negatives).

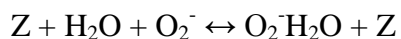
Whether doped or undoped, a sufficiently high concentration of sample will produce a proton bound dimer in the mobility spectrum. Very high concentrations may lead to the formation of trimers.

1.15 Ion-molecule reactions in the negative ions mode

In a manner similar to that for the formation of positive ions, negative ions are formed from initial collisions of molecules with electrons. The molecular cross-section is dependent on the energy of the electrons and the electron affinity of the molecule [106]. At ambient pressure, beta electrons from the ^{63}Ni radiation source will be rapidly thermalised to a low energy state. During this process, each beta particle ionises a considerable amount of N_2 and O_2 molecules. For example, the ionisation potential of N_2 is ~ 15.6 eV and so with an average energy of 17 keV, each beta particle could ionise ~ 1000 N_2 molecules producing ~ 1000 secondary electrons. In a pure nitrogen carrier gas the secondary electrons can be observed in the mobility spectrum [107] and act as ‘reactant ions’. The N_2^+ ions however have a very short lifetime and are therefore not seen in the mobility spectrum.

In air, the thermalised electrons attach to oxygen through three body collisions [108] to form O_2^- and its hydrates as follows:





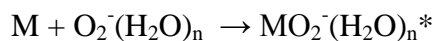
Where Z represents the stabilising third body which may be N₂, O₂, H₂O or another neutral molecule.

Table 1.2 lists ions seen in previous investigations by Spangler [109] and Carr [110] using IMS-MS systems. These are a result of using air with a significant CO₂ content. Ions containing Cl⁻ and CN are from impurities.

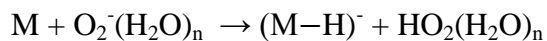
Table 1.2 Reactant anions observed in previous studies by Carr and Spangler [109,110]

m/z	26	32	35	35	42	46	50
(Carr)	CN ⁻	O ₂ ⁻	Cl ⁻		CNO ⁻	NO ₂ ⁻	
(Spangler)		O ₂ ⁻	Cl ⁻	(H ₂ O)OH ⁻		NO ₂ ⁻	(H ₂ O)O ₂ ⁻
m/z	52	53	60	64	68	76	
(Carr)	(H ₂ O) ₂ O ⁻		CO ₃ ⁻	O ₄ ⁻		CO ₄ ⁻	
(Spangler)		(H ₂ O)OH ⁻			(H ₂ O) ₂ O ₂ ⁻	CO ₄ ⁻	

With an analyte M present, the analyte may react with the reactant ions via charge exchange and a loss of water to form product ions as follows:



$MO_2^-(H_2O)_n^* \leftrightarrow MO_2^-(H_2O)_{n-1} + (H_2O)$ although other mechanisms such as proton abstraction can also occur, i.e.



1.16 Concluding remarks

In this first chapter, the concept of ion mobility spectrometry has been introduced in general along with the advantages of coupling to a mass spectrometer to gain additional information on the chemical processes taking place. Information specific to our instrument was mentioned and this will now be greatly expanded on in the following chapters. In chapter 2, the design and application of the instrumentation used to control principally the IMS section of the system will next be discussed.

CHAPTER 2 DEVELOPMENT OF THE IMS-QMS INSTRUMENTATION

In this chapter, the hardware aspects of the system and its instrumentation developed to control the IMS are discussed. Although the mechanical hardware is mentioned, this chapter chiefly concerns the development and application of the electrical and electronic parts of the system.

2.1 Practical system arrangement

Figure 2.1 below is a schematic drawing of the Birmingham IMS-QMS system showing the drift tube, differential and mass spectrometer regions, and the configuration of the air flows. This is a modification of the system originally used by the group for electron attachment studies [111] where a different type of drift tube was used, which was found to be unsuitable for our purposes.

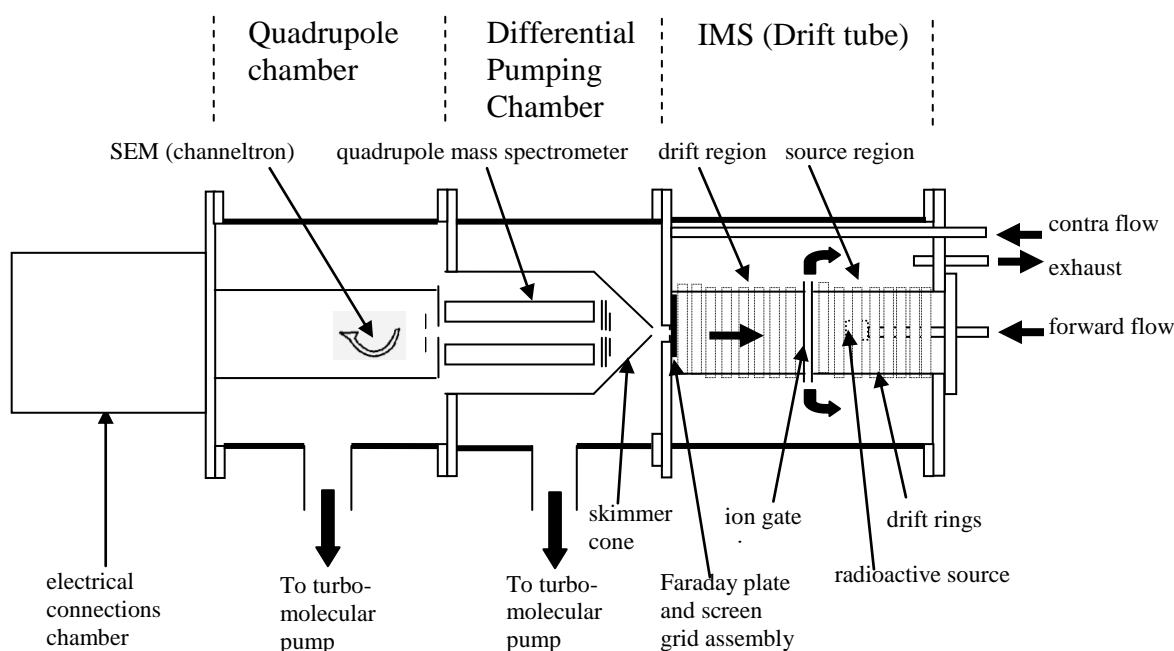


Figure 2.1 Schematic layout of the IMS-QMS system showing the IMS-QMS interface and flow of carrier gas

From figure 2.1 it is seen that in the drift tube, carrier gas is introduced as the forward flow in the source region, and as the contra flow in the drift region. The flows then pass through orifices drilled along the periphery of the guard ring connected to the ion gate, and out through the exhaust port.

A thermocouple is used to measure the temperature of the outer flange where the connections are made for the gas flows and electrical items. This provides a reasonably accurate value of the temperature of the carrier gas in the drift region (see appendix A4.11).

In order to gain maximum signal sensitivity, the channeltron is used in preference to the Faraday Plate (FP) within the mass spectrometer. Two issues to be aware of when using a channeltron are:

- Unlike a FP, a channeltron can be saturated when the signal strength is too high (or even damaged when excessively high) – which however is very unlikely in our system where analyte concentrations are typically in the ppbv range, resulting in relatively low signal counts.
- A FP has an absolute measure of sensitivity, however, the performance of a channeltron will gradually diminish over time as the emissivity of its surfaces degrades.

An important consideration is the amount of moisture present in the carrier gas flows. In order to remove as much moisture as possible from the carrier gas supply, a molecular sieve is connected in series with the source. In order to determine how effective the sieve is, the amount of moisture in ppmv was measured as described in the next section.

2.2 Measurement of relative humidity in the gas flows

The relative humidity (RH) is a measure of the amount of moisture present in the air and is expressed at a particular temperature as:

$$RH = \frac{\textit{amount of moisture present}}{\textit{maximum amount of moisture possible}} \times 100 \%$$

The ‘Dewpoint’ refers to 100% saturation of the air (corresponding to the denominator in the above equation) beyond which on any further cooling, condensation will occur. Since, cooler air can hold less moisture, the relative humidity increases as the temperature falls reaching 100% at the dewpoint. In order to measure the RH of the incoming clean air supply to the IMS, a dewpoint measuring instrument “EasiDew” manufactured by Mitchell Instruments was used.

[112]

In mass spectrometry, it is considered convenient to quote the moisture content of air in ppm by volume (ppmv). This can then be related to RH by a using conversion factor as explained in a technical article by Mitchell Instruments [113].

Moisture content of the lab air used

Using the ‘easidew’ portable hygrometer, the dewpoint (°C) was measured of the air flowing from the molecular sieve. The manufacturers recommended flow rates for obtaining an accurate reading are between 1 and 5 l/min, and so the flow rate was set at around 1.2 l/min (with 0.3 l/min in the forward flow and 0.6 l/min contra flow) to conserve the supply of gas.

After allowing an hour or so for the sensor to become conditioned, the air from the molecular sieve gave a reading of $-65.8\text{ }^{\circ}\text{C dp}$. which corresponds to a low water vapour concentration of 9.1 ppmv.

Without using the sieve, a reading of $10.6\text{ }^{\circ}\text{Cdp}$ was obtained which corresponds to a high water vapour concentration of 12778 ppmv. Thus, the molecular sieve effectively blocked most of the moisture in the air from reaching the system.

2.3 Carrier gas considerations

In Chapter 4 section 4.2.1, the dewpoint of the air in the drift tube is quoted as $-65.8\text{ }^{\circ}\text{Cdp}$ corresponding to 9.1 ppmv of water vapour. This level of moisture enabled the production of sufficient reactant ions to allow the system to be characterised. Since then, two factors regarding the gas flows have arisen that require addressing:

1. It may be necessary to have moisture levels down to around 2 ppmv for the investigations described in this chapter to be made.
2. It would be better not to have to shut down the system after use (which is necessary to avoid using up the bottled compressed air) but to leave the carrier gas flows permanently on. This would keep the system clean by avoiding the ingress of contaminants. It was also seen from the hygrometer readings that it took several hours for the moisture content in the system to diminish after switch-on of the gas flows and so this concern would also be addressed with a permanent flow of carrier gas.

In light of the long settling time also taken for the system to stabilise electrically after switch-on, (see Tests 4.9 and 4.10) the high voltage to the drift tube could then be permanently connected (since the system would then no longer require pumping down

after use). Clearly, a permanent supply of carrier gas precludes the use of bottles, and so a solution would be to pipe compressed air from an oil-free air compressor followed by a pressure swing drier to remove most of the moisture before passing through molecular sieves to trap any hydrocarbons present and to reduce the moisture content further.

Prior to having this facility of a permanent clean air supply, the investigations described in this thesis were made using bottled pure air or nitrogen as the carrier gas. The gas was passed through a series of molecular sieves to reduce the hydrocarbons to insignificant levels, and the moisture content in the gas flows to a few ppmv.

2.4 Calculating reduced mobilities

From mobility spectra, the reduced mobility of the analyte can readily be determined as follows:

Considering equation 1.4 in chapter 1 (page 21) and calculating K using in our case $T = 30^\circ\text{C} = 303\text{ K}$ and $L = 10.36\text{ cm}$, the equation for reduced mobility becomes;

$$K_0 \sim \frac{0.095462}{V} \times \frac{P}{t_d - t_{ms} - t_f} \quad (2.1)$$

where P is in mbar, t_d is in ms as measured at the detector (being the channeltron in the mass spectrometer), t_{ms} is the transit time of the ions through the mass spectrometer (i.e. Faraday plate-to-channeltron, $\sim 0.3\text{ ms}$) and t_f is the group delay time of the reconstruction filter ($\sim 0.2\text{ ms}$ when used). Note, the voltage across the drift region (measured at the gate) is 2194 V with 4.5 kV applied across the drift tube terminals. Thus, the voltage across the drift region is $\frac{2194}{4.5} \times V_{HT} = 487.56 \times V_{HT}$.

With V_{HT} in kV, equation 2.1 can be written as: $K_0 \sim \frac{95.462}{487.56 \times V_{HT}} \times \frac{P}{t_d - t_{ms} - t_f}$

i.e. $K_0 \sim \frac{0.1958}{V_{HT}} \times \frac{P}{t_d - t_{ms} - t_f}$ (2.2)

2.5 Electronics Development

This section describes the development processes for the electronics requirements of the IMS-QMS system. (The existing electronics for the mass spectrometer was manufactured by VG Quadrupoles.) For the mechanical aspects, an adaption was made of a set-up used previously in the group for electron attachment studies. This provided all the necessary requirements in terms of a drift tube, a mass spectrometer and associated vacuum pumps. However, an alternative drift tube was used that was found to give a better response. The main needs for which electronic circuitry was produced were for:

- Trigger and gate pulse generation for data acquisition and ion pulse control.
- Gate pulse interfacing (to the drift tube).
- Ion current amplification (using an electrometer).
- Switching the Faraday plate between ion collector and ion lens mode.
- Control of the drift tube heater.
- Acquisition of channeltron pulses and processing for tuned mass mobility.

The signal requirements of the LabVIEW data acquisition programs were also a consideration in the design of the electrometer in terms of the voltage level required to represent an ion current of 1 nA such that the onboard A/D converter was not

overloaded. The design and rationale for the requirements of the above sections are described in this chapter.

A common power supply consisting of a stabilised and over-current protected voltage supply of ± 12 V was used to power the circuits of all the sections mentioned above, except for the gate pulse interface unit, which has its own special power sources internally derived from the 230 V input mains supply.

2.6 Trigger and Gate Pulse Generator

A block diagram of the principle sections comprising this unit is shown in figure 2.2 following.

The trigger output connects to the LabVIEW interface box (where all the connections from the peripheral devices are made) and the gate output connects to the gate interface unit. Integrated circuits using the NE555 timer chip manufactured by Texas Instruments [114] were used for generating the astable and monostable functions.

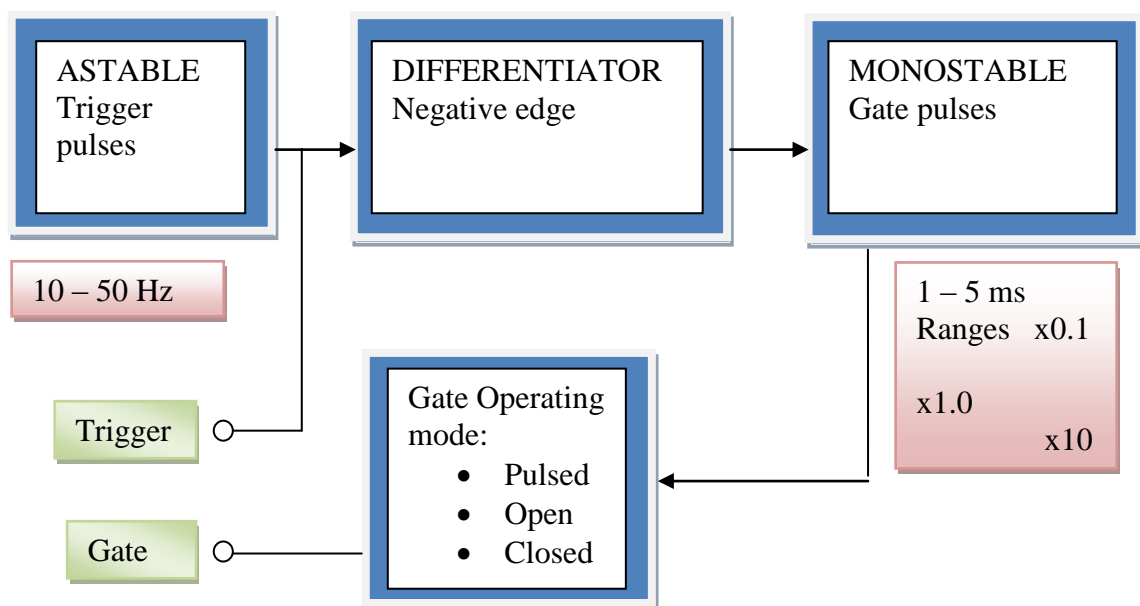


Figure 2.2 The functional blocks of the gate pulse generator

Figure 2.3 shows the circuit diagram of the basic astable (using IC1), differentiator, and the monostable (using IC2) sections developed for this project. Although more stable pulses could be derived from a crystal-controlled digital circuit using logic gates, this would be considerably more complex to design and build due to the fine variations in, and wide range of, pulse width and frequency required. By using the analogue timer, this enables the requirements of the pulse generator to be met more easily. With regards to stability, the NE555 is quite stable but although inferior to that of a crystal, it is of no consequence here since immediately the trigger pulse occurs, an accurate scan over 40 ms is taken by using the data acquisition board (NI6014) that accompanies LabVIEW. Subsequent scans only require that the trigger pulse occurs at fairly constant intervals of slightly greater than 40 ms. (If somewhat less than 40 ms, an extra partial scan is seen in the ion mobility spectrum.)

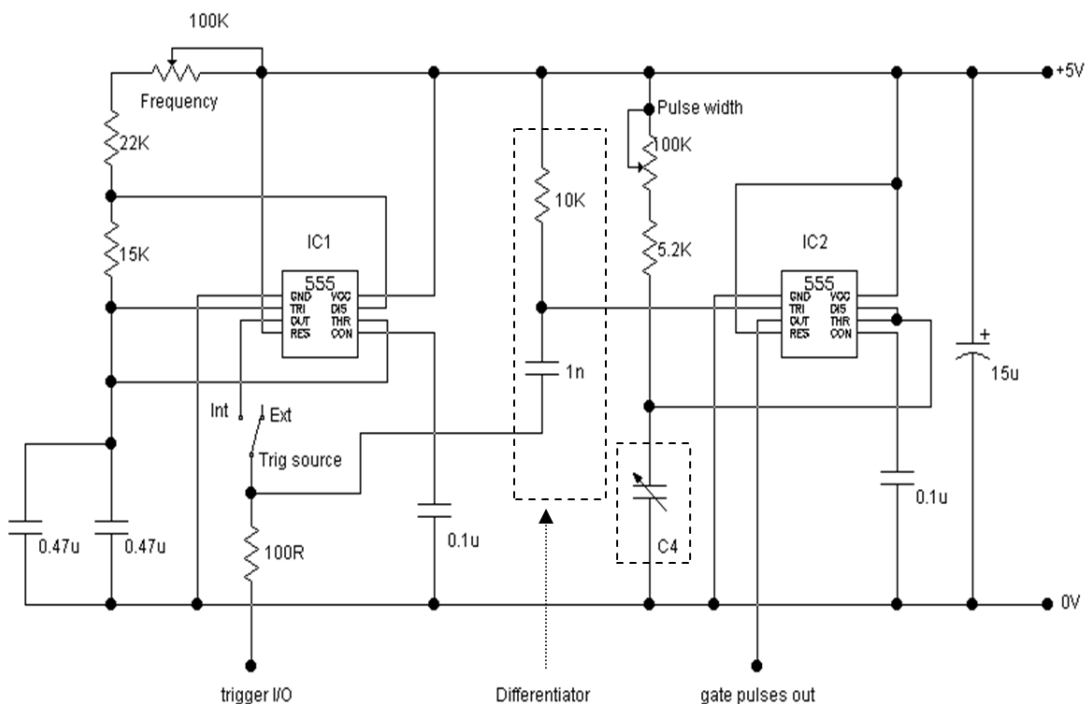


Figure 2.3 Circuit diagram showing the main operating sections of the pulse generator

IC1 forms the Astable multivibrator section providing trigger pulses for the LabVIEW data acquisition card (DAQ). It also (when switched to internal trigger) provides via

the differentiator circuit, trigger pulses for IC2 which forms the Monostable multivibrator section that provides the pulses out to the gate interface unit. C4 represents the ‘pulse width range extension’ section which is described later.

Design considerations for the pulse generator

The frequency of the gate pulses in IMS systems is typically 25 Hz corresponding to a time period of 40 ms for the ion mobility spectrum. For flexibility, it was decided to make this variable between 10 and 50 Hz. Figures 2.4 and 2.5 show how the connections are made to the ‘555 timer to obtain Astable and Monostable operation respectively. In the formulae for frequency and time calculations, $R_a = R_v + R_1$

$$f = \frac{1}{1.11C(R_a + 2R_b)} \quad (2.2)$$

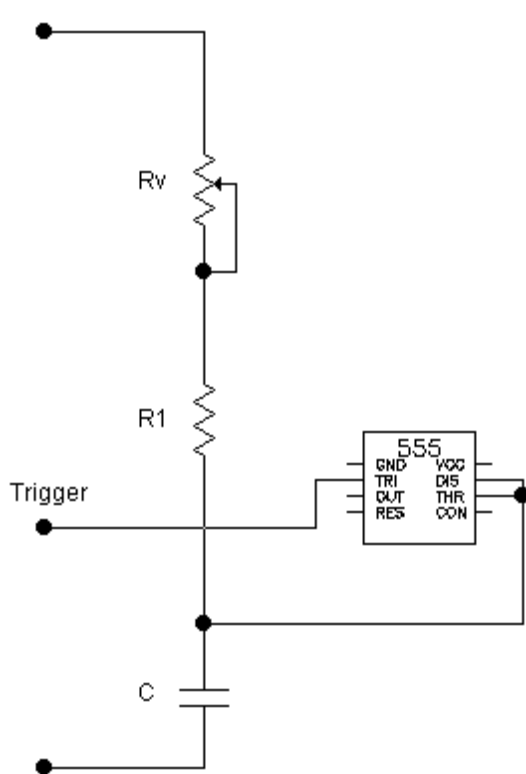


Figure 2.4 Astable timing component connections

$$t = 1.11CR_a \quad (2.3)$$

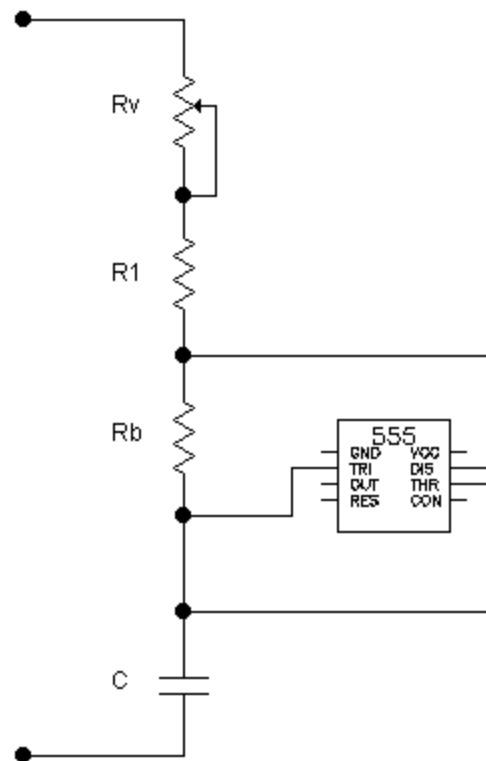


Figure 2.5 Monostable timing component connections

The actual calculations made for determining the values of the timing components are given in appendices A2.1 and A2.2.

The Differentiator circuit

Referring back to figure 2.3, the differentiator (shown dotted) is required to produce the negative edge to trigger the monostable. The time constant of $1 \text{ nF} \times 10 \text{ K}\Omega = 10 \text{ }\mu\text{s}$ is more than adequate for the minimum requirement of a $1 \text{ }\mu\text{s}$ trigger pulse width.

Enhancements made to improve functionality

Although the pulse width was initially variable between 1 ms and 5 ms, this range was extended by providing selectable range multiplication factors of $\times 0.1$, $\times 1$ and $\times 10$. This was accomplished by using two toggle switches to select appropriate values of capacitance as shown in figure 2.6. The $\times 10$ toggle switch was added later to investigate the effects of long pulse widths on various parameters (as described in chapter 4). If this extended feature is still desired, a rotary switch could be used in a future version of the pulse generator to replace the two toggle switches.

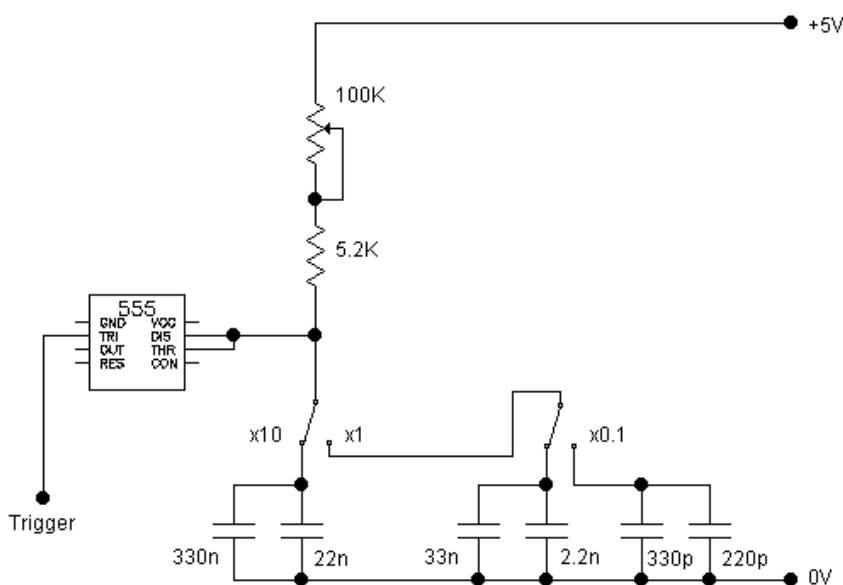


Figure 2.6 Pulse width range extension

A switch was used to enable the output to the gate interface unit to be either at 0V, connected to the pulse line, or at +5V corresponding to the gate being open, pulsed, or closed as shown in figure 2.7. The pulsed position is used when obtaining mobility spectra whereas the open position is used when obtaining mass spectra.

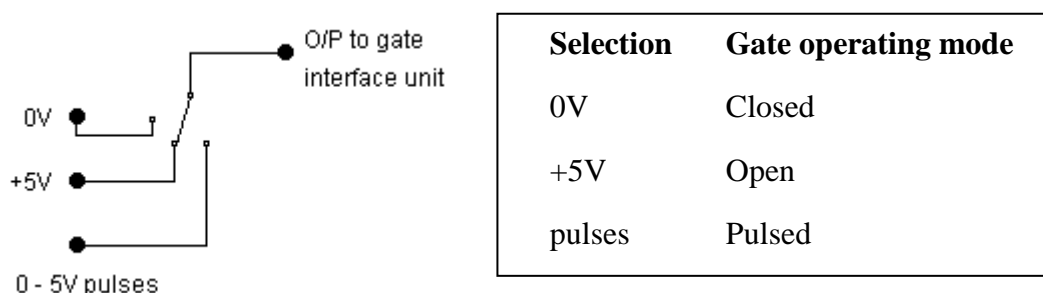


Figure 2.7 Control of gate operating mode. This provides a choice of either pulsed, open or closed gate operation.

A further modification was made to provide the capability of external or internal triggering of the gate pulse, as shown in figure 2.8. This was to allow LabVIEW to control the time that data acquisition began (an idea that was initially thought necessary when developing the tuned ion mass mobility software, but was eventually found to be not required for the particular solution that was employed). The facility to have digital control from LabVIEW may, however, be useful for any future enhancements to the system and so it has been retained.

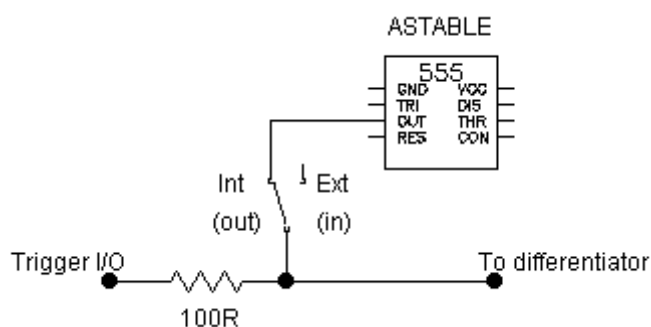


Figure 2.8 External/internal trigger selection

The circuitry was constructed on two generic '555 timer' printed circuit boards (RS number 434-071) from RS Components Ltd. [115]

2.7 The Gate Interface Unit

A block diagram of the principle sections of the gate interface unit is shown in figure 2.9. Here, it is important to ensure safety of personnel by effectively isolating the high voltages associated with the drift tube from the low voltage gate pulse generator circuitry. This is accomplished by using an opto-isolated interface whereby the input signals are converted to light by an Infra Red (IR) diode on the low voltage side, and then reverted back to electronic signals by a phototransistor on the high voltage side.

The mains transformer has been flash tested at 5 kV and so is guaranteed by the manufacturer to withstand this amount of voltage between its primary and secondary windings before breakdown. This is more than adequate since the highest voltage present on the gate is 2.25 kV. The internal power supply provides 110 V dc which connects to a variable regulator to control the voltage supplied to the output stage that then switches the voltage applied to the isolated grid in the B-N gate. Hence this provides regulated control of the amplitude of the gate pulse. The reference grid is connected to the adjacent drift ring. 30 V dc is connected across the opto-isolator section that contains a built-in Schmitt trigger so that a sharp pulse is obtained to operate the output stage.

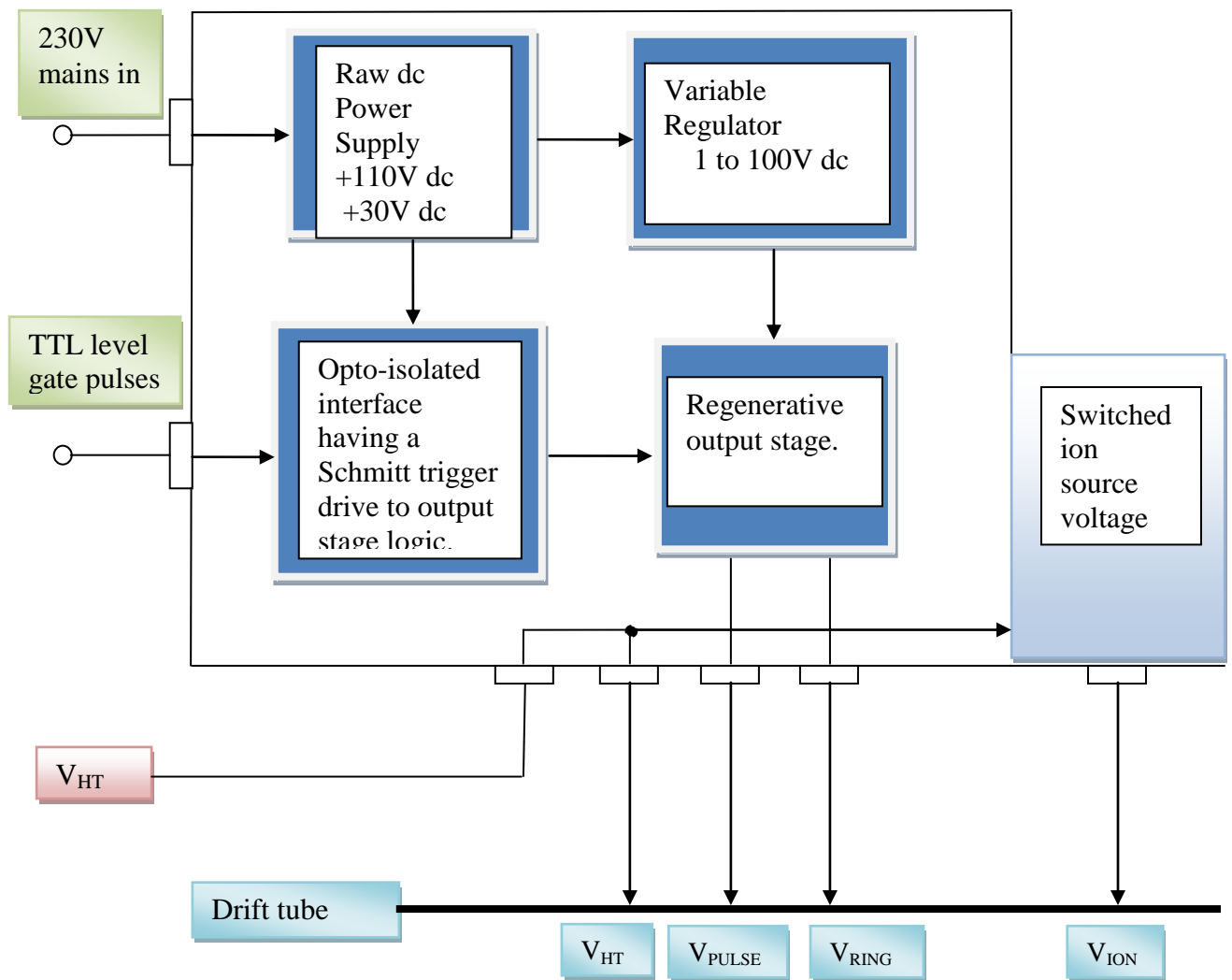


Figure 2.9 Principal sections inside the gate pulse interface unit

V_{HT} is the high tension voltage supply to the interface circuit. From this the adjacent ring voltage V_{RING} and ionisation source voltage V_{ION} are derived. V_{PULSE} is the gate pulse voltage.

The following sections provide details of the circuits used to implement each of the blocks shown in figure 2.9.

2.8 Raw dc Power Supply for the Variable Gate Voltage Regulator

The circuit diagram for this is shown in figure 2.10. In order to provide isolation from the mains supply and to keep the component size to a minimum, two miniature circuit

board mounting 230 V to 24 V step down transformers were used. They were certified as being flash tested at 5 kV which was considered sufficient to withstand the voltage differential of around 2.5 kV between primary and secondary windings.

After rectification and smoothing, shunt regulation using zener diodes was incorporated to limit the output voltage to the maximum required by the variable regulator.

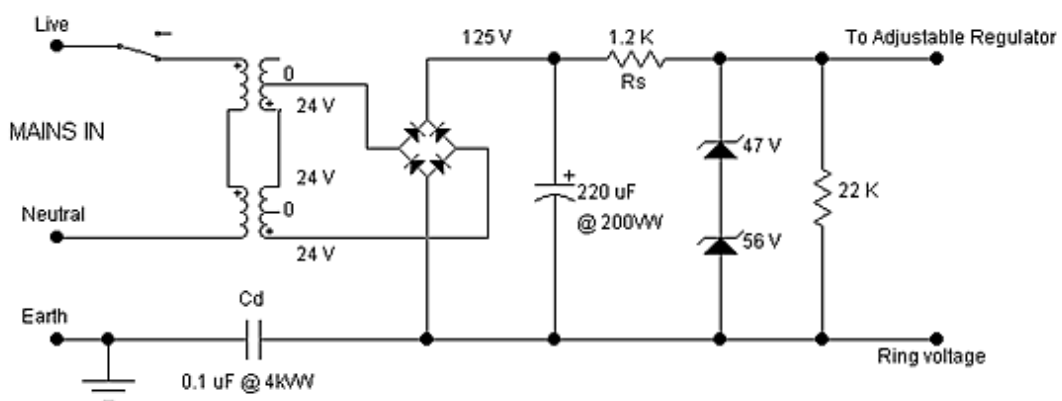


Figure 2.10 Raw dc power supply for the gate interface

The adjustable regulator used (TL783) takes 15.2 mA (as described in section 2.12).

To allow nominally 3.5 mA through the zener diodes resistor R_S can be calculated

$$\text{from } R_S = \frac{(125-103) V}{(15.2+18.7) mA} \text{ k}\Omega \text{ which to the nearest preferred value, is}$$

approximately 1.2 K

The capacitor C_d decouples mains hum which was found to be induced from the mains transformer onto the ring adjacent to the gate.

The 22 k Ω resistor was connected across the output to ensure that the 220 μ F output capacitor discharges within 30 s ($C \times R=4.8$ s) after switch off. This is to remove any possibility of accidental electric shock occurring if the circuitry were to be probed

afterwards. The power dissipated in the discharge resistor is calculated from the expression $\frac{V_Z^2}{22K}$ (mW) = 482 mW. As this is close to 0.5 W, a 1 W rating resistor was used.

2.9 Variable Gate Voltage Regulator

In order to maintain a stable and variable gate voltage, a circuit was used based around the 1.25 V to 125 V adjustable regulator type TL783 manufactured by Texas Instruments (Farnell order code 959-4582). The circuit diagram is shown in figure 2.11. The current supplied by the regulator to the gate pulsing circuit is negligible and so the current demand for this circuit is merely that required for the regulator.

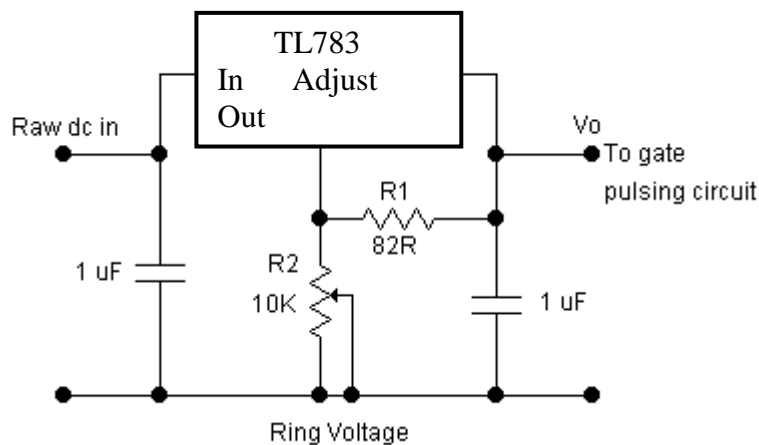


Figure 2.11 Adjustable voltage regulator for the gate pulses

The output voltage is governed by the equation:

$$V_o = V_{ref}(1 + R2/R1) \quad \text{where } V_{ref} = 1.25 \text{ V } (= V_o - V_{Adj}) \quad (2.4)$$

The value of R1 is that recommended by the manufacturer in order for the device to function correctly in accordance with the above equations. This sets the current

through R1 (and hence R2) to $\frac{1.25 \text{ V}}{82 \Omega} = 15.2 \text{ mA}$. (The current into the Adjust

terminal is fixed internally at 83 μA and so can be neglected.) Thus, choosing $V_o = 100\text{ V}$ and transposing equation 2.4 for output voltage in terms of R_2 ,

$$R_2 = R_1 \left(\frac{V_o}{V_{ref}} - 1 \right) = 82 \times \left(\frac{100}{1.25} - 1 \right) \sim 6.5\text{ k}\Omega$$

As a potentiometer of this value is not available, a standard value of $10\text{ k}\Omega$ was used. The effect of using this value is that linear voltage variation is obtained over 65% of the range of adjustment, the scale then widening out towards the extremes of 90 to 100 V. Checking on the power rating required, the maximum power dissipated will be when V_o is 100 V. i.e. 100 V across $10\text{ k}\Omega$ causes 1 watt to be dissipated. Consequently, a 1.5 W rated $10\text{ k}\Omega$ potentiometer was considered adequate for this purpose.

2.10 Opto-isolated input and regenerative output stage.

The work undertaken in this section required considerable planning regarding development, testing and safety considerations due to the potentially lethal voltages present. Although the gate voltage required to cut off ion current flow effectively is around 80 to 100 V, this potential actually sits on approximately $V_{HT}/2$ along the resistor chain due to the position of the gate in the drift tube. In view of the high voltage present, it was decided to isolate the pulses from the pulse generator that control the gate interface by using a Schmitt trigger based opto-isolator to maintain fast switching speeds. A special circuit was also devised (see Figure 2.14) so that fast field effect transistors (FETS) could be used to provide the gate pulses.

Generally, fast switching in high voltage or high power semiconductors is desirable because a semiconductor switch dissipates the most power during switching, i.e.,

while it is in a state between fully "off" and fully "on". By minimizing switching time and, therefore, heat losses in the semiconductor, it can be allowed to switch more power. However, in this application, self heating is very small and so is not a consideration since the gate takes negligible power. It is necessary though to have a high switching speed for the gate pulse in order for the shape to be rectangular at widths as small as 100 μ s ensuring that the initial ion swarm commences with minimal spread (which gradually becomes manifest due to diffusion as it travels along the drift tube). To improve the switching speeds of the MOSFETs, positive (regenerative) feedback can be used to form a Schmitt trigger arrangement.

Figure 2.12 shows a standard Schmitt trigger MOSFET switching circuit providing regenerative feedback. This circuit cannot be used directly since the high voltage requirements of the gate would cause breakdown of the MOSFET junctions. The circuit development to overcome this problem is described in the following sections.

2.11 Circuit development of the output circuit for the gate pulse interface

The basic function of the circuit is to take an input pulse at TTL levels and to then present it as a fast pulse at a voltage level appropriate to cause the gate to control the transmission of ions through it. Figure 2.12 illustrates this idea.

From experiment (as described in chapter 4), it was found that the voltage required across the grids at the gate to block all the ions was in the order of 100 V.

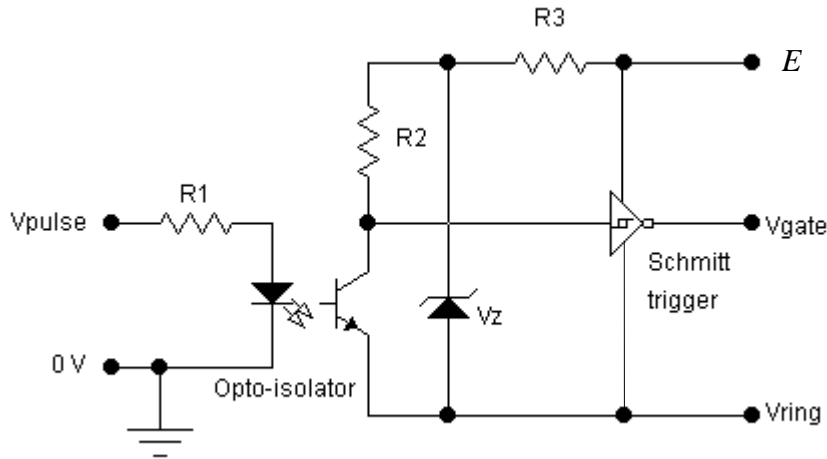


Figure 2.12 Basic circuit operation of the opto-isolated input and regenerative output stage. V_{gate} is the potential at the gate grid relative to the adjacent ring voltage, V_{ring} .

Referring to figure 2.12, E represents the voltage V_o that is supplied by the variable gate voltage generator shown in figure 2.11. Resistor R_1 limits the current flowing through the light emitting diode inside to opto-isolator. This also sets the maximum output current from the opto-coupled transistor. The ratio of output to input currents describes the transfer efficiency of the opto-isolator. The combination of R_3 and the zener diode together form a shunt regulator. This circuitry is necessary to reduce the applied voltage E to a level suitable for the requirements of the opto-isolator. Resistor R_2 sets the maximum current through the transistor to $(V_z - 0.6) \div R_2$.

Figure 2.13 shows the basic circuit required to establish Schmitt trigger operation using complementary enhancement type mosfets. This arrangement is commonly used in CMOS logic gates where junction voltages are low.

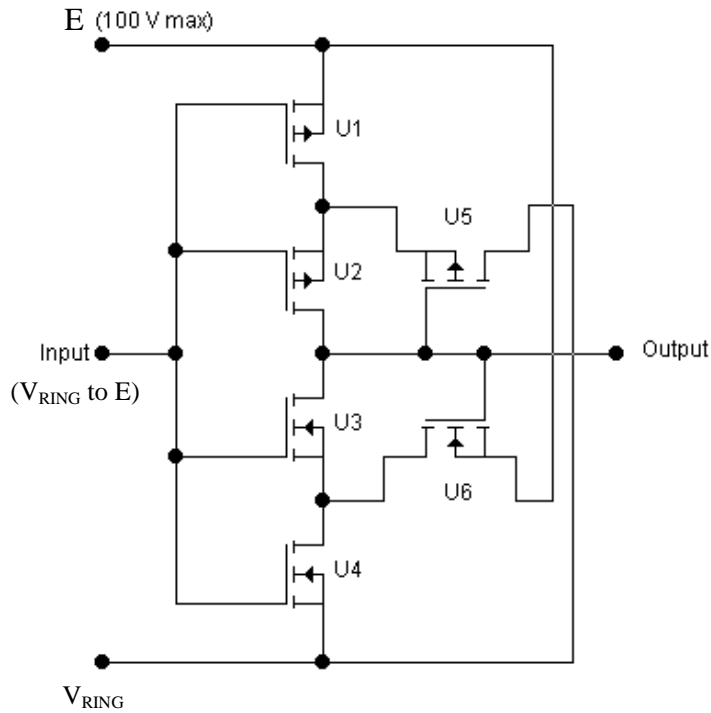


Figure 2.13 Basic Schmitt trigger using complementary MOS devices

The input voltage (obtained from the opto-isolator circuitry) swings between V_{RING} and $V_{RING} + E$ over a range of 100 V. If discrete mosfets were used in this circuit having a typical maximum gate-to-source voltage $V_{GS(max)}$ of 20 V, then in its present form, the circuit would be unsuitable since breakdown of the gate-to-source junctions would occur. In order to retain the active load configuration for providing maximum switching speed, an interface can be designed that limits $V_{GS(max)}$ to say, 10V for mosfets U1 to U4. (This covers the switching threshold for enhancement type MOSFETS which is between 3V and 4V.) Even so, mosfets U5 and U6 would still have the full rail voltage swing across V_{GS} and so this was also taken into account in the re-design of the circuit.

Considering the input circuit, the interface to switch the mosfets needs to perform as shown in figure 2.14.

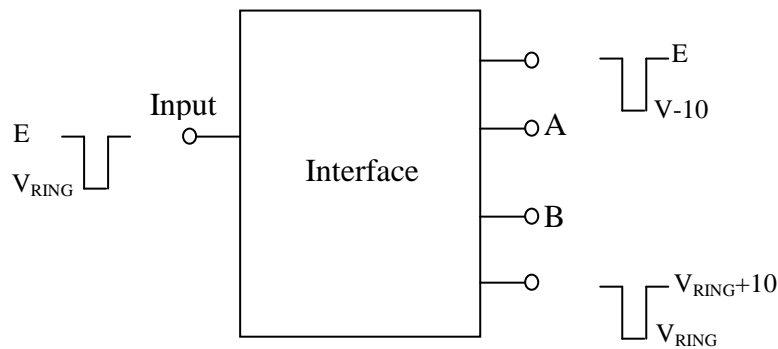


Figure 2.14 Interfacing requirements to prevent over-voltage of the gate drive circuitry

Bearing these requirements in mind, figure 2.15 shows the resulting circuit that was finally adopted with the necessary modifications included to overcome the breakdown problem. Drives A and B are obtained by using 10 V zener diodes to provide a 10 V offset voltage from the supply rails. The output mosfets are then switched using integrated circuit Schmitt triggers supplied by the 10 V offset-to-rail as appropriate to polarity. The switching threshold voltages for the Schmitt triggers are also provided by 10V zener diodes. An advantage of using this type of circuit is that CMOS drive voltages may be applied directly to the MOSFET gates. The benefit is thus simplified drive circuitry and so integrated circuit Schmitt triggers powered from the 10 V limit interface are used to fast switch the output mosfets U1 and U2. All the junction voltages are therefore now well below their breakdown levels.

Figure 2.15 also shows the opto-coupling required for isolation of the TTL level (0 to +5 V) input pulses from the common rail (which is held at the ring voltage).

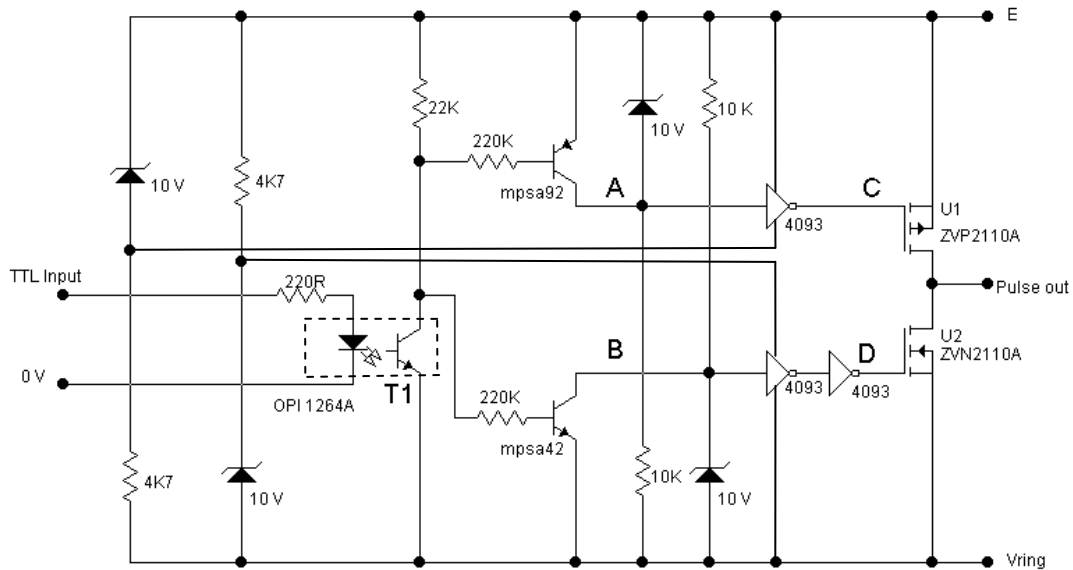


Figure 2.15 Input and output stages of the gate control circuit

2.12 Operation of the gate control circuit

When the input voltage to the opto-isolator is 0 V, the output transistor T1 will be off.

By setting the input voltage to +5 V, T1 will turn on. The way in which T1 controls the operation of the rest of the circuit is summarised in Table 2.1.

Table 2.1 Summary of gate control circuit operation

Input	V_A	V_B	V_C	V_D	U1	U2	Output
0 V	E - 10	$V_{RING} + 10$	E	V_{RING}	OFF	ON	V_{RING}
+5 V	E	V_{RING}	E - 10	$V_{RING} + 10$	ON	OFF	E

The transfer efficiency of the opto-isolator is 25% thus to allow 4 mA maximum to flow in its output transistor, the input diode current should be limited to 16 mA.

Hence, using Ohms law, the current limiting resistor for the opto-isolator diode is determined from:

$(5\text{ V} - 1.5\text{ V}) \div 16\text{ mA}$ giving approximately $220\ \Omega$. (The amplitude of the rectangular waveform from the pulse generator is 5 V and the forward voltage drop of the input light emitting diode is 1.5 V).

For supplying the Schmitt triggers, and allowing a minimum current of 3 mA at say $E = 40\text{V}$ through the zener diodes, this yields a value for resistor R_Z of $(40 - 10)/3\text{ k}\Omega = 10\text{ k}\Omega$.

Checking the power dissipations at $E = 100\text{ V}$:

The power in the zener diode $= V_Z \times I_Z$, but $I_Z = (100 - 10)/10\text{ mA} = 9\text{ mA}$.

Therefore $P_Z = 90\text{ mW}$ and so a 150 mW rated type will suffice.

The power in the resistor $R_Z = I_Z^2 \times R_Z = 810\text{ mW}$ and so a 1 W rated type is used.

The TTL input refers to the transistor-transistor logic compatible output from the pulse generator. The 'pulse out' terminal directly connects to the isolated gate terminal in the drift tube. V_{RING} is connected to the terminal for the drift ring common to the other side of the gate. E is the voltage obtained from the adjustable regulator (V_o) shown in figure 2.11.

2.13 Time response of the gate control circuit

In order to ensure that the circuit of figure 2.15 functioned correctly, its time response was measured by applying a 5 V , 10 kHz square wave to the TTL input and observing the output pulse on an oscilloscope. The objective of the active load output configuration was to produce sharp switching edges. This was found to be the case with rise and fall times in the order of 50 ns . However, a problem occurred with current breakthrough whereby both mosfets were conducting for a short period of

time during the changeover in output state. This effect is due to the relatively slow rise time of the output pulse from the optoisolator causing a time delay to be introduced when the Schmitt trigger switches. This effectively places an undesirable short circuit across the supply E . Although this problem is difficult to overcome, it was circumvented by introducing a passive (resistive) load instead. Thus, to eliminate current breakthrough mosfet U1 was replaced with a $10\text{ K}\Omega$ resistor and it was found that the rise time of the output pulse subsequently increased to $2\text{ }\mu\text{s}$ with the fall time staying at 50 ns due to U2. Hence, the disadvantage of a passive load is that it results in an increased rise time of the pulse with accompanying losses due power dissipation in the resistive load. The mosfet U2 being an active device, has an ON resistance of only a few ohms and so causes rapid discharge of the circuit capacitance to produce a very short fall time of the pulse edge. However, a rise time of $2\text{ }\mu\text{s}$ is only 1% of the $200\text{ }\mu\text{s}$ pulse width and so is deemed as acceptable in this case.

From previous trials, it was found that E needs to be in the order of 100 V above V_{RING} to close the ion gate in positive ion mode. (Only 30 to 40 V was seen to be required in negative ion mode.) This causes a second problem to arise with the circuit as it stands in that the collector to emitter voltage of T1 in the opto-isolator is only rated at 30 V maximum. The highest value seen for other similar devices is 70 V which is still insufficient. This problem was solved by limiting the collector voltage to 10 V by using a zener diode. Applying these ideas produced a considerable simplification to the circuit as is seen in figure 2.16. The value of $10\text{ K}\Omega$ for the load resistor R_L was chosen as a compromise between rise time and power dissipation.

With the ion gate in pulsed mode, the duty cycle is determined from gate pulse width – to – time between pulses, in this case being $0.2\text{ ms}:40\text{ ms} = 0.005$. Thus the power dissipated in R_L is only $0.0005E^2/R_L = 5\text{ mW}$. However, with the gate open (dc

mode) the power dissipation will be 1 W which would represent a sensible upper limit.

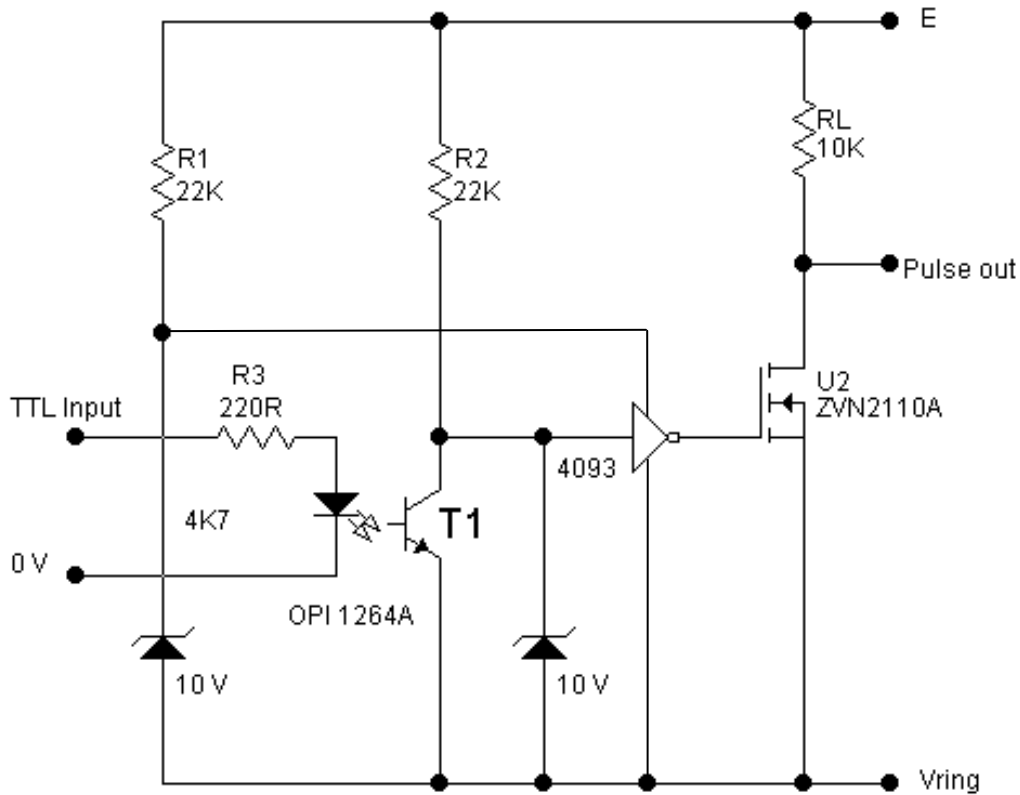


Figure 2.16 Simplified version of the gate control circuit

Referring to figure 2.16, the values of R1 and R2 were chosen to allow sufficient current through the zener diodes to keep them in regulation while minimising power dissipation in the resistors. The time response of the circuit is given in the timing diagrams shown in figure 2.17.

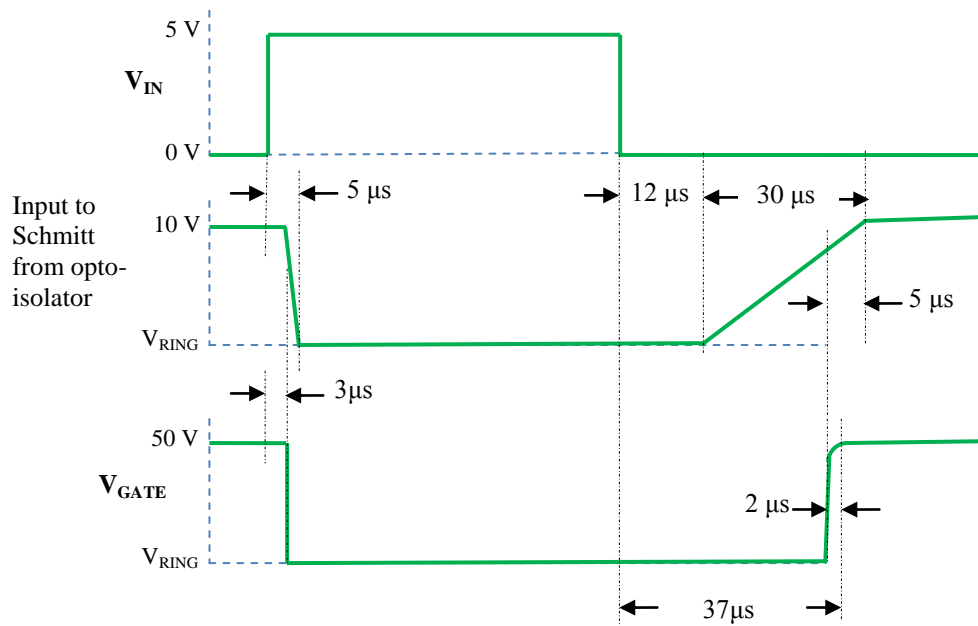


Figure 2.17 Switching waveforms for the simplified gate control circuit shown in figure 2.16

Referring to figures 2.16 and 2.17 together, the effect of the slow rise time of the opto-isolator is clearly seen. This results in an extension of the pulse width of 34 μs which is an appreciable portion of 200 μs . Thus, to get an accurate gate pulse width, the calibration of the pulse generator should be that an offset of -34 μs should be introduced into the timing circuit.

2.14 An alternative bipolar version of the gate control circuit

In this approach to obtain fast switching, the idea is to use high voltage bipolar transistors instead of mosfets. Here, regeneration (positive feedback) is used to enable a fast switching response in the output stage. The circuit developed is shown in figure 2.18 which is based on a modified discrete bistable multivibrator circuit.

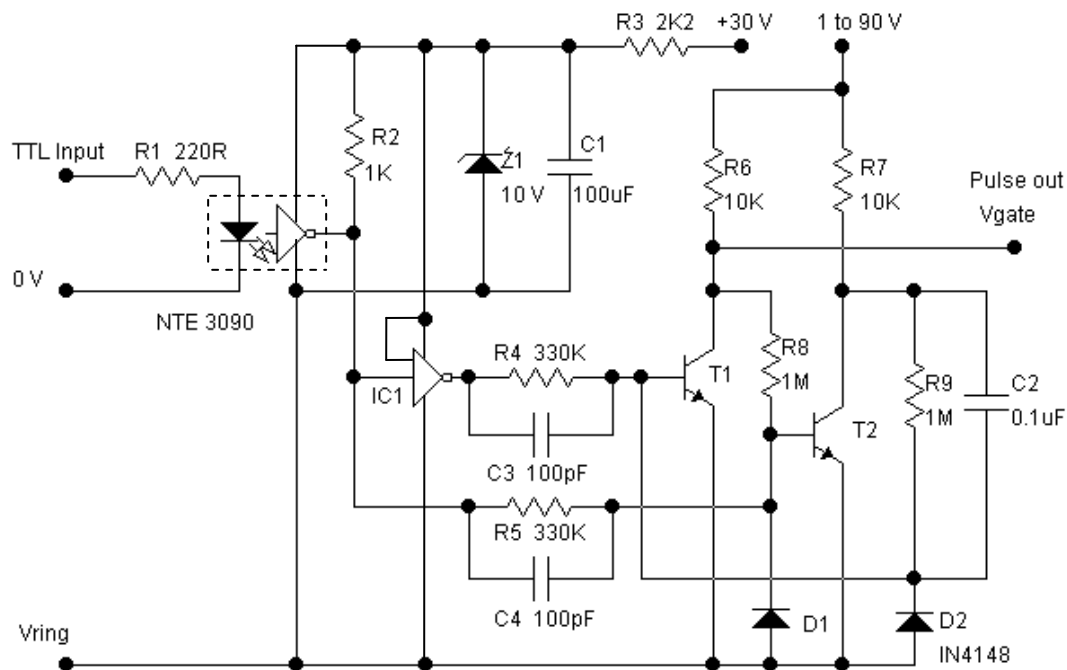


Figure 2.18 Gate pulse interface using a regenerative output stage with bipolar transistors

IC1 is a CMOS quad NAND gate type CD4093 having Schmitt trigger inputs. As only one of the gates is used (inputs on pins 1 and 2, output on 3), pins 5, 6, 7, 8, 9, 12 and 13 are tied to 0 V to prevent unwanted oscillation on the unused inputs.

Transistors T1 and T2 are high voltage types BF422. Resistor R9 provides positive feedback for fast regenerative switching and C2 acts as a “speed up” capacitor to get base charge into T1 more quickly. The values were optimised during the test since the circuit was subject to changes in the h_{FE} (current gain in the common emitter mode) of the transistors. The waveforms obtained are shown in figure 2.19 and are based on an input pulse width of 20 μ s to see the delays proportionally. (The actual pulse width used in the ion mobility experiments is 200 μ s.)

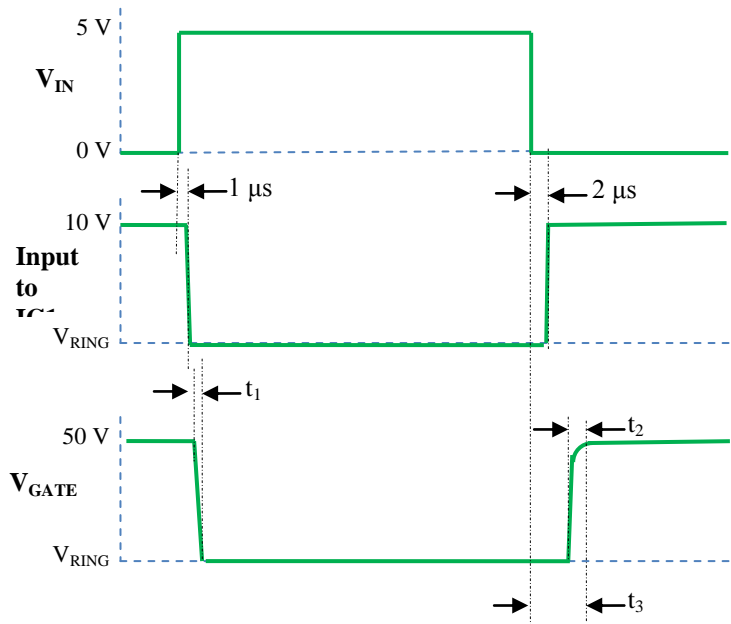


Figure 2.19 Switching waveforms for the regenerative bipolar output circuit shown in figure 2.18

Referring to figures 2.18 and 2.19 together, when testing the circuit, it was found that changing the value of R_4 from $100\text{ K}\Omega$ to $330\text{ K}\Omega$ reduced the saturation in transistor T1 which correspondingly reduced the rise time of V_{GATE} to $8\text{ }\mu\text{s}$ and the fall time to $0.5\text{ }\mu\text{s}$. Further increase in R_4 yielded no improvement up to $650\text{ K}\Omega$ when T1 came out of saturation and its V_{CE} began to rise. When changing the value of resistor R_5 from $100\text{ K}\Omega$ up to $1\text{ M}\Omega$ no effective increase in the switching speed of T1 was observed and so R_5 was also set to $330\text{ K}\Omega$.

The optimum value for the speed up capacitor C_2 across R_9 was found to be 100 pF – any increase on this caused a corresponding increase in t_1 but with little change in t_3 . This gave $t_1 = 3\text{ }\mu\text{s}$, $t_2 = 3\text{ }\mu\text{s}$ and $t_3 = 6\text{ }\mu\text{s}$. A speed up capacitor across R_8 had a detrimental effect and so was left out, however, 100 pF capacitors across resistors R_4 and R_5 reduced t_1 to $0.5\text{ }\mu\text{s}$, t_2 to $2\text{ }\mu\text{s}$ and t_3 to $5\text{ }\mu\text{s}$.

The effect of C2 on the base of T1 is to drive it on the negative edge excursion to -5 V, increasing to -6 V when adding C3. Since this is near the breakdown voltage of the base-emitter junction, it is necessary to protect the junction accordingly, and this is achieved by clamping the voltage with diode D2 (similarly for T2 with clamping diode D1) which safely reduces the negative bias to about -0.6 V. An additional advantage of the diodes is to reduce the recovery times of C2, C3 and C4 to fractions of a microsecond.

Although the circuit of figure 2.18 is somewhat more complicated than that of figure 2.16, the overall switching speed is similar, but the pulse width time extension is only 5 μ s now (representing 2.5% of the standard 200 μ s gate pulse width used), and so it was subsequently chosen for incorporation into the gate interface unit.

2.15 The Electrometer

This is basically comprised of a current-to-voltage converter stage followed by a voltage amplifier to bring the signal up to a level sufficient for signal processing.

Current to voltage converter stage (Also known as a Transimpedance Amplifier)

Considering the operational amplifier circuit shown in section 2 of figure 2.20, by connecting the feedback resistor from the output to the inverting input, a small input source current I_s (representing the source current from the Faraday plate) flowing into the inverting input must flow through the feedback resistor (because the input impedance of the op-amp is many times larger than the value of R_F).

The non-inverting input is connected to ground (0V). Due to the very high gain of the op-amp, the inverting input will also be virtually at 0V thus the input side of R_F is held at “virtual ground” potential. The output voltage will therefore be given by the

equation $V_0 = -V_{Rf} = -(I_s \times R_f)$. The minus sign indicates that the output voltage is an inverted form of the input current waveform.

Optimizing the current to voltage converter is required due to the stray capacitance around the FP and its wiring. This is symbolised by the equivalent capacitance C_S in parallel with the input terminals of the op-amp. The equivalent circuit of the FP as a source of current can be represented by a current generator with its associated leakage resistance R_S as seen in section 1 of figure 2.20.

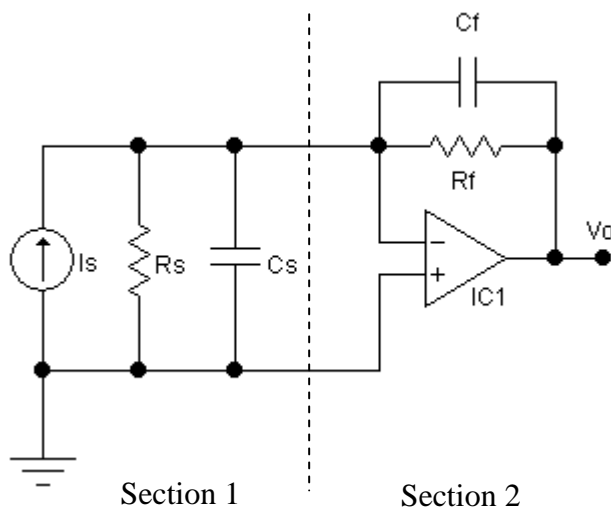


Figure 2.20 Representation of the equivalent circuit of the FP connected to the current to voltage converter

The equivalent capacitance C_S causes three detrimental effects to occur in the circuit as outlined below:

1. At high frequencies, C_S acts as a shunt across the current source I_s , reducing the bandwidth of the circuit.
2. Circuit instability can arise due to the combination of R_F and C_S acting as a low-pass filter in the feedback path. This causes a negative phase shift in the feedback loop, introducing instability, which can appear as overshoot and ringing.

3. It causes a peak in an otherwise flat frequency response. To restore stability the low-pass filter arising from R_F and C_S can be compensated for by adding capacitor C_F to introduce a high-pass filter with the combination of C_F and R_S in the feedback path to add a positive phase shift to the loop and hence tend to restore stability. Although this reduces the peak, the overall bandwidth is also reduced. This is because C_F and R_F form a low-pass filter in the forward signal path from I_S to V_O .

The feedback capacitor C_F across R_F is therefore required for optimising the circuit frequency response to obtain maximally flat gain. The value of C_F is found on test since it is not possible to compute a value due to unknown parameters such as source capacitance and resistance, and op-amp characteristics.

In practice, the value of C_F is very small and in the configuration used, it was found that only a fraction of a pF is required (see section 2.15.5).

To get a good signal-to-noise ratio (SNR), the TL081 op-amp manufactured by Texas Instruments was chosen as it has a low equivalent input noise voltage of $18 \text{ nV}/\sqrt{\text{Hz}}$. The physical wiring layout is such that inter-lead/component capacitance is reduced to a low value in order to keep time constants small to reduce the possibility of positive feedback introducing instability into the circuit. When detecting very small currents (in the pA range) from the FP, an important consideration is that of preventing circuit board leakage currents from interfering with the signal which would cause signal voltage drift and offset problems. This effect can be avoided in two ways:

- (i) By using a grounded guard ring around the input connection to conduct any leakage currents away.

- (ii) By using a ptfе stand-off to isolate the input connections from the main circuit board.

2.15.1 The complete electrometer.

For flexibility, the electrometer was initially implemented with selectable gain such that its range of current measurements could be digitally selected to give 1 V output for input currents of 10^{-7} , 10^{-8} , or 10^{-9} A to meet the voltage level requirements of the LabVIEW DAQ interface. Figure 2.21 shows a block diagram layout of the sections comprising the electrometer and its associated connections.

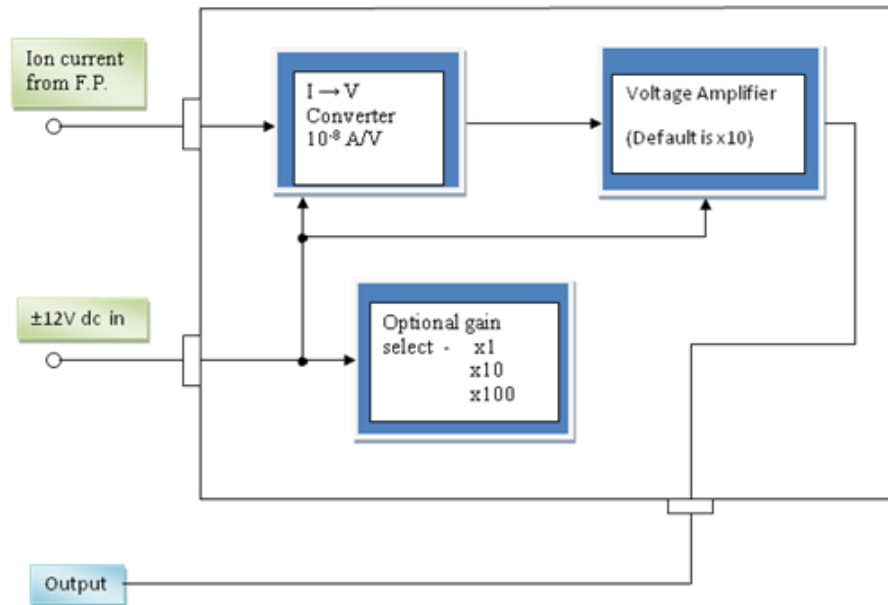


Figure 2.21 Block diagram of the electrometer stages

The electrometer is contained in an aluminium box to screen it from external signals and is mounted in close proximity to the FP and screen to reduce interference from external noise sources.

Figure 2.22 shows the overall circuit diagram of the electrometer. Here, a grounded guard ring is used as a screen for the input terminals to prevent or minimise leakage currents that may otherwise enter from other areas of the board.

Circuit description of the electrometer

The first stage built around IC1 is the inverting current to voltage converter which converts the ion current from the Faraday plate into a corresponding voltage that is then further amplified by the second stage amplifier built around IC2. This is a selective gain ($\times 1$, $\times 10$ or $\times 100$) non inverting voltage amplifier. The feedback arrangement differs from the usual single feedback resistor by using a potential divider arrangement. The advantage of this is that lower value resistors can be used, which are cheaper, have better precision and are less noisy than high value types in the Giga Ω range which are also more prone to producing error due to contamination from handling. (Moisture from the skin would act as a shunt resistor, considerably changing the resistance to an unknown lower value.) As the first stage gives an inverted output, the second stage was chosen to be non-inverting to allow a third inverting stage to be used for fine gain control and filtering out of noise from the signal. This then produces zero overall phase shift. In order to minimise the possibility of noise pick up or instability by direct switching of the second stage by mechanical switches, a 4066 CMOS transmission gate is used to allow isolation between the switch contacts and the switching signal. This furthermore provides the possibility of processor software control of the gain if required.

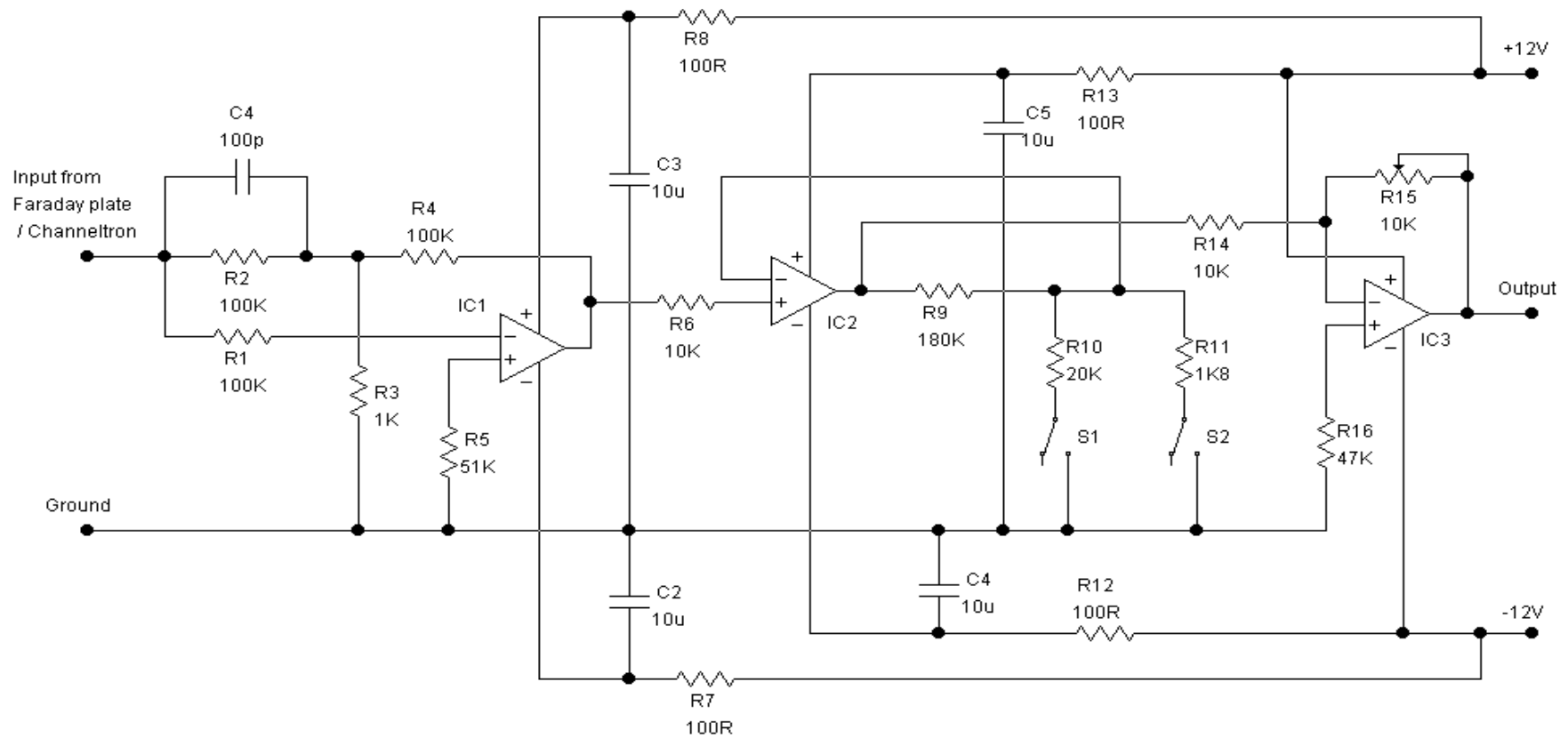


Figure 2.22 Circuit diagram of the Electrometer Amplifier for the IMS-QMS system
 IC1 forms the current to voltage converter.
 IC2 provides switchable gain ranges via switches S1 and S2.
 IC3 allows fine gain adjustment via variable resistor R15.

Amplifier gain control

The gain of the amplifier is defined by the combinations of switches S1 and S2. Referring to figure 2.22 switch S1 is contained in the 4066 bilateral switch and appears between pins 1 and 2 with the control of S1 on pin 13. Switch S2 appears between pins 3 and 4 with its associated control on pin 5.

The operation of the gain switch as mounted on the electrometer conversion ratio box is shown in figure 2.23.

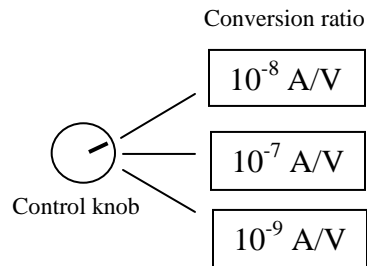


Figure 2.23 Operation of the gain control switch

The fine gain control (R15) is a calibrated 10 turn potentiometer to allow finer control of the gain variation between the switched ranges.

Although this circuit produced good results, in the interests of simplicity and reliability, and after a suitable gain value was obtained through testing (that was found to require no further adjustment), it was decided that a simpler approach could be taken whereby the converter and voltage amplifier were built as separate modules using pre-supplied generic PCBs (RS components, stock number 434-065). A single large value feedback resistor of 100 M Ω was also used in the converter instead of the three resistor Tee arrangement used in the original circuit of figure 2.22. This value was found to be quite adequate for the ratio of current to voltage conversion necessary and being less than 1 G Ω it does not suffer from the previously mentioned

disadvantages associated with high value resistors. It was found necessary to incorporate an offset null potentiometer to provide an output of 0V under quiescent conditions due to inherent dc drift of the amplifier.

2.15.2 Optimising the frequency response of the current-voltage converter

A test of frequency response showed that the bandwidth was 0 Hz (dc) to 10 kHz within the 3 dB points. Peaking of the output signal began after 1 kHz reaching a maxima at around 5.5 kHz as seen in figure 2.24.

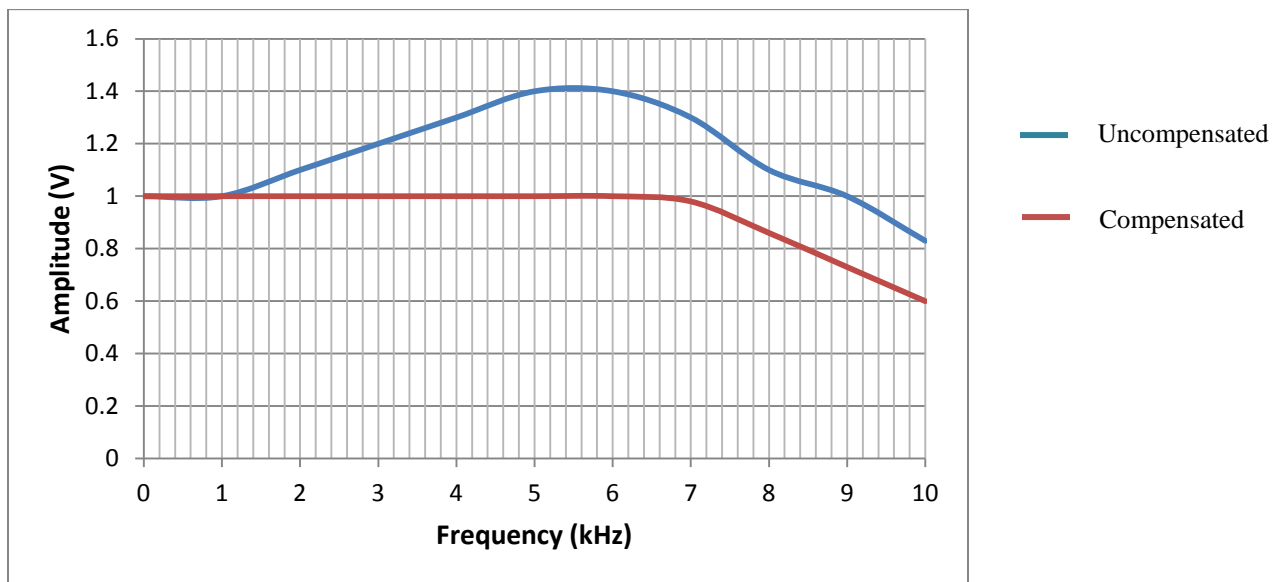


Figure 2.24 Frequency response of the current-to-voltage converter

The time response was observed by feeding the input terminals with 40 mV amplitude pulses via a 1 M Ω resistor to inject 40 nA into the input. When observing the output voltage time response to this step input (using a 5 kHz pulse waveform to simulate the ion gate pulse being 200 μ s wide) ringing was observed on the rising and falling edges of the output pulse. As mentioned in section 2.15.1 a small value of capacitance connected across the feedback resistor was used to

compensate for the frequency peaking effect to give a flat frequency response while also improving the time response. A calculation for the approximate value of capacitance for the compensation capacitor across the feedback resistor was made as follows:

To halve the response at say $f = 5$ kHz, the capacitive reactance X_C of the feedback capacitor would need to be the same as R_F , i.e. $100 \text{ M}\Omega$.

$$C = \frac{1}{2\pi f X_C} = \frac{1}{2\pi \times 5 \times 10^3 \times 100 \times 10^6} = 0.32 \text{ pF}$$

This value is too small to be obtained as a component and so such a very small value of capacitance (fractions of a pF) was fabricated by simply connecting a wire to one side of the feedback resistor and then positioning it parallel to the resistor. This produced a mutual capacitance between the wire and resistor R_F , the value of which could be altered by simply moving the wire a few mm nearer to, or further from the resistor. The effect of finding the best position was to produce a flat frequency response from dc, rolling off to a -3 dB point at about 9 kHz. When checking the time response, only a small amount of overshoot was observed on the rising and falling edges of the output pulse. The rise time to reach 4 V amplitude was 39 μs corresponding to a rate of change of 1.03×10^5 V/s. Note, theoretically, a sine wave $A \sin(2\pi ft)$ requires a minimum slew rate of change S of $2\pi f A$ V/s for a full sinusoidal swing in peak to peak amplitude equal to the supply voltage. [The rate of change of voltage (slew rate)

S is $\frac{d}{dt} (A \sin(2\pi ft)) = 2\pi f A \cos(2\pi ft)$ with a maxima at $t = 0$. Thus substituting $t = 0$ gives

$$= 2\pi f A.] \text{ From this, the equivalent frequency to achieve this slew rate is } \frac{S}{2\pi A} = \frac{1.03 \times 10^5}{2\pi \times 4} =$$

4.1 kHz which is a reasonable approximation to the cut-off frequency of 9 kHz seen on the oscilloscope.

2.15.3 Faraday plate switch

This facility enables the Faraday plate to be switched from between being used as an ion collector providing a current source (for ion mobility measurements) to acting as an ion lens (for ion mass measurements). An encapsulated reed relay is used to provide isolated switching, with leds indicating the chosen mode of operation. Figure 2.25 shows the circuit diagram of the unit.

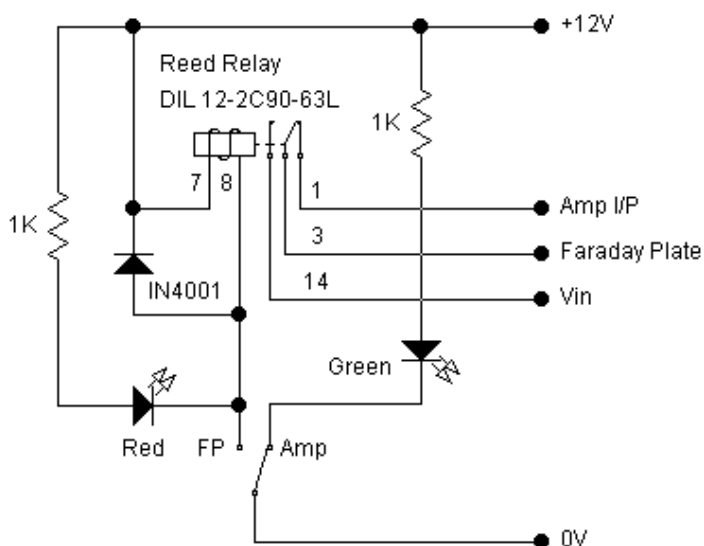


Figure 2.25 Switching the Faraday plate operation between electrometer amplifier input and as an electrostatic lens. When the green led is on, it indicates that the FP is switched to being used as the IMS detector. The red led is on when the FP is switched to being used as a lens for MS measurements

The dc source is obtained from a specially constructed external power supply containing a set of stabilised voltage sources used for applying appropriate potentials to various electrodes and electrostatic lenses in the IMS-MS system. Details of this are provided in appendix A2.3.

2.16 IMS drift tube heater controller

In order to ensure that the drift tube is kept scrupulously clean it is automatically baked out at 100°C using the concentric heater band around the drift tube. This is accomplished by using an external timer switch to bypass the temperature controller which maintains the tube temperature at 30°C for normal use. The timer is set to initiate baking out at 7:00 pm and to end the baking out process at 6:00 am on the following day. Precautions are built into the circuit to ensure that the drift tube voltage is reduced from 4.5 kV to 3 kV when the tube temperature rises above 35°C to prevent internal flashover which occurs when 4.5 kV is used at 100°C. This is done by using a thermal switch fixed to the outside surface of the heater band. In view of the importance of reliable operation of the thermal switch, two of them are wired in series in case one of them fails to operate. A separate circuit for monitoring the state of the switches is incorporated and shown on separate circuit diagrams (figures 2.30 and 2.31 discussed later). The overall circuit diagram for the heater controller is shown in figure 2.26

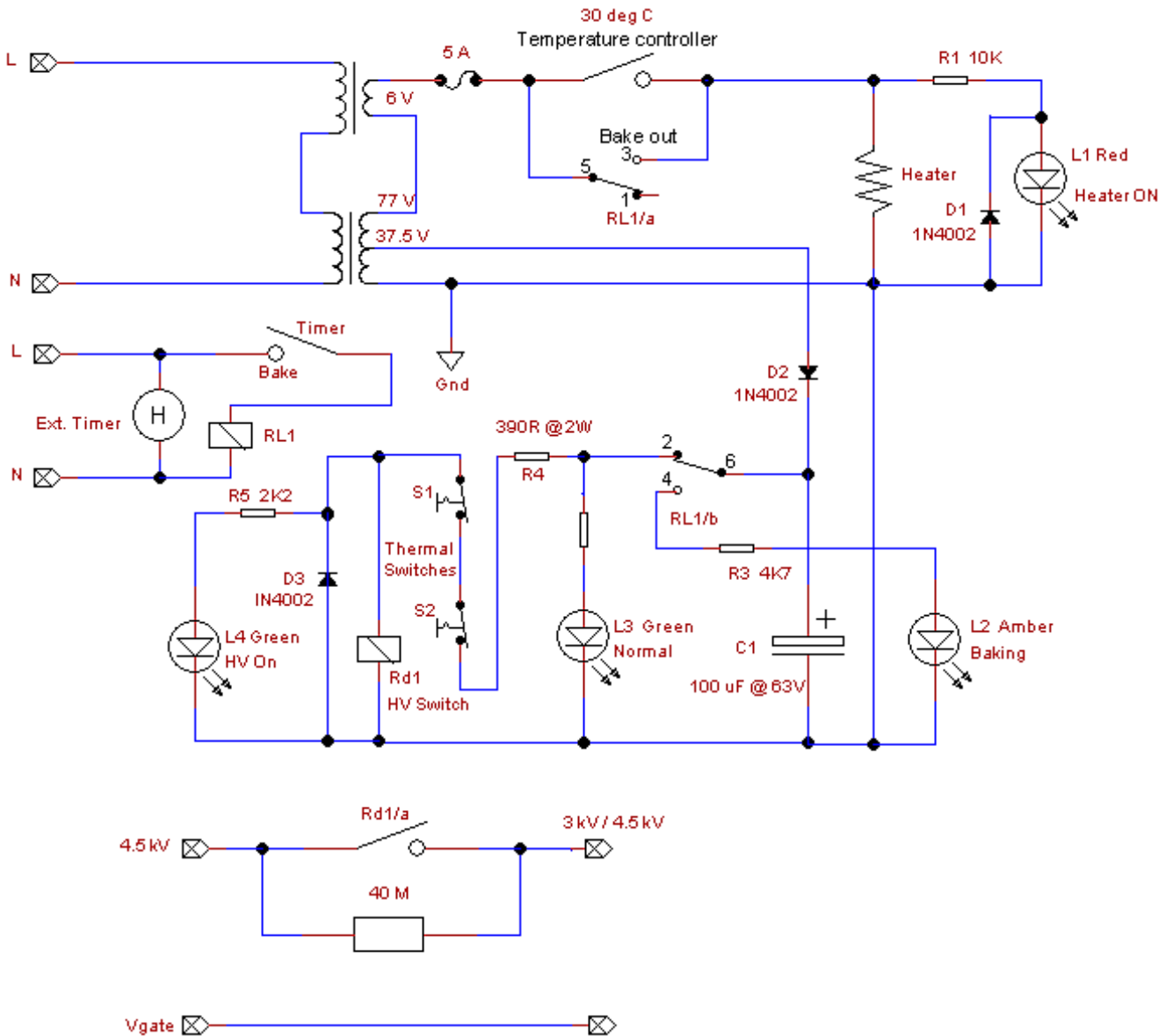


Figure 2.26 Overall circuit diagram of the heater controller

2.16.1 Circuit operation of the heater controller

Referring to figure 2.26, the contacts marked ‘30 deg C’ represent a solid state relay (SSR) which is controlled by the temperature controller. An alternative method could be to control the input signal to the SSR by using a diode OR gate (thus allowing operation from the switched dc signal from the temperature controller OR the constant dc signal required for baking out).

However, it was felt that as switching at the zero crossing point of the mains is desirable for normal operation, it is unnecessary in the case for baking out (as only two switching operations occur) and so the simpler method of directly switching with a relay contact was used. Note, the circuitry associated with Rd1 (i.e. Rd1, R5, L4 and the switched 40 MΩ resistor) are contained within the box on which all the high voltage connections to the drift tube are mounted.

When the relay contacts (RL1/a) short circuit the SSR, it causes the heater to continuously receive sufficient power for the temperature of the drift tube to rise to 100 °C.

Contacts (RL1/b) break the power to the reed relay coil and so the 40 MΩ resistor is brought into circuit reducing the voltage to the resistor chain across the drift rings to 3 kV. This is done to prevent any possibility of flash over within the drift tube. (It was found previously that breakdown occurred at 4.5 kV when the temperature was at 100 °C.)

The circuit is failsafe in that if RL1 fails to operate, the baking process is disabled. Also, if Rd1 fails to operate, the tube voltage is kept at the lower voltage of 3 kV preventing any possibility of flashover in the drift tube. The resistor chains in the drift tube and ion source voltage box combine to present a total resistance of 80 MΩ and so switching in an extra 40 MΩ in series will produce a drop in voltage (using the voltage divider equation) of $4.5 \text{ kV} \times 40 / (80 + 40) = 1.5 \text{ kV}$. Hence $4.5 - 1.5 = 3 \text{ kV}$ appears across the drift tube.

Note, it was seen that at 100 °C, the heater voltage was 69 V with 2.8 A flowing. (Found by using a variac (a variable voltage auto transformer) set at an applied voltage of 29% of the mains supply to the heater.)

The phasing of the two transformers connected across the mains supply is such that cancellation occurs giving a resultant voltage of $(77 - 6) = 69$ V. The centre tap provides the supply voltage for the rest of the circuit.

The thermal switches S1 and S2 in figure 2.27 are incorporated in order to prevent the full 4.5 kV potential from being applied to the drift tube when the system switches to normal (30°C) mode while the drift tube remains hot after the baking out process has elapsed.

2.16.2 Thermal Switch Monitoring

The basic idea of this is shown in figure 2.27 where the two switches S1 and S2 are wired in series so that if one of them fails to operate, the other will provide backup. The integrity of the switches is important to prevent flashover during the period when the drift tube cools down. It was therefore decided to incorporate a circuit to monitor the condition of each switch (mentioned later). The operation may be summarised as shown by table 2.2.

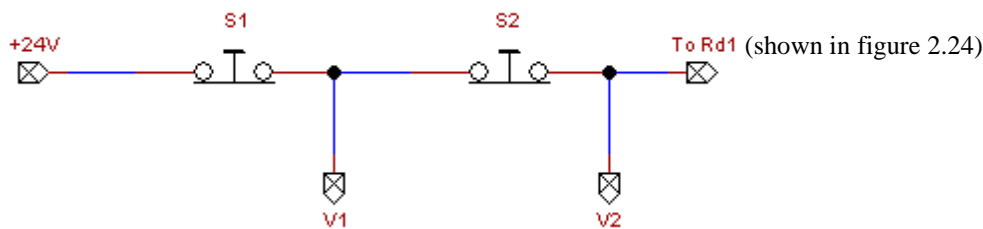


Figure 2.27 Series connection of thermal switches for flashover prevention

Table 2.2 Operation of the thermal switches

S1	S2	V1	V2
closed	closed	+24 V	+24 V
closed	open	+24 V	0 V
open	closed	0 V	0 V
open	open	0 V	0 V

The transition (or fault) states are shown in red and occur when either switch is in the opposite state. The first of these states where S1 fails to open with S2 (drift tube heating up) is unique for $V1 = +24\text{ V}$ and $V2 = 0\text{ V}$ and so can be detected with a logic circuit. The second state where S2 fails to open with S1 is not unique since $V1$ and $V2 = 0\text{ V}$ also occurs in the last state for both switches open (i.e. baking out), and so cannot be detected. The same problem occurs when cooling down.

An alternative method which overcomes these problems is to monitor the state of the switches via an isolated circuit and using led indicators. Figure 2.28 shows the final circuit developed. Here, the capacitors serve a dual purpose:

1. To block any undesired path for the +24 V supply to the high voltage switch Rd1
2. To limit the current flowing through the leds L1 and L2.

As the 9 V ac supply is double insulated from the main controller supply i.e. (no earth connection except to the transformer body, and a plastic enclosure), there is no possibility of interaction between the heater controller and the thermal switch monitor.

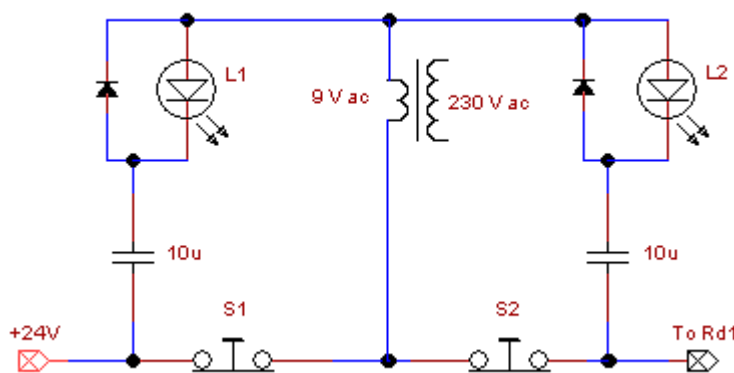


Figure 2.28 Circuit to monitor the state of the thermal switches (Rd1 is shown in figure 2.26)

A fault diagnosis table relating the led status to the state of the switches is shown in table 2.3.

The temperature thresholds for operation of the switches (open at 50°C when heating, close at 35°C when cooling) are used as datum points in the table for defining the cooled or baking modes of operation.

Table 2.3 Switch failure diagnosis

State	L1	L2	T < 35°C	T > 50°C
			Condition	Condition
1	ON	ON	Normal	Malfunction – turn off
2	ON	OFF	S2 stuck open	S1 stuck closed
3	OFF	ON	S1 stuck open	S2 stuck closed
4	OFF	OFF	Malfunction	Normal

The **malfunction** at state 1 will only occur if both thermal switches simultaneously fail to operate during heating towards bake out. As this is unlikely, it could only happen if one of the switches has stuck closed at a previous time and (although indicated on the leds) had not received attention. This particular fault is the most serious though since full HT voltage would then be applied to the drift tube with the possibility of flashover while at 100°C after the bake out period had elapsed and the system has switched over to normal operating mode.

The **malfunction** at state 4 is not so serious since the drift tube is maintained at the lower voltage of 3 kV where flashover does not occur. It will however produce a corresponding error in drift time which would also be immediately apparent in the mobility spectrum.

States 2 and 3 give a warning that one of the switches needs to be replaced and this should be done as soon as possible to avoid progression into the malfunction states.

In order to more closely monitor the operation of the switches, improvements can be made to draw attention to a particular switch fault by using two led's (red and green) to represent the

states and to sound an audible alarm when a fault occurs. (Note, the differences in opening and closing temperature thresholds of the switches cause an apparent fault during temperature changes, but this lasts for a few seconds only as the switching thresholds of each switch are fairly accurate.) Thus, two greens in normal mode or two reds when baking out represent correctly functioning switch operation. A red and a green light permanently on shows a stuck thermal switch contact.

Figure 2.29 shows the layout of the thermal switches and their monitoring leds.

Table 2.4 is an extension of table 2.3 for diagnosing which switch is faulty according to the status of the leds and the operating mode of the system.

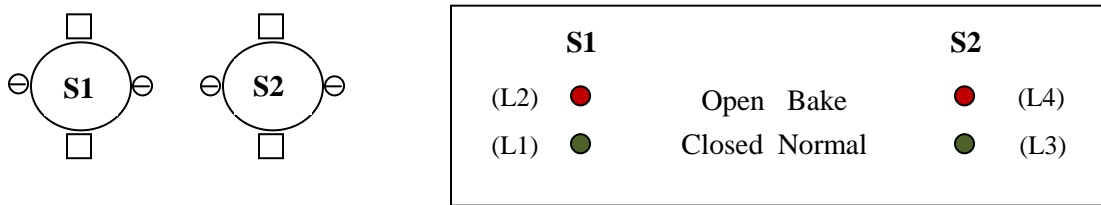


Figure 2.29 showing the physical layout of the thermal switches on the heater, and the monitoring led's on the monitor box

Table 2.4 Thermal switch fault diagnosis

		Condition	
S1	S2	T < 35°C	T > 50°C
● ●	● ●	Normal	S1 and S2 Malfunction- TURN OFF
● ●	● ●	S1 and S2 Malfunction	Normal
● ●	● ●	S2 stuck open	S1 stuck closed
● ●	● ●	S1 stuck open	S2 stuck closed

The final optimised circuit to achieve this is shown in Figures 2.30 and 2.31 which (for clarification) show the circuit split into two parts, A and B.)

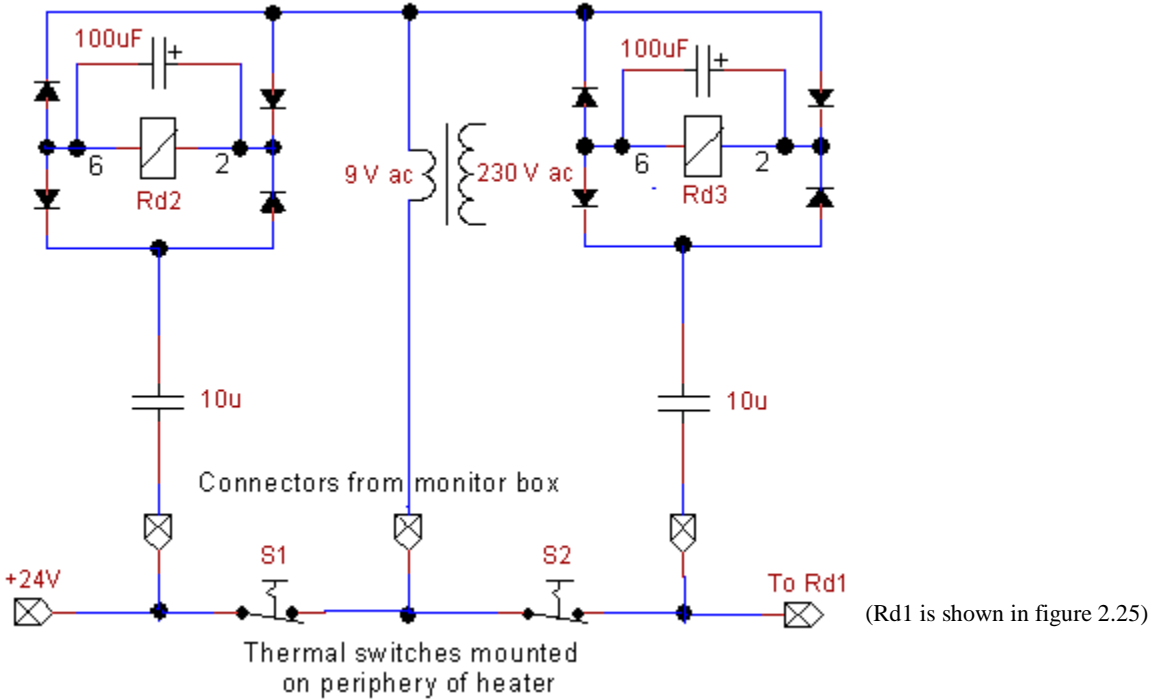


Figure 2.30 Optimised switch monitoring circuit – part A

The bridge rectifiers are encapsulated type W04M which can rectify up to 1 A at a maximum reverse voltage of 400 V. Reed relays Rd2 and Rd3 have a 200 Ω coil resistance and operate nominally at 5 V.

The contacts from the reed relays control the status leds and an audible warning as shown in figure 2.31. An exclusive OR gate is used to monitor for opposite states of Rd2 and Rd3 contacts. When this occurs, the mosfet is turned on and the sounder produces an audible warning signal indicating the failure of one of the thermal switches to operate. The cathode of the zener diode provides 3.6 V for the power supply to the CD4070 chip and the audible sounder.

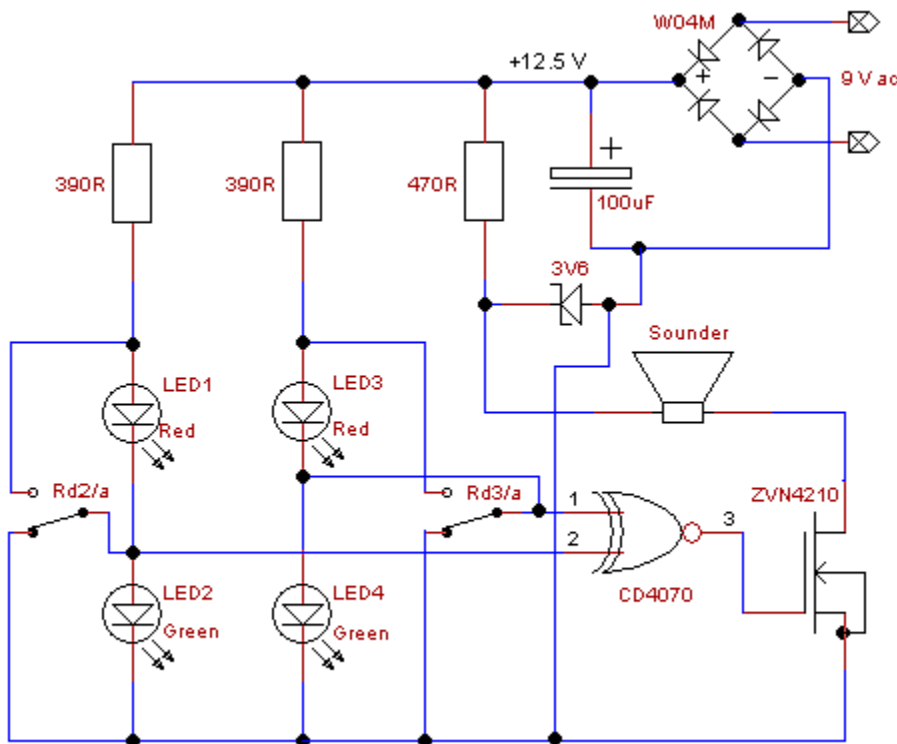


Figure 2.31 Optimised switch monitoring circuit – part B

As only one of the gates is used in the CD4070 quad exclusive OR package, to prevent oscillation on the unused inputs the pins were connected as follows:

0 V to pins 5, 6, 7, 8, and 9. +3.6 V to pins 12, 13 and 14.

A final circuit (although not implemented since this particular fault is very unlikely to occur as it would require the contacts of RL1 in figure 2.26 to be sticking), could if so desired, be incorporated for automatic and complete turn off of the high voltage switch. This may be achieved by using the circuit shown in figure 2.32. Here, anomalous operation of the HV switch is detected in the bake out condition, which could cause flashover to occur.

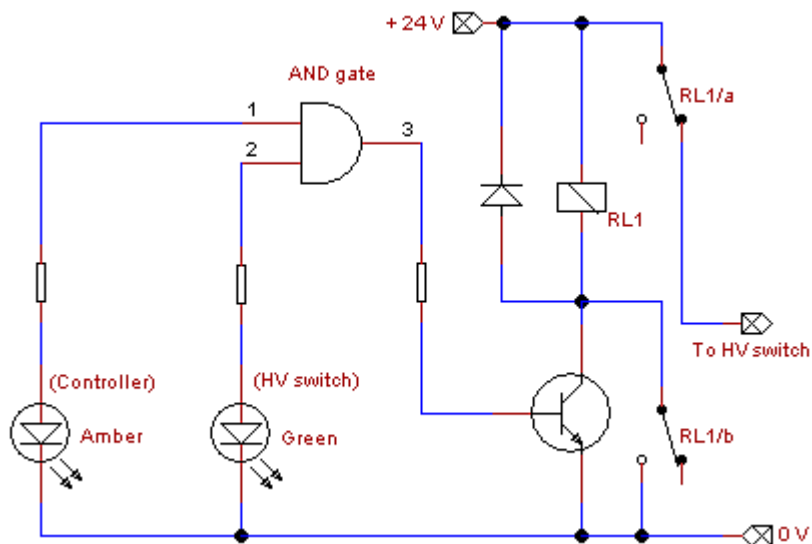


Figure 2.32 Flashover prevention circuit

Relay RL1 latches on via contacts RL1/b when the fault state of controller amber and HV switch green leds ON is detected. This permanently removes the +24 V supply to the HV switch via contacts RL1/a to prevent flashover until the fault is investigated and cured.

2.17 Acquisition of channeltron pulses and processing for tuned mass mobility

In either the selected (tuned mass) or total ions modes, the pulses from the channeltron preamplifier represent ions of a particular m/z that are then counted over fixed time intervals. By displaying the counts against time, a mass mobility spectrum is obtained. Although the LabVIEW DAQ card has two onboard timer/counters, they are unsuitable for this application as

their accuracy becomes unacceptable when the gating time approaches 1ms. This was found to be due to software overheads taking up a significant part of the timing period (the time required to stop the timing task, read the counter and then re-initiate it ready for another measurement). A vi (virtual instrument) is the term used when programming in LabVIEW instead of the more conventional “sub program“ and a limitation that precludes their use in this case is that the vi’s controlling the counters have a minimum resolution of 1 ms.

2.17.1 Hardware solution for converting ion counts from the channeltron into an analogue of the ion current

In order to overcome the software limitations of LabVIEW a hardware approach was taken whereby the ion count is obtained by using a TTL (transistor-transistor logic) counter. After passing the counter output to a digital-to-analogue converter (D/A), the pseudo analogue representation can be read into a LabVIEW program. This is done by treating the output from the D/A as a waveform that can be appropriately sampled in time with the fast onboard analogue-to-digital converter (A/D) used by LabVIEW.

The pulse count from tuning in to a particular mass lying under the peak in the IMS mobility spectrum needs to be read in a short time to achieve sufficient resolution. Too short a time would result in very low counts which may be lost in the background noise count whereas using too long a count period although giving a higher count, would result in loss of resolution such that two adjacent peaks may blend into one.

Assuming a minimum FWHM pulse width of 1 ms in the mobility spectrum, then to have acceptable resolution, the count time should be say 0.1ms giving an effective ‘sampling rate’ of 10 kHz. The fast A/D converter on the DAQ card (NI1604) can then be used in conjunction

with LabVIEW to sample the waveform at 100,000 samples/sec to regain the original count acquired at 0.1 ms intervals. This would in turn give ten samples per count value ensuring sufficient resolution in the resultant spectrum to be displayed. Once set up, the A/D converter does not require any further software commands.

By acquiring a waveform consisting of 4000 samples at a sampling frequency $f_s = 100$ kHz, (100 samples/ms) this would allow a plot of the spectrum over a 40 ms time period from the initiation of the sampling trigger pulse. This particular time period therefore results in a 25 Hz maximum limit on the trigger pulse repetition rate. The width of the IMS gate pulses will be in the range 0.2 to 0.5 ms. In order to obtain a 'clean' tuned mass response, the counts are accumulated over many scans so that random noise is averaged out to provide a sufficient signal-to-noise ratio.

2.17.2 Hardware considerations

Using an 8-bit counter over 0.1 ms will produce a maximum count reading of 255. Applying this to an 8 bit DAC will give an output voltage of 2.55V. The output register in the counter holds the count reading between each count and so the signal from the continuously converting D/A will be in the form of a discontinuous analogue representation of the counts from the channeltron as shown in Figure 2.33 below. This pseudo analogue signal can then be presented to a modified version of the IMS software written in LabVIEW that was originally designed to sample a continuous signal from the Faraday plate to show when a molecule having a particular m/z forming the peak in the mobility spectrum arrives at its particular drift time. The main differences between the two programs are that for mass mobility the vertical axis will be a reading proportional to the ion intensity in counts/s rather than ion current in nA, for ion

mobility. Also, 'external mass' control of the mass spectrometer is required for acquiring counts at a particular value of m/z for the ions over the scanning interval (of 40 ms) to get a mobility spectrum.

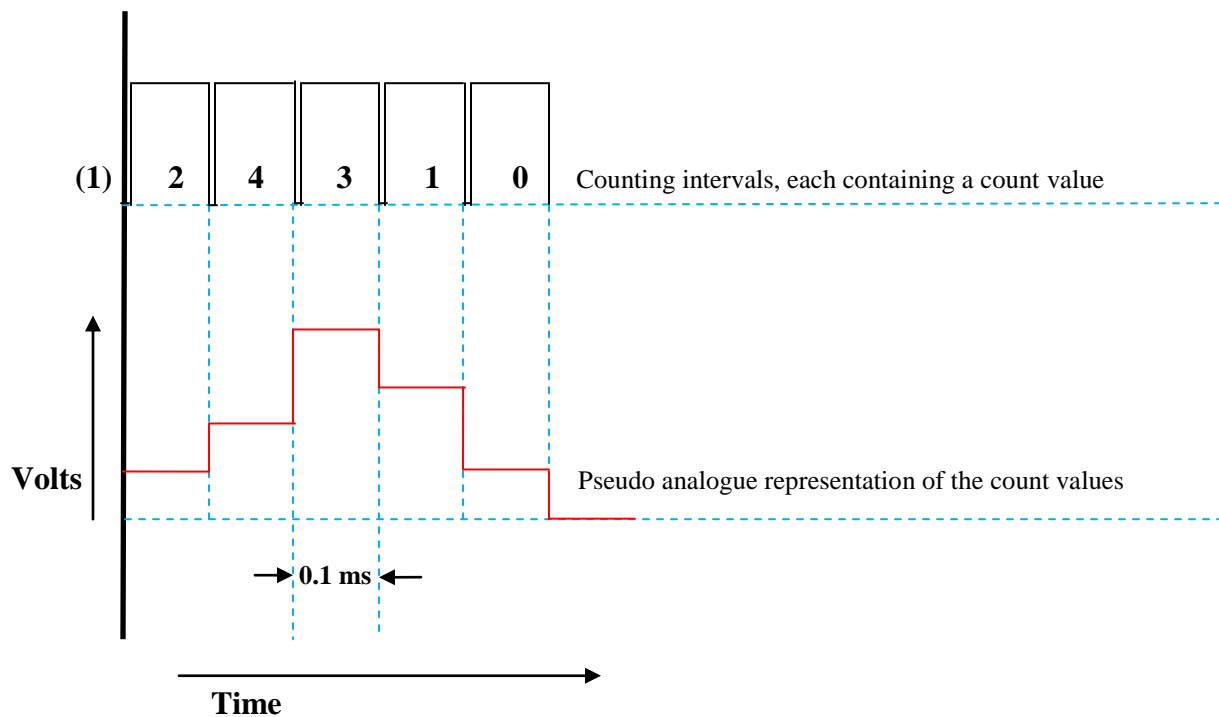


Figure 2.33 Ion count signal from the pulse converter

A schematic representation of the hardware solution is shown in figure 2.34. The sections following provide circuit diagrams of the implementation of each block along with a brief description of how the circuit operates. More detail is given of the counter control (synchronising pulses generator) since this is particular to this application and required considerable thought in the design and testing stages. The proceeding section then describes a practical validation of how the pulse generator performs over the range of ion intensities typically encountered. Finally, a theoretical analysis of the circuit response is made.

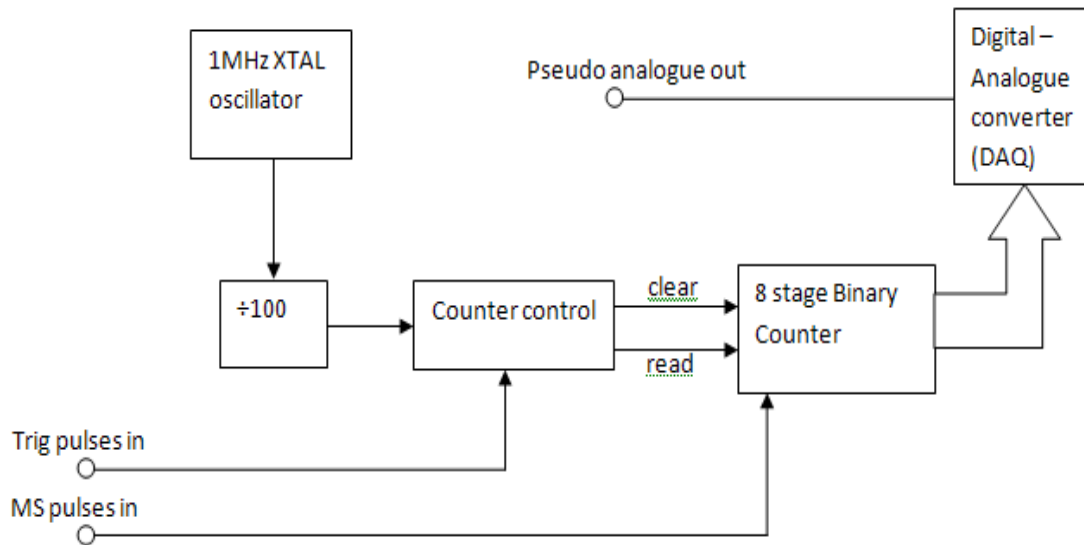


Figure 2.34 Block diagram of Pulse Count to Voltage Converter. The trigger pulses are derived from a crystal oscillator. MS pulses arrive from the channeltron inside the mass spectrometer.

2.17.3 Circuit diagrams and descriptions of the pulse converter stages

In order to achieve fast switching speeds, TTL gates having a propagation delay of 20 ns were used to implement the logic requirements.

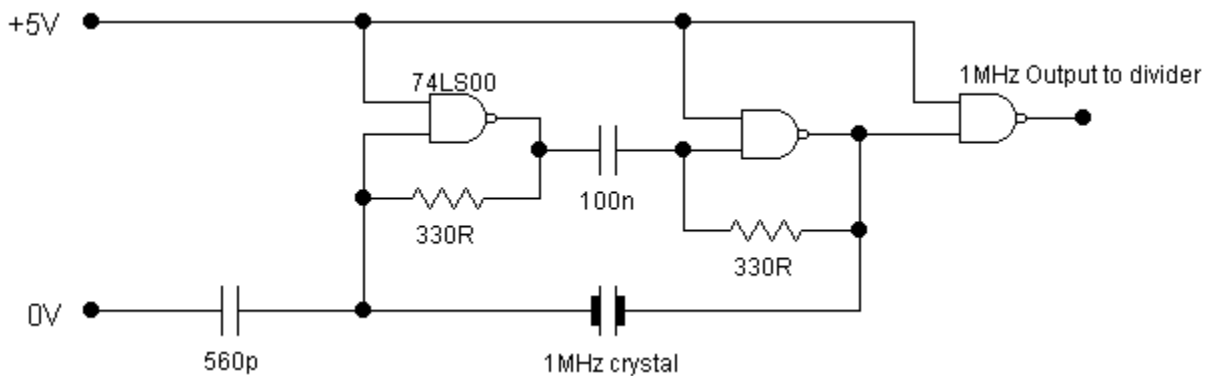


Figure 2.35 1 MHz time-base generator

In order to maintain an accurate time reference, a crystal-controlled clock pulse generator as shown in figure 2.35 is used for the time base. It operates in the series resonant mode using the fundamental frequency of the crystal. The $330\ \Omega$ resistors provide negative feedback to bias the inverters into their linear region. The final inverter acts as a buffer to produce a sharp square wave.

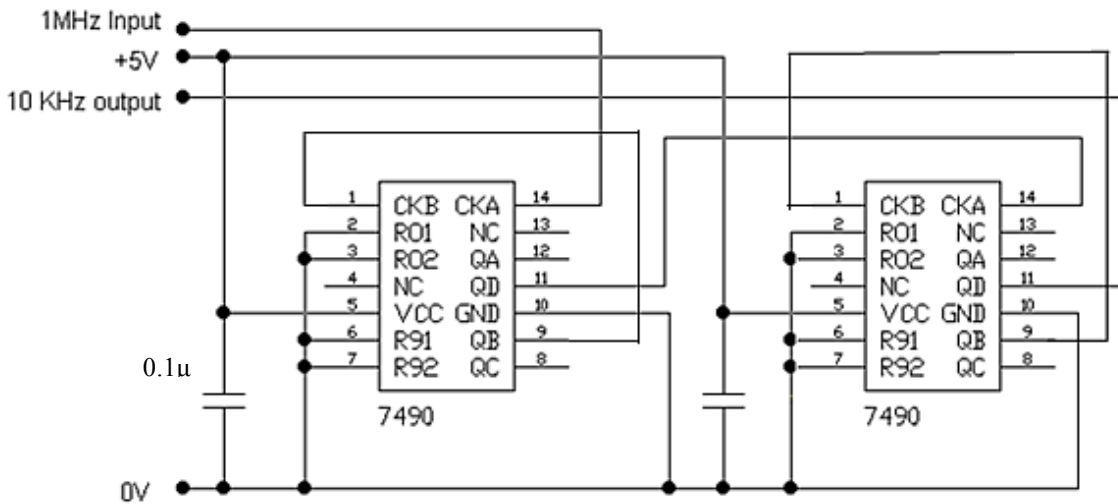


Figure 2.36 Two cascaded asynchronous decade counters are used to provide the overall $\div 100$ operation for reducing the clock frequency down from 1 MHz to the sampling frequency of 10 KHz. The decoupling capacitors are both $0.1\mu\text{F}$ and serve to prevent switching spikes caused by other circuits on the power supply from causing false counts.

2.17.4 Sync pulses generator

This section controls the operation of the ion pulse counter in terms of triggering, reading the count and clearing for the next measurement. The control pulses need to be as short as possible since they take up part of the time for the sampling window. The operation is best considered by use of the timing diagram shown in figure 2.37. The sequence is initiated by the rising edge of the 10 kHz clock pulse.

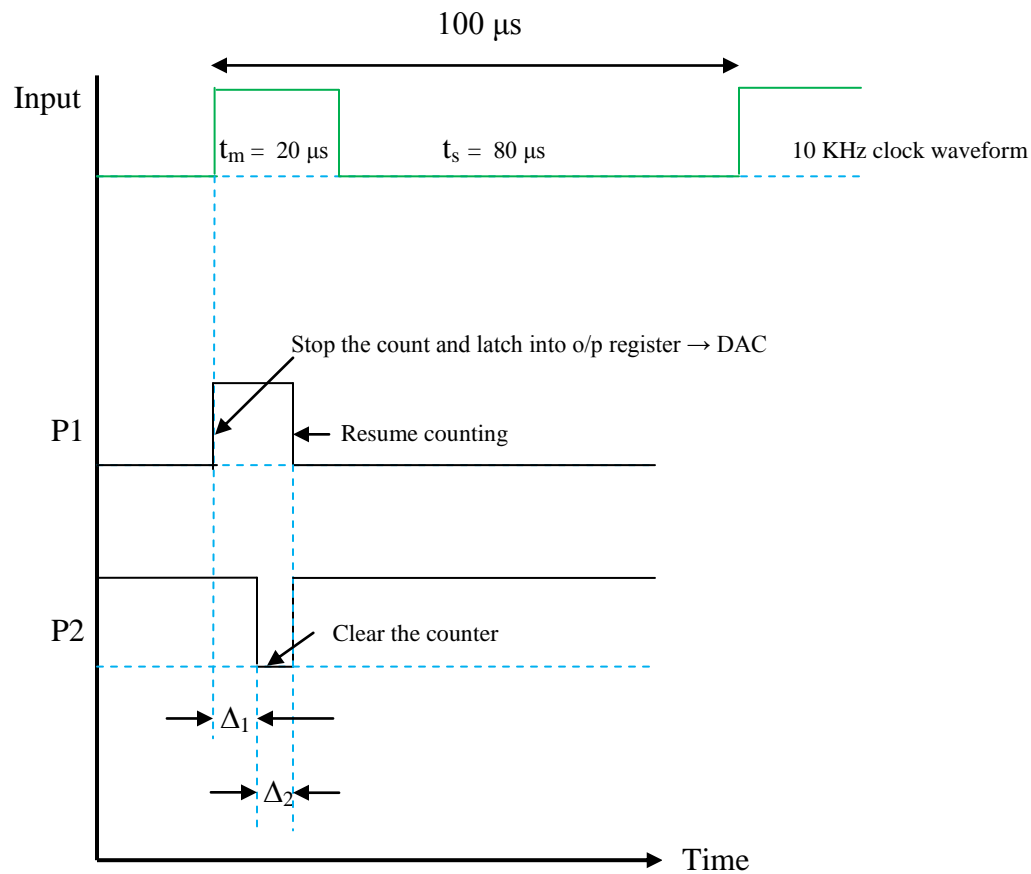


Figure 2.37 Sync pulses generator – timing diagram for displaying the temporal relationship between the control pulses P1 and P2.

Note, the outputs P1 and P2 are not to the same time scale as the input waveform since pulse P1 is only about $1\mu\text{s}$ long. The control pulses P1 and P2 can be obtained from the input waveform by producing another timing diagram as seen in Figure 2.38 showing the appropriate time delays and waveforms required to implement the circuit shown in Figure 2.39. Time delays Δ_1 and Δ_2 are made short since they form part of the 0.1 ms pulse counting window. By making them $0.5\mu\text{s}$ long, the reduction in the count time will be only 1%. Although Δ_1 and Δ_2 could be obtained from gating the output lines of the $\div 100$ divider stages, it is better if they are of a fixed duration independent of the clock pulse frequency from the oscillator. This allows more flexibility if ever a different count time was required by ensuring that suitable delay times are still maintained.

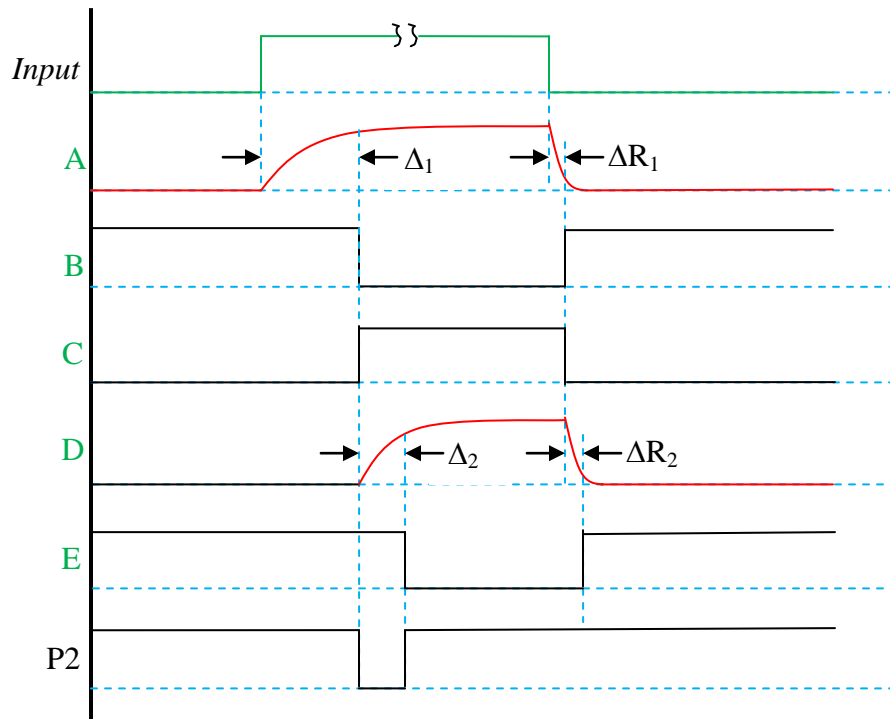


Figure 2.38 Sync pulse generator waveforms. The output $P1$ is obtained from the logical expression $P1 = \text{Input AND } E$. Δ_1 and Δ_2 are time delays (see text), ΔR_1 and ΔR_2 are their respective recovery times.

From consideration of the above timing diagram, the circuit shown in Figure 2.39 has been produced. The short time delays Δ_1 and Δ_2 are formed from the 10 k Ω and 47 pF combination to provide a time constant of 0.47 μs . Fast recovery times (ΔR_1 and ΔR_2) of 0.047 μs are ensued by the diode and the 1 k Ω combination shunting the 10 k Ω resistors. This ensures that the derived output $P1$ from the delays is kept short. The time delay Δ_1 allows time to latch the count into the storage register of the counter before clearing ready for the next count. Although a possible race hazard exists due to stopping and latching the count during a transition to the next count, (the counter is an asynchronous “ripple through” type) this is not expected to have any effect since its occurrence will be infrequent, and will also be lost over the many accumulations taken of the count readings. Time delay Δ_2 allows time for the counter to fully clear before moving on to the next count.

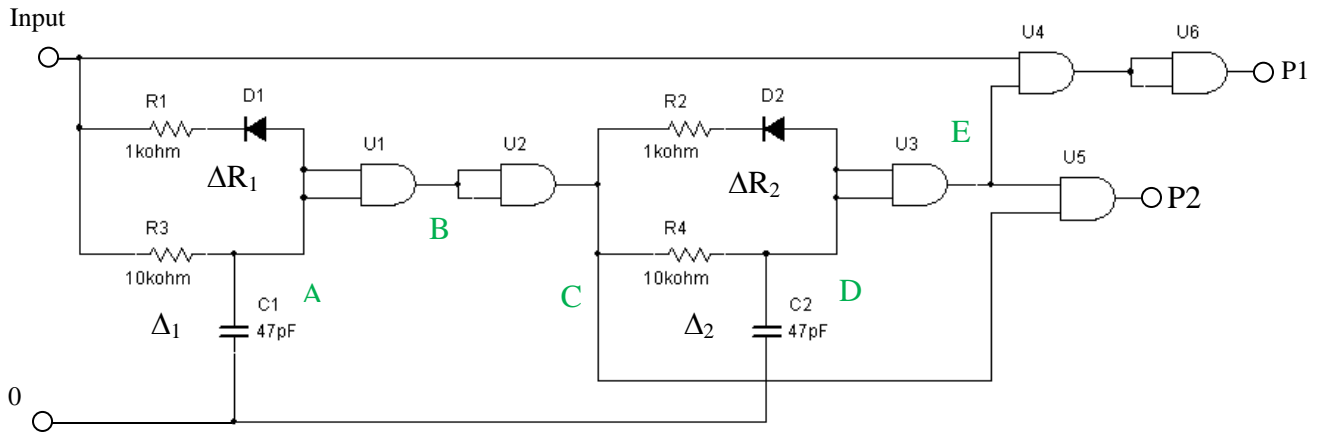


Figure 2.39 P1, P2 sync pulses generator

Note, the 100 ns contribution of the gates in the 0.1 ms pulse counting period is only 0.1% and so is deemed insignificant.

2.17.5 Pulse count considerations

By using an 8-bit counter (modulo 8), an output value of 0 to 255 can be read in 0.1 ms. A single count would represent an ion pulse frequency of 10 kHz and 255 counts would correspond to a frequency of 2.55 MHz. Such a high intensity of ion signal would not occur in practice and so it was decided that modulo 3 operation of the counter which represents an upper frequency of $(2^3-1) \times 10 \text{ KHz} = 70 \text{ KHz}$ will be sufficient. To achieve maximum SNR, the three most significant output bit lines from the counter (Q_A , Q_B and Q_C) are passed on to the upper three input lines (Bit3, Bit2 and Bit1) of the D/A converter as shown in Figure 2.40. Bits 4 to 8 of the D/A are grounded.

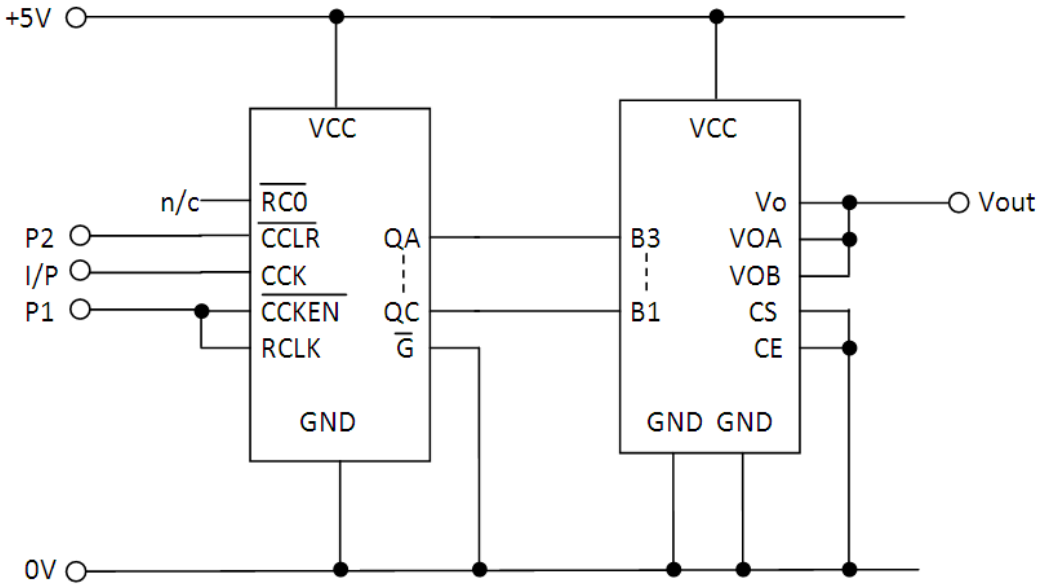


Figure 2.40 8-bit Counter and D to A Converter. Note, P1 is connected to CCKEN (counter clock enable) and RCLK (register clock), P2 is connected to CCLR (counter clear). The input pulses connect to CCK (the counter clock).

2.17.6 Data acquisition considerations

Although the 0.1 ms pulse counting interval is crystal controlled, the trigger pulse to the gate is derived from a circuit based on the analogue timer chip NE555. However, this has good stability but it is not synchronised with the clock in the pulse converter and so there could be up to 0.1 ms uncertainty on where the RIP actually lies with each scan of the mobility spectrum. Although at first sight, it may be thought that this would have a large effect on the shape of the RIP, the effect is actually much less since the difference in time between the edge of the trigger pulse and that of the counter pulse P1 will remain constant over a substantial time period compared to that of the counting window, and a difference in arrival time of the RIP of 0.1 ms is only a small fraction of the overall drift time. (If desired, the gate trigger pulse could be derived from the oscillator in the pulse converter by dividing the 10 KHz counter clock by 400 to give 25 Hz (40 ms) synchronised pulses.)

The pulses from the channeltron preamplifier are very short (25 ns wide) and if one of them happens to occur within the 2 μ s dead time of the 100 μ s pulse counting period (for latch, DAC and reset), it will be lost. However, since this still leaves 98% of the time available for seeing such pulses, then statistically, the effect is negligible.

Although the idea of “number of counts/second” is more applicable in dc mode where the gate is left open and ions are continually available, this can still be applied to the converter in pulsed mode where the output will be in “counts/0.1 ms” that can then be translated to counts/sec by multiplying by 10^4 if so desired. (When testing the converter, a set of fixed frequencies was inputted to check on the accuracy of conversion, i.e. using dc mode as discussed in section 2.18.)

The ion swarm drifts along the flow tube at around 5 m/s and then due to a drastic pressure decrease, undergoes an adiabatic expansion at supersonic speed when passing from the Faraday plate into the mass spectrometer. The time taken for the transition of the ions through the mass spectrometer ion optics to the channeltron detector although small compared to the drift time, is still significant, and the RIP seen in the mass mobility spectrum will be at a slightly longer time (~ 0.3 ms) than that of the ion mobility spectrum.

At lower ion intensities, it may be difficult to differentiate between the low counts over one scan since the chance of seeing an ion is dependent on the number of ions present. Thus by accumulating the ion count over many scans, it will be possible to obtain a better profile of the ion intensity.

2.17.7 Determining the relationship between the count reading given by LabVIEW and the frequency of the ion pulses

The 8-bit counter in conjunction with the 8-bit D/A is capable of a resolution of 10 mV/bit since the maximum output from the D/A with all inputs at logic ‘1’ as given in the datasheet is 2.55 V. i.e. $(2^8 - 1) \times 10 \text{ mV} = 2.55\text{V}$. Modulo 3 however is now being used and the fraction $2^8/2^3$ is $256/8$ giving a count ratio of 32:1. Thus with the bits as they are now connected (as shown in figure 2.40), the output from the D/A will correspondingly be $32 \times 10 \text{ mV} = 0.32 \text{ V/bit}$. Thus the output from the D/A is in the form of the quantum levels of voltage seen in Table 2.5:

Table 2.5 Relationship between pulse count and D/A output voltage

Q_C	Q_B	Q_A	$V_{D/A}$
0	0	0	0
0	0	1	0.32
0	1	0	0.64
0	1	1	0.96
1	0	0	1.28
1	0	0	1.60
1	0	1	1.92
1	1	1	2.24

From this, it is seen that the pulse count is given by $V_{D/A} \div 2.24 \times 7$

i.e. $\text{Count} = 3.125 V_{D/A} \quad (2.5)$

With an input pulse frequency of 10 kHz, one pulse will be seen within the 0.1 ms counting window which will then produce 0.32 V from the D/A converter. This will correspondingly be shown as a reading of 0.32 on the LabVIEW output screen. Thus, with 1000 accumulations, the reading will be $1000 \times 0.32 = 320$.

The bit count will increment with multiples of 10 kHz reaching a maximum of 7 at 70 kHz.

Note, intermediate frequencies will produce a “drift” of pulses across the counting window over time, resulting in a spread of the integer counts around a mean fractional value. By accumulating over many counts, a close approximation to the actual intermediate frequency will be obtained.

Let f_{in} = the equivalent counts/sec of an ion of a particular selected mass, and N_{acc} = the number of accumulations:

$$\text{Now, for the range } f_{in}(\text{kHz}) = 10 \text{ to } 70, \text{ Count} = \frac{f_{in}(\text{kHz})}{10 \text{ kHz}} \quad (2.6) \quad .$$

The corresponding reading will be $V_{D/A} \times N_{acc}$

$$\text{Substituting equation 2.5, Reading} = \frac{\text{Count}}{3.125} \times N_{acc}$$

$$\text{Substituting equation 2.6, Reading} = \frac{f_{in}(\text{kHz})}{31.25} \times N_{acc}$$

$$\text{Therefore } f_{in}(\text{kHz}) = \frac{\text{Reading}}{N_{acc}} \times 31.25 \quad (2.7)$$

2.18 Testing and verifying the operation of the pulse converter

These tests are performed by using a known pulse frequency from a function generator to simulate the output from the channeltron pre-amplifier so enabling a steady response to be seen when using the ion mass mobility LabVIEW programs. The function generator gave TTL compatible pulses that were varied over a range of pulse repetition frequencies covering 10 Hz to 100 kHz. The output frequency was set as accurately as possible (within the limits of function generator control) by monitoring with a counter/timer while adjusting the frequency control for

the best possible reading. Drift in frequency from the signal generator was seen as a variation in the displayed frequency of about 0.1% between readings (given at 0.5s intervals).

The main error was due to the limits in resolution of frequency adjustment since it is made using a potentiometer in the signal generator.

An initial trial was made with a fixed input count to the converter of nominally 25 kHz (best adjustment possible was 24.96 kHz) to the pulse converter. The number of accumulations was set at 500. On the screen, the continuous waveform of counts showed a mean count of 399 ± 10 counts. i.e. An error of about 2.5%.

Since the count is directly proportional to the number of accumulations (assuming that the counter inside the converter does not overflow), approx 800 counts would be expected with 1000 accumulations.

Upon trying this, 798 ± 10 counts were seen, i.e. an error now of 1.25%. In this case, doubling the number of accumulations seems to halve the error in the count.

With 2000 accumulations, 1596 ± 12 counts were seen, i.e. an error of 0.75%.

Although this error is not half of that with 1000 accumulations, it is still a further improvement.

Since an input of 25 kHz produces about 400 counts with 500 accumulations, the relationship between the input frequency and the displayed count can be described as:

$$\text{Input counts/sec (kHz)} = \frac{\text{Displayed count}}{\text{No.of accumulations}} \times 31.25$$

This confirms equation 2.7 derived in the previous section.

As a check, changing the input frequency to 20 kHz gave 320 ± 2 counts (0.625% error) with 500 accumulations.

Thus, applying equation 2.7,

$$f_{in}(kHz) = \frac{\text{Reading}}{N_{acc}} \times 31.25 = \frac{320}{500} \times 31.25 \text{ which correctly gives 20 kHz.}$$

Note, increasing to 1000 accumulations gave 640 ± 2 counts (0.31% error)

In order to see how the converter responds to a range of input frequencies, tests were done with 500 and 1000 accumulations at frequencies initially between 1 kHz and 100 kHz representing a weak signal count up to a strong count.

2.18.1 Characterisation Measurements

Here, the performance of the circuitry under controlled conditions is observed whereby the ‘ion counts’ are provided by a signal generator. With the number of accumulations set to 500 the results obtained are shown in table 2.6.

Table 2.6 Count variations with frequency using 500 accumulations

Result number	Input frequency (kHz)	Mean count and variation	Variation (%)
1	1	17.7 ± 1.5	8.5
2	5	82.2 ± 4	4.9
3	10	161.7 ± 0.3	0.2
4	15	240 ± 4	1.7
5	20	320 ± 1.5	0.5
6	25	401 ± 8	1.2
7	30	484.4 ± 1.3	0.3
8	35	562 ± 7	1.3
9	40	642 ± 0.3	0.5
10	45	722 ± 6	0.8
11	50	801.5 ± 1	0.1
12	100	$322.25 \pm .25$	0.1

In order to see what the effect of increasing the number of accumulations would be, results were also obtained at 1000 accumulations, as shown in table 2.7.

Table 2.7 Count variations with frequency using 1000 accumulations

Result number	Input frequency (KHz)	Mean count and variation	Variation (%)
13	1	35.4 ± 2.4	6.8
14	5	164.8 ± 4	2.4
15	10	323.7 ± 1	0.3
16	15	481.8 ± 4	0.8
17	20	640 ± 2	0.3
18	25	807.1 ± 5	0.6
19	30	968.2 ± 2	0.2
20	50	1600 ± 2.5	0.2
21	100	640 ± 1.5	0.2

For interest, at very low frequencies, the response was as seen in tables 2.8 and 2.9.

Table 2.8 Count variations at low frequencies using 500 accumulations

Result number	Input frequency (Hz)	Mean count and variation	Variation (%)
22	10	1.8 ± 0.17	9.4
23	50	2.44 ± 0.68	28
24	100	3.26 ± 0.9	28

Table 2.9 Count variations at low frequencies using 1000 accumulations

Result number	Input frequency (Hz)	Mean count and variation	Variation (%)
25	10	3.6 ± 3.5	97
26	50	4.9 ± 0.93	19
27	100	6.5 ± 1.3	20

It is seen that a transition in the output count occurs between results 11 and 12 (also 20 and 21).

In order to obtain the transition point, further measurements were taken as shown in table 2.10.

Table 2.10 Count variation around the transition frequency range using 500 accumulations

Result number	Input frequency (kHz)	Mean count and variation	Variation (%)
28	55	881 ± 4	0.5
29	60	961 ± 1	0.1
30	65	1040 ± 7	0.7
31	70	1119 ± 2	0.2
32	75	590 ± 30	5.1
33	80	35 ± 15	43
34	85	74 ± 10	14
35	90	153 ± 3.5	2.3
36	95	235 ± 4.3	1.8

Results 31 to 34 cover the region of counter overflow in the converter where the count decreases with increasing input frequency. Finer readings were taken around this region with the results shown in table 2.11

Table 2.11 Count variation around the transition point using 500 accumulations

Result number	Input frequency (kHz)	Mean count and variation	Variation (%)
37	71	1020 ± 19	1.9
38	72	943 ± 32	3.4
39	73	833 ± 29	3.5
40	74	702 ± 18	2.6
41	75	624 ± 30	4.8
42	76	490 ± 26	5.3
43	77	382 ± 20	5.2
44	78	255 ± 20	7.8
45	79	136 ± 20	14.7
46	79.9	64 ± 20	31.3
47	80.2	30 ± 9	30
48	80.4	14 ± 8.2	59
49	80.5	2.6 ± 0.6	23
50	80.7	6 ± 1.5	25
51	81	11.2 ± 2.4	21

2.19 Comments and discussion of the results obtained

This particular investigation whereby the instrument is thoroughly characterised, is important as it allows the relative accuracy of peaks having widely different magnitudes to be ascertained, and also to determine the practical working range of the pulse converter.

Considering result no.3, the pulse counting window in the converter produces count values at a rate of 10 kHz and so the probability of seeing input counts of 10 kHz that are also coincident with the window is high. Hence the low error associated with this. (Similarly at 100 kHz.)

As expected, increasing the number of accumulations generally produces a reduction in the amount of variation in counts about the mean.

Figure 2.41 shows a graph of mean count values against input frequency, where it is seen that they closely follow the expected straight line relationship.

From previous investigations described in chapter 4, at $m/z = 73$, the typical count obtained was 180 with 500 accumulations. Using equation 2.7, this corresponds to an input repetition frequency of:

$$\frac{180}{500} \times 31.25 = 11.25 \text{ kHz}$$

In this range, the error is <1% and so the pulse conversion technique will clearly give reliable results around this region. From the graph shown in figure 2.42 and taking into account the magnitude in the variation of counts, the working range is seen to be from 1 kHz to 70 kHz.

Also, from fig 2.42 it is seen that over the working range of 10 kHz to 70 kHz, the percentage variation about the mean is less than 2%.

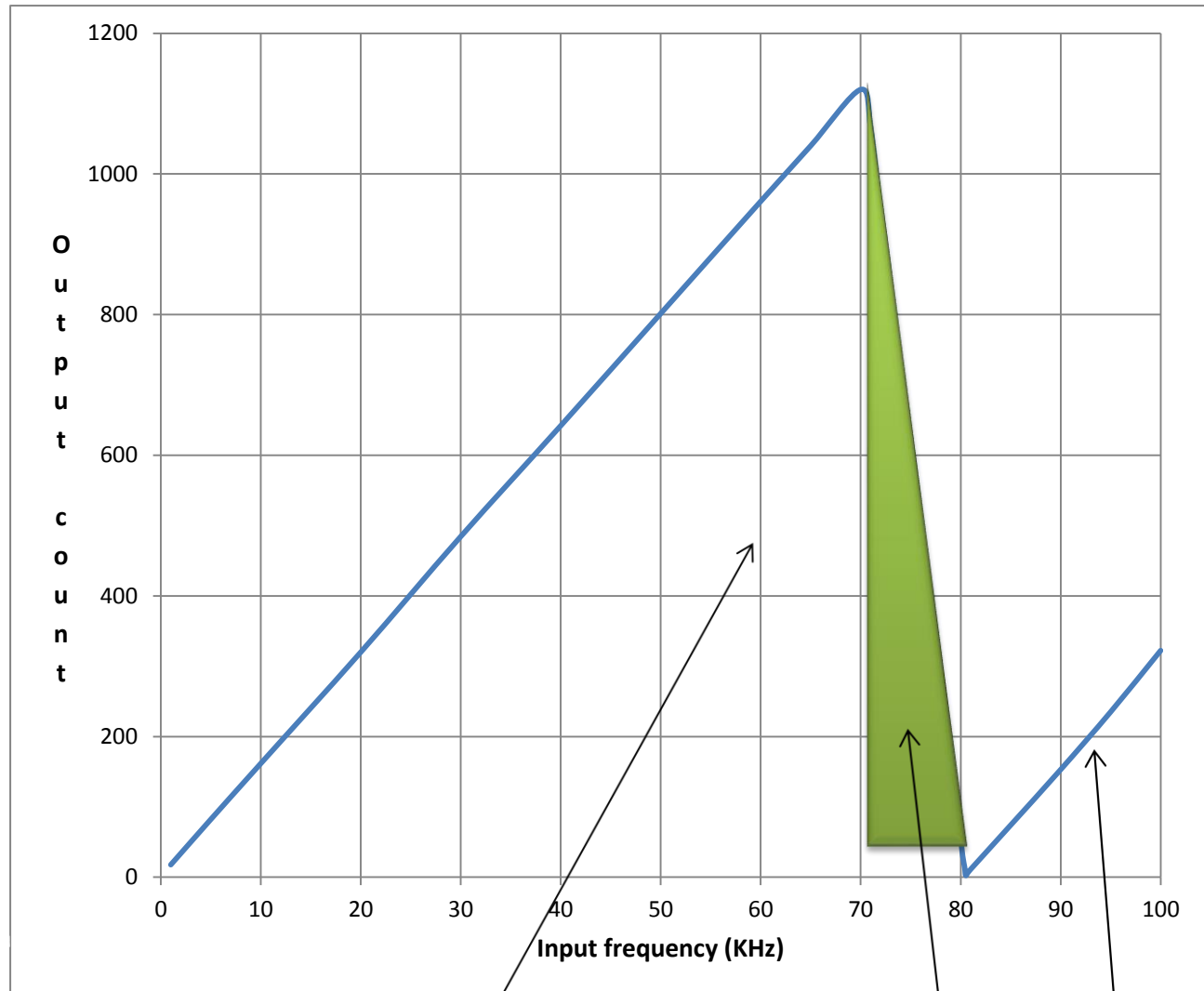


Figure 2.41 Plot of input frequency to output count with 500 accumulations

Normal counting region.

Counter overflow region.

Reflected counting region.

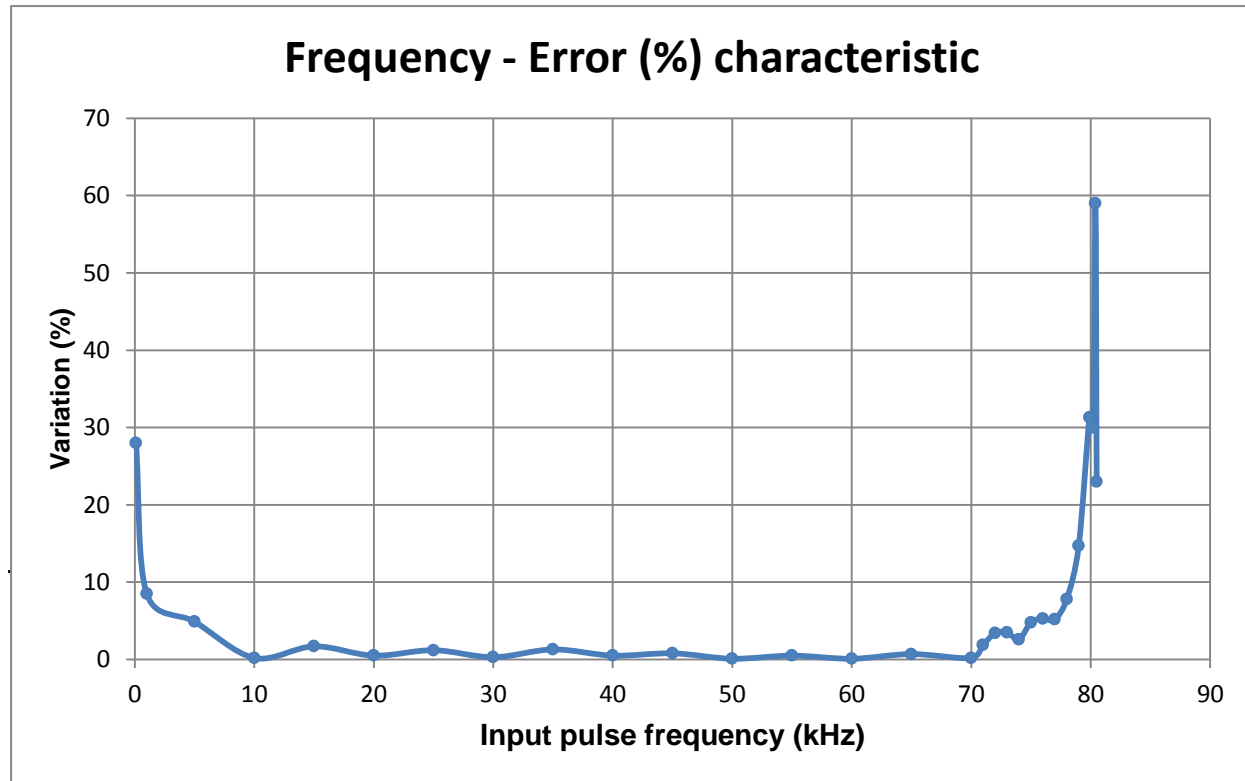


Figure 2.42 Percentage variation (error) in count with pulse frequency.
(500 accumulations)

Below 1 kHz, the error becomes unacceptable for reasonably accurate peak height comparisons, as seen in results 22 to 27 shown in tables 2.8 and 2.9. This is because the occurrence of pulses seen in the 0.1 ms window becomes less frequent as the pulse repetition frequency drops. In results 22 to 24, the number of accumulations is insufficient to be able to distinguish between noise and signal, and no trend is seen. In results 25 to 27 the counts are still virtually down in the noise levels, but are becoming more significant since the error at 10 Hz is (as expected), much higher than that at 50 or 100 Hz.

Of interest is to look at the transition from the end of the overflow region to the start of the next counting region theoretically starting at 80 kHz. From result 49 in table 2.11, the lowest count of 2.6 occurs at 80.5 kHz. This error of 0.63% can be attributed to the effect of the combined inaccuracies of the crystal controlling the counting window in the converter and that of the counter/timer used to monitor the signal generator frequency.

Considering the variation in count about the mean, the ‘beats’ are due to pulses at frequencies that are not at multiples of 10 kHz which, drifting in time across the counting window, appears to produce a peak variation that occurs at the maximum excursion between multiples of 10 kHz (i.e. at the mid-point that occurs with multiples of 5 kHz). This is covered theoretically in greater detail in section 2.20.1 following). Below 10 KHz, the variation becomes progressively larger at a steeply increasing rate because less pulses will be seen as the frequency of their occurrence becomes smaller.

Considering how the pulse converter operates, a formula relating the maximum working frequency to the division ratio of the counter and the repetition rate of the counter window can be deduced as:

$$f_{max} = f_{win}(2^n - 1) \dots\dots\text{eqn 2.8}$$

where n is the division ratio of the counter and f_{win} is the window repetition frequency.

Therefore, if so desired, the working range could easily be extended to 150 kHz by increasing the division ratio of the counter from 3 to 4, and so on.

At lower counts, the count at 500 accumulations may be around say, 18 corresponding to an input frequency of 1.1 kHz. The variation in count is seen to be 8.5% at 1 kHz. This could be improved on by increasing the number of accumulations to say, 2000 but the relative heights could alternatively be compared by using the mass spectra program where the count is made not over 0.1 ms (for arrival time) but nominally over 200 ms per increment of amu (for peak height) thus allowing a lot more time for the reading of counts to establish. The main purpose of the count converter is to give the arrival time of mass tuned ion peaks.

Considering figure 2.41, the psuedo-analogue count output varies linearly with the input frequency up to 70 kHz. After that, counter overflow occurs as shown by the shaded area. A 3-stage counter is used in the pulse converter thereby producing an output count of 0 to 7. The window frequency is 10 kHz (the counter is allowed to count up during intervals of 0.1 ms.) and so further increases crossing the 70 kHz threshold progressively produce a decrementing count that is aiming for zero. The up-count then recommences from zero at 80 kHz.

The slope of the line representing the counting region m_c is 16, while that of the overflow region m_0 is -112, thus $m_0 = -7m_c$. This is because the change from a maximum count of 7 to the minimum of 0 has to take place over the smaller range of 70 kHz to 80 kHz (i.e. within a 10 kHz window). However, m_c has a positive slope and presides over the normal operating range of 70 kHz and so is reduced by a factor of 7 relative to m_0 .

Considering equation 2.7 namely $f_{in}(kHz) = \frac{Reading}{N_{acc}} \times 31.25$

The slope m_c can be predicted by rearranging for $\frac{Reading}{f_{in} (kHz)}$

$$\text{i.e. } m_c = \frac{N_{acc}}{31.25} = \frac{500}{31.25} = 16$$

Referring to Figure 2.42, it is seen that the region of operation for minimum error is from 10 kHz to 70 kHz. Also seen is the previously mentioned ripple caused by the maximum excursion from the sides of the 10 kHz windows at the 5 kHz midpoints.

From 70 to 80 kHz the error accumulates to a maximum of about 60%.

The lack of detail from 100 Hz to 10 kHz is due to the scarcity of data points taken. If more points had been taken, it may be that a similar response to that over 70 to 80 kHz would have been obtained although the accuracy of the results is difficult to ascertain because the count values are almost down into the noise levels.

Although extending the counter from modulo 3 to modulo 4 would extend the frequency range to 150 kHz and also reduce the error (since there would be 16 quantisation levels instead of 8) it seems that the present setting is sufficient as the error is less than 2% over the working range of frequencies expected, and the response at 70 kHz would represent a signal with a very strong ion count which is above that normally acquired.

2.20 Theoretical considerations on the response of the pulse count converter to a steady input frequency

The pulse count converter can be more accurately described as ‘a gated digital pulse counter to pseudo analogue converter’. To describe its true response theoretically to a set of digital

pulses that are occurring as a continuously changing pulse stream in response to a Gaussian shaped input waveform (representing an ion peak in the mobility spectrum) occurring every 40 ms or so would be a complex task, and unnecessary since:

- a. From the experiments, the converter has been seen to fulfil its requirements for obtaining total ions and selected mass mobility spectra.
- b. Characterising the converter by using a set of steady input pulse frequencies (as performed in section 2.21) has enabled a theoretical investigation into its response to be more readily achieved.

It is therefore interesting to now consider the theoretical response to a pulse stream of steady frequency in order to gain a more fundamental insight into how the system operates.

The graph previously seen in figure 2.42, shows the response of the converter to a range of steady input frequencies for quantifying its operation in this respect. The actual input to the converter from the channeltron preamplifier is in the form of a spread of input count values within each 0.1 ms time slot, effectively giving an incremental sweep of input frequencies over the spectrum to produce a characteristic spectral response. This considerably complicates the issue especially at frequencies less than 10 kHz where the chance of seeing a pulse gets much less as the frequency reduces and so considerably more accumulations will be required to get a number of counts above those arriving from the background of system noise.

Figure 2.42 which gives the frequency-error characteristic of the converter shows that the linear relationship between input frequency and output count is only exact when the input pulse frequency is an integer i multiple of 10 kHz where $1 \leq i \leq 7$. For intermediate count pulse frequencies where i is non integer, an error ripple is seen. An exact mathematical description of the curve may be difficult to derive as it involves consideration of the

probability of the ions impinging on the channeltron in terms of ion intensity. (At low counts, it may take several accumulations before an ion is actually seen in a particular sampling interval.) To a first approximation however, an idea of what happens may be gained as described in the following section.

2.20.1 The pulse counting window

Assuming that the window commences when the input pulse commences, then on a temporal basis, figure 2.43 represents an input pulse of frequency between 10 and 20 kHz arriving within the $T = 0.1$ ms ($f_s = 10$ kHz) counting window between $t = T/2$ and $t = T$. At frequencies above 10 kHz, there is 100% probability of seeing a pulse.

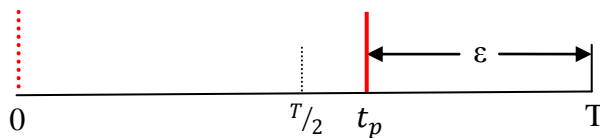


Figure 2.43 Representing a channeltron pulse arriving within the counting window

The interval ϵ represents the uncertainty in the measurement of the input pulse frequency (f_p) within the counting period T. Thus the error between the actual pulse frequency and that measured, that is $f_p - f_m$, will be 0 when $\epsilon = 0$, which occurs at $f_p = f_s$ when the pulse occurs simultaneously at $t_p = T$ and the harmonics of f_s . As ϵ approaches $T/2$ the uncertainty will become maximum and then drop to zero at $T/2$ when a pulse occurs at $T/2$ and T, (as seen in figure 2.44). (The curves shown in figures 2.44 to 2.46 were obtained using equations derived in section 2.23.2 following.)

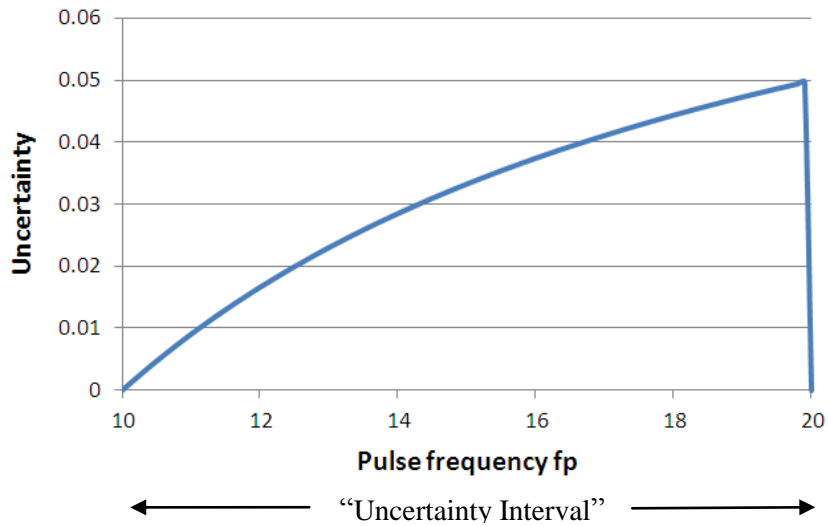


Figure 2.44 showing how uncertainty in measurement of f_p increases towards 20 kHz

When $t_p < T/2$ there will be two or more pulses occurring, hence giving a smaller value of ϵ (as shown below in figure 2.47). The maxima of ϵ will similarly reduce at each increasing harmonic as seen in figure 2.45.

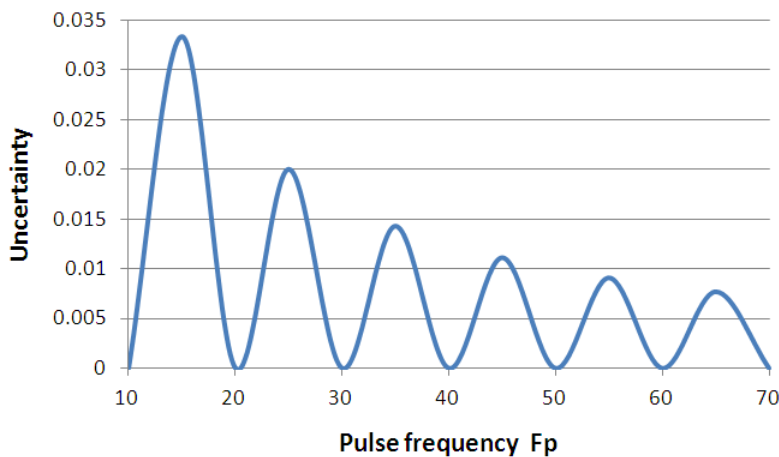


Figure 2.45 showing variation of uncertainty over the range 10 to 70 kHz

Note, in figure 2.45, only the harmonics and their mid points are plotted. The curve fit produced from Excel agrees with that obtained practically as previously shown in figure 2.42 where again only the data values at the harmonics and their mid points were obtained. Had a finer frequency range been taken, a more correct representation may have been produced of the form depicted in figure 2.46.

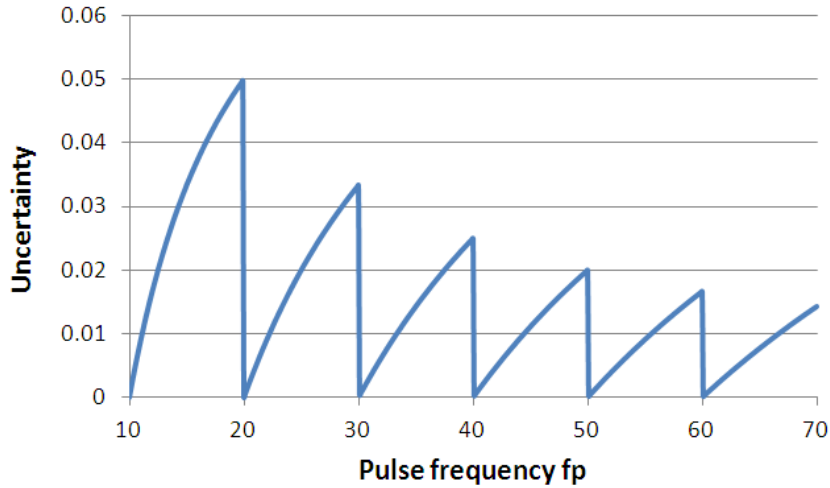


Figure 2.46 showing a more correct representation of variation of uncertainty over the range 10 to 70 kHz

Here, between the harmonics, the uncertainty correctly follows the form as seen in figure 2.44.

Considering figure 2.47 showing a counting window where $f_p > 20$ kHz, the uncertainty ϵ is given by $T - ct_p$ (2.8) where c is the number of counts within the window. Thus, in one counting period, when $t_p > T/2$ uncertainty ϵ reduces when t_p increases as was seen in figure 2.43. Conversely, when $t_p < T/2$ uncertainty ϵ reduces when t_p decreases as seen in figure 2.47. This shows that the point of maximum uncertainty lies immediately before $t_p = T/2$.

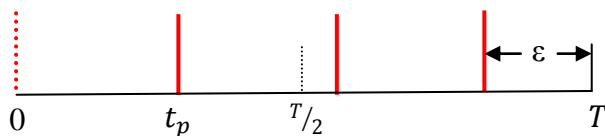


Figure 2.47 Representing channeltron pulses at $f_p > 20$ kHz

In order to get improved accuracy, the interval T needs to be as long as possible to allow more counts to be acquired. However the time required for peak resolution within the spectrum puts a constraint on T . To overcome this, an average of the count values obtained over many spectra may be performed. (Hence the value of 0.1 ms for the counting windows within a spectrum spanning over 40 ms as explained in section 2.17.1.) This approach

effectively widens the counting window by n where n = number of accumulations taken, which also gives the benefit of ‘averaging out’ of spurious noise pulses that would otherwise give additional errors in the measured pulse frequency. The effect is to reduce the error in measured pulse frequency f_m as the number of accumulations increases as explained in the following sections.

2.20.2 The effect of increasing the number of accumulations n on uncertainty ϵ

Note, in this theoretical consideration, it is convenient to take n accumulations of the pulses which may then be represented as a voltage via a D/A converter. In the practical case, the pulse count c within the window is converted to a voltage and the voltage values are accumulated over n spectra, which is equivalent since (in equation 2.5) $V_{D/A} = \text{count}/3.125$ and so the end result will be the same in both cases.

By effectively widening the sampling window to a width of nT , the uncertainty in measurement of t_p becomes $\epsilon = nT - ct_p$, but over n accumulations of spectra, the count obtained will be given by $c = \lfloor nT/t_p \rfloor$ thus $\epsilon = nT - t_p \lfloor nT/t_p \rfloor$ and in terms of frequency,

$$\epsilon = \frac{n}{f_w} - \frac{1}{f_p} \left\lfloor \frac{nf_p}{f_w} \right\rfloor$$

(A plot of ϵ vs f_p with $n=1$ was used to yield the curve previously shown in figure 2.44.)

By plotting ϵ vs f_p with $n=2$, as shown in figure 2.48, it is seen that $f_p = 15$ kHz is now resolved since three pulses will have been counted terminating at $\epsilon = nT - ct_p = 0$. The peak values of ϵ correspond to the periodic times t_p of the pulses (following the pulse positions as seen in figure 2.47).

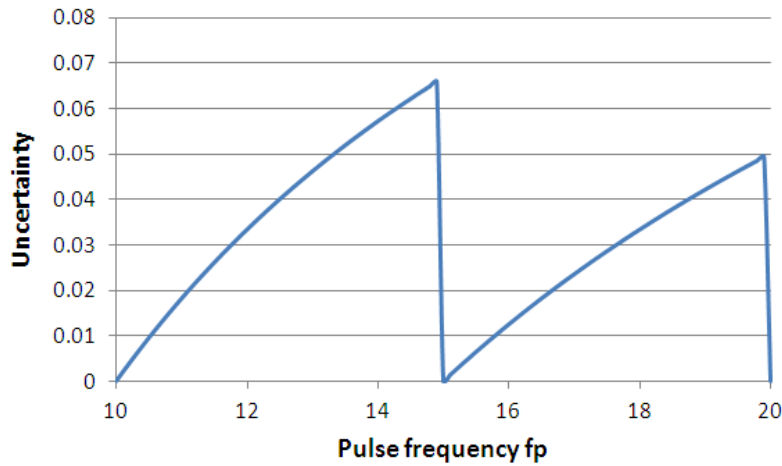


Figure 2.48 showing effect of $n=2$ on the uncertainty ϵ

Similarly, increasing n produces a further increase in frequency resolution with a proportionate increase in intervals of uncertainty as seen for the case with $n=4$ shown in figure 2.49.

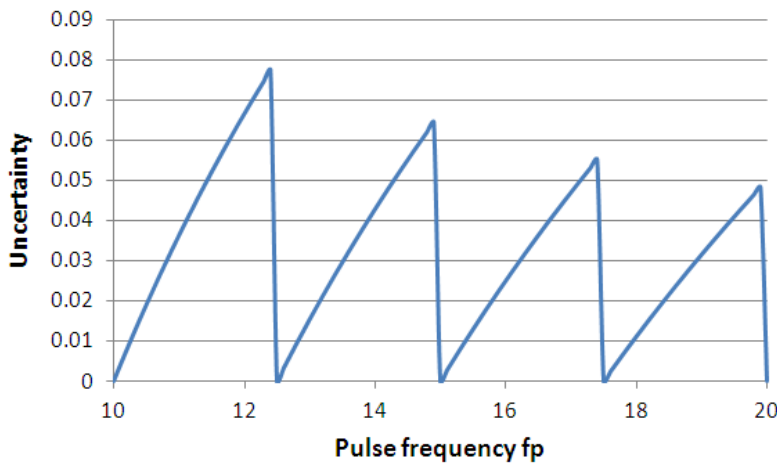


Figure 2.49 showing effect of $n=4$ on the uncertainty in measurement of f_p

2.20.3 The relationship between measured frequency and actual input frequency

Considering, the count obtained over n accumulations being $c = \lfloor n f_p / f_w \rfloor$ (2.9)

the measured frequency f_m is related to the count by $f_m = \frac{c}{nT} = \frac{c f_w}{n}$ (2.10).

The error in f_m occurs due to the finite number of accumulations required to get a satisfactory

degree of accuracy. This may be seen quantitatively by relating the measured f_m to the actual f_p pulse frequencies by equating equations 2.9 and 2.10 in terms of c ,

$$\text{thus, } f_m = \frac{f_W}{n} \left| \frac{nf_p}{f_W} \right| \quad (2.11)$$

2.20.4 Plotting the error curve

The number of accumulations n required for $\varepsilon = 0$ depends on the particular value of f_p relative to the window length T . In order to calculate n an iterative procedure must be used whereby t_p is incremented by c counts until the c^{th} count coincides with the end of the n^{th} counting window (i.e. at $\varepsilon = 0$). An example is given in figure 2.50 below showing an accumulation of counting windows where $nT = ct_p$ (or $\frac{n}{f_w} = \frac{c}{f_p}$) after the 4th accumulation.

Hence $t_p = 4 \times T/5 = 0.08$ ms when $T = 0.01$ ms giving the measured pulse frequency as $f_m = 12.5$ kHz. This confirms the equations used to produce the graph shown in figure 2.49 whereby $n=4$ also resolves f_p at 12.5 kHz.

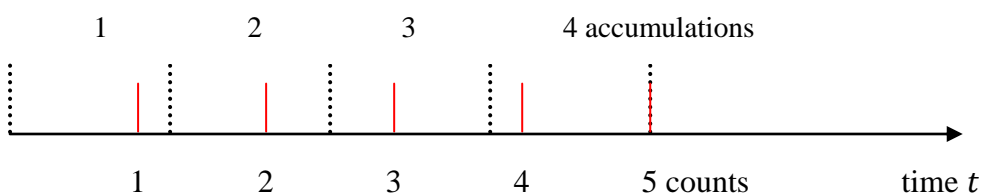


Figure 2.50 finding the minimum n at a particular value of f_p

When incorporating this into a routine for calculation on a computer, an intermediate value of n is found in a for-next loop from $\frac{cf_w}{f_p}$ where c is the loop counter (i.e. the pulse count), and the count is terminated when n becomes an integer (i.e. $\varepsilon = 0$). A program to accomplish this (written in Visual BASIC) follows with the user form shown in figure 2.51.

```

Private Sub CommandButton1_Click()
'Program to calculate minimum number of accumulations to resolve  $f_p$  at zero
uncertainty)

'declarations and input

fw = 10 'frequency of counting widow

fp = Val(TextBox1.Text) 'input the pulse frequency

'calculations

f = fw / fp 'calc here to avoid repetition in for-next loop

For c = 1 To 1000 'c is the pulse count
P = Str(c) + " "
n = c * f 'intermediate value of n
S = S + Str(n) + " "
If n = Int(n) Then GoTo endit 'i.e.  $n - \text{int}(n) = 0$  ( $e = 0$ ) so  $ctp = nT$ 
Next c

endit:

'output

TextBox2.Text = Str(n)
TextBox3.Text = Str(c)

End Sub

```

Figure 2.51 User form for calculation of least no. of accumulations to resolve f_p

Using results from the program, a plot of n versus f_p at intervals of 0.5 kHz is shown in figure 2.52 where it is interesting to see that the curve is symmetrical either side of 15 kHz. Again, because of the coarse intervals in frequency, the curve is only a partial representation of a curve that would be obtained for a much finer range. For example, $f_p = 10.2$ kHz requires $n = 50$ to resolve whereas $f_p = 10.1$ kHz requires $n = 100$ to resolve, with $f_p = 10.05$ kHz requiring $n = 600$ to resolve!

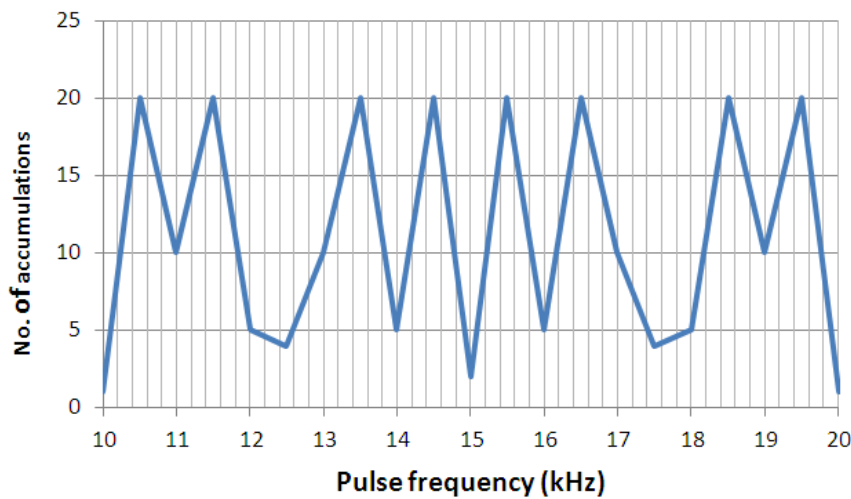


Figure 2.52 showing the effect of f_p on n at $\varepsilon = 0$

The effect of the number of accumulations on the percentage error in measuring f_p may be determined as follows: Consider figure 2.47, then over n accumulations, $\varepsilon = nT - ct_p$ where nT is the total accumulated window time over which the integer count of c pulses spaced t_p apart occurs. f_p will always be $\geq f_m$ since $ct_p \leq nT$.

i.e. $\frac{1}{ct_p} \geq \frac{1}{nT}$ and so $\frac{f_p}{c} \geq \frac{f_w}{n}$ hence $f_p \geq \frac{cf_w}{n}$ thus from equation 2.10, $f_p \geq f_m$

The fractional error E_{f_m} in the measured pulse frequency (due to the uncertainty ε) relative to the actual pulse frequency can therefore be represented by:

$$E_{fm} = \frac{f_p - f_m}{f_p} = 1 - \frac{f_m}{f_p} \text{ and substituting equation 2.10, } E_{fm} = 1 - \frac{cf_w}{nf_p}$$

$$\text{Also, substituting equation 2.9 for c, } E_{fm} = 1 - \frac{f_w}{nf_p} \left| \frac{nf_p}{f_w} \right|$$

The error expressed in percent will be:

$$E_{fm} (\%) = \left[1 - \frac{f_w}{nf_p} \left| \frac{nf_p}{f_w} \right| \right] \times 100 \quad (2.12)$$

A plot of E_{fm} (the error in measured frequency f_m) against f_p for particular values of f_w and f_p (normalised to $f_w = 10$ with f_p in the range 0.1 to 70) with $n = 1$ produces the error curve seen in figure 2.53

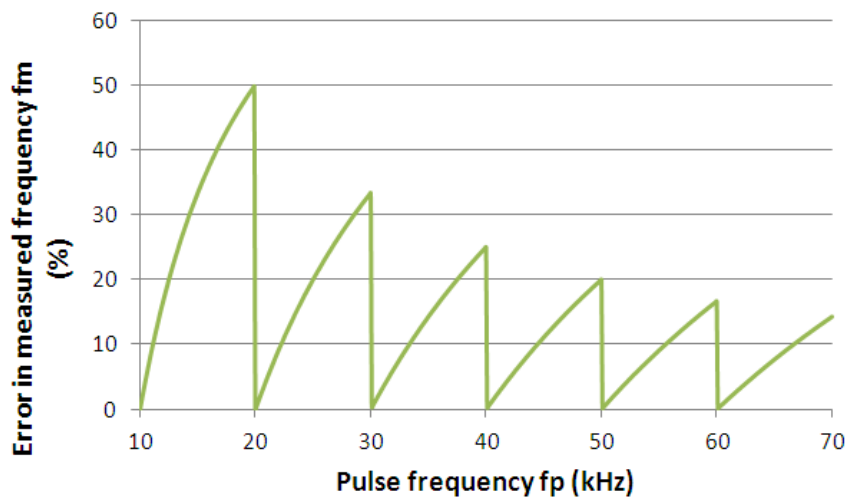


Figure 2.53 Variation of error in measured pulse frequency f_m with $n=1$

It is seen in figure 2.53 that the shape of the curve follows that of the variation in uncertainty shown in figure 2.46. The error at 15 kHz is 33.3% and that immediately before 20 kHz is 20%.

Increasing the number of accumulations will have a varying effect on the frequencies being resolved as is seen in the cases shown in figures 2.54 ($n=2$) and 2.55 ($n=3$).

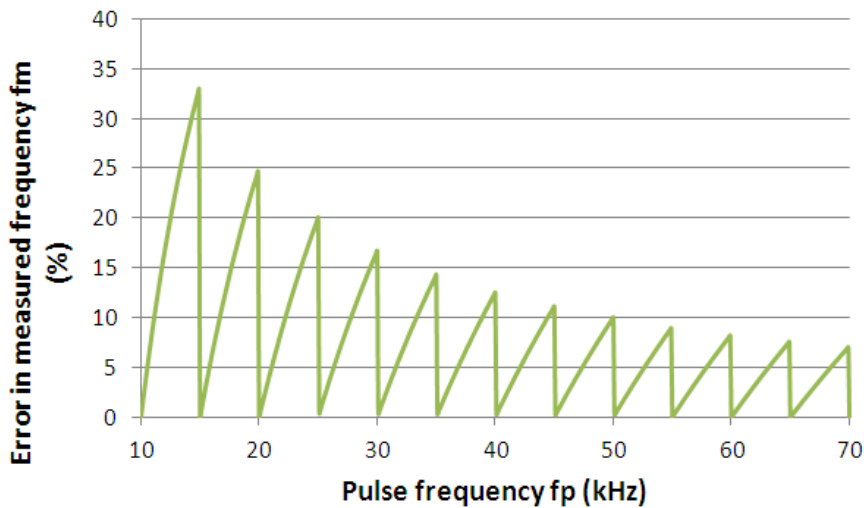


Figure 2.54 Variation of error in measured pulse frequency f_m with $n=2$

In figure 2.54, it is seen that at 15 kHz the error is now 0 while at 20 kHz it has reduced down to 25 %.

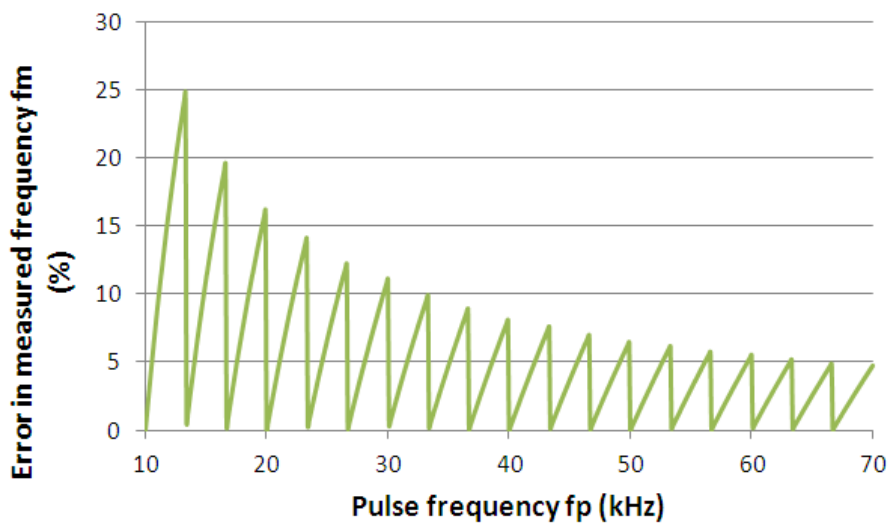


Figure 2.55 Variation of error in measured pulse frequency f_m with $n=3$

In figure 2.55, the error at 15 kHz is now 11.1% with that immediately before 20 kHz being reduced to 16.3%. Thus the effect of increasing n selectively improves frequency resolution with a trend converging to the correct value.

In this section, it was seen that the number of accumulations theoretically required to eliminate the error at a particular frequency is finite and relatively small compared to what was found when making practical measurements where:

- a. Pulse frequencies are not exact integers or having a value with large fractional parts, but may actually have small changes around a particular value of frequency (due to circuit instability and drift) requiring considerably more accumulations to resolve (as indicated in figure 2.52)
- b. The probability of seeing a pulse at frequencies < 10 kHz within individual spectra becomes an inherent factor, and thus the total elimination of error becomes impractical.
- c. Extraneous pulses caused by circuit noise require many accumulations to provide an adequate S/N ratio.

A further complication arises where the spectral length is greater than time T . (So far, only accumulations of a single repeating time slot have been used.) In the case where a spectrum is sampled comprising of a 'frame' of time slots, (e.g. over a spectral length of 40 ms with each time slot taking 0.1 ms, there will be 400 time slots in the frame containing the spectral data), a continuous pulse stream will therefore be 'out of sync' within certain time slots in the frame. This may be seen in the example shown in figure 2.56 below where the spectral length comprises of four frames.

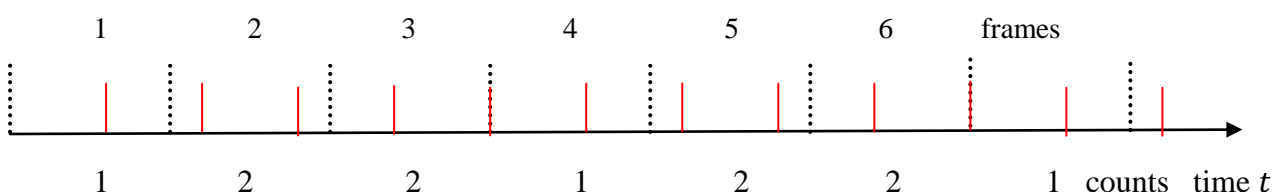


Figure 2.56 Phase relationship of the pulses between frames

Thus, more accumulations will again be required to reduce inter-frame measurement error as the frames drift in and out of sync with the pulse stream. This manifests itself as a small variation of counts around the correct value when observed in the mobility spectrum (e.g. when using a large number of accumulations such as 500). The amplitude of the variation was seen to depend on the number of accumulations taken and the test frequency as was observed when using the TIMMS program previously to take practical measurements (section 2.18.1).

This concludes the section on the theoretical analysis of the behaviour of the pulse converter to a pulse stream of set frequency. It is seen that the equations derived confirm the practical results and also allow a more accurate representation of the actual response to the pulse stream to be made over that seen in the practical measurements.

2.21 Reconstruction filter

This is a low-pass filter that provides a smooth transition between the discontinuities in the output waveform obtained from the D/A converter. Thus it produces a better approximation to the actual shape of the ion pulse as would be obtained from the faraday plate.

In order to obtain a ball park figure for cut-off frequency of the filter, the following considerations were made:

The width of the RIP is approximately 0.5 ms at its base. The shape of the pulse can hence be roughly considered as a rectified sinewave of frequency 1 kHz. Thus, to smooth out higher pulse frequencies with minimal attenuation of the RIP, the roll-off of the low pass filter could be associated with a 3 dB cut-off point of say, 3 kHz. The range could be extended by using a variable resistor in the C-R circuit to provide an optimum amount of filtering.

In tests, a passive single pole filter configuration providing a roll-off of 6 dB/octave as shown in figure 2.57 was found to provide sufficient smoothing.

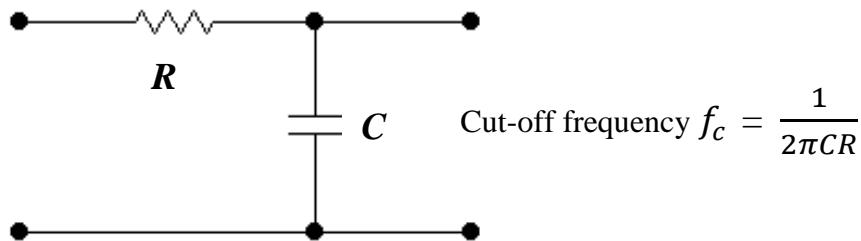


Figure 2.57 Basic single pole low-pass filter

Choosing $f_c = 3$ kHz and $C = 1$ μ F and rearranging for R , gives $R = \frac{1}{2\pi C f_c} = 530 \Omega$.

Therefore a 1 k Ω variable resistor would provide sufficient flexibility in the degree of filtering.

The final version used is shown in figure 2.58 which also incorporates a switch to either bring the filter into circuit, or switch it out. Note, in the OUT position there is very little signal lost across the variable resistor due to the very high input impedance of the DAQ card.

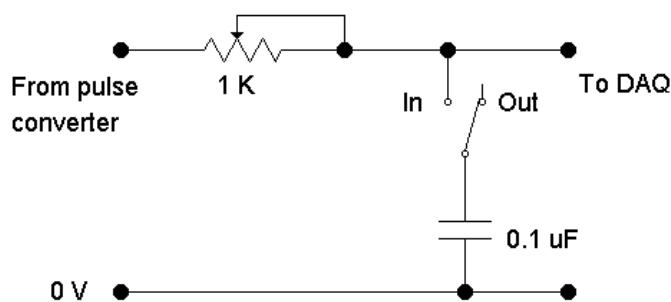


Figure 2.58 Final version used for the reconstruction filter

2.22 Ion Pulse Simulator

This simulates the pulses arriving from the SPC10 channeltron preamplifier to the pulse converter. Its purpose is for fault finding purposes in the absence of signal response when viewing mass mobility spectra (i.e. TIMMS or SIMMS). The simulator enables testing of the correct operation of the converter, data acquisition and associated software over a switchable frequency range of 1 kHz to 110 kHz in steps of 10 kHz. The simulator unit is attached to the lid of the pulse converter. The circuit shown in Figure 2.59 is comprised of two sections, these being a Schmitt trigger based astable multivibrator to provide the basic rectangular wave pulses and a fast monostable to change the waveform into a set of needle pulses approximately 40 ns wide. The actual pulses from the preamplifier are 25 ns wide provided via a monostable using ECL technology. As a simpler circuit is gained with using TTL or high speed CMOS, this is the chosen method, the slightly longer pulse width of 40 ns being sufficient for the simulation.

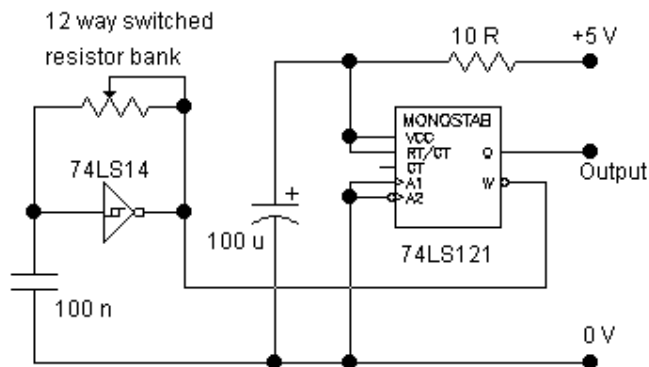


Figure 2.59 Circuit diagram of the ion pulse simulator

Supply decoupling of high frequencies/spikes is accomplished by the 10 R – 100 μ combination. In conjunction with the 100 nF timing capacitor, the 12 way switched resistor bank comprises of a 12 way rotary switch that selects a resistance value corresponding to a

particular test frequency. Table 2.12 shows the resistance values required for the corresponding test frequency.

Table 2.12 Resistance values required to produce various test frequencies

Frequency (kHz)	Resistance (Ω)	Nearest preferred value(s)
1.0	3120	2200 + 910
10	630	620 + 10
20	300	270 + 33
30	190	180 + 10
40	133	120 + 12
50	98	91 + 6.8
60	76	68 + 8.2
70	57	56 + 1
80	47	47
90	36	33 + 3.3
100	28	27 + 1
110	22	22

The 74LS121 monostable multivibrator is triggered by the rising edge of the pulses from the 74LS14 Schmitt trigger inverter and due to the absence of any timing components, produces a needle pulse of approximately 40 ns duration each time it receives a trigger pulse. The switching and interconnections between each circuit within the converter unit are shown in figure 2.60.

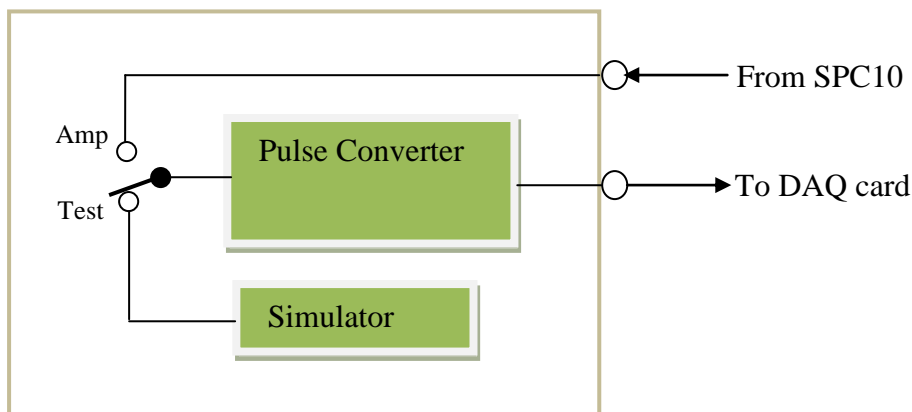


Figure 2.60 Pulse converter and simulator system connections

2.23 Concluding Remarks

In this chapter, it was seen how the electrical requirements for the control of the IMS operating parameters were met, taking advantage of new ideas to improve the operation over previous systems in terms of:

- Isolation of the pulses to control the ion gate using opto-isolation allowing greater flexibility in terms of gate pulse width and linearity, and increased electrical safety.
- Development of a novel pulse count to pseudo analogue converter for obtaining increased sensitivity in ion mass mobility mode measurements by using the channeltron in count mode with pulse count to analogue conversion, rather than using the less sensitive Faraday plate inside the mass spectrometer.
- Incorporation of safety features to prevent flashover when baking out.

Following on from this, chapter 3 now covers the development of the software functions required to control the system.

CHAPTER 3 SOFTWARE DEVELOPMENT FOR THE IMS-QMS SYSTEM

In this chapter, program development for software control of the IMS-QMS system to obtain ion mobility and mass spectra is described. Information is also given on the configuration of the hardware used for signal acquisition and data presentation. Following this, chapter 4 describes how the system was tested and characterised using the suite of programs that are now to be described.

3.1 A short description of the LabVIEW programming environment

LabVIEW programs are produced using a graphical programming technique [116]. The terminology is different to that normally used when writing software but the ideas are similar. Programs written for LabVIEW are called VIs (virtual instruments). There are two main sections involved when writing a VI:

1. The **Front Panel** is the user interface where data is input using *controls*, and the output may be displayed using *indicators*. Examples of controls are various types of electrical switches. Indicators may be numeric or text boxes, meters, charts and graphs.
2. The **Block Diagram** is the actual executable program. Data passes to and from the block diagram via the front panel objects. On the block diagram, a corresponding *terminal* will appear. These act as sources or sinks of data. Additionally, *nodes* are used to control the program flow, or operate on the data. An example of a node is a summing block to add two data values together, or a timer to insert a time delay. Nodes can also operate like the functions, operators and loops encountered in normal programming. Terminals and nodes are connected together by wires (in a similar fashion to connecting electrical elements in a circuit) which are the paths for the data to take between the source and destination terminals. Wire colours relate to the type

of data variable (orange for floating point, blue for integer, green for Boolean and purple for string.)

Thus, the front panel represents the operating screen for the user and the block diagram is the “program code” in graphical form.

3.2 Program development

There are four user programs associated with the IMS-QMS system which are identified by their filenames (shown in brackets) as follows:

Ion Mobility Spectra (IMS) – This provides the Ion Mobility Spectrum using the signal acquired from the Faraday Plate.

Mass Spectra (MS) – produces the Mass Spectrum of the ions obtained from the SEM after passing through the quadrupole.

Total Ions Mass Mobility Spectra (TIMMS) – This provides the Mobility Spectrum for all the ions that pass through the quadrupole and is equivalent to the total ion mobility spectrum from the FP.

Selected Ions Mass Mobility Spectra (SIMMS) – shows the Selected (or Tuned) Mass Mobility Spectrum which is the ion mobility spectral response based on a single ion m/z selected by the quadrupole. It is here where there could be a difference to the ion mobility spectrum obtained from the FP due to CID occurring in the IMS to MS interface, whereby fragments at lower m/z may be more pronounced.

Note, when using these programs it is important to ensure that the following points are observed:

- Program “IMS” requires the FP switch to be in the ‘Amp’ position (Green led on). The quadrupole is not used. The gate switch is to be in the ‘pulsed’ position. Here, the FP provides ion current that is fed to the input of the electrometer.

- Program “MS” requires the FP switch to be in the ‘ V_{FP} ’ position (Red led on). The quadrupole is used in ‘external mass’ mode and the gate switch is to be in the ‘open’ position. Here, the FP acts as an electrostatic lens to allow transportation of a sample of the ions through the orifice in the FP and into the quadrupole.
- Program “TIMMS” requires the FP switch to be in the ‘ V_{FP} ’ position (Red led on) with the gate pulsed. The quadrupole is used in ‘internal mass’ mode with ‘total ions’ selected and ‘first mass’ selected at 10 amu with a “mass span” of 0.
- Program “SIMMS” requires the FP switch to be in the ‘ V_{FP} ’ position (Red led on). The quadrupole is used in ‘external mass’ mode, with the gate pulsed.

The user is given a reminder of what should be done when running a program according to the above points.

3.3 Hardware considerations.

Before writing the software, the way in which signals are to be acquired needed consideration. In order to display an ion mobility spectrum, it is necessary to read in samples of the waveform of the ion current from the Faraday plate over the spectral time length. This is done by using a proprietary DAQ (data acquisition) card (type PCI-6014) supplied by National Instruments, who also produced the programming language LabVIEW (version 7.2) which was used to write all the necessary software for displaying the various spectra obtained from the IMS-QMS system. The PCI 6014 is a multifunction DAQ device and Figure 3.1 shows the I/O connector pin assignment for the connector block used to wire the signals from the IMS-QMS system to the DAQ card.

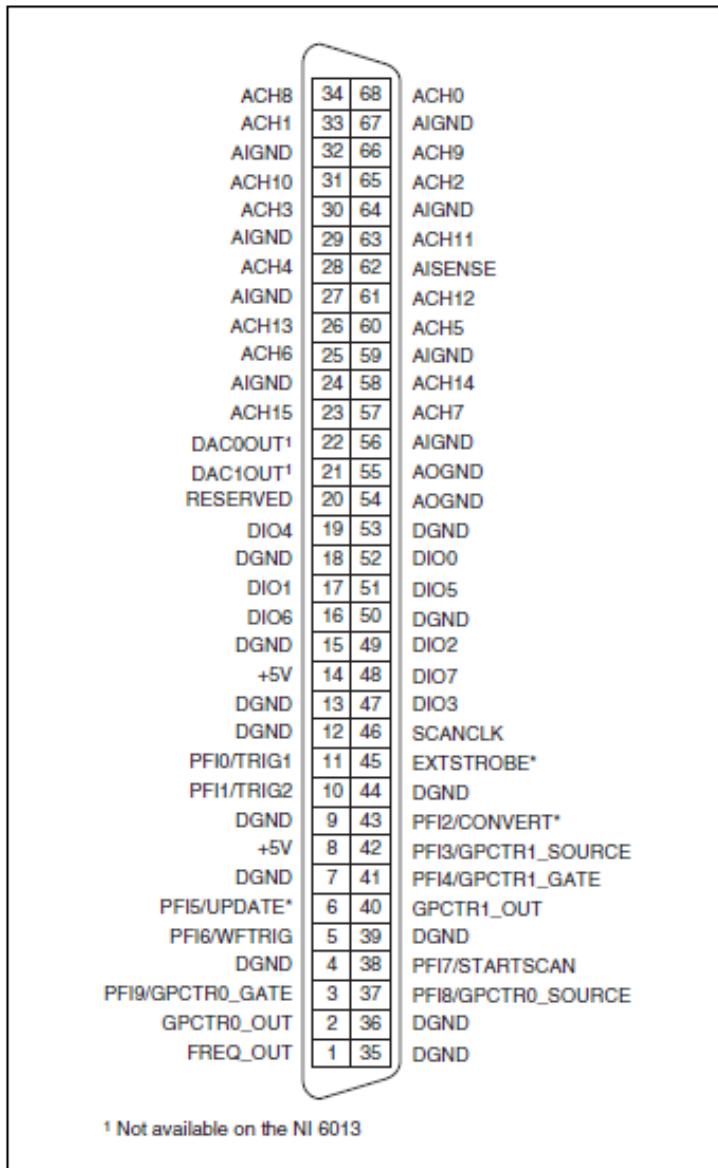


Figure 3.1 Pin assignment for the PCI 6014 DAQ card connector box [96]

The specifications of prime interest for the DAQ card [96] are:

Analog Input

Channels **16**, **8**
 Single-Ended Channels **16**
 Differential Channels **8**
 Resolution **16 bits**
 Sample Rate **200 kS/s**
 Max Voltage **10 V**

Analog Output

Resolution **16 bits**
 Max Voltage **10 V**
 Update Rate **10 kS/s**
 Current Drive Single **5 mA**

Digital I/O

Bidirectional Channels **8**
Timing **Software**
Logic Levels **TTL**
Input Current Flow **Sinking , Sourcing**
Output Current Flow **Sinking , Sourcing**
Current Drive Single **24 mA**
Maximum Input Range **0 V , 5 V**
Maximum Output Range **0 V , 5 V**

Counter/Timers

Counters **2**
Maximum Range **0 V , 5 V**
Max Source Frequency **20 MHz**
Minimum Input Pulse Width **10 ns**
Pulse Generation **Yes**
Resolution **24 bits**
Logic Levels **TTL**

Assigning the connections to LabVIEW

Considering the pin assignments shown in figure 3.1 and the requirements of each program, the terminations were assigned as follows:

Trigger out to LabVIEW	pin 11 TRIG1 (trigger to start analogue I/P) pin 44 DGND (digital ground) - cable screen
Analogue in to LabVIEW (from electrometer)	pin 30 ACH3 (analogue I/P+ differential mode) pin 63 ACH11 (analogue I/P- diff. mode - cable screen)
Analogue in to LabVIEW (from pulse converter)	pin 33 ACH1 (analogue I/P+ differential mode) pin 66 ACH9 (analogue I/P- diff. mode - cable screen)
Mass output from LabVIEW to SXP unit	pin 22 DAC0OUT (analogue output) - blue wire pin 55 AOGND (analogue out ground) - brown (cable screen)
Preamp out from SPC10 pulse count to LabVIEW	pin 37 GPCTR0_SOURCE (counter 0 input pulses) pin 4 DGND (digital ground) -cable screen
Trigger in from LabVIEW	pin 16 DIO.6 (digital O/P channel 6)
Unused (spare digital O/P)	pin 50 DGND (digital ground) - cable screen

Note, when using the differential input mode (which is recommended for small signals to minimise common mode noise), analogue channel pairs are used as ACH(i, i+8) where i is the positive (non-inverting) input and i+8 is the corresponding negative (inverting) input of the particular channel amplifier.

3.4 Program operation.

In the interest of user friendliness and ease of operation, the user interface is designed to be similar in appearance with all of the programs although their functions can be quite different. The first program to be developed following the construction of the system was IMS as there was a requirement to obtain a mobility spectrum in order to check for correct functioning of the drift tube and its associated electronics.

The following sections provide descriptions of the operation and functionality of each program.

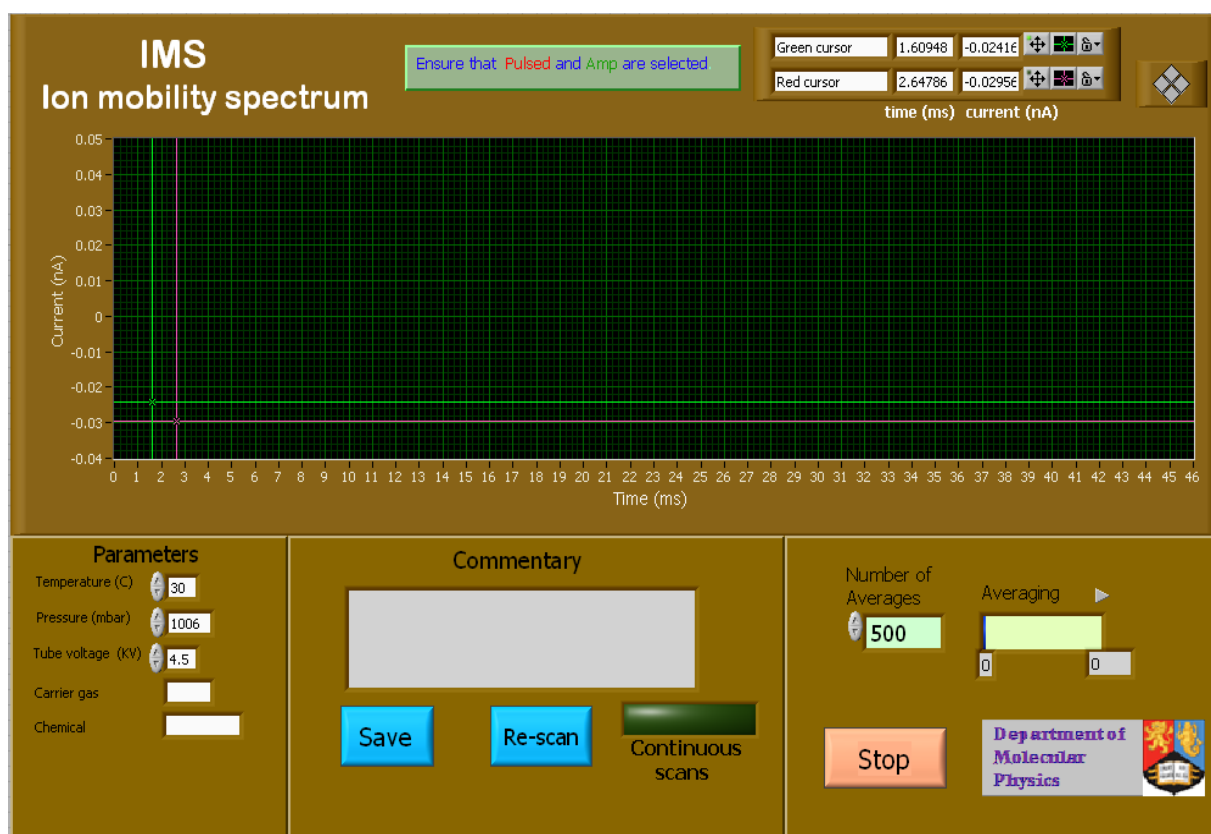


Figure 3.2 IMS Front Panel

Program input

The incoming data to the program is in the form of a digitised version of the ion current sourced by the Faraday Plate (FP). The sampling rate and number of samples for each 'waveform' acquired (corresponding to a mobility spectrum) are preset inside the block diagram and may be changed if so desired by simply inserting a new value into the box referring to that particular parameter as explained below.

User input options

Referring to figure 3.2 showing the front panel which is the user display, various parameters and conditions can be set or recorded by the user. The IMS operating parameters to be inputted are drift tube temperature, pressure, the total voltage across the drift tube, the carrier gas used (normally air) and the symbol of the chemical sample being investigated. These parameters are recorded along with the spectral data when the SAVE option is selected. In order to provide a spectrum of acceptable signal-to-noise ratio (S/N) the user can input the number of spectra to average over before plotting the final ion mobility spectrum. The plot shows the value of the ion current in nA over the spectral timebase which is preset at 40 ms. If it is desired to change this time to another value (e.g. 60 ms) then this is done by displaying the block diagram (before running the program) by pressing control E and then changing the parameter box for number of samples to take from 4000 to 6000. With the sampling rate at 100 kHz, this then provides a total sampling time of $6000 \div 100000 = 0.06$ s or 60 ms.

Operating modes

The program operating modes are either single or continuous scans, where in each case an averaged mobility spectrum is provided at each scan, and the program may be ended by pressing the pink Stop button. The continuous scans mode can be toggled on or off by

clicking on the green ‘Continuous Scans’ indicator, saving a spectrum however is not possible as this choice is blanked from the screen since it is inappropriate in this mode of operation. In the single scan mode, the spectrum remains visible until the user clicks on the blue Re-scan button.

The commentary box provides information to the user at various stages of program operation when acquiring data or when a choice is to be made. When the blue SAVE button is clicked on at the end of a scan, all of the information gathered by the program is stored in spreadsheet format, the file name and location being decided by the user. The current time and date is also automatically included in the file.

3.4.1 IMS program functionality

A simplified version of the block diagram for the IMS program is provided by the program **simple-averaging.vi** presented in figure 3.3 to aid in the understanding of the basic ideas from which the programs were developed. Here, a number of individual spectra are acquired and averaged to improve the signal to noise ratio of the final spectrum to be displayed.

Although other signal processing techniques have been investigated and proposed, [117] within the present scenario signal averaging although more time consuming, is found to provide the best noise extraction and representation of the signal with least distortion and so, (as is common in most other IMS systems) is the method chosen for our system.

Various sections relating to particular “tasks” in the block diagram (the “program”) numbered one to three are referred to in the following description of the program operation. The first objective is to set up these tasks to accomplish the desired operation of the hardware associated with the program. Referring to figure 3.3 a description of the tasks now follows.

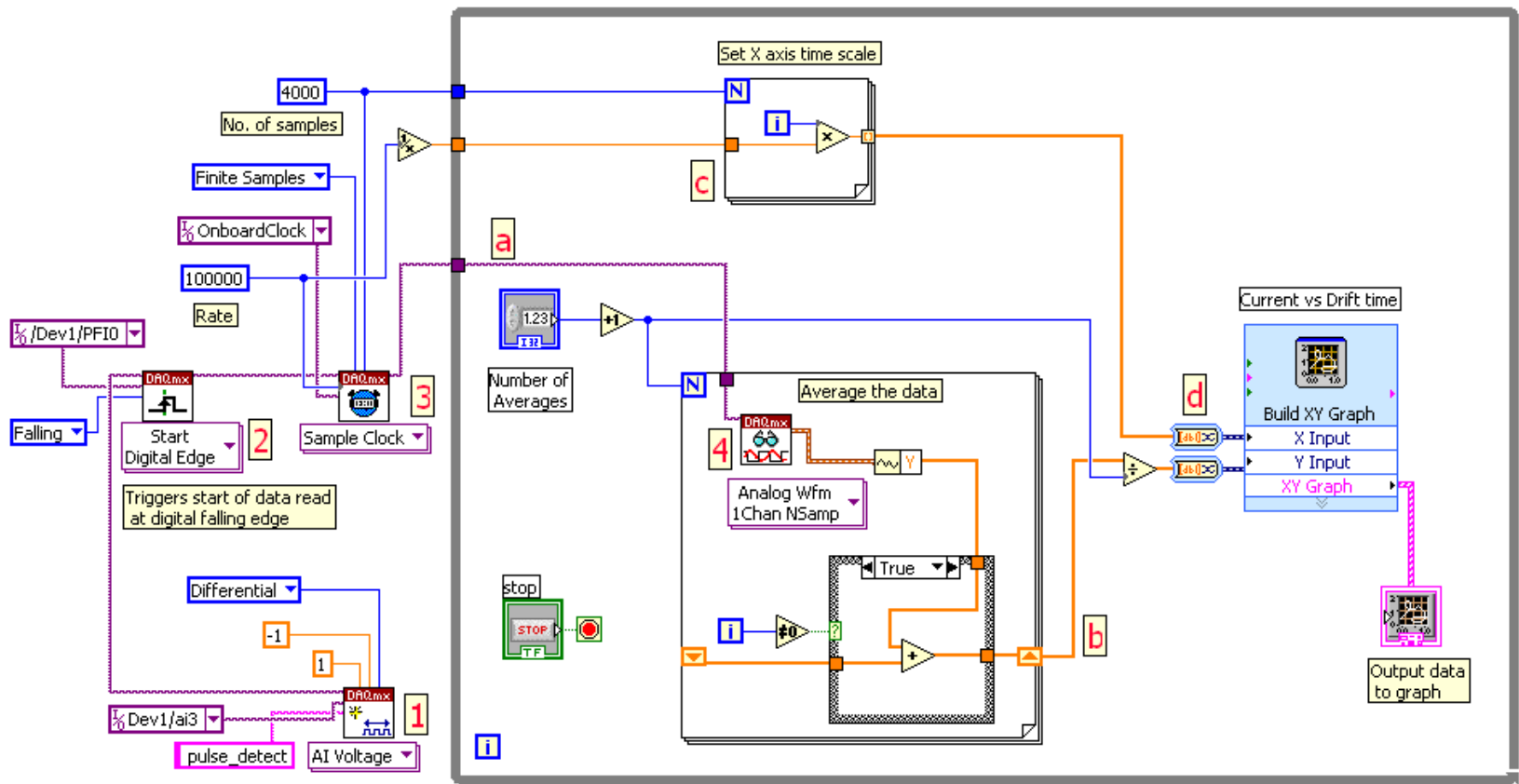


Figure 3.3 Block diagram showing the data acquisition and signal averaging sections of the program IMS

Section **1** refers to the *DAQmx Create Virtual Channel* task which creates a channel. i.e. it deals with setting the following parameters:

- type of input signal, (AI Voltage) meaning analogue voltage in this instance
- physical name of the channel (Dev1/ai3) meaning the DAQ card, analogue input channel 3
- triggering mode (pulse_detect) meaning a square wave trigger pulse
- input terminal configuration (differential) meaning the differential operating mode
- The minimum and maximum values of the input signal (-1 V and +1 V)

The data then flows to section **2** which refers to *DAQmx Start Digital Edge (Trigger)* that configures the task to start acquiring samples on the (falling) edge. Here, sub-parameters of the above parameters chosen in section **1** are set up as:

- start on the falling edge of the trigger pulse (Falling-)
- trigger pulse source (/Dev1/PF10) which is the DAQ card, trigger 1

The data then passes on to section **3** which refers to *DAQmx Timing (Sample clock)* for configuring the DAQ onboard clock to synchronise the acquisition of the data samples. It sets the source of the sample clock, its rate in samples/s and the number of samples to acquire. Here, the sample mode is set to acquire a finite number of samples (as opposed to continuous sampling). i.e:

- The clock is located on the DAQ card (OnboardClock)
- The sampling rate (Rate) is assigned a constant value of 100,000 meaning a sampling rate of 100 kHz.

- The sampling mode (Finite Samples–) allows a chosen number of samples to be acquired between trigger pulses, representing the waveforms to be averaged before plotting mobility spectra.
- The number of samples is chosen here as 4000 and so with a 100 kHz sampling rate this allows a mobility spectrum to be acquired over $4000/100000 = 0.04$ s or 40 ms.

From section 3 the data flows into the main while loop at point a whereby i increments by 1 (starting from zero) with each waveform acquired. In the for-next loop (for $i = 1$ to N) shown at c, a value of $1/\text{Rate}$ (i.e. the time interval between samples) is inputted and used to supply the time intervals for the graphical display. In this case, $1/\text{Rate} = 10^{-5}$ s and so the loop generates an array of 4000 elements with each one incrementing from the previous by a value of 10^{-5} . Thus an array of time values is produced with each value corresponding to the averaged Y (amplitude) sub-array value obtained from section 4 which is also contained within a for-next loop. It is here that N waveforms are read in by the *DAQmx Read Analogue Waveform* task (Analog Wfm 1Chan NSamp) and from this, a sub-array of the waveform (Y) amplitudes only is obtained. This Y data matrix then flows into the true case loop where using the shift registers (when $i > 0$), the incoming matrices are added together and accumulated. When initially $i = 0$, the false case loop is selected as shown in figure 3.4 where the sum node is replaced by a direct link as there is only one amplitude matrix. This is passed from the output shift register back into the input one on the next increment ready to be summed with the next arriving matrix and so on.

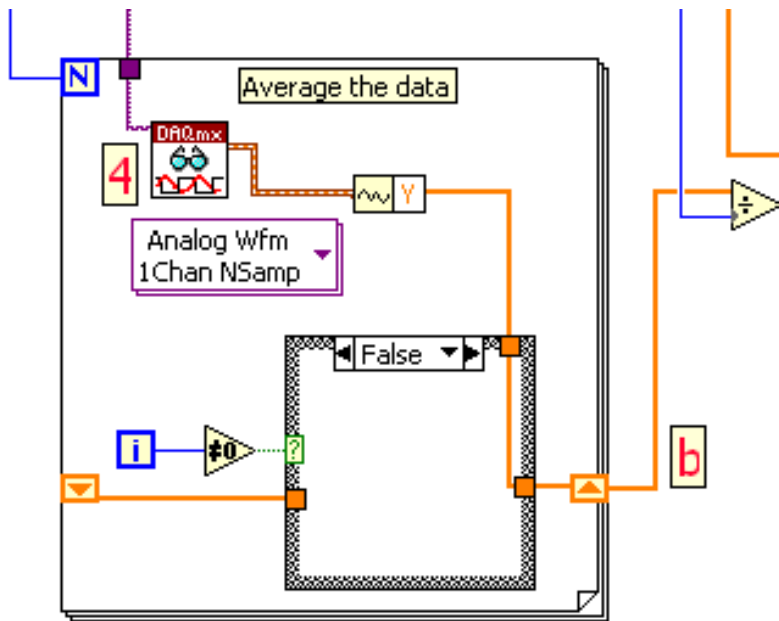



Figure 3.4 This figure shows the false case that is selected when $i = 0$

After N iterations (the number of averages to take) have been completed, the array of data containing the accumulated sum of the waveforms appears at point **b**. It is then divided by the number of averages (plus one to escape an overflow error if the user decided on zero averages) to produce the final array of averaged data. Note, the effect of using $N + 1$ rather than N is insignificant since N will normally be greater than 500. The data contained in the amplitude and time matrices is then converted to 'dynamic' data at point **d** before finally being presented to the 'Build XY Graph' vi for display of a mobility spectrum on the front panel.

3.4.2 Saving results in a spreadsheet

A permanent record of the operating parameters (the 'header') and the resulting spectrum plotted is gained by saving the settings and the composite XY matrix to a spreadsheet that can be later imported to packages such as Excel or Origin.

There are several tools provided for achieving this with LabVIEW and the method devised for incorporation into the programs is that of writing the data in string form (ascii format) as shown by the block diagram in figure 3.5. Here, the header is first generated as a set of delimited (by carriage returns ) strings representing the operating conditions that are then concatenated together and appear at point **A**. Following this, the spectral data at point **B** is converted into a two dimensional string array in the correct order representing sampling intervals and corresponding ion current, appearing at point **C**. The two sets of string data are then passed into the conditional case loop where, if the Boolean value from the Save to File control is true, the data is written into a spreadsheet file.

The location of the file is automatically handled by LabVIEW whereby the user is given a browse window for selection of where the file is to be stored.

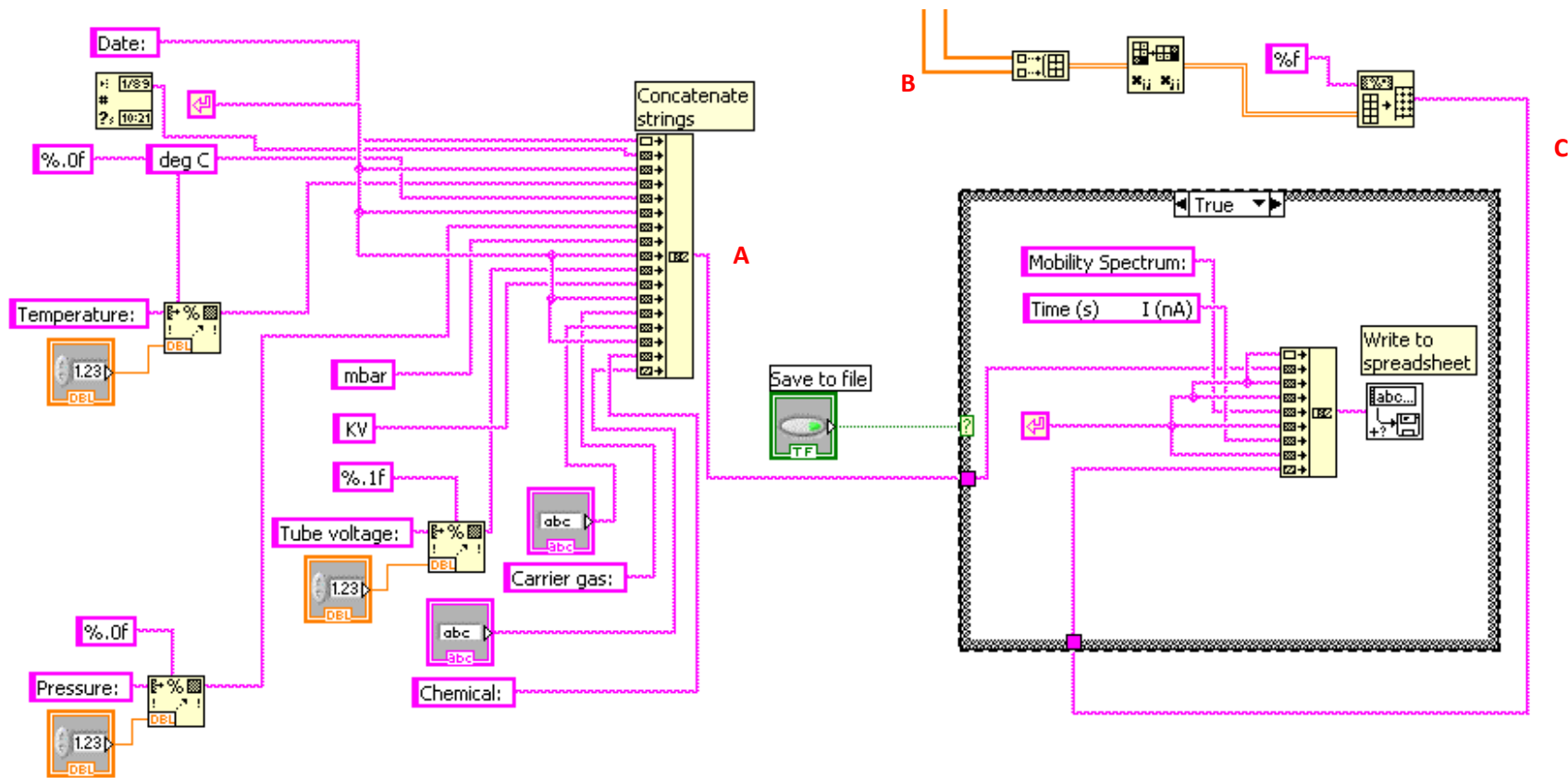


Figure 3.5 Writing sets of data strings to a spreadsheet

3.5 Descriptions of the programs making up the suite

In order to preserve clarity and continuation of reading, the complete block diagrams for the programs are given in the appendices since they cover several pages.

3.5.1 Ion Mobility Spectra - IMS.vi

Figure 3.2 given previously shows a screen shot of the front panel (the human – machine interface) of the IMS program. The corresponding block diagram is shown in Appendix 3.1. Referring to these figures and bearing in mind the information given in sections 3.4.2 and 3.4.3 a summary of the program operation can now be given:

Following a prompt given by the gate trigger pulse, the program IMS reads a set of samples in from the data acquisition card (DAC) which are then internally represented as a “waveform”. The number of samples and sampling rate in this case are preset in the program and accessed via the block diagram. In order to gain a significant improvement in signal-to-noise ratio (SNR), a user selectable number of waveforms are averaged and then presented in a “waveform chart”. This provides the user with the ion mobility spectrum. An option to save the spectrum to a spreadsheet file is then given otherwise another spectrum can be obtained either by initiating manually or by selecting continuous operation which automatically updates the spectra as they arrive.

3.5.2 Total Ions Mass Mobility Spectra - TIMMS.vi

Figure 3.6 shows a screen shot of the front panel of the TIMMS program and the corresponding block diagram is shown in Appendix 3.2. A large section of the program IMS is used within this program, which produces a spectrum of the total ions reaching the channeltron as they arrive in time.

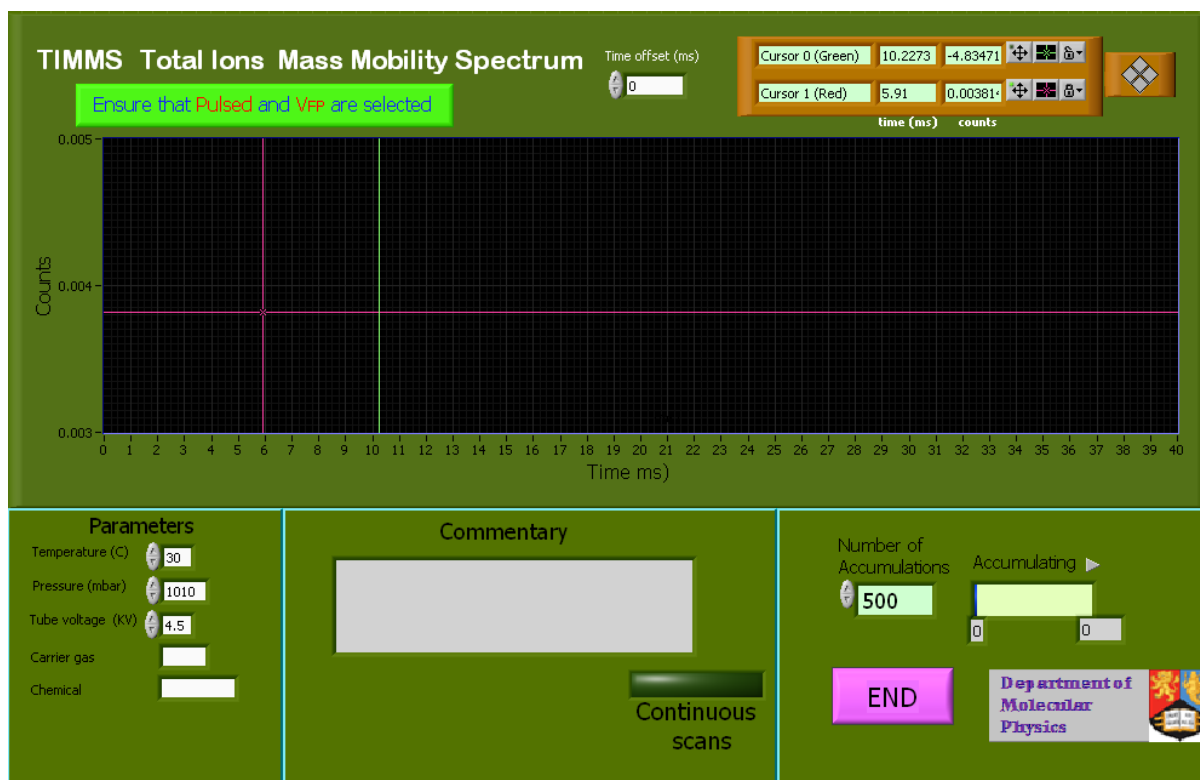


Figure 3.6 TIMMS Front Panel

Although the output from the channeltron is in the form of digital pulses where their frequency is representative of the intensity of the ions (and hence ion current), they are converted into an equivalent pseudo-analogue form by the “pulse converter” (described in detail in chapter two) so that the analogue acquisition part of the IMS program can be used in the same way as is done for plotting ion mobility using the Faraday plate in the drift tube. (The only difference being that the analogue input is from another channel as described in section 3.3.1.) This procedure is necessary since the speed of operation of LabVIEW was found to be inadequate for enabling the data in its raw digital form to be acquired and processed sufficiently fast in software.

3.5.3 Operating the TIMMS program

Before running the program, the appropriate operating parameters for the mass spectrometer need to be entered into the controller as described in appendix A4.5.

Program input

The incoming data to the program is in the form of a digitised version of the pseudo analogue signal obtained from the pulse converter unit as detailed in chapter 2, representing the total ion count from the channeltron inside the mass spectrometer. Since this is acquired over a similar timebase to that for the IMS program, it provides an alternative display of the ion mobility spectrum that is in fact of much better S/N since the microphony effect (described in chapter 5) is not present in this case. As with IMS, the sampling rate and number of samples for each 'waveform' acquired (corresponding to a mobility spectrum) are preset inside the block diagram and may be changed if so desired by inserting a new value into the box referring to the particular parameter.

User input options

The TIMMS operating parameters (similar to those for the IMS program) are drift tube temperature, pressure, the total voltage across the drift tube, the carrier gas used (normally air) and the symbol of the chemical sample being investigated. These parameters are recorded along with the spectral data when the SAVE option is selected. In order to provide a spectrum of acceptable signal-to-noise ratio (S/N) the user can input the number of spectra to accumulate before plotting the final total ions mass mobility spectrum. The plot shows the value of the ion count in kHz over the spectral timebase which is preset at 40 ms. If it is desired to change this time to another value (e.g. 60 ms) then this is done in a similar fashion to that previously given in the description of the IMS program.

Operating modes

Referring to figure 3.6, the program operating modes are either single or continuous scans, where in each case an accumulated mobility spectrum is provided at each scan, and the

program may be ended by pressing the pink Stop button. The continuous scans mode can be toggled on or off by clicking on the green 'Continuous Scans' indicator, saving a spectrum however is not possible as this choice is blanked from the screen since it is inappropriate in this mode of operation.

The commentary box provides information to the user at various stages of program operation when acquiring data or when a choice is to be made. When the blue SAVE button is clicked on at the end of a scan, all of the information gathered by the program is stored in spreadsheet format, the file name and location being decided by the user. The current time and date is also automatically included in the file.

A user variable time offset is built into the program to accommodate for the increase in time before detecting the arrival of the ion swarm due to ion transit time through the mass spectrometer. This transit time is mass dependant but is generally in the order of approximately 0.3 ms for water clusters. The time offset can also be used to allow for the extra 0.2 ms introduced by the post-filter mentioned in chapter 2 when it is connected to the output of the pulse converter. In the IMS program, an average over all of the individual spectra obtained from each acquisition sequence is plotted in order to improve on S/N ratio as there is a direct relationship of 10^{-9} V/A between the ion current and the voltage out from the electrometer. However, in the TIMMS program, in order to improve on S/N, the individual spectra are accumulated rather than averaged since the numerical value of the digital count (a maximum of 7) within each sampling period is much less than the number of accumulations (typically 500), and so by accumulating only (so not averaging), the integer nature of the resulting count is preserved. The block diagram of the program TIMMS is given in appendix 3.2 where the similarities in data acquisition to program IMS (appendix 3.1) are apparent.

3.5.4 Selected Ions Mass Mobility Spectra - SIMMS.vi

Figure 3.7 on the following page shows a screen shot of the front panel of the SIMMS program and the corresponding block diagram is shown in Appendix 3.3.

Here, the program TIMMS developed for total ions mass mobility is used with a modification so that rather than total ions, the m/z of the ions arriving over time may be selected in order to identify them in a particular peak. This allows for the temporal response of a user selected single ion m/z to be plotted (m/z 73 in this case) as is seen in figure 3.7. To achieve this, the mass spectrometer is put into external mass mode so that it acts as a mass filter whereby ions only of a particular mass are transmitted according to the voltage level present on the mass select input terminal. (In our instrument, 0 to 10 V d.c. covers a range of m/z 0 to 600.)

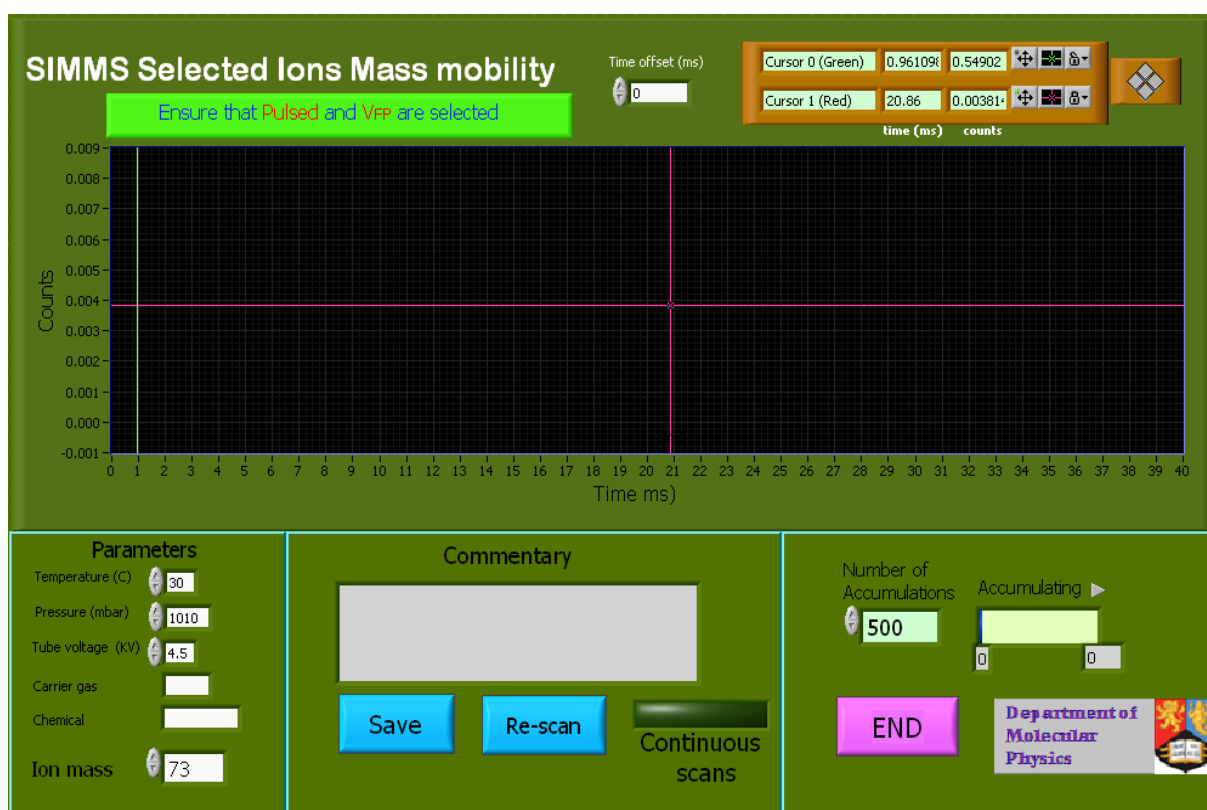


Figure 3.7 SIMMS Front Panel

Mass selection is performed in LabVIEW as shown in figure 3.8 where it is seen that at point **a** the desired mass is obtained from the front panel. The mass value is then divided by 100 and passed on to the DAQ Assistant where digital to analogue conversion takes place to produce a proportional output voltage of 0 to a maximum of +5 V. This voltage representing the required mass is then presented to the mass spectrometer which is configured to be in external mass mode and hence it acts as a mass filter for the selected value.

As with IMS and TIMMS, the sampling rate and number of samples for each ‘waveform’ acquired (corresponding to a mobility spectrum) are preset inside the block diagram and may be changed if so desired by inserting a new value into the box referring to the particular parameter.

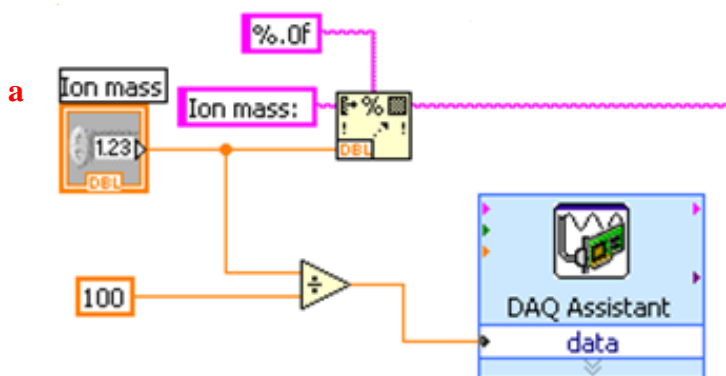


Figure 3.8 Mass selection in the SIMMS program

User input options

The SIMMS operating parameters are similar to those for the TIMMS program with the additional choice of the single mass of the ions for plotting over the timebase. The rest of the program operation is in accordance with that described previously for TIMMS.

A mass mobility spectrum from the SIMMS program is shown in figure 3.9 illustrating a water cluster of $m/z = 55$ Da arriving at 19.9 ms.

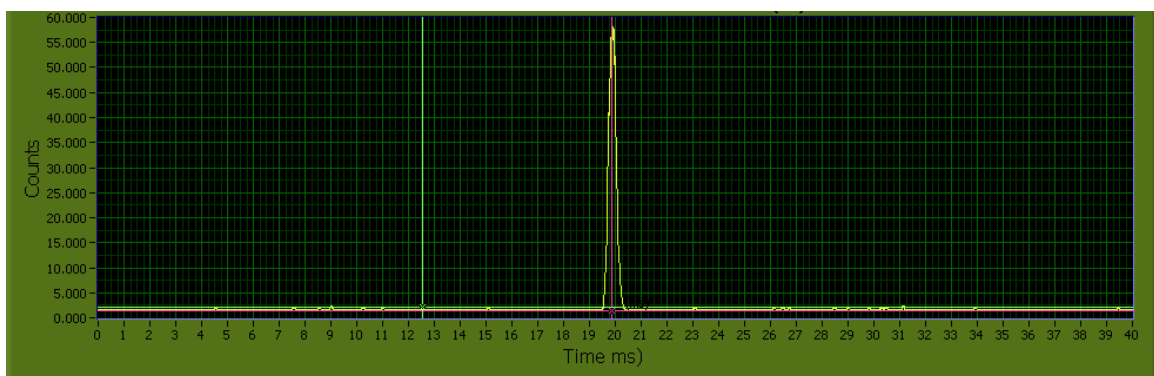


Figure 3.9 A screenshot of the spectrum provided by the SIMMS program showing the RIP for water clusters of m/z 55

3.5.5 Mass Spectra - MS.vi

Figure 3.10 shows a screen shot of the front panel of the MS program and the corresponding block diagram is shown in Appendix 3.4. Unlike in the previous programs whereby mobility spectra were plotted, this program gives a mass spectrum of the ions passing through the quadrupole. In contrast to the other programs which operate on analogue data, program MS uses the conditioned digital pulses from the channeltron as its input data stream. The representative ion counts over a user selected dwell time at each mass increment are displayed over the user selected range of m/z to cover the masses of interest. The size of each increment in m/z is also user selectable from the figure entered for the number of steps (increments) over the mass scan. An example is given in figure 3.11 showing the mass spectrum for water clusters (seen at m/z 37, 55 and 73) and also contaminants appearing in the drift tube at around m/z 250 and 278 prior to baking out.

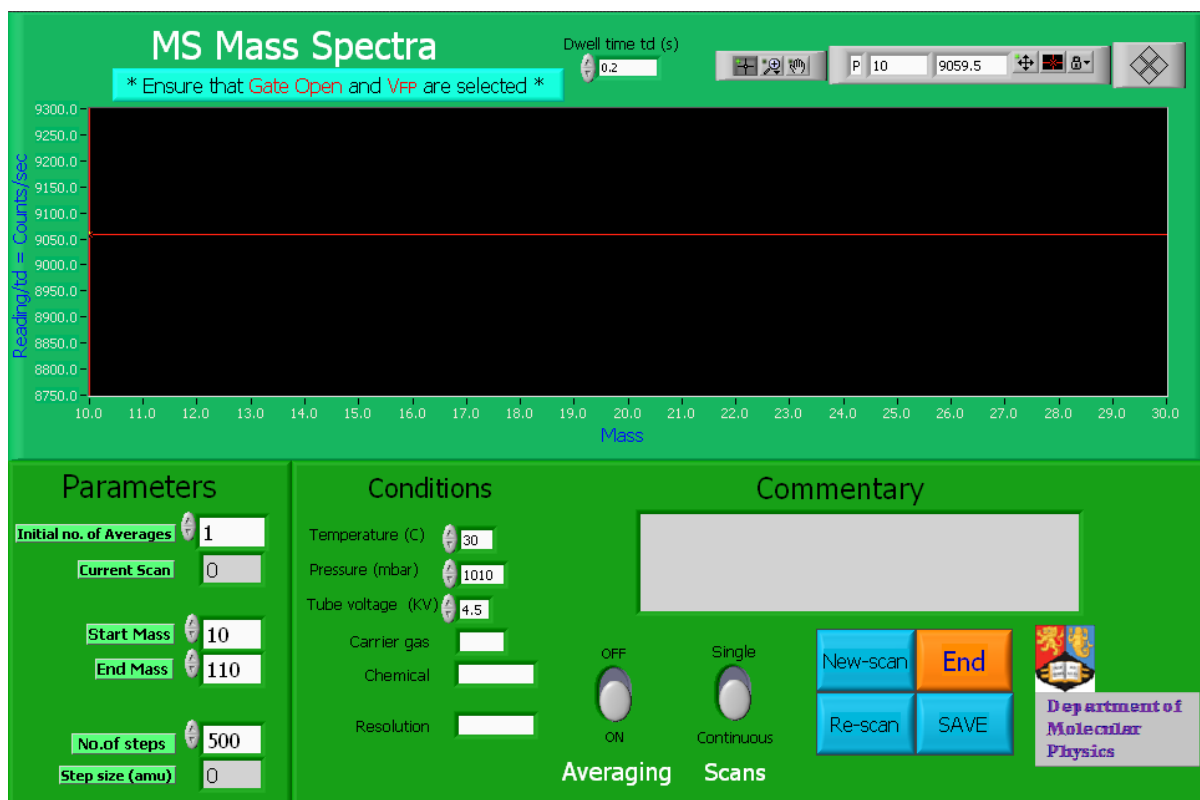


Figure 3.10 The MS Front Panel

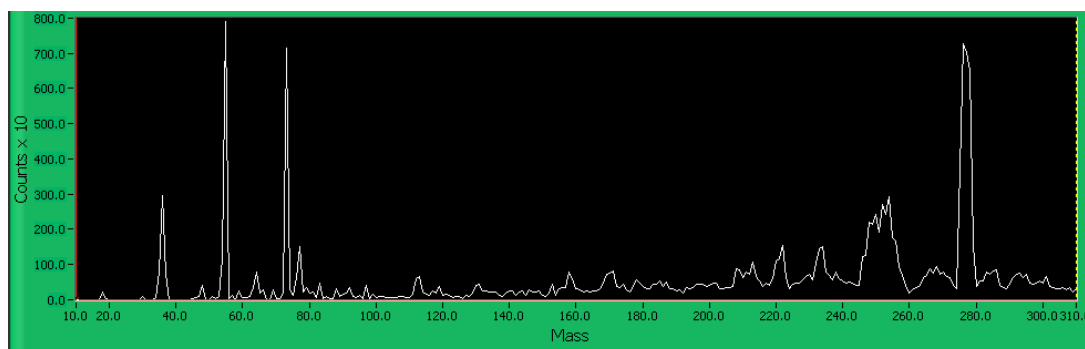


Fig 3.11 A screen shot of the mass spectra program showing water clusters and contaminants before baking out

Operating the MS program

Before running the program, the operating parameters for the mass spectrometer need to be entered into the controller. These are detailed in appendices A4.6 and A4.7.

The program works by counting the number of ion pulses arriving from the channeltron amplifier at a particular mass over a user-selected dwell time (preset in the program at 0.1 s).

Referring to figure 3.10, the ion count is then plotted with the vertical axis scaled in counts/s according to the dwell time. The horizontal axis is scaled in amu according to the mass range chosen by the user.

There are three choices of operating mode :

- Single scan
- Multiple scans with averaging
- Continuous scans

In all modes, and at any time, a brief click on the orange END button will stop the scan process to allow the user to select a blue button to either 'Re-scan' again from the beginning using the existing set up for mass range and number of steps in amu for each count, or to begin a new scan using a different mass range or number of steps.

When first running the program, the information on the operating conditions (temperature, pressure, voltage, chemical) and mass range/number of steps may be set dynamically (i.e. during the scanning process) but do not take effect until the scan cycle has been completed.

This way of operation has been chosen so that the default values may be used to avoid repetition each time the program is run over several similar experiments. The blue option buttons for 'New-scan' 'Re-scan' and 'SAVE' are inhibited during the scan plotting process.

Single scan mode

To aid in simplicity of operation, in this mode, the parameters for averaging of scans are not displayed.

After a scan has been completed the user is given the options of re-scanning, performing a new scan or saving the mass spectrum along with the mass parameters and operating conditions to a spread sheet. The date and time of saving are also recorded in common with the previously described programs. A choice of operating in one of the other modes may also be made.

Multiple scans with averaging mode

Here, the user sets the initial number of running averages (number of scans – 1) to take and a reading of the number of scans performed is then displayed as the process proceeds. At any time during the process the user may dynamically increase the number of averages chosen. After the process has completed, further scans may if desired be added to the averaging process. As in the single scan mode, the blue buttons may then be used as appropriate.

Continuous scans

In this mode, to aid in simplicity of operation the averaging parameters and blue option buttons are not displayed. The program then repeatedly displays scans of mass spectra until the user either ends the program or dynamically selects single scan mode before the present scan has completed, where the blue option may again be used as appropriate.

Basic operation of the MS program MS.vi

The overall block diagram is relatively complex compared to the previous programs but the essential features for selecting the scan parameters and acquiring the ion counts are relatively easy to follow and are described as follows:

Referring to figure 3.12, this shows the part of the block diagram that deals with the selected scan parameters from the front panel, being first mass, last mass and number of steps.

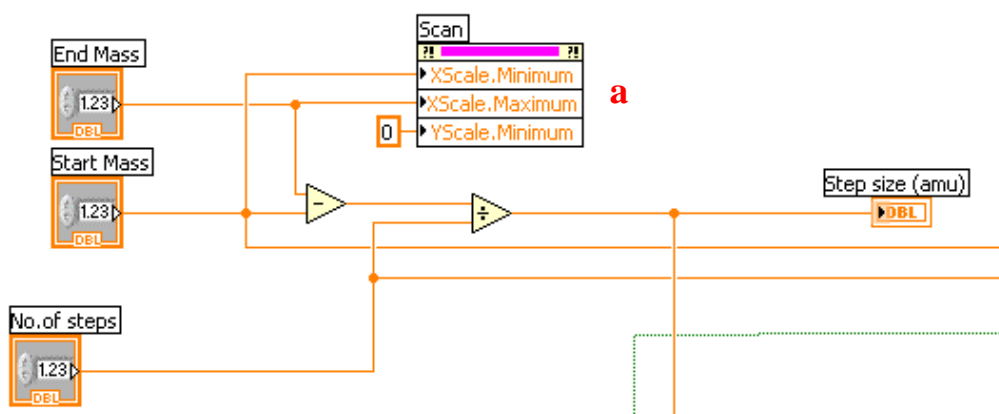


Figure 3.12 Setting up the mass range over which the mass spectrum is plotted

The step size (i.e. the increment in mass (amu) between each point plotted in the mass spectrum) is found by subtracting the start mass from the end mass to give the mass range, and then dividing the mass range by the number of steps. This is displayed on the front panel when the program executes. The plotting parameters are defined according to the minimum and maximum values of X (horizontal) and Y (vertical) as seen at point **a**.

The section that deals with the actual acquisition of the ion count at a particular mass over a pre-determined dwell time is shown in Figure 3.13.

Referring to figure 3.13, the current mass requires to be divided by 100 (as seen at point **a**) before passing on to the DAQ Assistant in order to convert to a voltage suitable for passing on to the mass spectrometer electronics when in external mass mode. 6 V dc would correspond to 600 amu in this case. The current mass also acts as the scan parameter defining the current X position (as seen at point **b**). The time frame relating to dwell time then follows where the start task for the counter appears at point **c**, this initiates the counter clearing the count to zero. Within the while loop, the task for counting the incoming pulses relating to the ions is seen at point **d** and the dwell time over which this counting process continues is controlled by the Elapsed Time function (at point **e**) according to the value of the user set dwell time. After time-out, the process ends when the stop task (point **f**) executes which halts the counter, and the count value is passed on to the next stage of the process where it is stored in an array and displayed on the mass spectrum output screen. Depending on the number of steps chosen the counting tasks repeat at the next mass and so on until the final mass is processed and the complete mass spectrum is displayed.

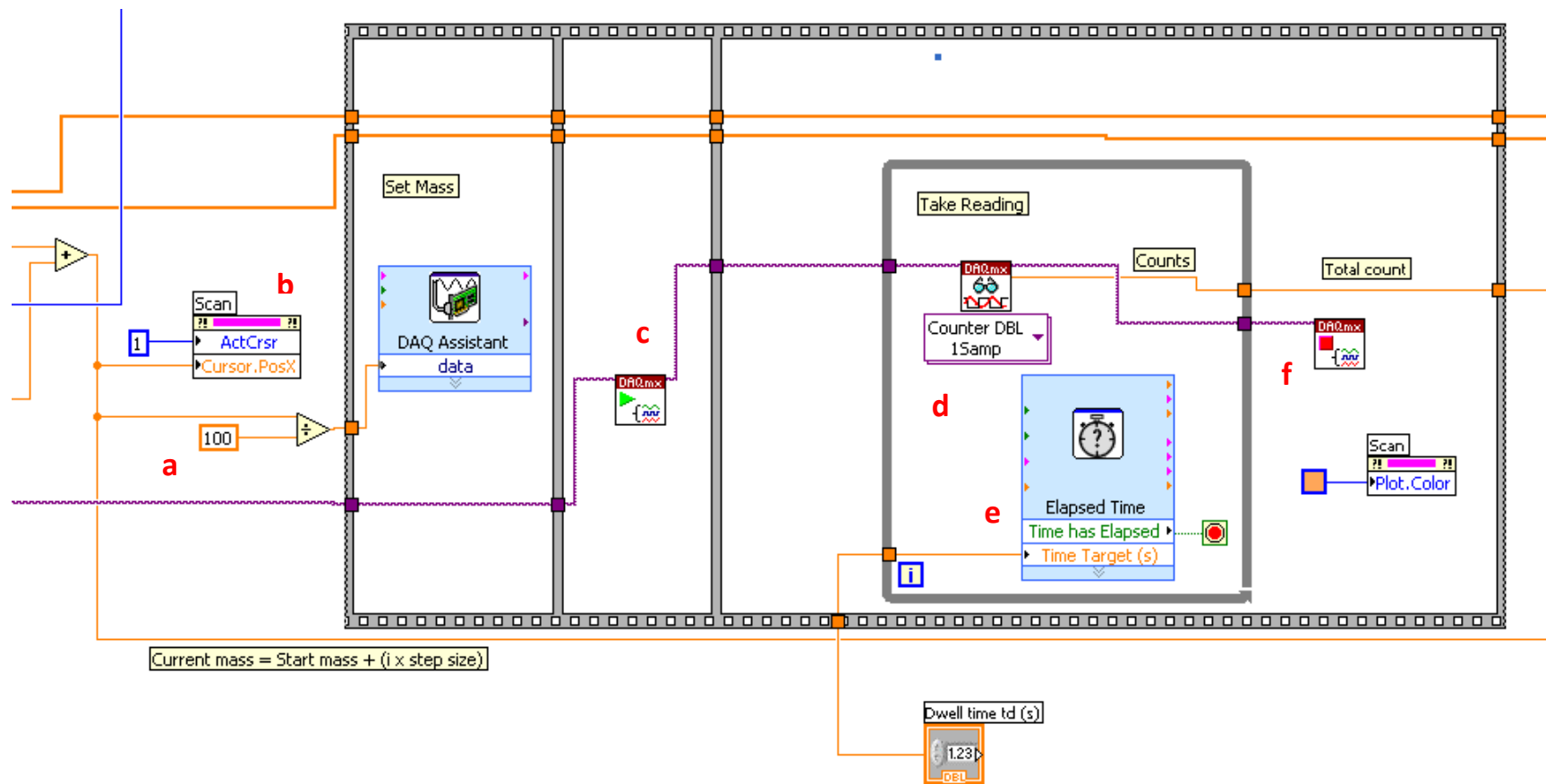


Figure 3.13 Obtaining the ion count over a pre-determined dwell time

The rest of the program deals with the users requirements in terms of whether to display concurrent spectra (run continuously) or display once and stop, or whether to average over a number of spectra, whether to store the mass spectrum to a spreadsheet etc. in a similar fashion to the other programs previously described.

Appendix A3.1 gives the entire 'listing' of the block diagrams associated with the program suite.

Since the development of the suite of programs described in this chapter, a different version of the IMS program has been published [118] although in comparison, the present version described is in the authors opinion more user friendly albeit not directly giving a reduced mobility calculation (as is a feature of the other program). This could be incorporated in a future revision of the present IMS program.

CHAPTER 4 CHARACTERISING THE IMS-QMS SYSTEM

4.1 System tests

Having completed the assembly of the IMS-QMS system and associated operational and data capture software, it was necessary to determine its performance and response to various changes in operating parameters. This was done by examining the ions in d.c. mode (continuous transmission) for mass spectra, and pulsed gate mode for mobility spectra. It is important to know how these responses vary with changes in parameters such as operating voltages (drift tube, screen grid and Faraday plate).

In order to determine the best conditions of operation and to maximise the sensitivity of the instrument, a set of tests were carried out using clean air for the carrier gas. When these tests were initiated, the drift tube was operated at the ambient temperature of the lab, but subsequently, it was decided to operate at a fixed temperature of 30 °C to reduce any errors caused by ambient temperature fluctuations during measurements [119]. The pressure inside the drift tube (influenced by ambient weather conditions) was noted at the start of each test. When refitting the IMS drift tube after any dismantling was required, it was baked out over a few days at 100 °C to remove contaminants arising from exposure to the ambient lab air.

Recalling Chapter 3, the LabVIEW programs developed and used with various tests were:

- IMS – for obtaining Ion Mobility Spectra from the Faraday Plate
- SIMMS – for obtaining a Selected Ion Mass Mobility Spectrum
- TIMMS – for obtaining a Total Ions Mass Mobility Spectrum (Note, this program was a later development used with the tests described in Chapter 5)
- MS – for obtaining Mass Spectra

4.2 Testing Rationale

Referring to the list of tests performed (listed in section 4.3 below), tests 4.1 and 4.2 describe the initial investigations made in dc mode (i.e. with the gate open for ion flow) using the IMS system only, shortly after it had been assembled. The fundamental operating parameters such as drift tube voltage and screen grid voltage required optimising in terms of ion transmission, in preparation for use with the mass spectrometer.

Following this, the operation in pulsed mode was investigated with optimisation of signal-to-noise ratio (S/N) in conjunction with ion transmission. Aspects of this are covered in tests 4.3 to 4.7. Within this, test 4.6 highlights an extra delay in drift time that is encountered when the ions traverse the mass spectrometer before being detected at the channeltron, rather than at the Faraday Plate.

As all systems of this type require a settling time after switch on, the operation of the system over a few hours was observed as detailed in tests 4.8 and 4.9.

Finally, test 4.10 shows the fragmentation of water clusters caused by various potential differences in the region between the FP and the cone at the entry to the mass spectrometer.

Note, some tests were performed with assumed values for parameters that were not under test at the time, but were required however as ‘default values’ in order for the test to proceed.

In order to get a satisfactory SNR over a mobility spectrum (see test 4.4), an average over 500 spectra was generally taken when using the IMS and SIMMS programs.

4.3 List of Tests Performed

Note, the capital letters in square brackets refer to the program(s) used with the test.

Test 4.1 – The effect of varying the drift tube voltage on the ion current (dc mode). [IMS]

Test 4.2 – The effect of varying the screen grid voltage on the ion current (dc mode). [IMS]

Test 4.3 – The effect of varying the gate pulse width on the RIP. [IMS]

Test 4.4 – The effect of averaging on the quality of the ion mobility spectrum. [IMS]

Test 4.5 – Investigating the microphony effect between the screen and the Faraday plate [IMS]

Test 4.6 – The effect of varying the screen grid voltage on the RIP amplitude. [IMS, SIMMS]

Test 4.7 – Effects on RIP (drift time and height) when varying the drift tube voltage. [IMS]

Test 4.8 – Observing the change in ion mobility spectrum with time. [IMS]

Test 4.9 – Observing the change in mass mobility spectrum with time. [SIMMS]

Test 4.10 – The effect of varying the Faraday plate-to-cone voltage on the mass spectra. [MS]

The following sections describe the results from each of these tests.

Test 4.1 – The effect of varying the drift tube voltage on the ion current (dc mode).

The relevant parameters relating to the test are summarised below in table 4.1. This format is also applied to all of the other tests described in this chapter.

Table 4.1 listing the test parameters

Test Parameters (Fixed)		Test Parameters (Variable)	
<i>IMS Temperature (°C)</i>	23	<i>Tube pressure (mbar)</i>	998
<i>V_{SCREEN} (V)</i>	24	<i>Gate mode</i>	<i>open</i>
<i>Fwd flow (l/min)</i>	0.25		
<i>Contra flow (l/min)</i>	0.5		

This test was performed with the screen grid nominally set at 24 V. This value was obtained from pre-test results, but is expanded on in Tests 4.2 and 4.5. The program IMS was used. Although the ion current is continuous, 500 averages were taken at each measurement in order to get a better SNR.

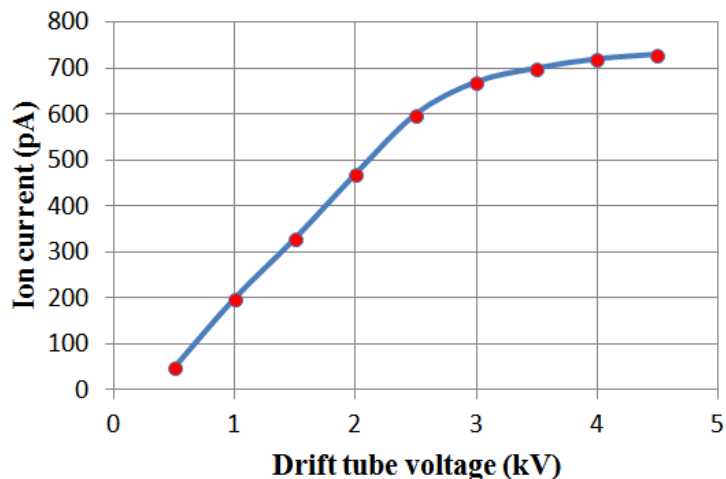


Figure 4.1 Plot of ion current vs drift voltage

Discussion

Considering the graph shown in figure 4.1, the current appears to rise in a linear fashion but then gradually approaches a maximum value (due to the limit of ionising beta radiation which imparts a corresponding limit of ion density). Although the total charge summed over all the ions is independent of tube voltage (since that is determined by the energy and flux of the β particles in the radioactive source), it seems that the ions are being lost at lower voltages, possibly caused by radial diffusion and Coulombic repulsion. At higher voltages the ion plume may be more 'stretched' since the ions will be moving more quickly and so the amount of radial diffusion/cm and Coulombic repulsion should be correspondingly less. This effect is rather more complicated since in the reaction region close to the ion source, Coulombic repulsion towards the walls of the drift tube is a dominant factor and so more ions will be pulled out at higher voltages since the radial distance covered by the ions when diffusing will be shorter due to the increase in longitudinal acceleration at higher voltages. Along the drift region past the gate, both Coulombic and radial diffusional effects take place. [120]. A compromise must be met between temporal resolution (ability to separate the peaks) at lower voltage (although individual peaks would also be broadened) and higher signal intensity at

high voltages. As a compromise, an electric field strength of 200 to 250 V/cm is generally used in IMS systems, being 212 V/cm in our case.

Test 4.2– The effect of varying the screen grid voltage on the total ion current (dc mode). Program used: IMS

Test Parameters (Fixed)		Test Parameters (Variable)	
Tube Temperature (°C)	20	Tube pressure (mbar)	998
Tube voltage (kV)	4.5	Gate mode	open
Fwd flow (l/min)	0.25		
Contra flow (l/min)	0.5		

Referring to figure 4.2, as the voltage on the screen grid increases, the current from the FP rises non-linearly towards a limiting value of 800 pA. From the curve, a reasonable choice for the operating voltage to provide a nominal ion transmission is at approximately 30 V.

Note, for minimal field distortion, this corresponds to a screen grid-to-FP separation of

$$\frac{30 \text{ V}}{212 \text{ V/cm}} = 0.14 \text{ cm}$$

which is in good agreement with the physical separation of around 0.1

cm in the drift tube.

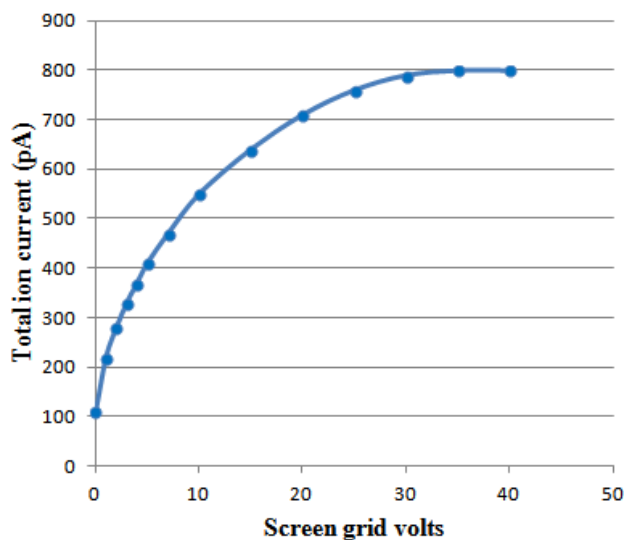


Figure 4.2 Plot of ion current vs screen voltage

Discussion

Again, a maximum limit (or saturation point) for the ion current occurs due to the finite amount of ionising radiation that is available from the ion source. Apart from screening the Faraday plate from the electric field due to the approaching ion swarm, varying the voltage on the screen grid will also change the strength of the electric field between the screen and the Faraday plate. When the positive voltage on the screen is low, the repulsion of the ions will be small thus causing many of the ions to collide with the screen and dissipate their charge, leaving a small remainder to get through to the FP (thus effectively acting as a potential barrier). As the voltage is increased, repulsion of the ions away from the screen will correspondingly occur allowing more of them to pass through the holes in the screen, until a point is reached where the field caused by the screen-to-FP voltage is the same as that due to the ring electrodes, where maximum transmission is reached. Note, the presence of the grid will still cause some reduction in current due to its sheer physical size in the ion path compared to that of the ions, and so some collisional loss will be inevitable.

Test 4.3– The effect of varying the gate pulse width on the RIP intensity

Program used: IMS

Test Parameters (Fixed)	
<i>Tube temperature (°C)</i>	23
<i>Tube voltage (kV)</i>	4.5
<i>V_{SCREEN} (V)</i>	25
<i>Fwd flow (l/min)</i>	0.25
<i>Contra flow (l/min)</i>	0.5
<i>Gate pulse frequency (Hz)</i>	25

Test Parameters (Variable)	
<i>Tube pressure (mbar)</i>	998
<i>V_{SCREEN} (V)</i>	24

It is expected that the amplitude of the RIP current peaks should increase linearly with gate pulse width since the amount of charge transmitted by the gate per second (the current) is directly controlled by the width of the gate pulse.

Discussion

Looking at the graph in figure 4.3, it can be seen that the relationship is in fact far from linear and so clearly, other factors are involved when the width of the gate pulse is changed. The shape of the curve shown in blue through the data points resembles that of a somewhat distorted rising exponential function of the form $i = I \left(1 - e^{-\frac{t}{\tau}} \right)$, where i is the amplitude of the RIP current, I is the maximum current (pA) available, t is the gate pulse width time (ms), and τ is the ‘time constant’ imposed by the drift tube characteristics.

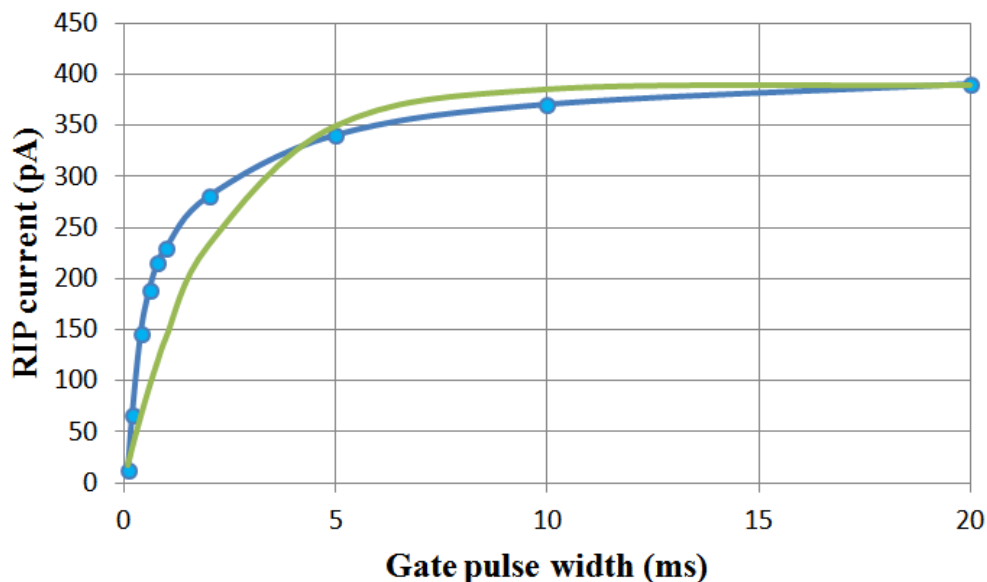


Figure 4.3 Plot of RIP vs gate pulse width

The nearest fit to the data using the exponential function previously stated is that of the curve shown in green where $i = 390 \left(1 - e^{-\frac{t}{2.2}} \right)$ and so the results are only an approximation to this type of equation. To improve the fit, further terms are required. However, there would not be much point in pursuing this further since gate widths larger than 0.5 ms are not

normally encountered in practice and the extension of up to 20 ms was chosen for investigative purposes only.

The complex and interacting factors having an influence on the shape of the curve can be attributed mainly to diffusional/space charge effects along the drift region, and ion retention in the gate.

Common gate pulse widths

As mentioned, the range of gate pulse widths more appropriate to practical IMS systems (obtained from a compromise between resolution and sensitivity) is commonly found to be approximately 0.2 to 0.5 ms. It is interesting to note the response over the range 0.2 to 0.8 ms where here, as seen in figure 4.4, a polynomial relationship of the form $y = -336.29x^2 + 581.16x - 34.561$ offers the best fit between i and t as shown in figure 4.5.

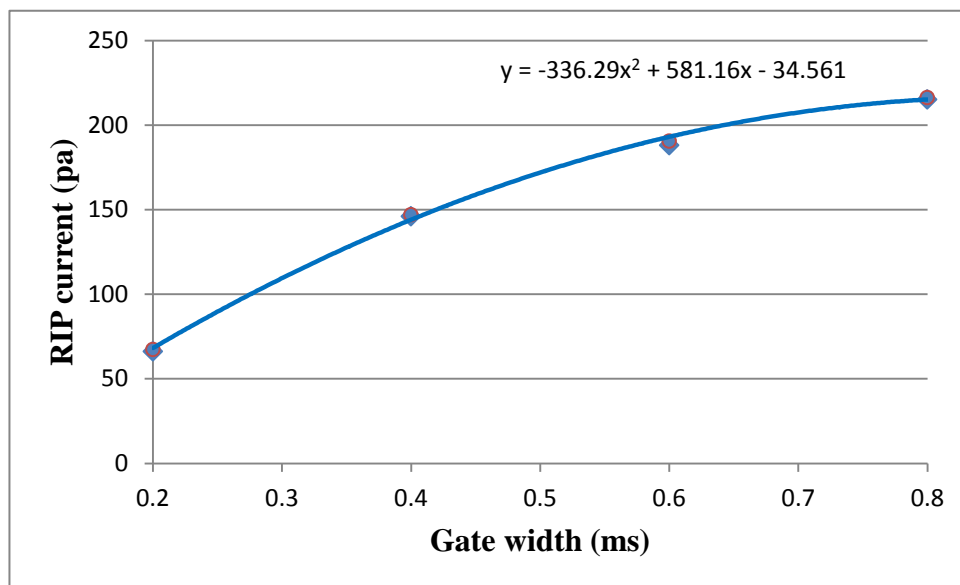


Figure 4.4 - Magnified section of Figure 4.3

In relation to the effect of gate width on resolution, Siems et al [53] consider that 0.1 to 0.2 ms provides the best results. In their instrument, (which has a drift tube of similar size to ours), with a drift voltage of 2kV, the resolution at a gate pulse width of 0.1 ms is about 45 dropping to 40 at 0.2 ms. At 0.5 ms, their resolution had further dropped to 25. However, sensitivity is considerably reduced at 0.1 ms and so as a compromise on resolution and sensitivity, a gate pulse width of 0.2 ms to 0.3 ms is suitable, which is also that generally chosen for the pulse width most commonly used in other IMS systems.

Test 4.4 The effect of averaging on the quality of the ion mobility spectrum.

Program used: IMS with a varying number of averages

Here, the IMS ion mobility program is used to obtain the spectra. In order to obtain a satisfactory SNR an average over a number of spectra is taken and here, the result on the definition of the RIP is observed over an increasing number of averages. Note, the improvement in SNR is proportional to the square root of the number of averages taken. (i.e. to improve the SNR by a factor n , it is necessary to average over n^2 spectra) [121].

Considering the signal taken from the Faraday plate, it is interesting to observe the progression in improvement of signal-to-noise ratio (S/N) as the number of averages of the spectra taken is increased. Note, in the spectral plots, the amplitude scale is reduced as the number of averages increases to maintain optimum scaling. The reactant ion peak (RIP) is composed of water clusters formed from the moisture content of the air used for the drift gas.

The noise pickup is caused by the microphony effect due to the vicinity of the screen grid to the Faraday plate. An alternating voltage is induced between the screen and Faraday plate from capacitance changes caused by the vibration from the two turbomolecular pumps (about 1 KHz in frequency) and the beats due to slight speed differences between the pumps are seen as an amplitude modulation of the induced noise signal. A modification suggested by Smiths

Detection was to improve the S/N by doming the screen grid to make it more rigid and therefore much less susceptible to mechanical vibrations from the pumps. Although this was attempted, it was very difficult to achieve owing to the springiness of the material used for the screen grid and consequently no significant improvement was seen after reassembly.

When using the SIMMS (selected mass ion mobility spectrum) program, the microphony effect is not present because the ion signal is obtained from the channeltron and not the Faraday plate. The IMS spectra shown in figures 4.5 to 4.8 were obtained using the following parameters:

Test Parameters (Fixed)	
Tube voltage (kV)	4.5
V_{SCREEN} (V)	24
Fwd flow (l/min)	0.25
Contra flow (l/min)	0.5
Gate pulse width (ms)	2

Test Parameters (Variable)	
Pressure (mbar)	1010
Tube Temperature (°C)	20

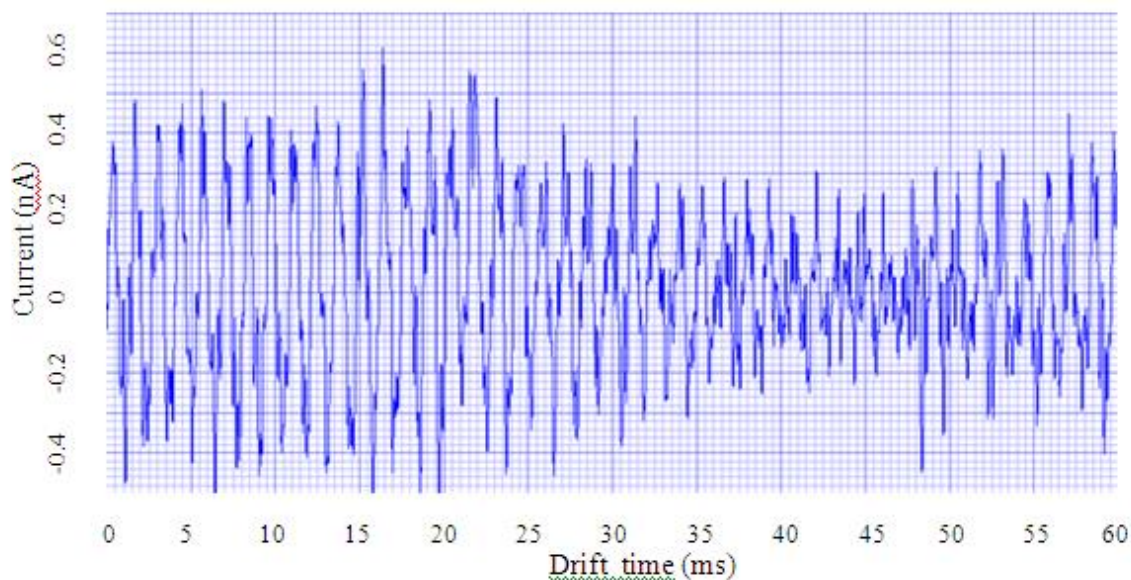


Figure 4.5 IMS spectrum with two averages

Referring to figure 4.5, the RIP is indistinguishable from the noise. In figure 4.6, the node and antinode of the beat frequency between the turbomolecular pumps can be seen.

Figures 4.5 to 4.8 illustrate how simple averaging of multiple scans can produce a large improvement in signal-noise ratio. Note, when scanning over four hundred averages for figure 4.8 the time taken to do this was $400 \times (60 \text{ ms scan time}) = 24 \text{ s}$.

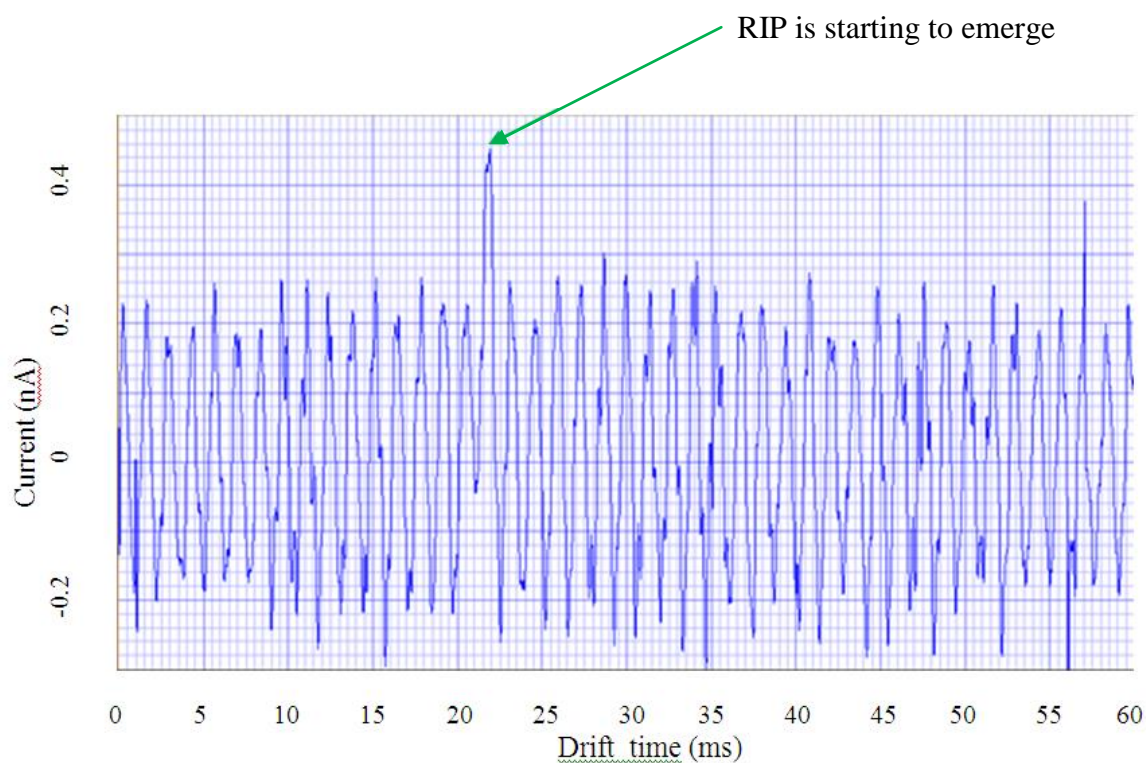


Figure 4.6 IMS spectrum with ten averages

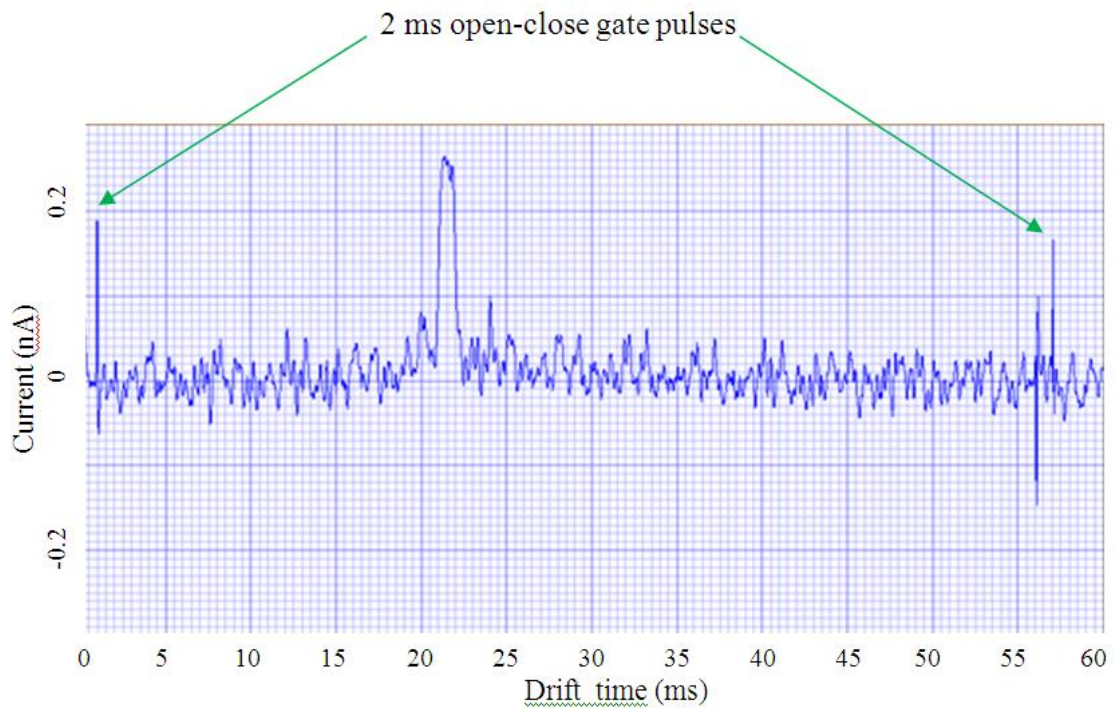


Figure 4.7 IMS spectrum with one hundred averages

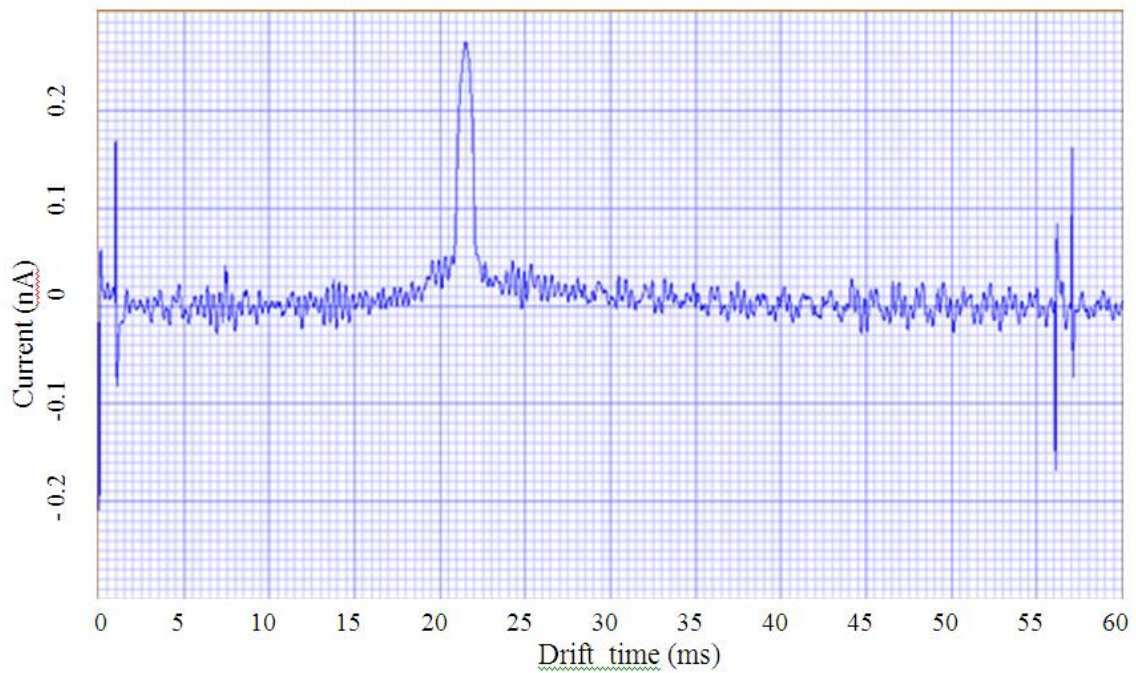


Figure 4.8 IMS spectrum with five hundred averages

The spectrum shown in figure 4.8 now has an acceptable S/N ratio of $2.7 \div 0.05 = 54$ or (expressed in decibels) $20 \times \log 54 \sim 35$ dB.

Test 4.5 – Investigating the microphony effect of the voltage between the screen grid and the Faraday plate

Program used: IMS

This test was conducted under various conditions and is separated into parts 1 and 2

Part 1 Observations made under quiescent (no signal) conditions at low and high pressures

Test Parameters (Fixed)		Test Parameters (Variable)	
<i>Tube Temperature (°C)</i>	23	<i>Pressure (mbar)</i>	1 and 1002
<i>Fwd flow (l/min)</i>	0.25	V_{SCREEN} (V)	24
<i>Contra flow (l/min)</i>	0.5	<i>Gate mode</i>	open – pulsed

Initially looking at the signal from the Faraday plate with no applied voltages to the drift tube (apart from the screen voltage to set up a charge between the screen grid and Faraday plate for obtaining microphony) with the pressure at 1 mbar (shut down pressure), the noise current was ~ 30 pA on average with peaks at ~ 70 pA. When the pressure was increased to atmospheric (normal operating pressure) at 1002 mbar, the noise reduced to ~ 5 pA on average with peaks at ~ 10 pA. This is because at low pressure, it is easier for the screen grid to vibrate in sympathy with the vibration from the turbo pumps. At high pressure, the viscosity effect due to increased density of molecules causes a greater resistance to motion due to the increased frequency of collisions. This also confirms the idea that the noise arises from the microphony effect from the screen grid to FP. It was found that switching on the 4.5 kV tube voltage and the gate interface unit had no effect on the noise level. However, when the gate operating mode was switched to ‘pulsed’ a signal was seen in the mobility spectrum. This signal was the differentiated 0.2 ms gate pulse (seen as sharp complementary switching spikes of -100 pA and +120 pA amplitude) due to capacitive coupling between the gate and

the Faraday plate. This signal is very useful as it provides a timing reference when making drift time measurements.

Part 2 Optimising the SNR from observations made under signal conditions

Test Parameters (Fixed)		Test Parameters (Variable)	
<i>Tube Temperature (°C)</i>	30	<i>Pressure (mbar)</i>	1002
<i>Tube voltage (kV)</i>	4.5	<i>V_{SCREEN} (V)</i>	0 to 40
<i>Fwd flow (l/min)</i>	0.25		
<i>Contra flow (l/min)</i>	0.5		
<i>Gate pulse width (ms)</i>	0.2		

Table 4.2 Optimising SNR

V_{SCREEN} (V)	Ave noise (pA)	RIP current (pA)	S/N ratio
10	5	50	10
12	5	50	10
14	5	60	12
16	5	65	13
17	5	70	14
18	5	70	14
19	5	70	14
20	5	75	15
21	5	75	15
22	5	75	15
23	5	76	15.2
24	5	77	15.4
25	6	78	13
26	7	78	11.1
30	8	80	10

Each reading shown for average noise and RIP current was an average of three results.

Discussion

Referring to Table 4.1, it is seen that the screen grid voltage to give the best signal-to-noise (S/N) ratio is nominally at 24 V. At 30 V, there is a 4% increase in current but the S/N deteriorates by 35%. In dc mode (test 4.2) it was seen that the nominal value for the maximum ion current of 800 pA was at 30 V and at 24 V the current was 750 pA, which is a reduction of only 6%. Note, slightly higher RIP currents were observed during subsequent

tests following baking out of the drift tube at 100 °C since ions that would have been lost to impurities were now available.

Test 4.6 – The effect of varying the potential difference between the screen grid and FP on the amplitude of the RIP

Programs used: IMS and SIMMS

Test Parameters (Fixed)	
<i>Tube Temperature (°C)</i>	30
<i>Tube voltage (kV)</i>	4.5
<i>V_{SCREEN} (V)</i>	24
<i>Fwd flow (l/min)</i>	0.25
<i>Contra flow (l/min)</i>	0.5
<i>Gate pulse width (ms)</i>	0.2

Test Parameters (Variable)	
<i>V_{Faraday plate} (V)</i>	20
<i>V_{CONE} (V)</i>	14
<i>Pressure (mbar)</i>	991
<i>Tuned mass m/z (Da)</i>	73

The basis of this test is to look at the effect on the amplitude of the RIP when the system is used in the selected ion mass mobility mode (i.e. using counts) as a comparison to that made in the previous test that used ion current. This can also be considered to give the same result as that when looking at the total ion count because (due to switching of the water clusters along the drift region), the water clusters appearing at different masses will overall have the same drift time.

Referring to table 2 following, t_w is the width of the RIP at half maximum. The RIP was obtained using the SIMMS program rather than IMS since in this mode of operation, the SNR is significantly improved as the signal is now unaffected by microphony from the screen-to-Faraday plate.

Table 4.3 RIP characteristics for various screen-to Faraday plate voltages

	V_{screen} (V)	$V_{screen-FP}$ (V)	Count	t_d (ms)	t_W (ms)
$V_{screen} \leq V_{FP}$	16	-4	4	21.5	1
	17	-3	16	21.2	0.9
	18	-2	40	20.8	0.9
	19	-1	70	20.45	0.5
	20	0	90	20.36	0.5
$V_{screen} > V_{FP}$	21	1	95	20.34	0.4
	22	2	100	20.32	0.4
	23	3	118	20.27	0.36
	24	4	120	20.23	0.32
	25	5	115	20.1	0.32
	26	6	110	20.1	0.32

Discussion

From the results shown in Table 4.2, it can be seen that a screen voltage of 24 V provides an optimum result with the gate in pulsed mode, and that the ion transmission is actually reduced at voltages above this. This is convenient since it is in agreement with the nominal value selected in test 5.5 for an optimum SNR.

SIMMS time offset

When comparing RIP results from using the SIMMS program to the RIP in the ion mobility spectrum under the same conditions, it was noticed that the drift times for the RIP in the ion mobility and mass mobility modes were separated by an offset of +0.3 ms when working in the selected mass ion mobility mode. This factor must be taken into account when conducting further tests or experiments. This can be attributed to several causes such as:

Electronic: Delay in the pulse converter unit (a few microseconds).

Slight differences in processing time between the IMS and SIMMS LabVIEW programs (fractions of a millisecond).

Spatial: Delay caused from the extra path taken from the Faraday plate to the channeltron in the mass spectrometer, which is considered to be the main contribution to the delay, (approximately 0.3 ms). [122]

Test 4.7 – Effects on RIP (drift time and amplitude) with varying drift tube voltage.

Program used: IMS

Test Parameters (Fixed)		Test Parameters (Variable)	
<i>Tube Temperature (°C)</i>	23	<i>Pressure (mbar)</i>	1003
<i>V_{SCREEN} (V)</i>	24	<i>Gate mode</i>	<i>pulsed</i>
<i>Fwd flow (l/min)</i>	0.25		
<i>Contra flow (l/min)</i>	0.5		
<i>Gate pulse width (ms)</i>	0.2		

The voltage applied to the drift tube was varied in steps of 100V from 2 kV up to 4.5 kV (flashover in the drift tube was found to occur beyond about 5 kV).

From theory given in chapter 1, the ion mobility K at constant temperature and pressure is:

$$K = \frac{L^2}{Vt_d} \quad (1.4)$$

Thus, when t_d is plotted against $(V_{HT})^{-1}$ a straight line relationship should be obtained from the results.

Discussion

The graph shown in Figure 4.11, shows that there is an inverse relationship between drift time and drift tube voltage.

Considering validity of the results, At 4.5 kV, $t_d = 20.6$ ms.

Therefore at the extreme of 2 kV, t_d should theoretically be $20.6(4.5/2) = 46.4$ ms.

From the results, at 2 kV, $t_d = 45.8$ ms. This is only about a 1% difference, so to a first approximation allowing for experimental error, the results show a good agreement with those predicted from theory.

Similarly, at 4 kV, $t_d = 23.1$ ms \therefore at 3 kV t_d should be $23.1(4/3) = 30.8$ ms.

From the results, $t_d = 30.6$ ms at 3 kV (about 0.7% error) and so the equation holds over the full range of variation in V .

Velocity of the ion swarm

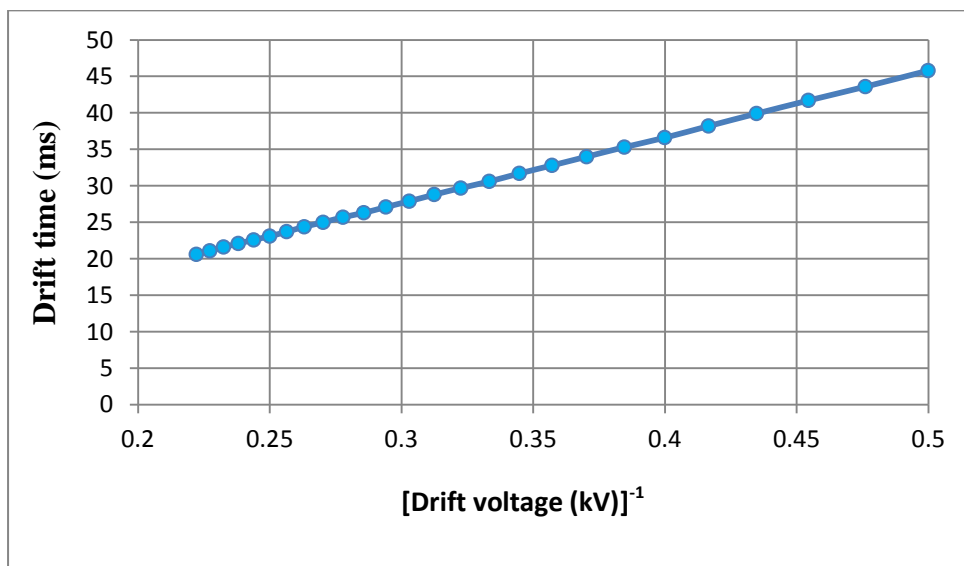


Figure 4.9 Effect of drift tube voltage on drift time

The arrival time as seen in Figure 4.9 is influenced by a set of complex interactions due to collisions with the neutral gas molecules slowing down the ions, and accelerations due to the electric field. This results in an overall ‘constant’ drift velocity dependent on the mass, shape and cross-section of the ion, the pressure and temperature in the drift tube, and the type of buffer gas used. At proportionally lower voltages, the acceleration after a collision will be less than at higher voltages and so over the mean free path of the ion, the time between

collisions will proportionally increase (since its velocity is less). Thus t_d will have an inverse relationship to V as was seen in the results

Effect of drift tube voltage on the amplitude of the reactant ion peak (RIP)

Considering the amplitude of the RIP current from the FP as shown in Figure 4.10, this is seen to initially increase in proportion to drift voltage, but with a reducing rate of change with further increases in voltage. This again is due to the ion signal reaching its maximum value – resulting in the non-linear ‘drift tube resistance’ effect also seen when in dc mode as discussed in test 4.1. The curve seen in figure 4.10 shows that the RIP gradually reaches a plateau corresponding to the maximum ion collection efficiency.

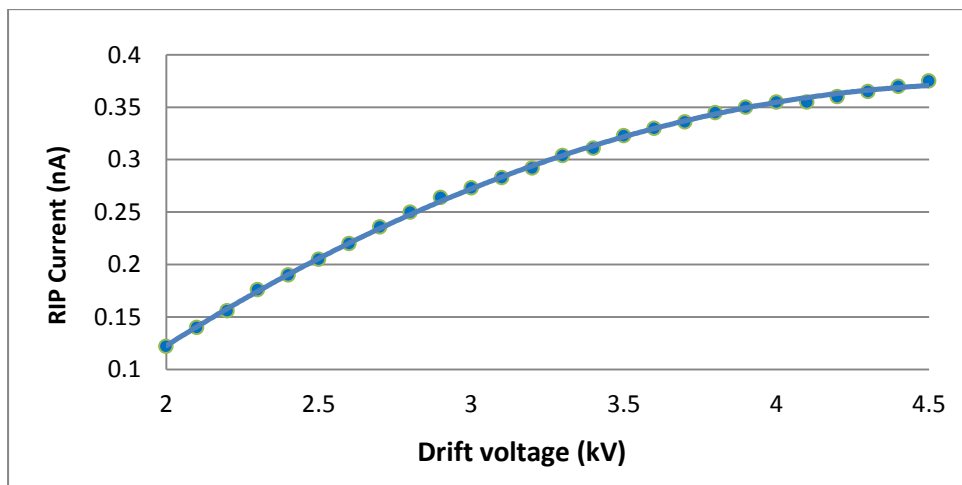


Figure 4.10 Effect of drift voltage on RIP Current

A further complication that affects the amplitude of the RIP is caused by the increasing resolution available at higher voltages. The reason for this is that as the voltage increases, peak broadening decreases because the shorter drift time reduces the amount of diffusional spreading. Thus, at low drift voltages, diffusion is the main factor in determining peak width since the ion swarm drifts at a lower velocity which allows more time for diffusional spread

than with higher voltages (where the initial gate pulse width becomes the main factor to cause pulse spread).

In terms of resolution, Chapter 1 of this thesis (section 1.2.6) shows that the resolution of our instrument is ~ 69. In the investigation made by Siems et al [123] on factors affecting resolution, they looked at the effect of changing the drift tube voltage. The length of the drift region in the drift tube they used (11.6 cm long) is similar to ours (10.5 cm long). They found that there is a maximum drift voltage (around 1.6 kV) which gives the best resolution. Above this value, the resolution steadily decreases, but below this value the resolution falls off more rapidly. However, it is usual to operate at a higher voltage as a compromise between resolution and sensitivity (a similar compromise to that found in test 4.3). From figure 4,10, it can be seen that the ion current approaches its limit at around 4.5 kV (which produces 2.25 kV across the drift region). Thus, a suitable compromise may be to have 2 kV across the drift region by applying 4 kV to the drift tube.

Test 4.8 – Investigating the change in ion mobility with time

Program used: IMS

Test Parameters (Fixed)	
<i>Tube Temperature (°C)</i>	30
<i>Tube voltage (kV)</i>	4.5
<i>V_{SCREEN} (V)</i>	24
<i>Fwd flow (l/min)</i>	0.25
<i>Contra flow (l/min)</i>	0.5
<i>Gate pulse width (ms)</i>	0.2

Test Parameters (Variable)	
<i>Tube pressure (mbar)</i>	999

Clean lab air was passed through an undoped molecular sieve and so the ionisation products were based on water chemistry producing protonated water clusters. The RIP current was seen to vary around a mean value and so several readings were taken at each time interval with the average value being recorded.

Results and discussion

Considering the shape of the curves shown in figures 4.11 and 4.12, the cause of the transient effect is not fully understood. The effect appeared to diminish significantly after about three hours, where a steady state condition was reached of RIP current ~ 80 pA, with a drift time $t_d = 20.3$ ms.

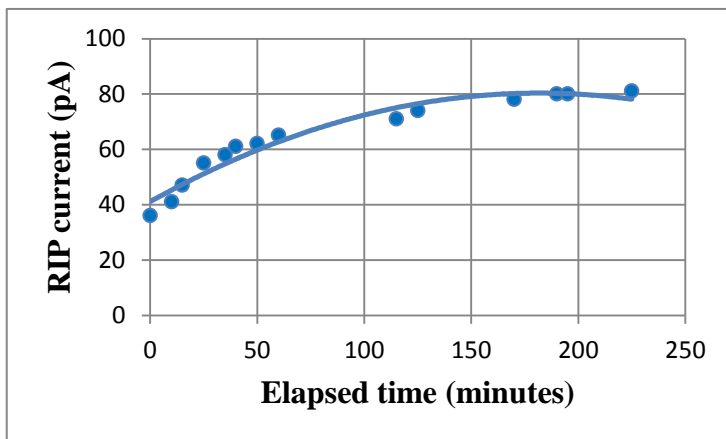


Figure 4.11 Variation of RIP current with elapsed time

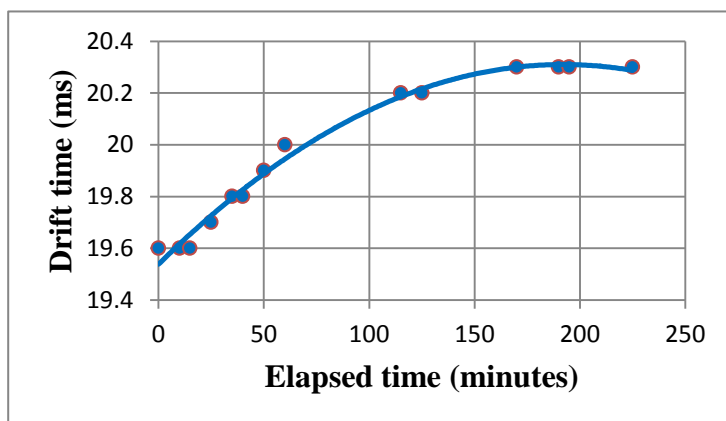


Figure 4.12 Variation of drift time with elapsed time

This effect indicates that we should wait for around four hours for the system to settle after switch on. Note, subsequent to these tests being performed, a modification was made to

produce a stable drift voltage independent of the drift ring resistors forming the divider chain and this was found to remove the effect. (See appendix A4.13.)

Test 4.9 – Investigating the change in ion mass mobility with time

Program used: SIMMS

Test Parameters (Fixed)		Test Parameters (Variable)	
<i>Tube Temperature</i> (°C)	30	$V_{Faraday\ plate}$ (V)	20
<i>Tube voltage</i> (kV)	4.5	V_{CONE} (V)	14
V_{SCREEN} (V)	24	<i>Tube pressure</i> (mbar)	1017
<i>Fwd flow</i> (l/min)	0.25	<i>Tuned to m/z</i> (Da)	73
<i>Contra flow</i> (l/min)	0.5		
<i>Gate pulse width</i> (ms)	0.2		

This test examines the change in the mobility over time, of the predominant water cluster ions in the RIP having m/z 73, and can be compared to the previous test 4.8 which looked at the RIP in the ion mobility spectrum, which is made up of several masses (including m/z 73) due to variable amounts of water clustering on the ions as they drift down the tube. The results of this investigation are shown in table 4.4 below.

Table 4.4 Variation of drift time and RIP count over time

Time interval (min)	Peak RIP count	Drift time t_d (ms)
0	26	20.23
10	27	20.30
20	28	20.35
30	29	20.40
45	30	20.50
65	31	20.55
85	31	20.63
125	31	20.65

In order to get an idea of how much background noise was present in the mass spectrometer, an initial observation was made on the quiescent noise count level with the operating voltage

of the channeltron set to 0V. Over 0 to 40 ms drift time, the observed random noise level was consistently low at around 1.7 counts.

Discussion

It can be seen from table 4.4 that again, there is a similar gradual increase in drift time and peak count to that encountered in test 4.8 over the two hour period before eventually settling down (after three hours) to around 20.6 ms and 31 counts. A possible explanation for this delay in the response may be that it is caused by a 'charging' effect. This could be due to the fact that the drift rings are on the outside of the glass drift tube and thereby introduce a capacitance between the ion cloud and the rings with the glass acting as the dielectric. The initial 'displacement current' required for charging up this capacitance would be supplied by the charge on the ions as they are extracted from the swarm by electrostatic attraction to the inner surface of the drift tube, thus resulting in a lower amplitude of the current pulse from the FP and consequently, a lower ion count from the channeltron.

The difference in drift times between tests 4.8 (ion mobility) and 4.9 (selected mass ion mobility) is 0.3 ms due to the time taken for the ions to transit through the quadrupole and can be compensated for in the SIMMS program where a variable negative time offset is incorporated.

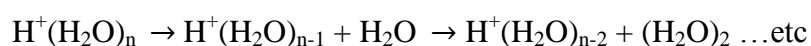
Test 4.10 – The effect of varying the voltage between the Faraday plate and cone on the mass spectra of the water cluster ions

Program used: MS

This test was performed in order to determine the optimum FP-to cone voltage that gives the best compromise between ion transmission and cluster ion fragmentation.

Test Parameters (Fixed)		Test Parameters (Variable)	
<i>Tube Temperature</i> (°C)	30	$V_{Faraday\ plate}$ (V)	14 TO 28
<i>Tube voltage</i> (kV)	4.5		
V_{SCREEN} (V)	25		
<i>Fwd flow</i> (l/min)	0.25		
<i>Contra flow</i> (l/min)	0.5		
<i>Gate pulse width</i> (ms)	0.2		
V_{CONE} (V)	14		

The protonated water clusters $H^+(H_2O)_n$ formed at atmospheric pressure in the drift tube can be fragmented due to collision-induced dissociation (CID) after passing through the pinhole in the Faraday plate (FP) and into the region of low pressure between the FP and the cone in the IMS - quadrupole interface [124]. Because the pressure is much lower, the mean free path is now much longer than in the drift tube. Therefore the ions can reach considerably higher velocities (due to the electric field between the FP and cone) before colliding and so the energy they gain is also considerably larger than that provided by the electric field in the drift region (where their thermal energy is constant). Thus the larger clusters after the pinhole will fragment into smaller water clusters, which in turn may continue to fragment down to the reactant ion as:



Note, as a rough guide to mean free path lengths, for neutral air at room temperature the mean free path as quoted by Harris [125] is:

$$\lambda = \frac{6.4 \times 10^{-3}}{P} \text{ cm where } P \text{ is the pressure in mbar.}$$

Thus, $\lambda \sim 6.3 \times 10^{-6}$ cm at atmospheric pressure and is ~ 640 cm at 10^{-5} mbar. (The mean free path will be considerably less in proportion for the ions in the drift tube, due to their

increased cross section caused by their charge providing an additional electrostatic effect between themselves and any potentially colliding polarised neural molecules).

The effect of changing the ion acceleration voltage between the Faraday plate and cone will be to vary the fragmentation i.e. the amounts of water clusters having a particular degree of clustering across the region (with greater fragmentation occurring with increasing voltage).

Using the mass spectra program MS, observations were made on the water clusters seen at m/z 37, 55 and 73.

Practical considerations and results

To obtain the results more quickly than using a mass scan over say m/z 30 to 75, it was found to be more convenient to use the mass spectra program over the ranges 36 – 38, 54 – 56, 72 – 74 separately over 40 steps (giving a step size of 0.05 amu). An average reading over three scans was taken at each mass. The screen voltage V_{SCN} was set at +30 V for optimum ion transmission since the S/N ratio in the IMS mode of operation is not a consideration here, and the voltage on the FP maximised at +28 V. (The ion current is depleted at smaller screen-to-FP voltages as was found in test 4.3.) This allows a 14 V variation in FP-to-cone voltage with the cone held at 14 V.

The amount of fragmentation caused by FP-to-cone voltage changes is obtained from the results shown in the plot of counts for the clusters at various voltages as given in figure 4.13.

Also from the results in figure 4.13, the branching ratios may be obtained by plotting the fraction formed by the count at each m/z to the sum of the counts, at a particular voltage, as shown in figure 4.14.

A plot of the total ions over the voltage range shows the transmission characteristics as seen in figure 4.15.

By extrapolating back to $V_{FP-CONE} = 0$ V, the distribution of the clusters in the drift region just before the FP may be determined from consideration of figure 4.14 showing the branching ratios of the cluster ions. (It is not physically possible to see the ions at $V_{FP-CONE} = 0$ as the transmission through the pinhole in the FP is then virtually zero.)

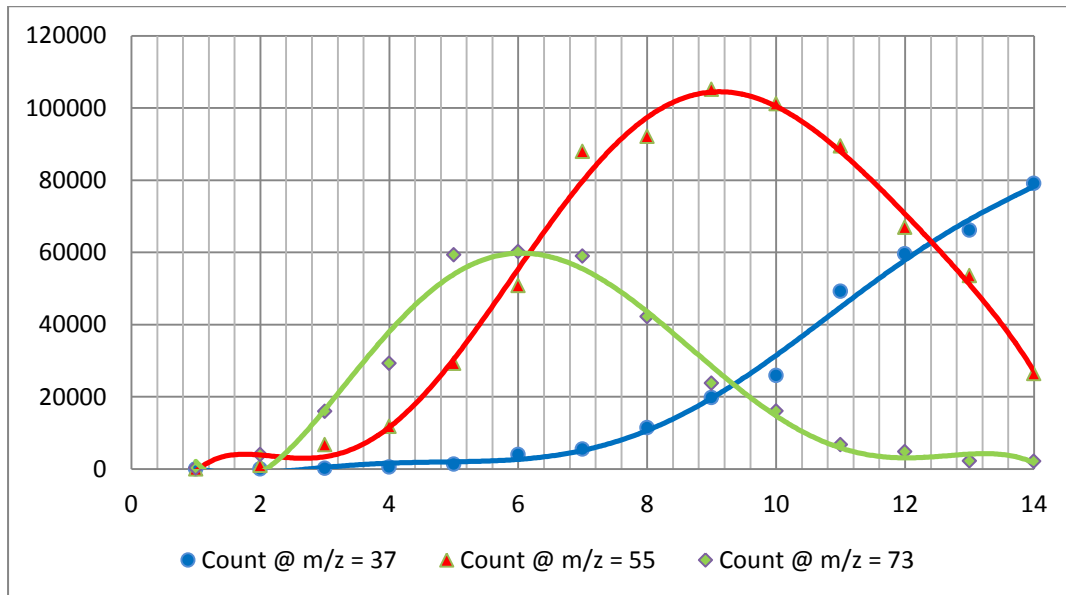


Figure 4.13 Counts over $V_{FP-CONE} = 1$ to 14 V

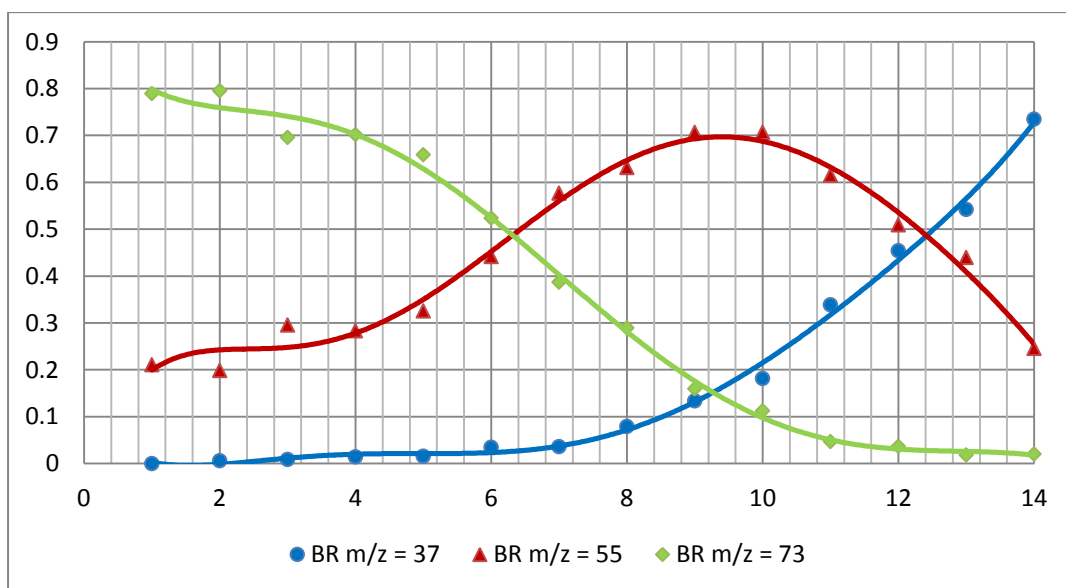


Figure 4.14 Branching Ratios for $V_{FP-CONE} = 1$ to 14 V

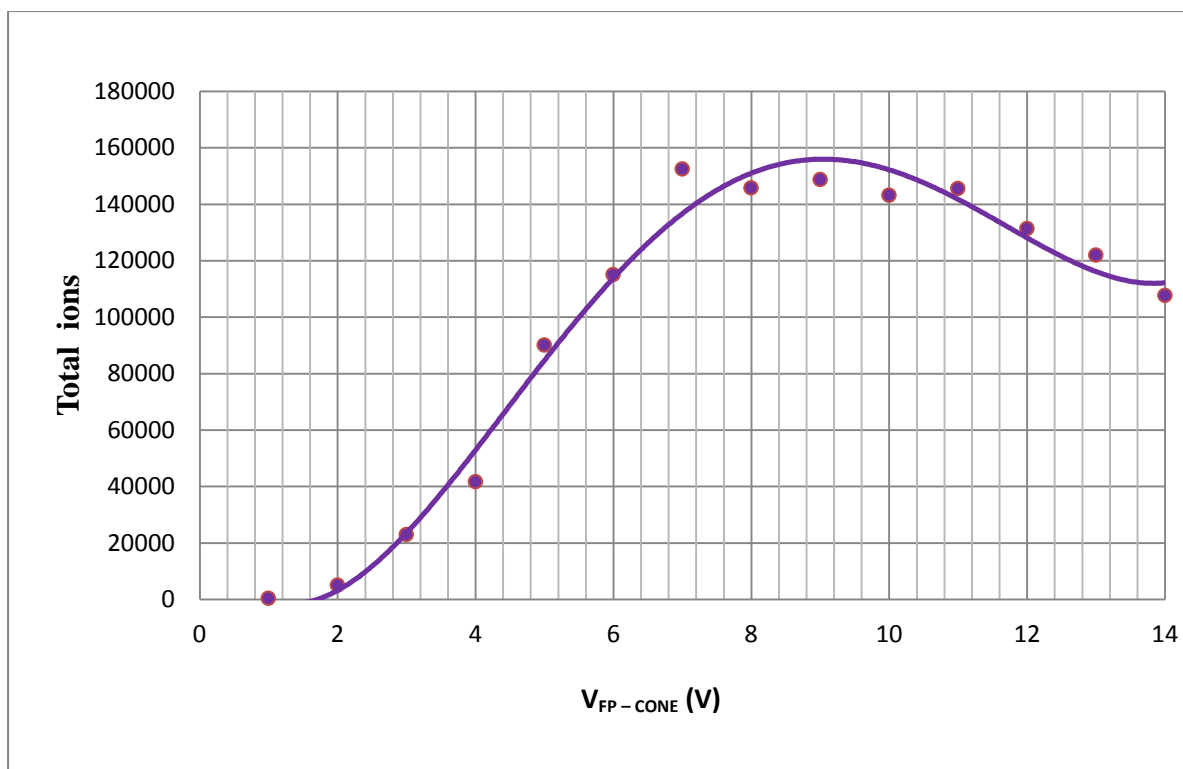


Figure 4.15 Total Ion transmission

Discussion

Looking at figure 4.15, the FP-to-cone voltages that give maximum ion transmission are around 7 to 11 V. However, considering figure 4.13, fragmentation also occurs at 7 V where the number of ions at $m/z = 73$ decreases as those at $m/z = 37$ and 55 continue to increase.

From figure 4.15, at 6 V, there is a reduction in ion count of approximately 150000 to 115000 ie 23%. Thus, as a compromise between best transmission and the onset of fragmentation, a voltage of say, 6.4 V may be considered appropriate.

Of interest, fragmentation of $m/z = 55$ is then seen at approximately 9 V. At this point, the number of ions at $m/z = 37$ increases sharply due to the increased contribution from fragmentation of both sets of cluster ions at higher masses.

From figure 4.14, it can be seen that fragmentation occurs immediately as the voltage is increased from 1 V (at 0 V, there is an absence of ion transmission). Clearly, for the

branching ratios to be meaningful, they must also be considered alongside the corresponding ion transmission shown in figure 4.13. in order to see if the number of ions at a particular branching ratio is in fact significant.

This process of compromise between transmission/fragmentation may be required to be done when other types of reactant ions are used.

This concludes the tests required to examine the relevant parameters of the IMS-QMS system and their interactions to sufficiently characterise the system in readiness for its use in the investigation of ion-molecule reactions.

Chapter 5 CHARACTERISATION OF THE IMS-QMS SYSTEM IN POSITIVE ION MODE

5.1 Introduction

This chapter relates to how the IMS-QMS system was characterised by using it to enable investigations to be made into the response of various compounds used as analytes in the positive ions mode of operation. Initially, analytes that had been previously investigated by other workers in the IMS community were chosen in order to confirm the correct operation of the system by comparing results. These particular compounds were:

- Tertiary butanol ($C_4H_{10}O$) – used to compare with earlier studies in order to prove the system.
- Acetone (C_3H_6O) – a common IMS dopant in CWA detectors, again used here to characterise the system and also as a precursor to investigating diacetone as an analyte.

New measurements were then made using compounds not previously investigated with a tandem IMS-MS system, those being:

- Diacetone – used here in order to compare the structure of the acetone dimer with that of the diacetone monomer.
- Dipropylene glycol methyl ether (DPGME) – used to safely simulate a target CWA for confidence testing of an IMS system

The strategy employed to obtain the required information from each investigation was to:

- Use the peaks(s) in the total ions mobility spectrum from the channeltron electron multiplier to adjust the analyte concentration to give the characteristic three peaks representing RIP, monomer and dimer.
- Look at the mass spectra to observe the individual components of the chemical under investigation.

- Look at the selected mass mobility spectra for the mass components of interest seen in the mass spectrum to determine which particular ions make up the mobility peaks seen in the total ions spectrum.

5.1.1 Analyte Sample Preparation

Various techniques may be used to appropriately introduce analyte into an IMS system [126] with the method chosen for the present experiments being “headspace sampling with a syringe”. A sample containing the analyte to be investigated was presented to the IMS via a syringe mounted in a syringe drive allowing sample vapours to be injected into the forward flow of carrier gas. Various concentrations of analyte may be presented by varying the setting for the rate of delivery from the syringe drive. The glass syringe used for the experiments was of diameter 23 mm with a nominal volume of 30 mm³. A dilution rig (see appendix 5.4 for details of use) was used to dilute the liquid analyte sample down to a level of dilution suiting the flow rates of the syringe drive and carrier gas for obtaining the desired concentration in the gas flow(s) in the IMS. To prepare, the liquid analyte is initially poured into a container which is then fitted to the dilution rig with the dilution chamber pumped down to vacuum. In order to remove any air and impurities from the sample, a freeze-pump-thaw cycle can be made, or alternatively the sample can be exposed to vacuum to pump out the headspace. The sample valve is then opened to allow the sample vapours to produce an initial pressure in the system. Introducing pure air at a greater pressure then allows an initial dilution to be made. Alternatively, if the sample is initially prepared in a syringe mixed with pure air taken from the IMS system, then by knowing the partial pressure of the saturated vapour, the initial concentration of the analyte can be calculated as detailed in the following experiments. By using the dilution rig in conjunction with the dilution chart given in appendix 5.6 the final concentration required in the syringe is obtained.

Appendix A5.1 shows how the calculation of syringe flow rate required to give a final concentration in the forward gas flow is determined. A short computer program (syringe.bas) given in appendix 5.2 then enables quick calculations of syringe delivery rate to be made given the concentration of analyte in the syringe (drawn from the dilution rig) and the carrier gas flow rate in the forward direction. Throughout the investigations, the reduced mobility K_0 for a particular ion was determined using equation 2.2 (see chapter 2, section 2.4) namely:

$$K_0 \sim \frac{0.1958}{V_{HT}} \times \frac{P}{t_d - t_{ms} - t_f} \text{ cm}^2 \text{ V}^{-1} \text{ s}^{-1} \quad \text{With } V_{HT} \text{ measured in kV, } P \text{ in mbar,}$$

and $(t_d - t_{ms} - t_f)$ in ms.

5.2 Investigation using tertiary butanol in an undoped system

In this detailed experiment to characterize and prove the system further, known concentrations of the analyte were used to produce a total ions spectrum showing ion mobilities for the three peaks typically seen in IMS systems, these being:

- The RIP $\text{H}^+(\text{H}_2\text{O})_n$ where $n = 1$ to 4
- The tertiary butanol monomer $\text{MH}^+(\text{H}_2\text{O})_{n-1}$
- The tertiary butanol dimer $\text{M}_2\text{H}^+(\text{H}_2\text{O})_{n-1}$

Also included in the results is a comparison of the system response with that from some earlier studies made by Bell et. al. on an IMS-QMS system. [127]

Tertiary butanol is also known as 2-methyl-2-propanol and its formula is $(\text{CH}_3)_3\text{COH}$. The analyte sample was injected into the forward flow of the IMS system by piercing a septum with a syringe operated by a variable delivery rate syringe drive in the manner previously described in section 5.1.1.

5.2.1 Determining the flow rate of the syringe drive for a given concentration.

In a saturated mixture, the analyte sample vapour forms from its partial pressure, a concentration of $\frac{P_s}{P_a}$ where P_s is the partial pressure of the sample and P_a is the total pressure of one atmosphere (1013 mBar).

Tertiary butanol has a partial pressure of 41.3 mBar at 20°C. Thus its concentration when its vapour is saturated in air at this temperature is $41/1013 = 40.8 \times 10^{-3}$ or 4.08×10^4 ppmv. If this is the concentration in a syringe, then to get a lower concentration of say, 10 ppbv, a dilution rig can be used. Note, in the dilution rig, the sample pressure is raised to just below its SVP to avoid condensation. After n dilutions of one tenth in the dilution rig, the concentration will fall to $C_n = C_0 \times 10^{-n}$. In ppmv notation, $C_n = C_0 \times 10^{6-n}$ ppmv. For example, two stages of $\div 10$ dilution using the dilution rig could initially be made to reduce the concentration down to 408 ppmv. This would then be followed by injection of the diluted analyte/air mixture into the forward flow of air to the drift tube via a syringe driven by the syringe drive. To determine the syringe drive flow rate applicable for the required final concentration, the formula (derived in appendix A5.1) was used in the computer program 'syringe.bas' (see appendix A5.2). In this case (using a 30 ml volume syringe) the program yielded a low value of 0.1 ml/hour. When initially performing the investigation it was found that the forward flow of air past the sample injection point was extracting the sample at a similarly low rate due to the pressure gradient, as it was observed that even with the syringe drive switched off, some sample was still entering the system. A better solution was then to reduce the concentration in the syringe even further so that a higher syringe drive rate could be used. Using the dilution rig, repeated dilutions were made to yield a final value of 7.9 ppmv in the pressure vessel, from which the sample was drawn off into the syringe via a septum.

5.2.2 Resultant spectra for water clustered tertiary butanol

The carrier gas (pure air of zero grade (99.9999% purity thereby giving <0.1 ppm of hydrocarbon pollutants) was passed through a moisture trap to reduce the moisture content down to approximately 3 ppmv. The forward flow rate was 300 ml/min and the contra flow rate was 500 ml/min. The IMS temperature was maintained at 30°C.

The resulting spectra are shown in the following figures. Initially, spectra were obtained with no sample present to ensure that the mass and ion mass mobility spectra of the water cluster ions were as expected as seen in figures 5.2.1 and 5.2.2.

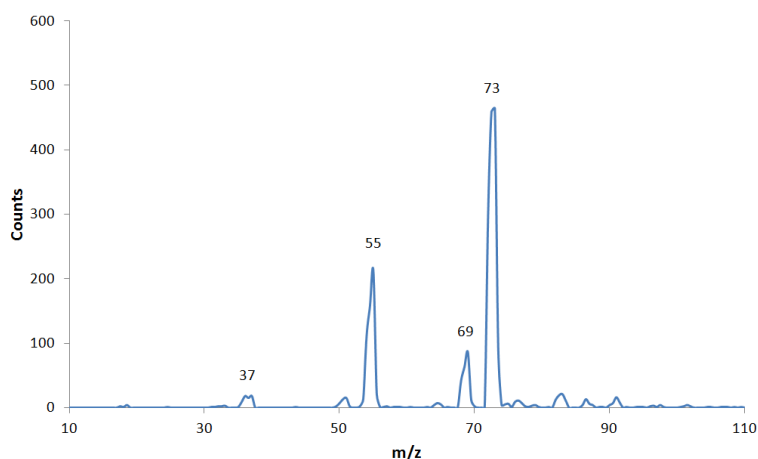


Figure 5.2.1 Mass spectrum for the water RIP $H^+(H_2O)_n$ showing cluster ion peaks at $n = 2$ to 4

In figure 5.2.1, m/z 37, 55 and 73 are due to the expected protonated water clusters $H^+(H_2O)_n$ where $n = 2, 3,$ and 4. The peak at m/z 69 may be due to a trace impurity (e.g. isoprene C_5H_9 m/z 68) present in the newly fitted moisture trap for the carrier gas. (The peak was found to disappear a few days after this experiment). The corresponding RIP in the total ions mass mobility spectrum is shown in figure 5.2.2 following.

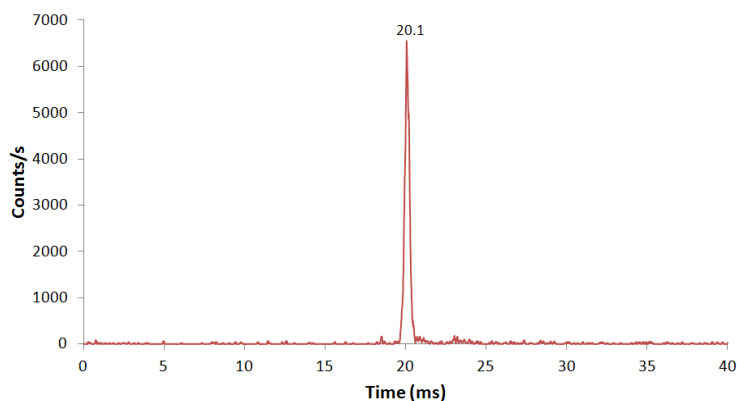


Figure 5.2.2 TIMMS spectrum for the protonated water clusters shown in figure 5.2.1

It is seen in figure 5.2.2 that only one peak (the RIP) due to the protonated water clusters is seen. A low concentration of tertiary butanol was then introduced into the forward flow via a syringe drive. Using a syringe drive delivery rate of 15 ml/hour (corresponding to a concentration of around 16 ppbv) produced the spectrum seen in figure 5.2.3 where the water clusters forming the RIP are depleted as the small concentration of tertiary butanol has reacted with some of them to produce further ions being the:

- protonated hydrated monomers $MH^+(H_2O)$ at m/z 93 and $MH^+(H_2O)_2$ at m/z 111
- protonated dimer M_2H^+ at m/z 149
- protonated hydrated dimer $M_2H^+(H_2O)$ at m/z 167

where M represents the tertiary butanol analyte molecule $(CH_3)_3COH$.

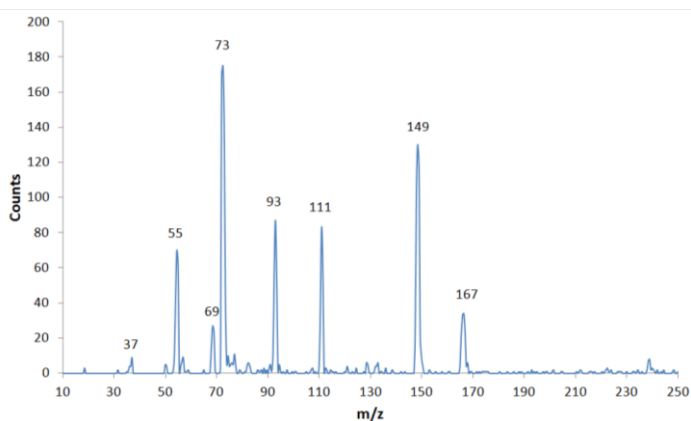


Figure 5.2.3 Mass spectrum with tertiary butanol injected at a rate of 15 ml/hour

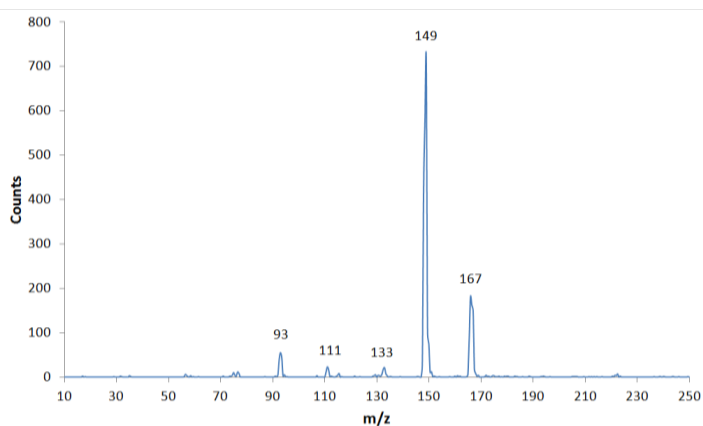


Figure 5.2.4 Mass spectrum with tertiary butanol injected into the forward flow at a rate of 20 ml/hour

Figure 5.2.4 shows the mass spectrum when the concentration was increased by 33% when setting the syringe delivery rate to 20 ml/hour. Virtually all of the reactant ions are used up and the system is said to be saturated. The effect is to produce a broad peak in the total ions mass mobility spectrum as seen in figure 5.2.5. The peak at m/z 133 in figure 5.2.4 is assumed to result from an impurity.

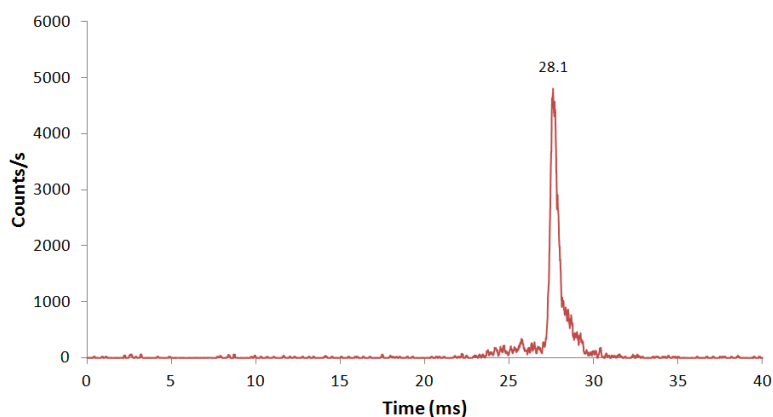


Figure 5.2.5 Total ions mass mobility spectrum with syringe rate set at 20 ml/hour

Reducing the syringe flow rate back to 15 ml/hour resulted in a mobility spectrum which contains the RIP, protonated monomer and protonated dimer ions as shown in figure 5.2.6.

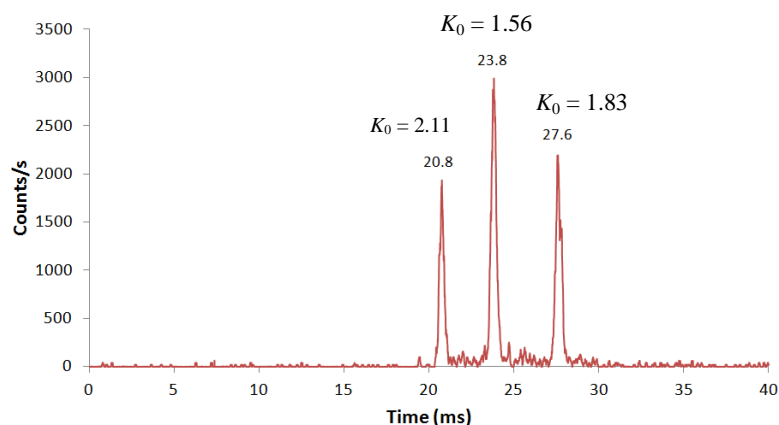


Figure 5.2.6 Total ions mass mobility spectrum with syringe rate set at 15 ml/hour

Figure 5.2.6 shows a mobility spectrum with the preferred proportions of ion peaks that aid in the identification of a chemical. (More information is present to provide a better ‘fingerprint’ than in the case of figure 5.2.5). In order to identify which ions are in the peaks, tuned (or ‘selected’) mass mobility spectra were obtained for each of the dominant m/z peaks shown in figure 5.2.3, with the syringe delivery rate set to 15 ml/hour. The corresponding spectra are shown in figures 5.2.7 to 5.2.13 below. Note, the concentration of tertiary butanol in the forward flow at this setting is approximately 16 ppbv showing that the system is very sensitive.

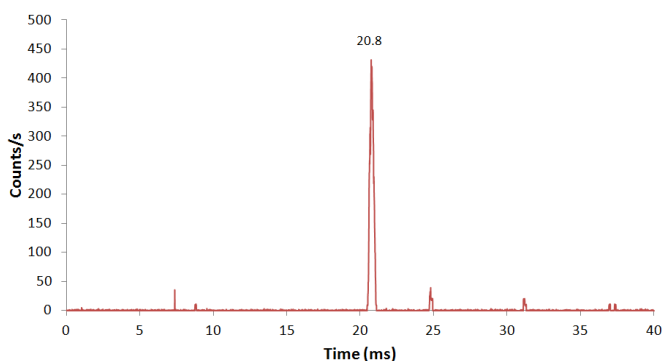


Figure 5.2.7 Selected mass ion mobility spectrum for m/z 55, $H^+(H_2O)_3$

Figure 5.2.7 confirms that the protonated water cluster $\text{H}^+(\text{H}_2\text{O})_3$ m/z 55 component of the RIP occurs at 20.8 ms

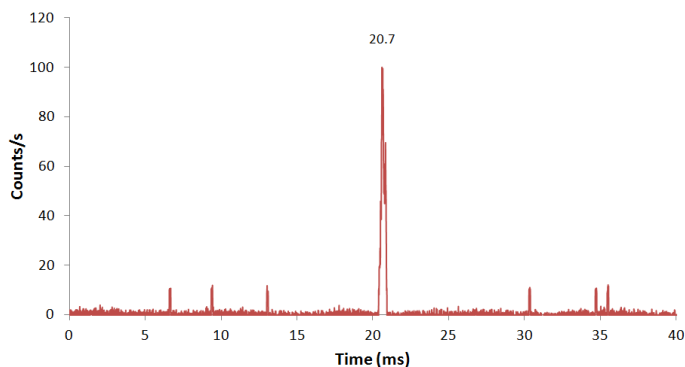


Figure 5.2.8 Selected mass ion mobility spectrum for m/z 69, (impurity)

The peak shown in figure 5.2.8 corresponding to m/z 69 although occurring at a time similar to the RIP is considered to be due to an impurity, possibly isoprene having protonated m/z of 69. Figure 5.2.9 below for m/z 73 which is the protonated water cluster $\text{H}^+(\text{H}_2\text{O})_4$ confirms that the RIP is at 20.8 ms since it coincides with that for m/z 55 (but with a higher count rate) indicating that the water clusters are constantly switching along the drift region. It is also seen from figure 5.2.3, that m/z 73 is the dominant water cluster ion.

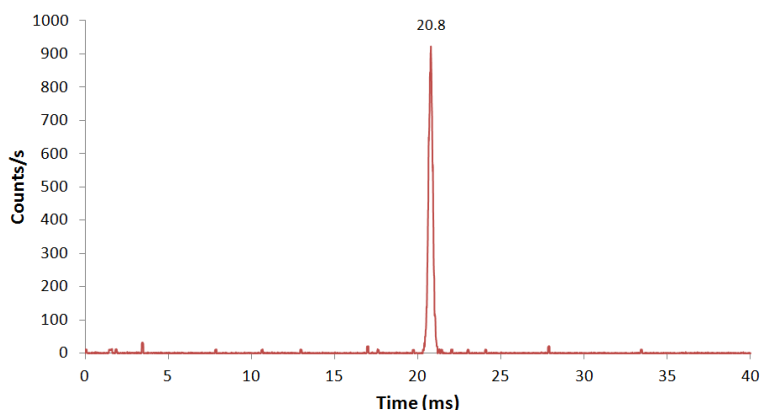


Figure 5.2.9 Selected mass ion mobility spectrum for m/z 73, $\text{H}^+(\text{H}_2\text{O})_4$

Figures 5.2.10 and 5.2.11 show that the protonated monomers of t.b. with interchanging water cluster sizes (H_2O and $(\text{H}_2\text{O})_2$) occur at similar times.

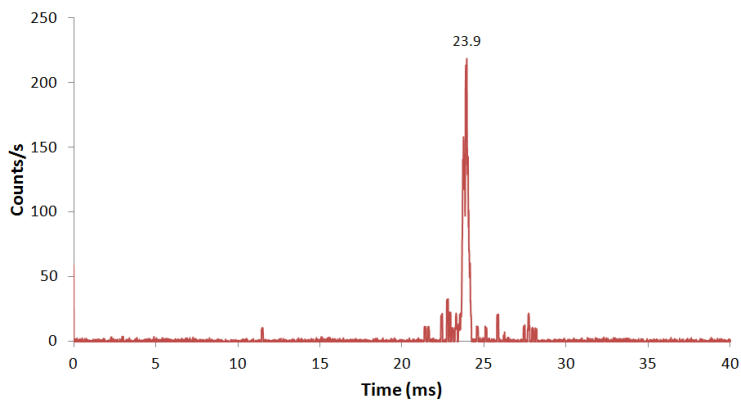


Figure 5.2.10 Selected mass ion mobility spectrum for m/z 93, $\text{MH}^+(\text{H}_2\text{O})$

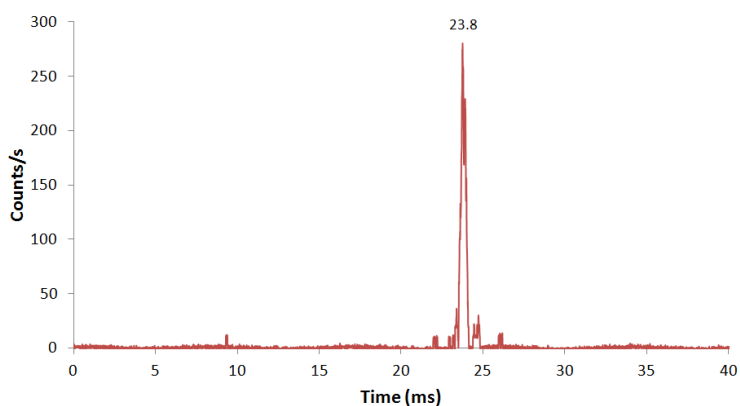


Figure 5.2.11 Selected mass ion mobility spectrum for m/z 111, $\text{MH}^+(\text{H}_2\text{O})_2$

Figures 5.2.12 and 5.2.13 show that the protonated dimer and the protonated hydrated dimer occur at similar times, again indicating that the water cluster H_2O is attaching and detaching with the t.b. dimer along the drift tube.

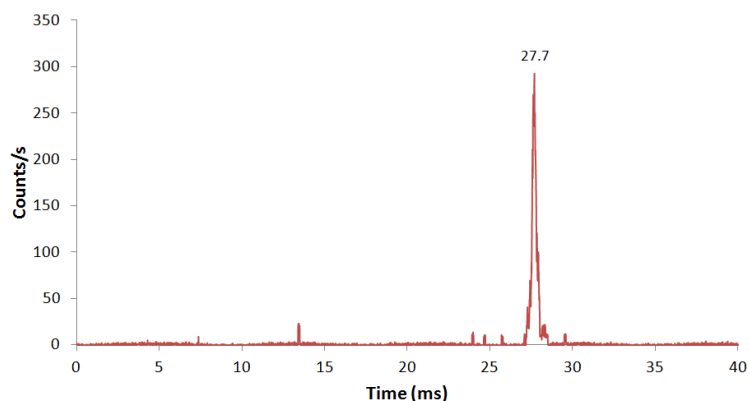


Figure 5.2.12 Selected mass ion mobility spectrum for m/z 149, M_2H^+

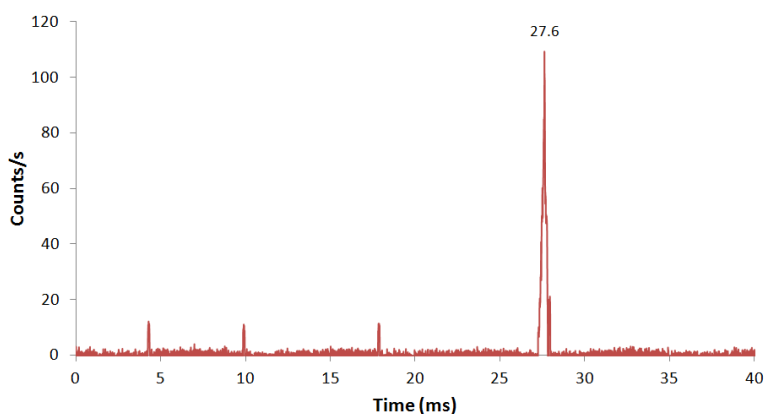


Figure 5.2.13 Selected mass ion mobility spectrum for m/z 167, $M_2H^+(H_2O)$

Figure 5.2.14 reproduces the IMS spectrum that Bell et.al. [127] obtained for tertiary butanol and comparing this with figure 5.2.6 it is seen that the clarity of the peaks from our system shows a distinct improvement. Figure 5.2.15 shows their tuned mass ion mobility spectra can be compared directly to figures 5.2.10 to 5.2.12 obtained from our system, again showing significantly improved results. In figures 5.2.14 and 5.2.15, tertiary butanol is identified as ROH where R refers to the CH_3 methyl group within the molecule.

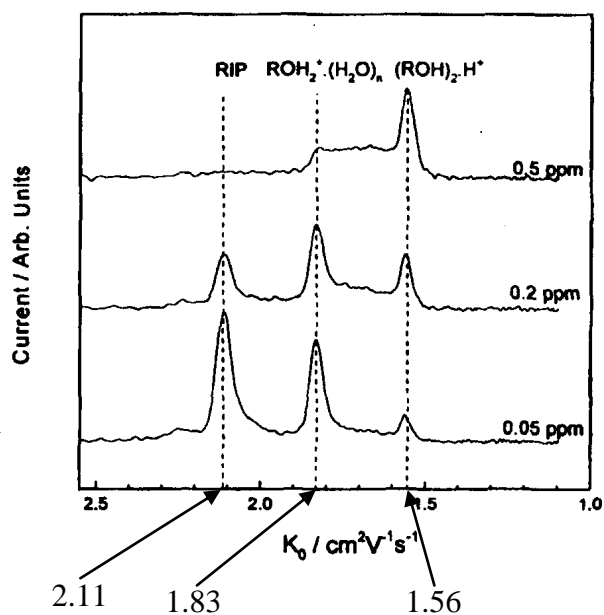


Figure 5.2.14 IMS spectra for tertiary butanol from earlier studies [48]

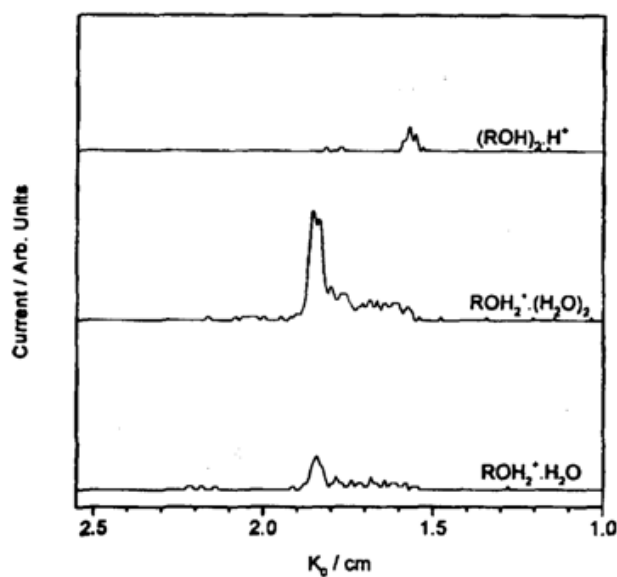


Figure 5.2.15 Tuned mass ion mobility spectra for tertiary butanol from earlier studies [48]

5.2.3 Reduced mobilities

From the results obtained using the SIMMS program, the drift time of the peaks may be converted into reduced mobilities using equation 2.2. Note, only 0.3 ms is subtracted from the drift times to take account of the transit time of the ions through the mass spectrometer, as

the reconstruction filter was switched out. The operating conditions were $P = 1014$ mbar, with $V_{HT} = 4.5$ kV and the moisture content in the air at 3 ppmv.

For the $H^+(H_2O)_n$ water RIP, $t_d = 20.8 - 0.3$ ms and therefore $K_o = 2.11$ cm²/Vs.

When introducing tertiary butanol the drift time of the monomer $MH^+(H_2O)_n$ was at 23.5 ms corresponding to a K_o of 1.85 cm²/Vs. A dimer $M_2H^+(H_2O)_n$ occurred at 27.3 ms giving a K_o of 1.56 cm²/Vs. When comparing these values with those obtained by Bell as shown in figure 5.2.14, it is seen that they are in close agreement.

5.3 Investigation using acetone (Ac) in an undoped system

The chemical formula for acetone is CH_3COCH_3 and so its mono-isotopic nominal protonated mass is 59 Da. In this experiment the sample concentration range covered was from roughly 10 ppbv to 1 ppmv. In order to obtain these low concentrations the dilution rig was again used to provide an initial low concentration that was followed by injection of the diluted acetone/air mixture into the forward flow of air to the drift tube via a syringe drive. The rate of delivery from the syringe drive was adjusted in order to provide the final concentration required.

5.3.1 Determining the flow rate of the syringe drive

Using the Antoine equation [128,129] (see appendix A5.7) at 22 °C the partial pressure of Acetone is 272.6 mbar, thus (assuming standard atmospheric pressure) when a sample was prepared in pure air within a syringe containing a wad of cotton wool soaked in acetone the initial concentration would be $272.6 \div 1013 = 0.269$. However, on this occasion, a sample vial containing liquid acetone was fixed to the inlet of the dilution rig (see appendix A5.4, figure A5.1) and after several dilutions a final concentration of 85 ppmv in pure air was obtained. This was then expelled into a 30 ml glass syringe. The syringe drive flow rate

applicable for the required final concentration was again determined using the program 'syringe.bas'.

5.3.2 Resultant spectra for acetone

Before starting the experiment, as an initial check, the water RIP was recorded and found to be as seen in previous experiments.

The sample was then introduced via a septum into the forward flow. A low concentration of acetone of about 85 ppbv was present in the forward flow when adjusting the syringe flow rate to 15 ml/hour. The corresponding mass spectrum is shown in Figure 5.3.1

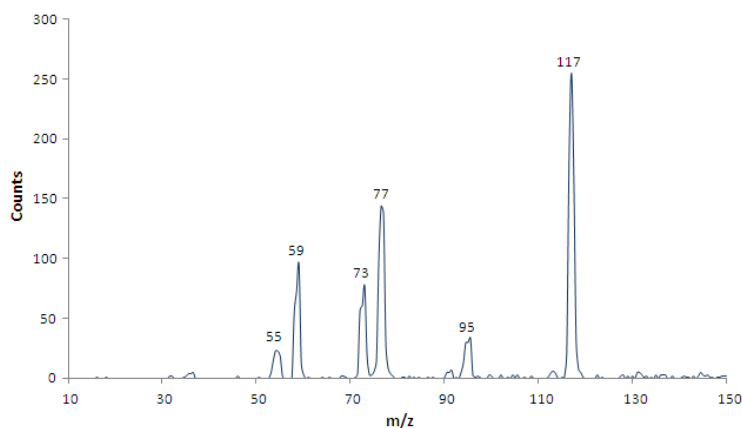


Figure 5.3.1 Mass spectrum for acetone sample at 85 ppbv in pure air

Table 5.3.1 Mass assignments for the peaks seen in figure 5.3.1

m/z	55	59	73	77	95	117
ions	W ₃ ⁺	Ac ⁺	W ₄ ⁺	AcW ⁺	AcW ₂ ⁺	Ac ₂ ⁺

Ac = Acetone, W = Water, + refers to protonation (H⁺)

From table 5.3.1 it can be seen that the spectrum shows peaks corresponding to water clusters, acetone and hydrated acetone. A TIMMS spectrum was then obtained as shown in

figure 5.3.2 in order to see the temporal relationship between the m/z components. This shows ion mobilities for the three peaks:

- The RIP $\text{H}^+(\text{H}_2\text{O})_n$ where $n = 2$ to 4 (as determined from figure 5.2.1)
- The acetone monomer $\text{Ac H}^+(\text{H}_2\text{O})_{n-1}$
- The acetone dimer $\text{Ac}_2 \text{H}^+$

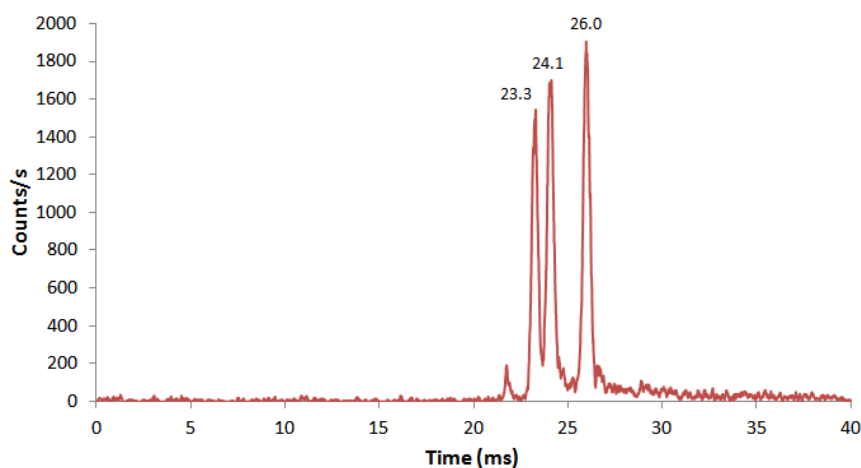


Figure 5.3.2 Total ions mass mobility spectrum at a syringe rate of 15 ml/hour

The assignments of the peaks are shown in table 5.3.2. The small peak appearing at about 22 ms is due to a slight impurity present in the system (which was also seen when initially checking the RIP before sample introduction).

$t_f = 0$ since the reconstruction filter was not used and $t_{ms} = 0.3$ ms.

The tube pressure $P = 1018$ mbar.

Table 5.3.2 Ion assignments for the peaks shown in figure 5.3.2

Drift time (ms)	Reduced mobility K_0 (cm^2/Vs)	Component
23.0	2.16	Water RIP
23.8	2.09	Hydrated monomer
25.7	1.94	Dimer

Confirmation of the peak assignments (other than known water cluster ions at m/z 55 and 73) was made by taking selected ion mass mobility spectra, as summarised in table 5.3.3.

Table 5.3.3 Temporal values of the masses shown in Figure 5.3.1

m/z	Drift time (ms)	Mass assignment	Identity
59	24.1 and 26.0	Ac^+	Monomer
77	24.1	AcW^+	Hydrated monomer
95	24.1	AcW_2^+	Hydrated monomer
117	26.0	Ac_2^+	Dimer

At a higher concentration where a dimer is formed it is seen in figure 5.3.3 that two peaks occur at m/z 59. The peak at 24.1 ms is due to the acetone monomer whereas that at 26.0 ms can be attributed to dissociation of the protonated dimer in the region of the interface between the high pressure IMS and the low pressure QMS.

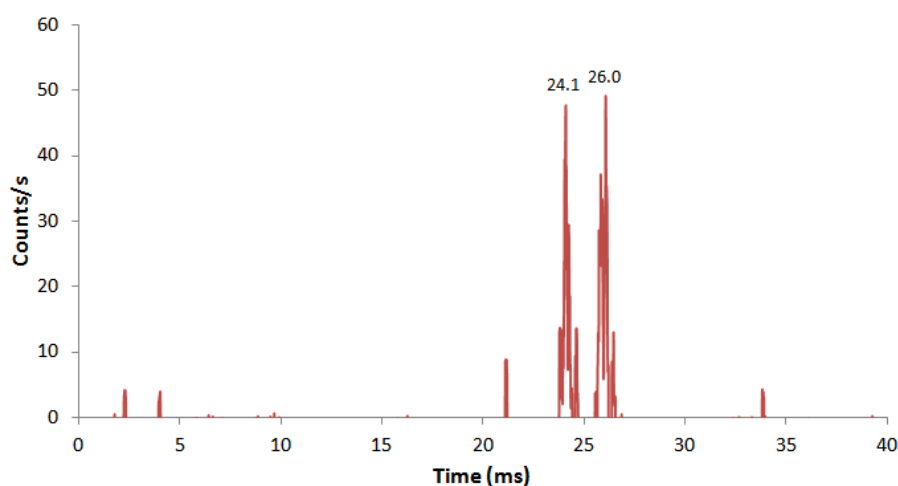


Figure 5.3.3 Selected ion mass mobility spectrum at m/z 59 with dimer present

In an earlier acetone investigation made by Watts [130] the reduced mobility values obtained are summarised in table 5.3.4 in comparison with our values. It is seen that although they fall within 5 % of each other, this is outside the commonly accepted range of $\pm 2\%$ between

different IMS systems [131]. The reason for this must be due to drift since in the tertiary butanol investigation, our values of K_0 were seen to be in excellent agreement with those of Bell et.al. [127] who used the same apparatus as Watts [130]. Using the then obtained value of $K_0 = 2.11$ for the RIP, Watts's value of 2.08 is 1.4% below, indicating drift within their system. Our value of 2.16 is 2.36% above, again indicating a drift problem (which was later cured – see appendix A4.13).

Table 5.3.4 Results from an acetone study made by Watts [51]

Component	Reduced mobility K_0 (cm^2/Vs) from present study	Reduced mobility K_0 (cm^2/Vs) According to Watts	Deviation %
Water RIP	2.16	2.08	3.7
Hydrated monomer	2.09	2.01	3.8
Dimer	1.94	1.85	4.6

An excess of sample was then introduced such that it caused saturation (loss of RIP) as seen in figure 5.3.4.

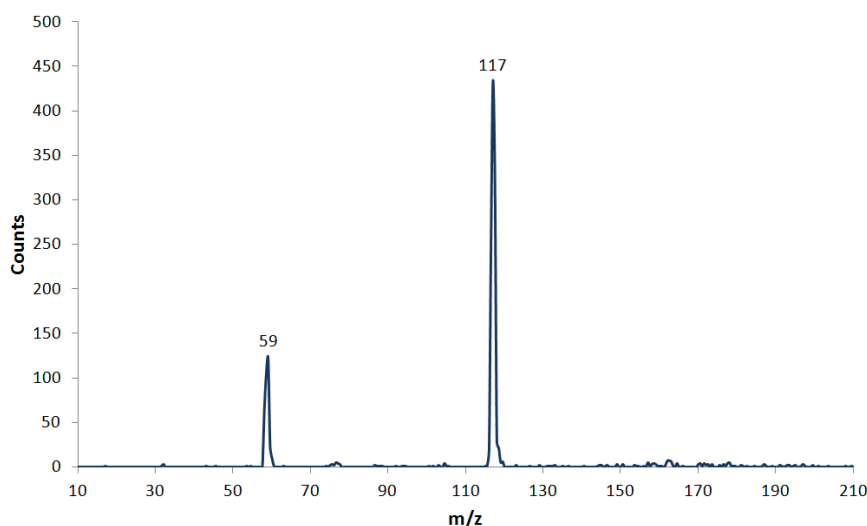


Figure 5.3.4 Mass spectrum obtained at a higher concentration of acetone

Here, it is seen that the protonated dimer is the dominant peak. A TIMMS spectrum was then taken as shown in figure 5.3.5 where it is seen that the concentration has progressively increased so that only the protonated dimer is now present.

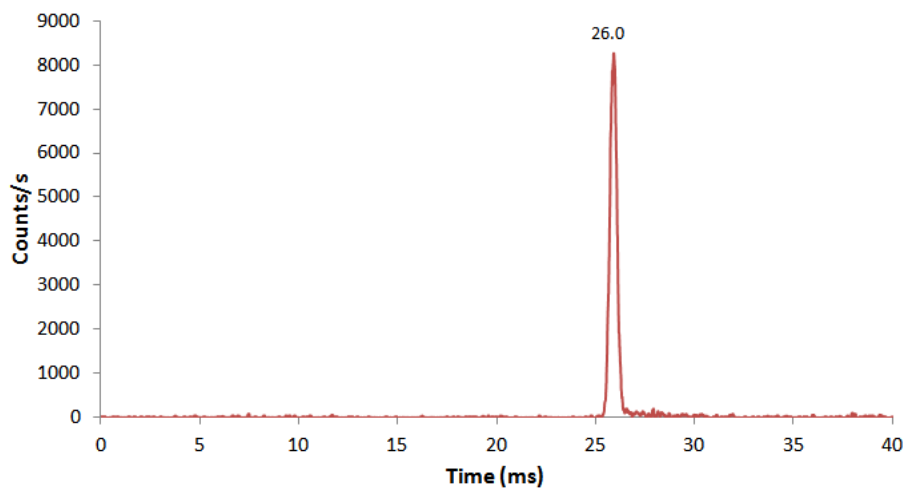


Figure 5.3.5 Total ions mass mobility spectrum showing presence of the protonated acetone dimer only with high sample concentration

SIMMS spectra appropriate to this condition show dissociation at m/z 59 (290 counts/s) in figure 5.3.6 and a strong arrival peak (1300 counts/s) for the dimer in figure 5.3.7

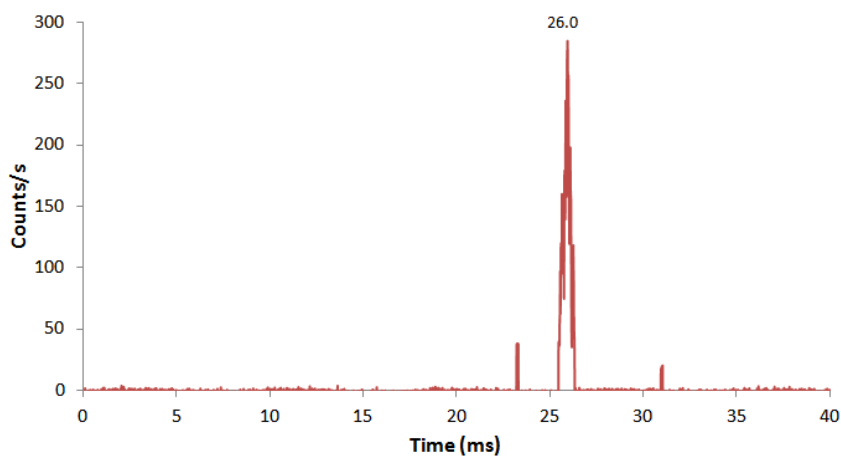


Figure 5.3.6 showing dissociation of the protonated acetone dimer at m/z 59, no monomer is seen

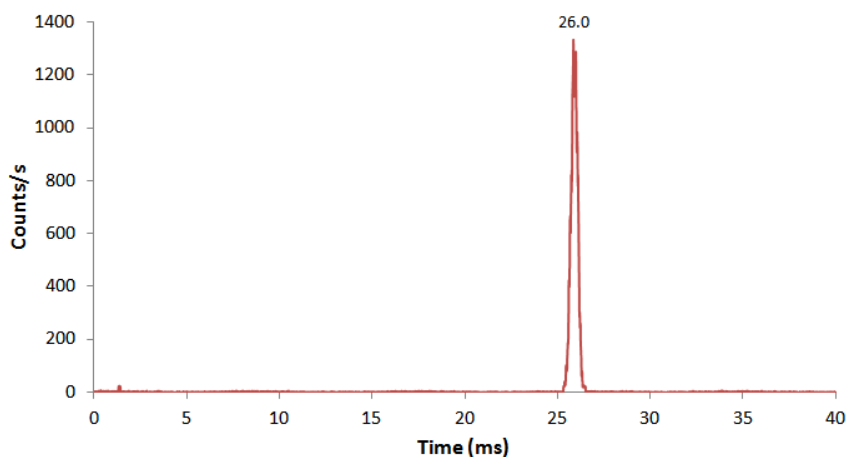


Figure 5.3.7 showing the majority of the dimer at m/z 117

5.4 Investigation using diacetone in an undoped system

Also known as 4-methyl-2-Pentanone, 4-hydroxy, the molecular formula for diacetone is $C_6H_{12}O_2$ and so it has a protonated mass of 117 Da. Using the Antoine equation with coefficients obtained from the NIST [102] web site, it is seen that diacetone has a significantly lower partial pressure (1.96 mbar at 22°C) than that of acetone (272.6 mbar at 22°C) and so appropriately less sample dilution was made, again using the dilution rig.

As a check on the system, a TIMMS spectrum was initially obtained in the absence of sample, and the results were as expected. Mass spectra were then taken at two levels of sample concentration with the corresponding results shown in figures 5.4.1 and 5.4.2.

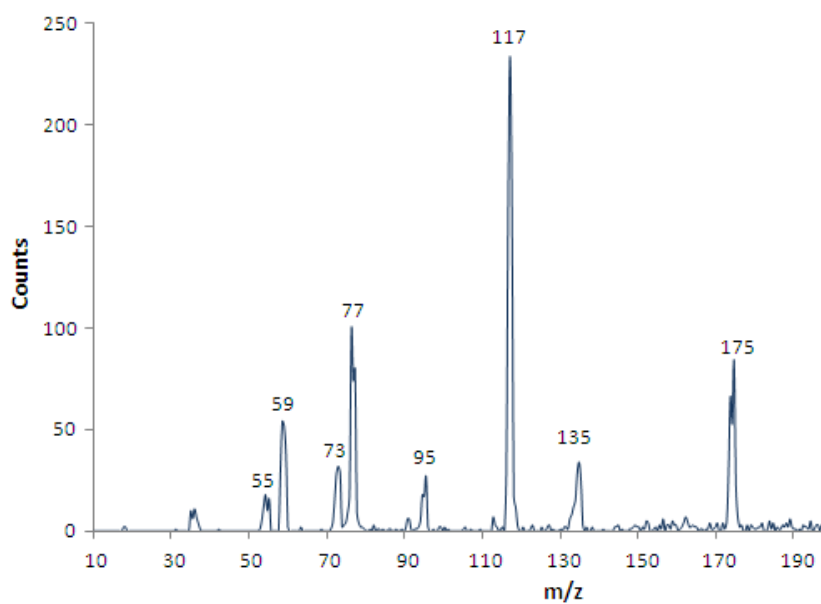


Figure 5.4.1 Mass spectrum of diacetone at low concentration

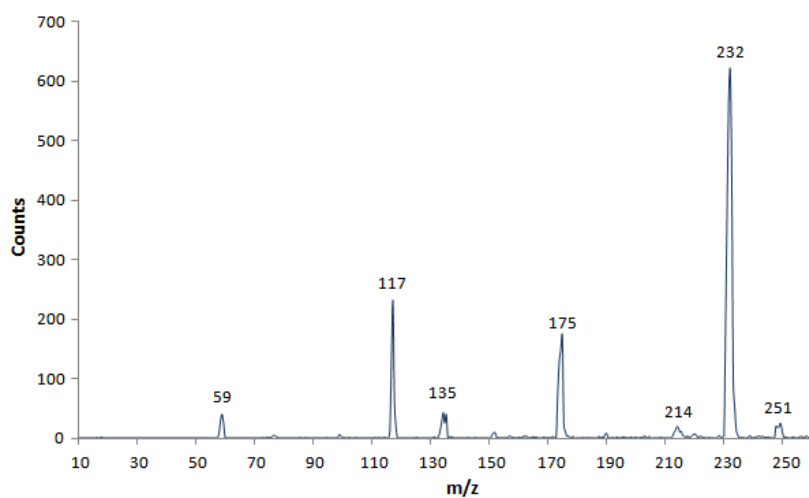


Figure 5.4.2 Mass spectrum of diacetone at higher concentration producing a dimer

From the masses seen, table 5.4.1.gives the chemical assignment for the ions where;

W = water (H₂O), Ac = acetone, M = diacetone, + means protonated (i.e. H⁺)

Table 5.4.1 Ion mass assignments

m/z	55	59	73	77	95	117	135	175	233	251
ion	W_3^+	Ac^+	W_4^+	AcW^+	AcW_2^+	M^+	MW^+	Ac_3^+	M_2^+	M_2W^+

Total ions mass mobility spectra were also taken at similar extremes of concentration as shown in figures 5.4.3 and 5.4.4.

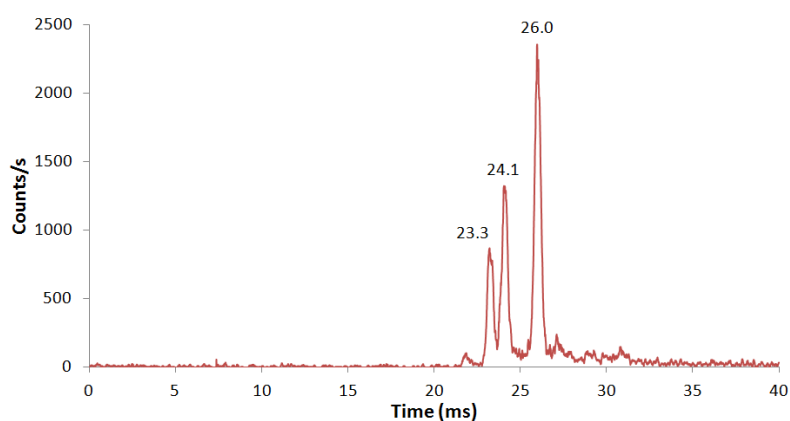


Figure 5.4.3 TIMMS spectrum at lower diacetone concentration with absence of dimer

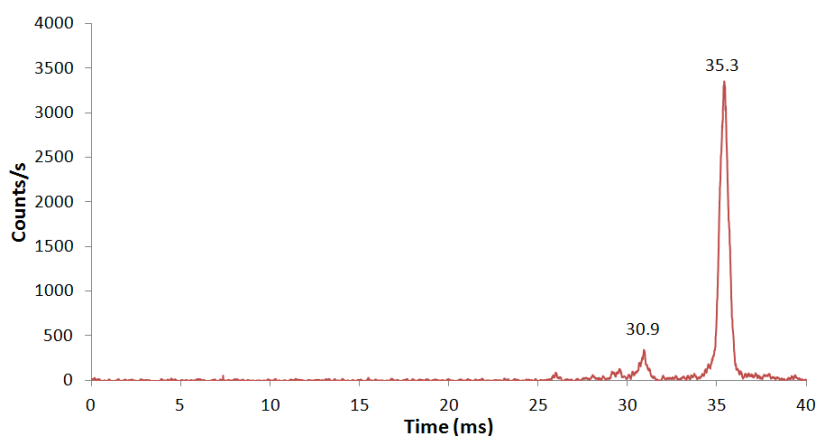


Figure 5.4.4 TIMMS spectrum at higher concentration of diacetone showing predominance of dimer

To determine which ions are present in the TIMMS peaks, SIMMS spectra were taken at the masses shown in table 5.4.1. From the SIMMS spectra, table 5.4.2 allocates the drift times to each mass.

Table 5.4.2 Drift times for selected ion masses

m\z	59	73	77	95	117	135	175	233
t_d (ms)	26.0	23.3	24.1	24.1	26.0	27.3	30.9	35.3

Considering the drift times shown in table 5.4.2, it is seen that ions at m/z 59 and m/z 117 both appear at the same time, although as is seen in figure 5.4.1, the intensity at m/z 117 is much higher. The ions at m/z 59 can be accounted for as being due to CID of the diacetone ions in the IMS-QMS interface causing them to break up. Relating the drift times of the other ions to the peaks seen in the TIMMS spectra allows them to be described as given in table 5.4.3. The drift times also agree with those shown in table 5.3.3 in the previous investigation using acetone (as would be expected under the same atmospheric conditions).

Table 5.4.3 Ion mass assignments for the peaks shown in the TIMMS spectra of figures 5.4.3 and 5.4.4

(VHT = 4 kV, P = 1018 mbar)

td (ms)	23.3	24.1	26.0	30.9	35.3
ions	H ⁺ (H ₂ O) _n	H ⁺ (H ₂ O) _n Ac	H ⁺ (M)	H ⁺ (Ac) ₃	H ⁺ (M) ₂
K₀ cm²/Vs	2.16	2.09	1.94	1.63	1.42

The peaks at 24.1 and 30.9 ms are due to an acetone component. This may probably have formed as a product of the diacetone sample when in the ionisation region of the drift tube. Since the TIMMS spectrum for water only (initially obtained in the absence of sample, showed only the water RIP and a small contaminant at a lower drift time, this indicates that there was no acetone left over in the system from the previous investigation).

5.5 Investigation using DPGME in an undoped system

Introduction

Dipropylene glycol methyl ether is a commercial solvent and is a mixture of four geometric isomers two of which are in dominant proportions. The structures of these two are shown in the figures 5.5.1 and 5.5.2 below.

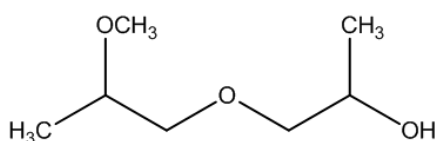


Figure 5.5.1 Molecular structure of DPM(A)

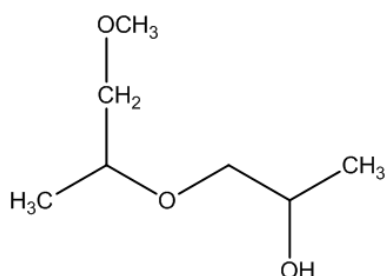


Figure 5.5.2 Molecular structure of DPM(B)

Its structural formula is $\text{CH}_3(\text{OCH}_2\text{CH}_2)_2\text{OH}$ giving its nominal mass as 148 and so when protonated, its m/z will be 149.

DPM(A) is present in 40-45% and DPM(B) in 40-50% with the remainder comprising the minor isomers. An important use of DPGME is also as a ‘confidence tester’ when sprayed into the inlet port of an IMS detector in order to test the detection capability of the system. In this case it acts to safely provide a peak in the ion mobility spectrum occurring at a similar drift time to that of an organophosphate nerve agent. There does not appear to be any studies made on the ion-molecule reactions occurring in an IMS-MS system and so this surprisingly represents the first time that the reaction processes have been reported.

The operating conditions during the experiment were tube pressure $P = 1002$ mbar, tube temperature $T = 303$ K, with the voltage applied to the drift tube $V_{\text{HT}} = 4.0$ kV.

Resultant spectra for DPGME

Figure 5.5.3 shows the TIMMS spectrum obtained when a high concentration of sample was present. It is seen that the system is 'saturated' as the RIP is completely removed.

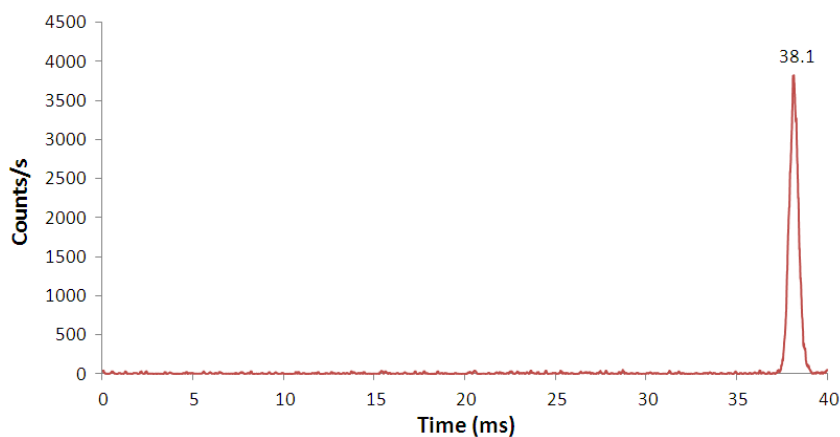


Figure 5.5.3 TIMMS spectrum at high concentration of DPGME

The mass spectrum as seen in figure 5.5.4 shows a dominant peak at m/z 297 indicating that the peak seen in figure 5.5.3 is comprised of the proton bound dimer. A small peak at m/z 149 is also seen that corresponds to the protonated monomer. SIMMS spectra were taken at these masses as shown in figures 5.5.5 and 5.5.6. Interestingly they both appear at the same drift times. This indicates that the peak seen at m/z 149 is due to CID of the protonated dimer in the interface between the IMS and QMS regions. The other small peak appearing at m/z 315 is due to a water cluster attaching to the dimer. (Table 5.1.1 shows the ion mass assignments.)

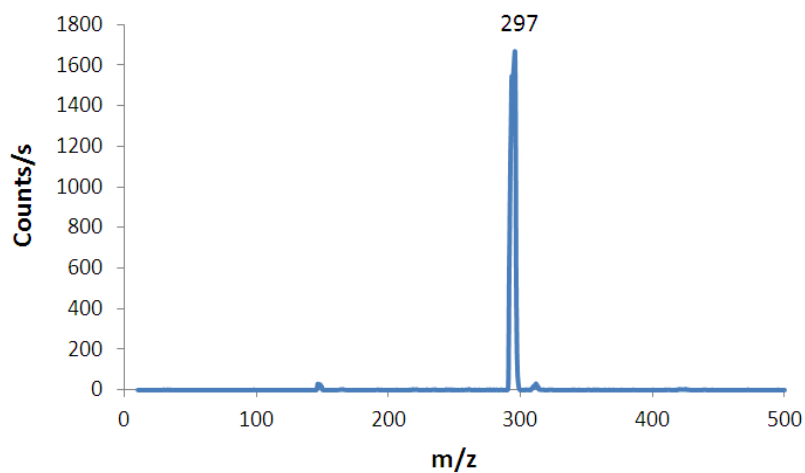


Figure 5.5.4 Mass spectrum for DPGME showing that dimer is dominant

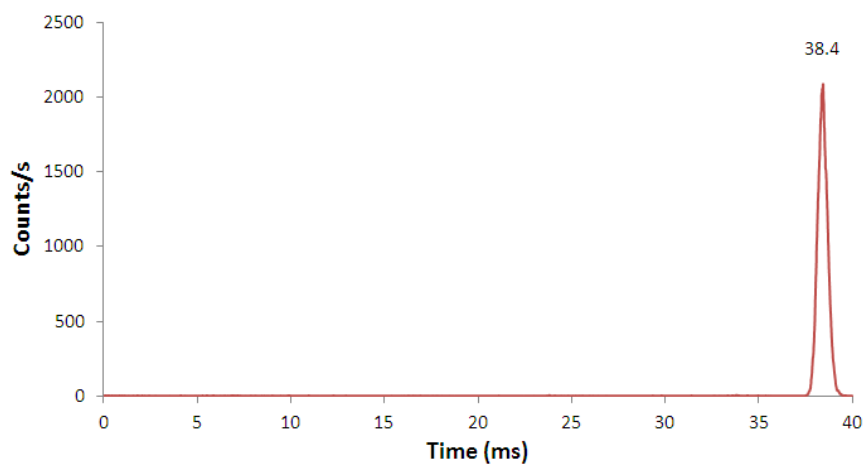


Figure 5.5.5 SIMMS for DPGME showing drift time at m/z 297

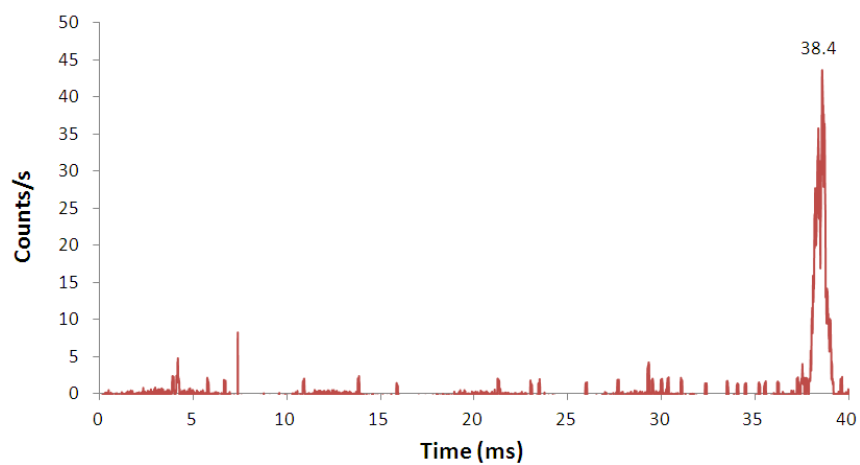


Figure 5.5.6 SIMMS showing drift time of DPGME at m/z 149

Spectra were then taken at a sufficiently low concentration to give the characteristic three peaks in the TIMMS spectrum as seen in figure 5.5.7.

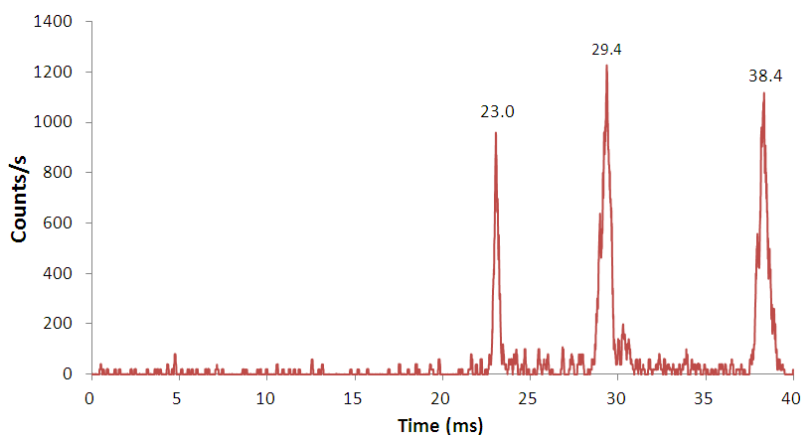


Figure 5.5.7 TIMMS spectrum at a lower analyte concentration of DPGME

The mass spectrum corresponding to this is given in figure 5.5.8

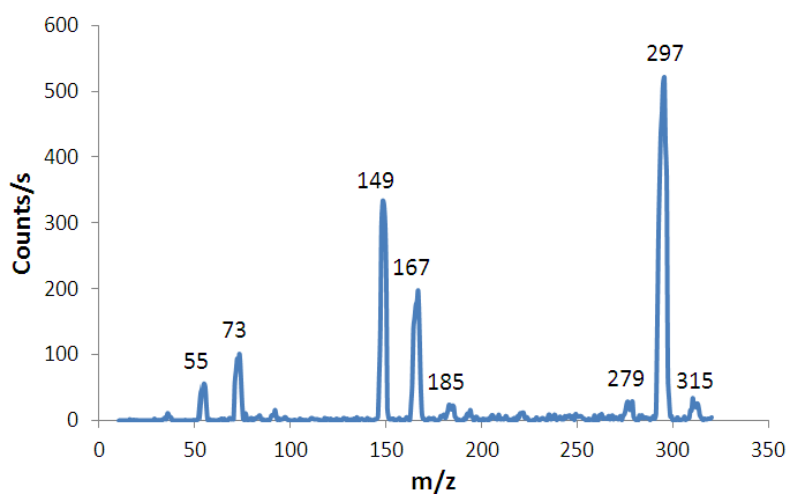


Figure 5.5.8 Mass spectrum of DPGME at lower concentration

Table 5.5.1 gives the chemical assignments to each of the masses seen in the spectrum of figure 5.5.8 (apart from the well known water cluster ions at m/z 55 and 73).

Table 5.5.1 Ion mass assignments

m/z	149	167	185	279	297	315
Assignment	MH ⁺	MH ⁺ (H ₂ O)	MH ⁺ (H ₂ O) ₂	[M ₂ -H ₂ O]H ⁺	M ₂ H ⁺	M ₂ H ⁺ (H ₂ O)

The peak seen at m/z 279 was unexpected as it corresponds to a loss of water from the dimer, whereas only water adducts had been seen in the previous investigations we have made using other analytes. However, looking at figures 5.5.1 and 5.5.2 it is seen that there are three sites in the molecule where oxygen is located, and a proton could (more favourably) attach to the hydroxyl (OH) group to exothermically form H₂O, the energy being released by the resulting loss of water.

Spectra were then taken as the concentration diminished further such that the dimer was diminished, as seen in figures 5.5.9 and 5.5.10.

Figure 5.5.9

Total Ions Mass mobility spectrum at diminishing concentration of DPGME

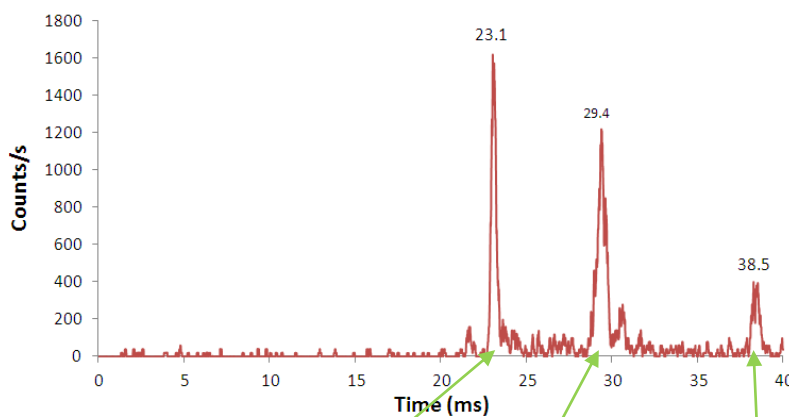
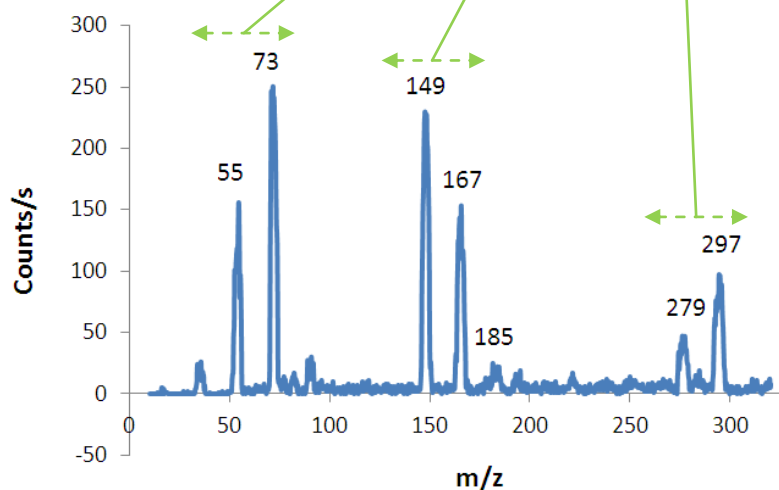


Figure 5.5.10

Mass spectrum at diminishing concentration of DPGME



A further set of spectra were then obtained as the concentration of analyte reduced to a level where the RIP became dominant as shown by figures 5.5.11 to 5.5.13.

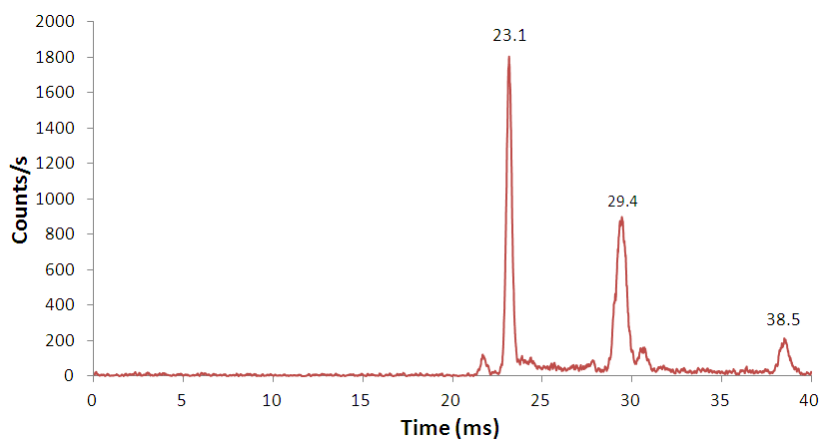


Figure 5.5.11 TIMMS showing dominant RIP at 23.1 ms

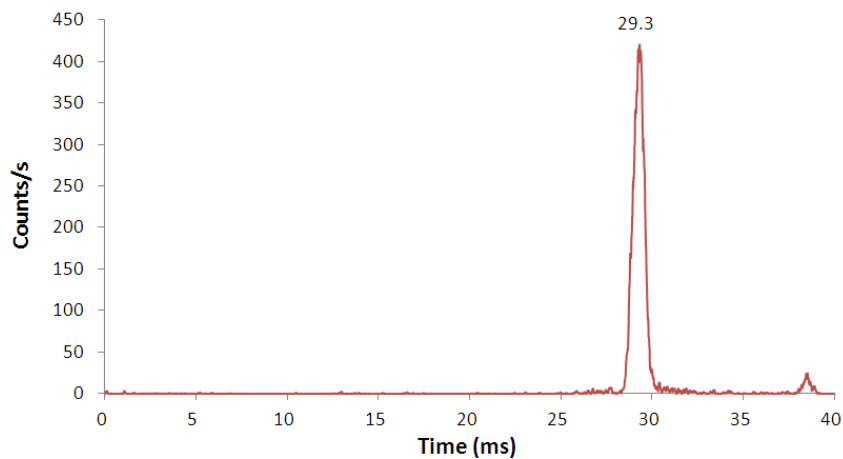


Figure 5.5.12 SIMMS for DPGME at m/z 149

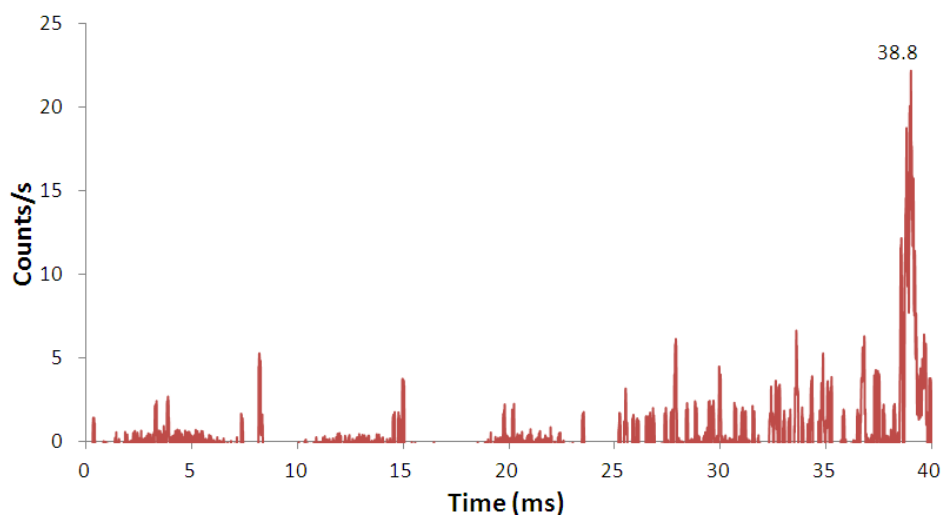


Figure 5.5.13 SIMMS for DPGME at m/z 279

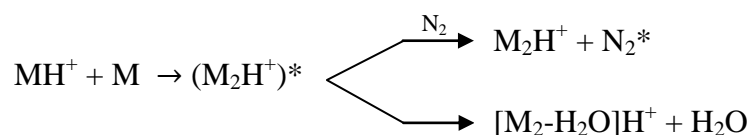
By using the results from the selected ions mobility spectra shown in figures 5.12, 5.13 and 5.5, at m/z 149, 279 and 297 respectively, the reduced mobilities were calculated and are summarised in table 5.5.2. When taking the SIMMS spectrum at m/z 279 as seen in figure 5.5.13, the peak has a very low count rate of 23 counts/s which is approaching circuit noise levels, and so the value of its drift time is approximate in this case.

Table 5.5.2 Ion assignments summarizing the results from the DPGME investigation

m/z	td	K_0	Identity
149	29.3	1.69	MH^+
279	38.8	1.27	$[M_2-H_2O]H^+$
297	38.4	1.29	M_2H^+

After the initial appearance of the protonated monomer MH^+ , a sufficiently high concentration of M allows the process to continue to form the excited proton bound dimer. This can then lose energy through a three body process of collisional stabilization with N_2 to leave the dimer M_2H^+ , which is the dominant channel. In addition (as seen in table 5.5.1 at m/z 279) there is also a small branching ratio associated with a bimolecular channel resulting in the loss of H_2O from the $(M_2H^+)^*$ complex.

i.e.



5.6 Summary and review

A review of the results from the experiments is given in table 5.5.3 below. Where possible, the hydrated product ions are not included, since the mobilities of the protonated analyte ions are mainly of interest.

Table 5.5.3 Listing of ions obtained when operating the IMS in the positive ion mode with their results

Compound	Product ions	Mass (m/z)	K_0 (cm^2/Vs)
Clean air	RIP $\text{H}^+(\text{H}_2\text{O})_n$	19, 37, 55, 73	2.11
Tertiary butanol (t.b.)	$\text{MH}^+(\text{H}_2\text{O})_n$	93	1.85
	M_2H^+	149	1.56
Acetone (Ac)	$\text{AcH}^+(\text{H}_2\text{O})_n$	59	2.09
	Ac_2H^+	117	1.94
Diacetone (DiAc)	DiAcH^+	117	1.94
	DiAc_2H^+	233	1.42
Dipropylene glycol methyl ether (D _{PGME})	$(\text{D}_{\text{PGME}})\text{H}^+$	149	1.69
	$(\text{D}_{\text{PGME}}\text{-H}_2\text{O})\text{H}^+$	279	1.27
	$(\text{D}_{\text{PGME}})_2\text{H}^+$	297	1.29

Chapter 6 CHARACTERISATION OF THE IMS-QMS SYSTEM IN NEGATIVE ION MODE

6.1 Introduction

This chapter complements chapter 5 in that it describes investigations made using the negative ion mode of operation again using clean air as the carrier gas. This mode is more suited to the detection of explosive threat agents since their proton affinities (PA) are generally less than the PAs for $(\text{H}_2\text{O})_n$ ($n \geq 2$) and so are not able to be detected in the positive ion mode. However, they readily react with negative ions.

The analytes used in the present investigations were:

- methyl salicylate (MS) – used as a safe confidence tester in IMS systems for detection of nerve agents.
- 1,3 dinitrobenzene (1,3 DNB) – used in the manufacture of explosives, solvents and dyes.
- 2,4 dinitrotoluene (2,4 DNT) – used in the manufacture of TNT and polyurethane foams.
- 2,6 dinitrotoluene (2,6 DNT) – similar characteristics to 2,4 DNT but is less used.
- 1,3,5 trinitrobenzene (1,3,5 TNB) – used as a high explosive in commercial mining.
- 2,4,6 trinitrotoluene (2,4,6 TNT) – used as a high explosive and as the standard measure of explosive power.
- hexachloroethane – used as a dopant in IMS detectors to generate Cl^- ions in order to enhance selectivity (used here in conjunction with the TNT investigation).

Initially the spectra of the RIP were recorded, followed by investigations using the above compounds. Two of the compounds (MS and 1,3-DNB) to our knowledge have not previously been investigated on an IMS-MS system and so the results from these are new.

In chapter 5, headspace from a syringe was the chosen method to introduce analyte into the system. However, due to the low volatility of explosives, in the following experiments the

headspace from a heated vial containing a small sample of the analyte is used to interface with the forward flow entering the ionisation region of the drift tube.

6.2 Ion spectra observed in clean air using the present system

The following procedures allow a comparison to be made with the ions seen in the present system and those obtained by Spangler and Carr [109,110] shown in table 1.2 of chapter 1 and for convenience, given again in this chapter. After putting the mass spectrometer into negative ion mode (see appendix A6.1 for the connection diagram) the voltages on the electrostatic lenses were adjusted in order to provide optimum sensitivity, the values being given in appendix A4.6.

The operating conditions of the drift tube were: $V_{HT} = 4 \text{ kV}$, $P = 1012 \text{ mbar}$ and $T = 30^\circ\text{C}$

A total ions mobility spectrum (see figure 6.2.1) was obtained using the TIMMS program.

It was thought that the small peak at 21.2 ms shown in figure 6.2.1 was due to a slight impurity in the system. However, the drift times of the various ion masses making up the RIP as shown in table 6.2.2 obtained using the SIMMS program, were all found to coincide with that for the total ions peak of 22.5 ms. Thus they are all components resulting from switching reactions based around the O_2^- reactant ion molecule. The small peak was not noticed in the SIMMS spectra and so it is concluded that it is an artefact from the mass spectrometer when put into total negative ions mode. (The peak does not occur when put in positive ions mode). It cannot be attributed to a software problem since the SIMMS and TIMMS data acquisition routines are identical. As a further check, the spectrum obtained from the Faraday plate using the IMS program showed an absence of this small peak.

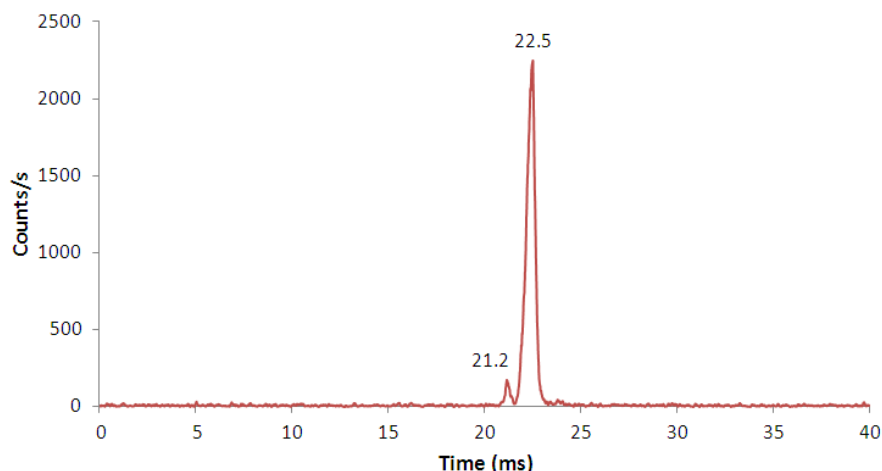


Figure 6.2.1 TIMMS spectrum showing RIP in clean air in negative ion mode

Using $K_0 \sim \frac{0.1958}{V_{HT}} \times \frac{P}{t_d - t_{ms} - t_f}$ (equation 2.2) with $V_{HT} = 4$ kV and $P = 1012$ mbar,

$t_{ms} = 0.3$ ms and $t_f = 0$ (the reconstruction filter was not required), the peak at 22.5 ms equates to a reduced mobility K_0 of $2.23 \text{ cm}^2/\text{Vs}$ (to within 5% - see section 1.2.8 in chapter 1).

This figure is in good agreement with that given in a recent paper by Vautz et al [101] of $2.22 \text{ cm}^2/\text{Vs}$ and quoted by them as “the result of many years of experience in ion mobility measurements” although they do not state the temperature and humidity at which the measurement was taken, but it is implied in another set of their results as being 23°C and so a similar amount of water clustering to our system would be present. Both ion mobility values are however somewhat higher ($\sim 3\%$) than that given by Spangler [109] of $2.16 \text{ cm}^2/\text{Vs}$. The corresponding mass spectrum is seen in figure 6.2.2.

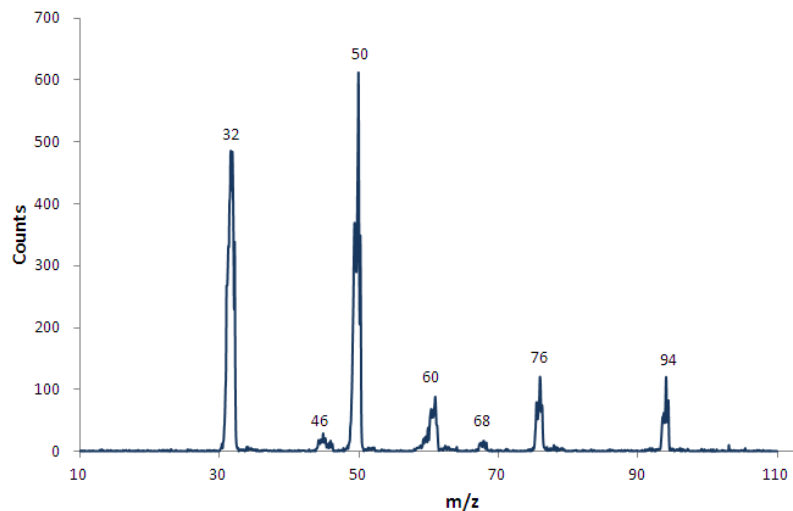


Figure 6.2.2 m/z of the RIP components in the negative ion mode

The m/z values of the ions seen in the mass spectrum (summarised in table 6.2.1) correspond with those seen by Spangler and Carr (repeated below from chapter 1) although a smaller number were seen in our system, probably due to the greater purity of the air used as the carrier gas at present.

The ion at m/z 94, which was not observed by Spangler and Carr may be due to a greater level of moisture residing in our IMS - QMS system than that with the systems of Spangler and Carr which were operated at higher temperatures.

Table 1.2 Reactant anions observed in previous studies by Carr and Spangler

m/z	26	32	35	35	42	46	50
(Carr)	CN ⁻	O ₂ ⁻	Cl ⁻		CNO ⁻	NO ₂ ⁻	
(Spangler)		O ₂ ⁻	Cl ⁻	(H ₂ O)OH ⁻		NO ₂ ⁻	(H ₂ O)O ₂ ⁻
m/z	52	53	60	64	68	76	
(Carr)	(H ₂ O) ₂ O ⁻		(CO)O ₂ ⁻	O ₄ ⁻		(CO ₂)O ₂ ⁻	
(Spangler)		(H ₂ O)OH ⁻			(H ₂ O) ₂ O ₂ ⁻	(CO ₂)O ₂ ⁻	

Table 6.2.1 Reactant anions observed in the present IMS-QMS system

m/z	32	46	50	60	68	76	94
Ion	O ₂ ⁻	NO ₂ ⁻	(H ₂ O)O ₂ ⁻	(CO)O ₂ ⁻	(H ₂ O) ₂ O ₂ ⁻	(CO ₂)O ₂ ⁻	(H ₂ O)(CO ₂)O ₂ ⁻

6.3 Investigations using analytes

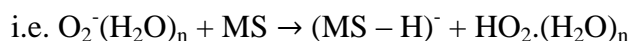
The following investigations complete the experimental research for this thesis and some are believed to be unique in that their ion-molecule reactions have not previously been studied on an IMS-MS system and so the results can be used to further explain the chemistry behind the reactions.

6.4 Investigation using methyl salicylate (MS) as the analyte

Methyl salicylate (C₈H₈O₃), *m/z* 152, is more familiarly known as ‘Wintergreen Oil’ and is naturally produced by many plant species (wintergreens in particular) hence its common name. It is used as a fragrance and also in rubbing ointments for treating joint and muscular pain. In IMS systems, it acts as a safe confidence tester to simulate nerve agents and mustard gas due to its similar ion mobility.

In the investigation, the parameters were: V_{HT} = 4 kV, P = 1008 mbar, T = 30°C (303 K)

The mass spectrum shown in figure 6.4.1 was obtained at a low concentration of MS. The peaks at *m/z* 32, 50 and 60 indicate that the concentration of MS was insufficient to completely deplete the reactant ion signal. It is interesting that the product ion peak appears at *m/z* 151 whereas the actual parent *m/z* of MS is 152 amu. Thus a proton has been abstracted from the neutral molecule.



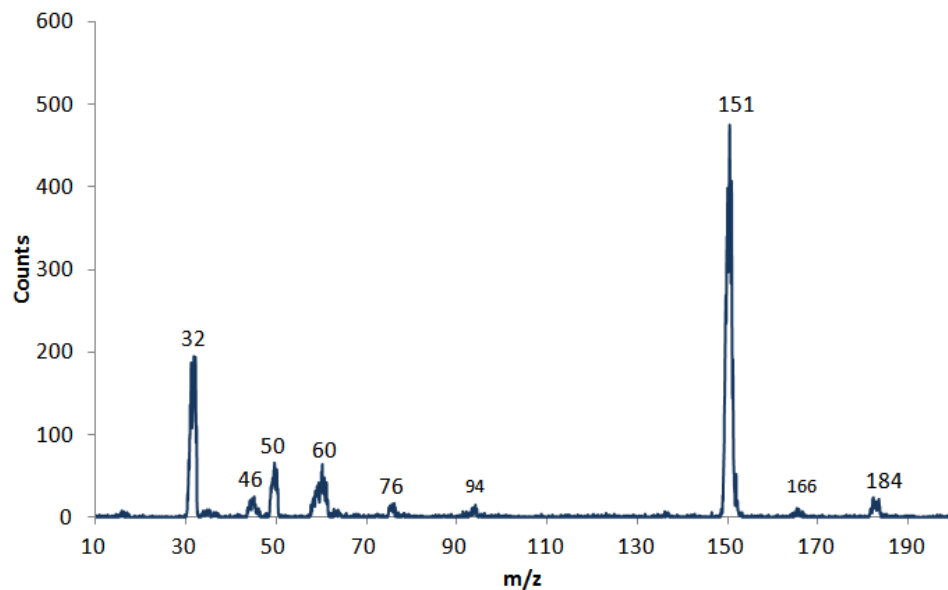


Figure 6.4.1 Mass spectrum for a low concentration of methyl salicylate

A selected ion mass mobility spectrum (SIMMS) at m/z 151 was obtained and is shown in figure 6.4.2. The drift time of 31.9 ms corresponds to a reduced ion mobility of $1.56 \text{ cm}^2/\text{Vs}$.

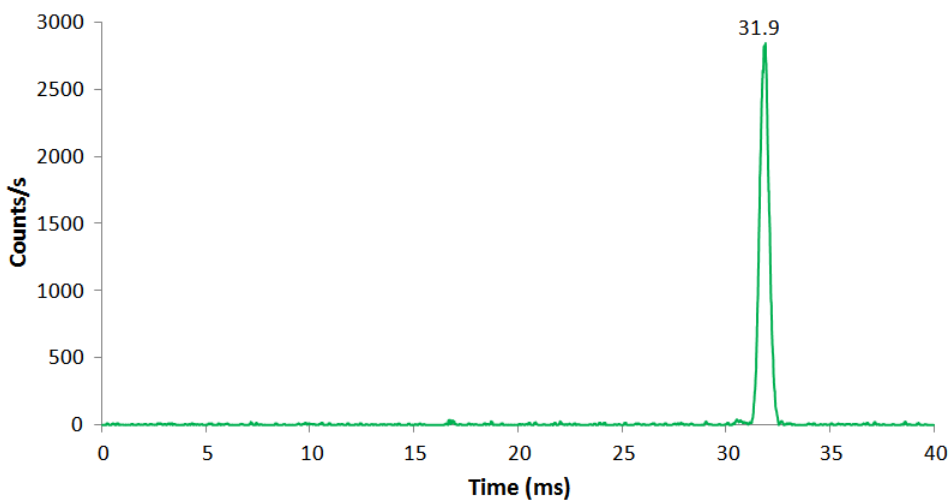


Figure 6.4.2 SIMMS spectrum of MS at m/z 151 for MS

The TIMMS spectrum is shown in figure 6.4.3 where the small peak at 21.6 ms is due to the artefact previously mentioned. In addition to the main MS monomer peak at 31.9 ms, two other peaks are seen corresponding to the RIP at 23.0 ms and possibly an impurity at 24.4 ms.

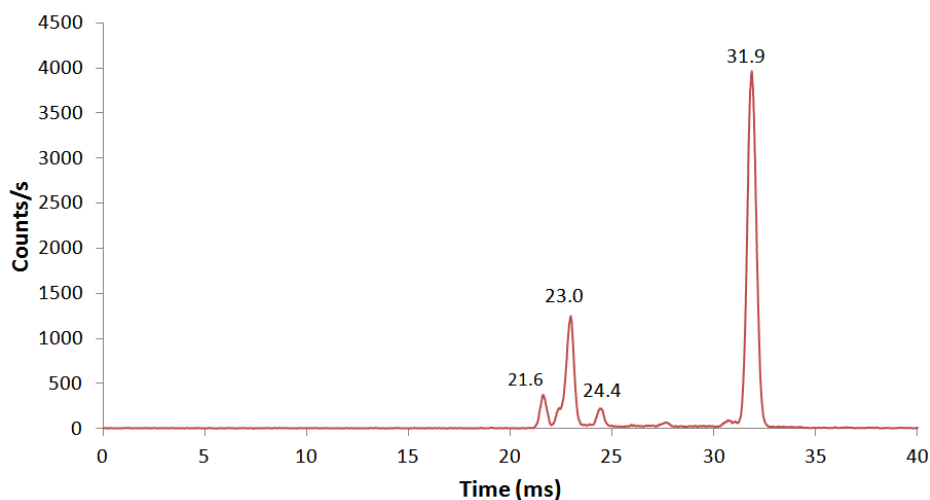


Figure 6.4.3 TIMMS spectrum of MS

The concentration of analyte was then increased such that the RIP disappeared in order to investigate what secondary ion-molecule reactions take place. The resulting mass spectrum is shown in figure 6.4.4 where it is seen that new peaks at m/z 199, 212 and 332 occur. Increasing the concentration further resulted in the mass spectrum shown in figure 6.4.5 where m/z 212 becomes the dominant product ion.

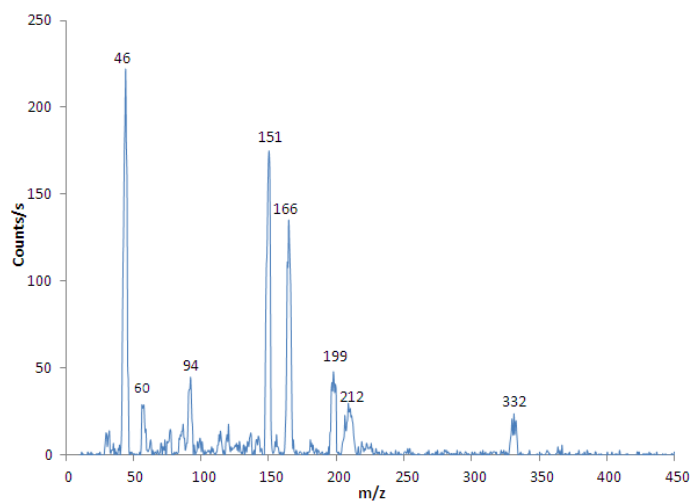


Figure 6.4.4 Mass spectrum at higher concentration of MS analyte

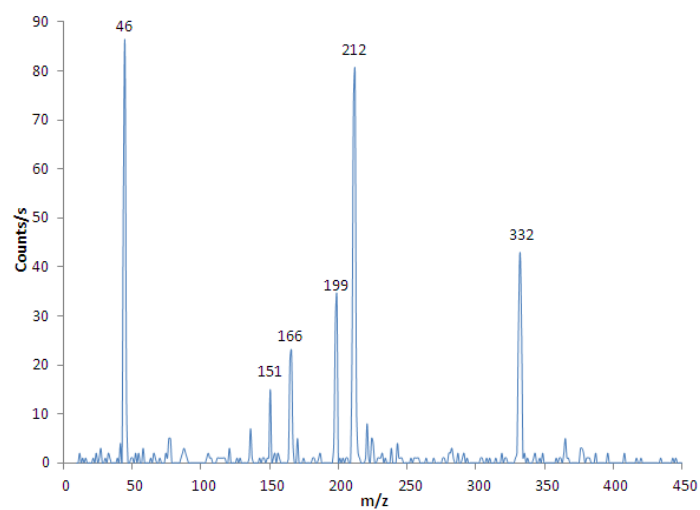


Figure 6.4.5 Mass spectrum at higher concentrations of M.S. showing dominance of m/z 212

Selected ion mass mobility spectra were obtained for all the masses seen and the overall results are given in table 6.4.1 which shows the ion mass assignments, their drift times and reduced mobilities.

Table 6.4.1 Ion m/z , drift times, relative intensities and calculated K_0 values at low concentration of MS. The dominant peak at m/z 151 is set to an arbitrary scale of 100

m/z	32	46	50	60	94	151	166
ion	O_2^-	NO_2^-	$(H_2O)O_2^-$	$CO(O_2)^-$	$(H_2O)CO(O_2)^-$	$(M-H)^-$?
t_d (ms)	23.0	21.6	23.0	21.6	23.0	31.9	31.9
Arb. units	27	7	16	13	8	100	5
K_0 (cm^2/Vs)	2.17	2.32	2.17	2.32	2.17	1.56	1.56

m/z	184	199	212	332
ion	$M O_2^-$?	$MCO(O_2)^-$?
t_d	31.9	28.4	28.8	36.7
Arb. units	8	20	6	6
K_0	1.56	1.76	1.74	1.36

The identities of the ions at m/z 166, 199 and 332 are unknown.

Common groups are identified by the same drift time. Since they represent different m/z values within these groups, they must have arisen from CID in the IMS-QMS interface. The peaks occurring at $t_d = 23.0$ ms are due to the RIP. The remaining peaks seen at higher drift times stem from the analyte.

6.5 Investigating 1,3 DNB

1,3 dinitrobenzene has the chemical formula $C_6H_4N_2O_4$ with an m/z of 168 Da. It is a man-made substance used to make explosives, and is also used in the manufacture of solvents and dyes. Yellow in colour, it is a crystal-like solid at room temperature and has no odour or taste. At a very high temperature, it will explode. 1,3-DNB is formed during the manufacture of the explosive trinitrotoluene (TNT). Its vapour pressure is very low being 0.003 mbar at 25°C. In the experiment, the conditions were: $P = 996$ mbar, $V_{HT} = 4$ kV and $T = 30^\circ C$

Before introducing the analyte, the mass spectra of the RIP was taken to check for contamination. It was seen that the m/z of the ions detected were as expected and the contamination was low.

The headspace from a vial containing the analyte was then introduced into the forward flow of carrier gas (pure air) into the IMS. A mass scan was then taken, the resulting spectrum being shown in Figure 6.5.1. It is seen that the predominant peak is at m/z 168 corresponding to M^+ .

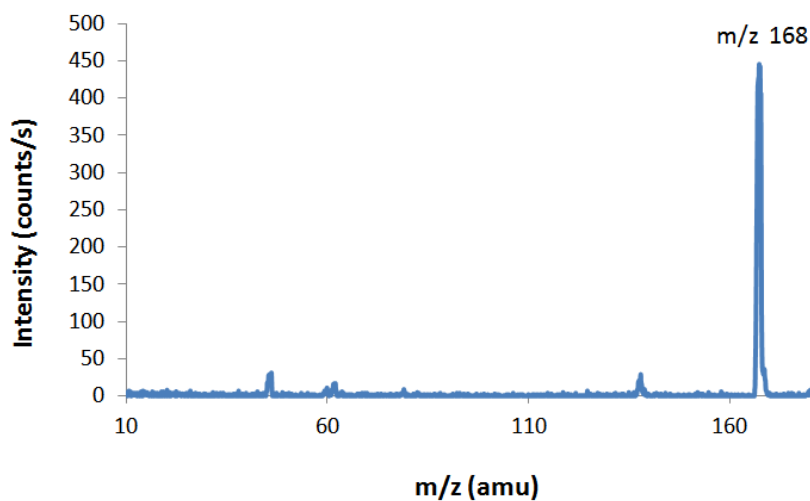


Figure 6.5.1 Mass spectrum of 1,3 DNB

A TIMMS spectrum was then taken as shown in figure 6.5.2 where again, no RIP is seen, and the peak due to the high concentration of analyte dominates.

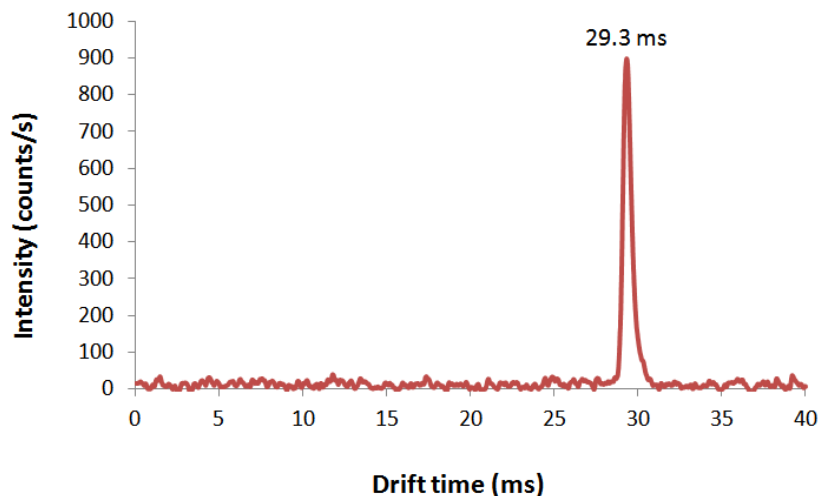


Figure 6.5.2 Total ion mobility spectrum of 1,3 DNB

A SIMMS scan at m/z 168 is shown in figure 6.5.3 where the same drift time as that seen in figure 6.5.2 confirms that the peak is indeed due to 1,3 DNB.

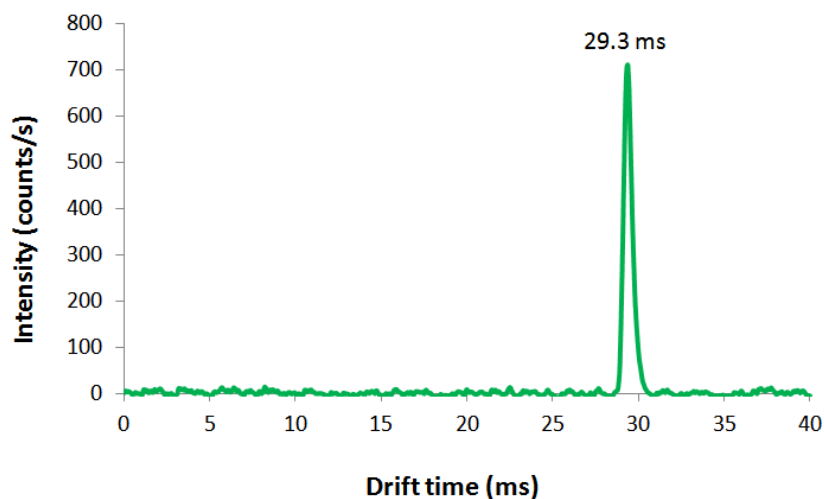


Figure 6.5.3 Selected ion mass mobility spectrum at m/z 168 for 1,3 DNB

The vial containing the sample was then removed and TIMMS spectra were observed over a period of 2½ hours. During this time, the predominant peak due to the analyte ions gradually

diminished although its drift time remained unchanged, while the RIP became dominant with only a small amount of analyte ions remaining as seen in figure 6.5.4.

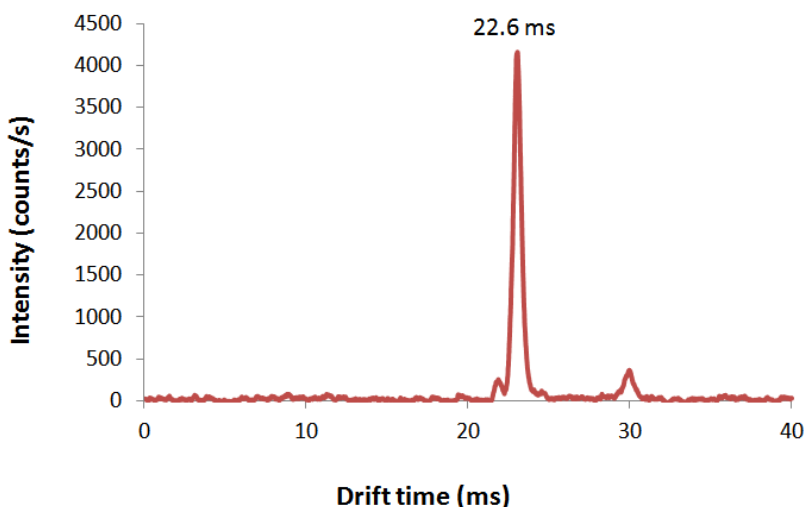


Figure 6.5.4 TIMMS showing reversion to RIP after 2½ hours

Using the drift time of 29.3 ms for 1,3 DNB, its reduced mobility K_0 is calculated to be 1.68 cm^2/Vs

Using a commercial IMS, Kanu & Hill 2007 [132] quote $K_0 = 1.71 \text{cm}^2/\text{Vs}$ which, being < 2% difference, is in good agreement with our value.

6.6 Investigating 2,6-DNT

This organic compound 2,6-dinitrotoluene has the formula $\text{CH}_3\text{C}_6\text{H}_3(\text{NO}_2)_2$ with an m/z of 182 Da. It is a pale yellow crystalline solid with similar physical characteristics to 2,4 DNT. The measurement conditions were: $P = 992 \text{ mbar}$, $V_{\text{HT}} = 4.0 \text{ kV}$, $T = 30^\circ\text{C}$ and $t_{\text{GATE}} = 0.3 \text{ ms}$.

Sampling the headspace from the analyte into the forward flow of the IMS produced the following mass spectra:

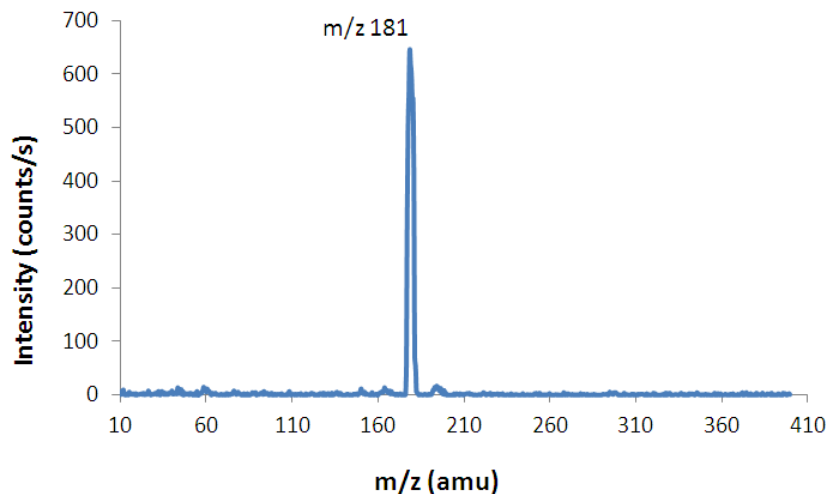


Figure 6.6.1 Mass scan for 2,6 DNT

Homing in on the peak seen in figure 6.6.1 by scanning over 178 to 183 amu at high resolution produced the spectrum shown in figure 6.6.2 where it is seen that the peak shown in figure 6.6.1 is of course composed of two peaks, the first at m/z 181 (representing $[M-H]^-$) and the second peak at m/z 182 resulting from the ^{13}C isotope.

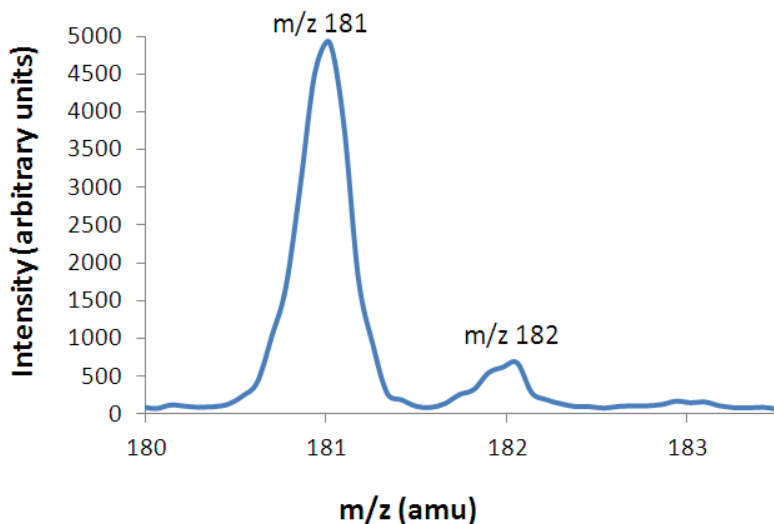


Figure 6.6.2 Expanded view of the mass peak around 181 amu for 2,6 DNT.

The total ions mobility spectrum was then obtained as seen in figure 6.6.3 where only one peak is seen occurring at 30.3 ms.

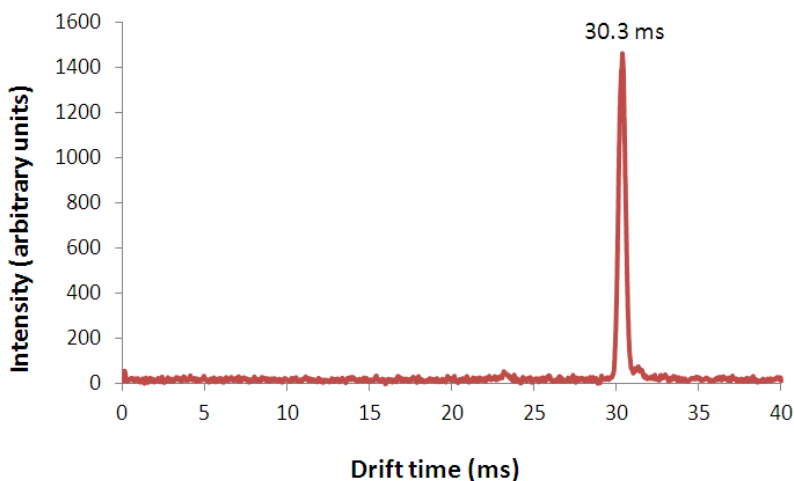


Figure 6.6.3 TIMMS scan for 2,6 DNT

The drift time of 30.3 ms corresponds to reduced mobility $K_0 = 1.62 \text{ cm}^2/\text{Vs}$ for $[M-H]^+$. Ewing *et al.* [135] quote $1.61 \text{ cm}^2/\text{Vs}$ whereas Kanu and Hill 2007 [132] quote $K_0 = 1.67 \text{ cm}^2/\text{Vs}$, (literature value = $1.65 \text{ cm}^2/\text{Vs}$) which are less than 2.5% different.

6.7 Investigating 2,4 DNT

The organic compound 2,4-dinitrotoluene is an isomer of 2,6 DNT and so has the same formula $\text{CH}_3\text{C}_6\text{H}_3(\text{NO}_2)_2$ and hence the same m/z of 182 Da. It is a pale yellow crystalline solid used as a precursor to trinitrotoluene (TNT) for which it is a gelatinizing and waterproofing agent, although it is more commonly produced as a precursor to toluene diisocyanate used to produce polyurethane foams. Its vapour pressure is 0.0051 Torr at 20°C .

In the experiment, the conditions were: $P = 992 \text{ mbar}$, $V_{\text{HT}} = 4 \text{ kV}$ and $T = 30^\circ\text{C}$

The headspace from a vial containing the analyte was introduced into the forward flow of carrier gas into the IMS. When taking a TIMMS spectrum (figure 6.7.1) it was seen that unlike with 2,6 DNT where only one peak was seen, there were now two peaks separated by 1 ms.

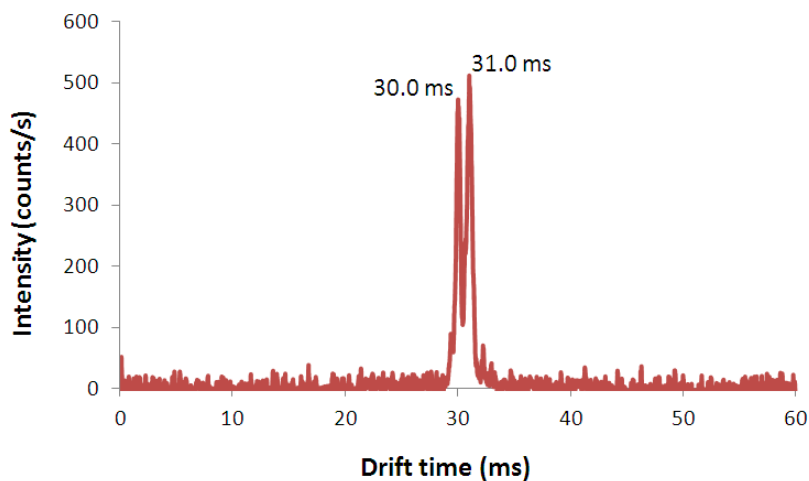


Figure 6.7.1 TIMMS for 2,4 DNT

The region around 29 to 32 ms is expanded below in figure 6.7.2 to show the two peaks present;

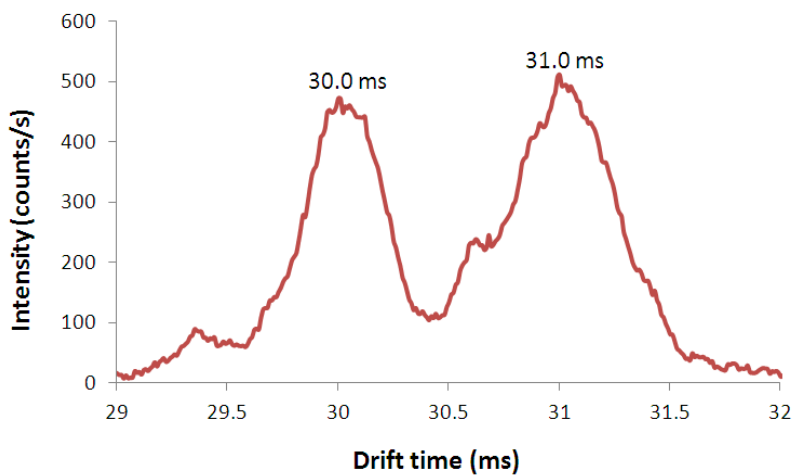


Figure 6.7.2 Expanded view of TIMMS for 2,4 DNT

A low resolution mass scan was then taken, the resulting spectrum being shown in Figure 6.7.3.

Here, it is seen that the predominant peaks are at m/z 181/182 and m/z 196/197. The peaks at m/z 196/197 remain unassigned.

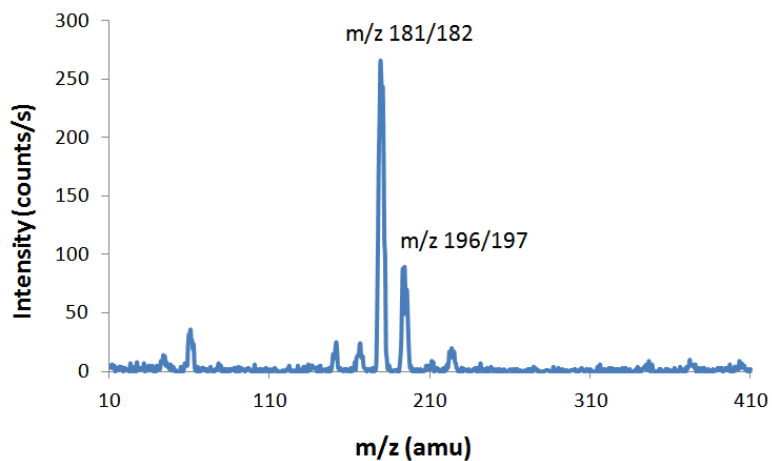


Figure 6.7.3 Mass scan for 2,4 DNT

In order to see the peaks more clearly, a high resolution mass scan was taken over the range 180 to 183.5 amu as seen in figure 6.7.4.

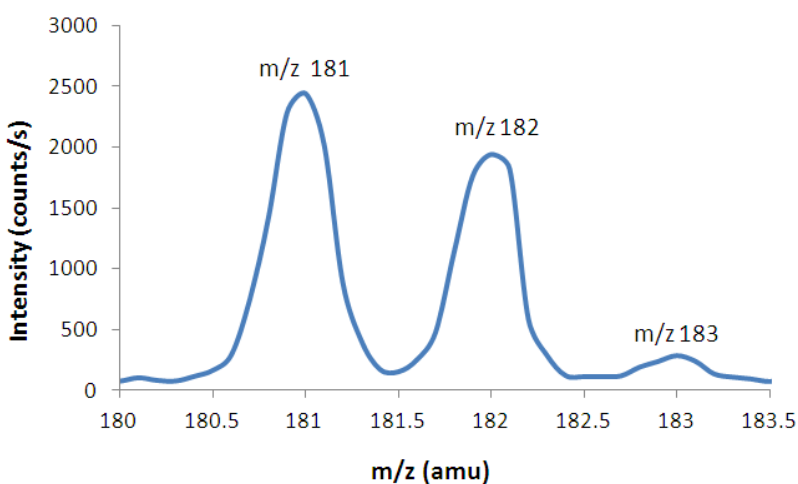


Figure 6.7.4 Exploded view of the peaks obtained around 181 amu for 2,4 DNT

Clearly the peak at m/z 182 is much higher than could be accounted for from the ^{13}C isotope for m/z 181, and therefore it has a dominant contribution from M^+ . This raises the question as to why M^+ is observed for 2,4 DNT but not for 2,6 DNT.

Turning our attention now to the peak seen around m/z 196 in figure 6.7.1, a high resolution plot over 195 to 199 amu produced the spectrum shown in figure 6.7.5

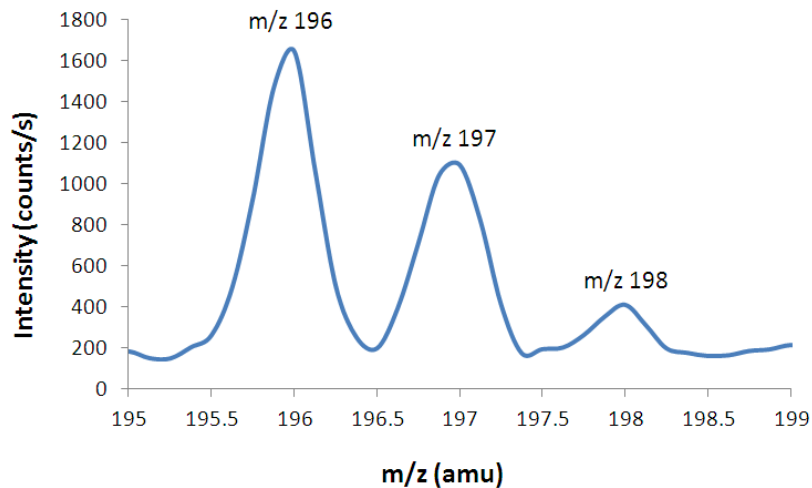


Figure 6.7.5 Exploded view of the peaks obtained around 196 amu for 2,4 DNT

A low resolution selected mass mobility scan was taken at m/z 181 as seen in figure 6.7.6 where two peaks are seen. These correspond to the peaks at m/z 181 and 182.

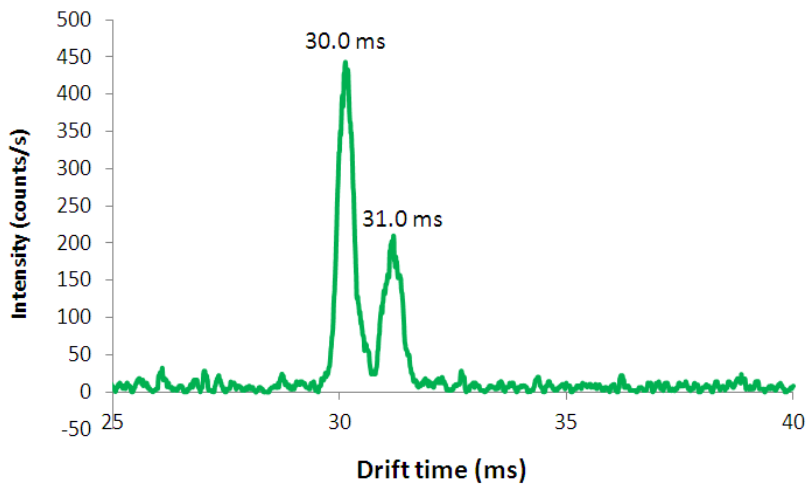


Figure 6.7.6 SIMMS scan at m/z 181 for 2,4 DNT

The drift times of 30.0 and 31.0 ms correspond to reduced mobility values of $K_0 = 1.63 \text{ cm}^2/\text{Vs}$ for $[\text{M-H}]^-$ and $1.58 \text{ cm}^2/\text{Vs}$ for M^- .

The values given in the paper by Spangler and Lawless [133] are $1.67 \text{ cm}^2/\text{Vs}$ and $1.61 \text{ cm}^2/\text{Vs}$ respectively which are 2.5% higher than our values. However, it is generally recognised that reduced mobility values within different IMS systems are at best accurate to around 2% [131] and so on this basis, there is good agreement with published data.

Tuning to m/z 196 produced the spectrum seen in figure 6.7.7

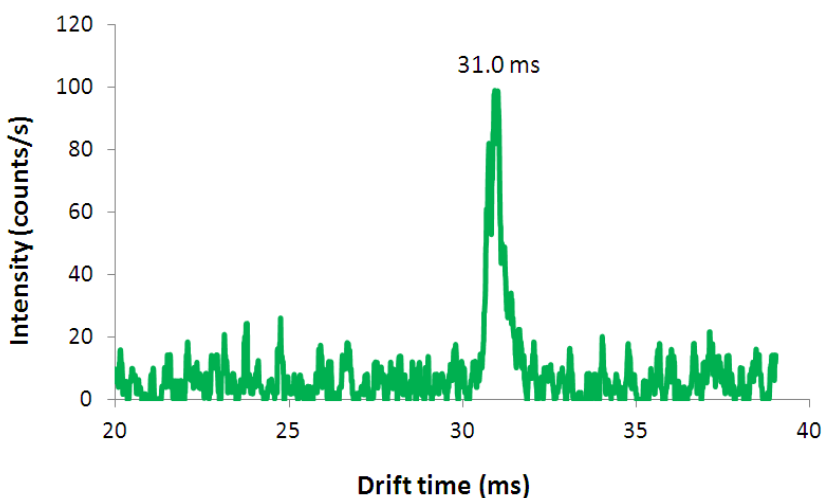
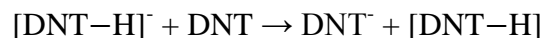


Figure 6.7.7 SIMMS scan at m/z 196 for 2,4 DNT

From figure 6.7.7, only a single peak for m/z 196 is seen at a drift time of 31.0 ms, which is similar to the drift time of the peak selected at m/z 182 corresponding to M^- , as seen in figure 6.7.6. Therefore we propose that m/z 196 is $\text{M}^- \cdot \text{N}_2$.

In contrast to the results from the 2,6 DNT investigation where only one peak was observed in the TIMMS and MS spectra, the 2,4 DNT analyte shows two mass peaks and two mobility peaks corresponding to $[\text{M-H}]^-$ and M^- . A later investigation into 2,4,DNT showed that the second peak

is concentration dependent since it disappeared as the concentration of analyte diminished. One possibility for this is a secondary ion reaction:



6.8 Investigating 1,3,5 TNB

1,3,5-Trinitrobenzene (TNB) is classified as a high explosive. It is fairly explosive in liquid form but extremely explosive as a dry powder where it will detonate under strong shock. Its colour ranges from clear to light yellow. TNB is used mainly in mining and military use. Another use is as an agent to vulcanize natural rubber. Its molecular formula is $\text{C}_6\text{H}_3\text{N}_3\text{O}_6$ with an m/z of 213 Da. During the experiment, the operating pressure was 998 mbar, $V_{\text{HT}} = 4.0$ kV and $t_{\text{GATE}} = 0.4$ ms. A TIMMS spectrum was obtained as seen in figure 6.8.1 where there is a good balance between the RIP and the analyte monomer and an unidentified peak at 37.2 ms.

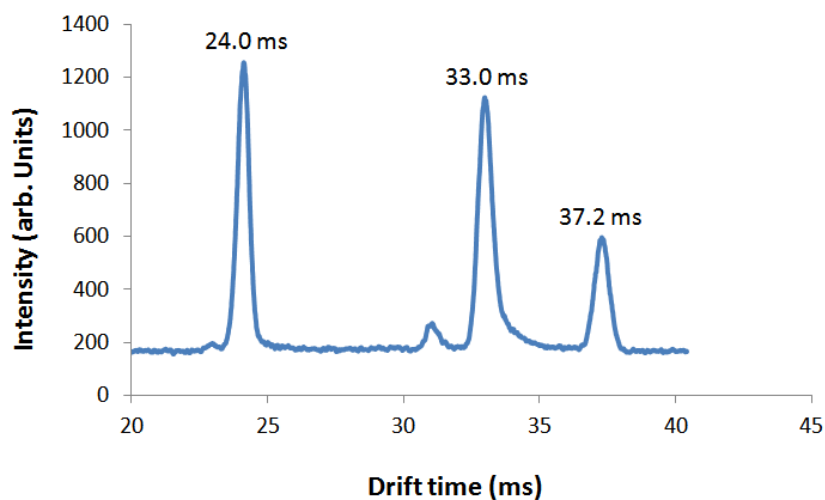


Figure 6.8.1 TIMMS scan for TNB

A mass scan was then taken as shown in figure 6.8.2

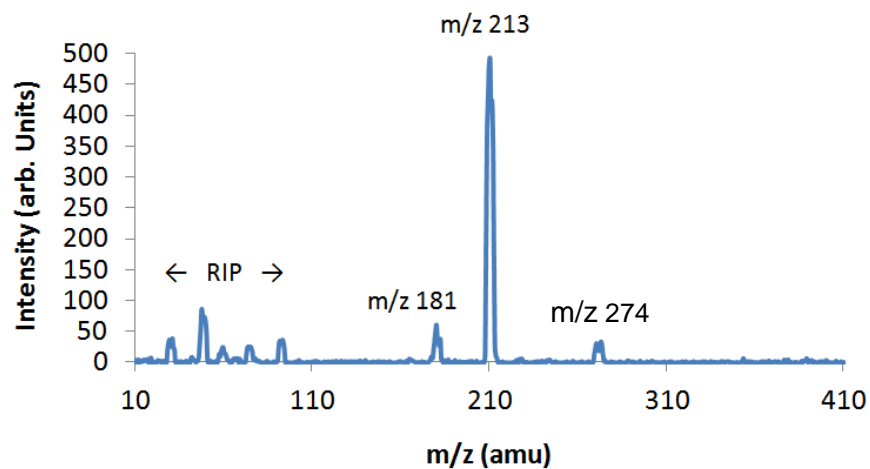


Figure 6.8.2 MS scan for TNB

The dominant peak was at m/z 213 corresponding to $[M]^-$.

Tuning to m/z 213, a SIMMS scans was taken which showed two peaks as seen in figure 6.8.3.

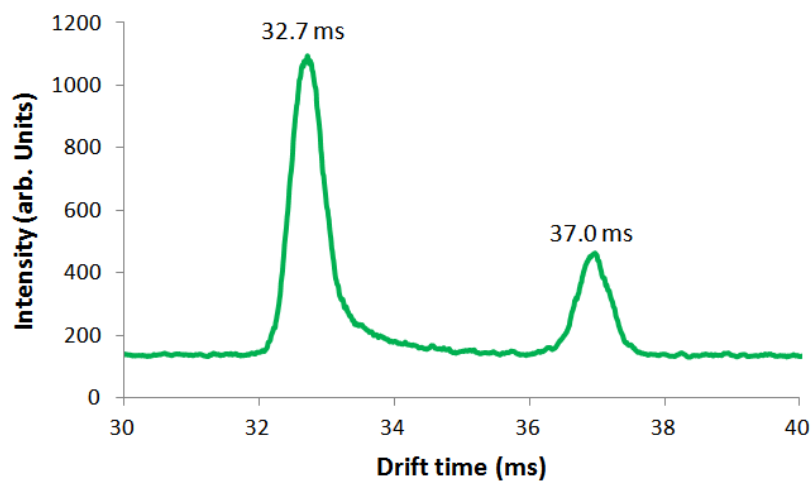


Figure 6.8.3 SIMMS scan at m/z 213 for TNB

The peak at 32.7 ms is assigned to be the monomer ion whereas that at 37.0 ms may result from the dimer ion TNB_2^- which fragments as a result of CID to TNB^- and TNB after exiting the FP.

The FP to cone voltage was then reduced to 5.6 V and a mass scan taken, but no masses corresponding to the dimer were observed. It was noticed however, that m/z 274 increased as $V_{\text{FP-cone}}$ was reduced.

Taking a SIMMS scan at m/z 274 and with V_{FP} at -5.6 V instead of the usual -9 V gave the spectrum shown in figure 6.8.4.

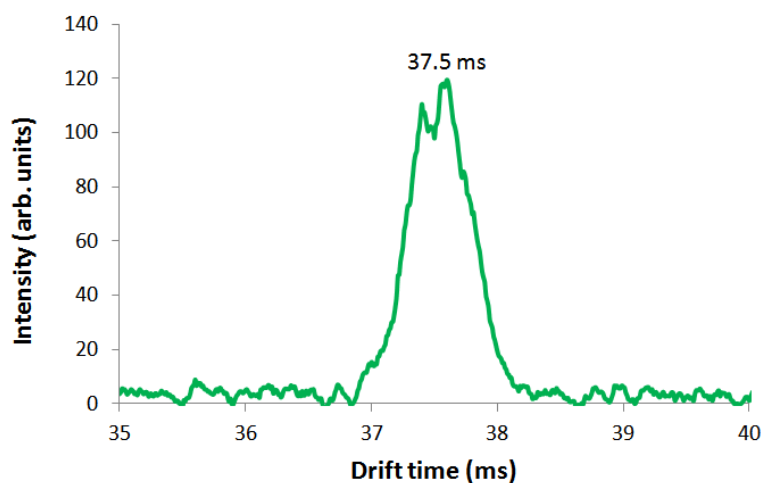


Figure 6.8.4 SIMMS scan for TNB at m/z 274

After a one hour break, a mass scan was taken as shown in figure 6.8.5, to see if any significant changes had occurred.

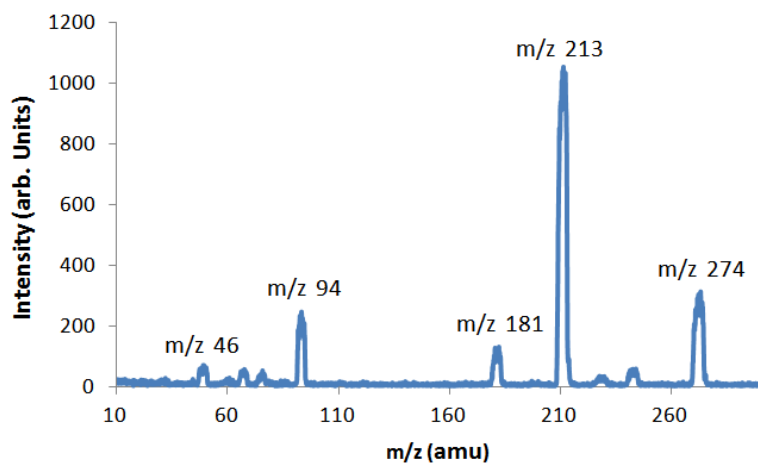


Figure 6.8.5 MS scan for TNB

Here, it is seen that the peak at m/z 274 is more prominent than when seen in the earlier mass scan shown in figure 6.8.2, its identity is not known but most probably results from CID of the dimer. Looking at the signal from the FP shows the amplitude of the peaks in their true proportions. (See figure 6.8.6).

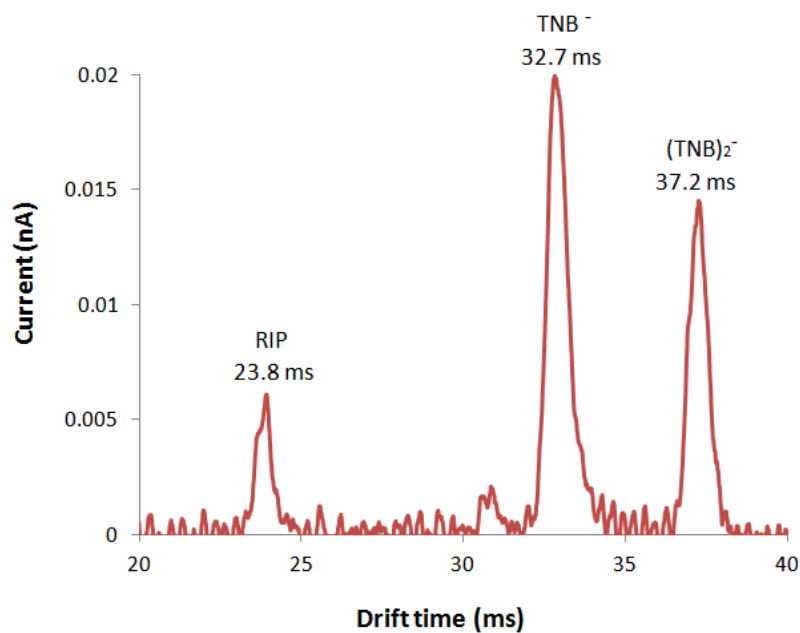


Figure 6.8.6 IMS scan for TNB

The drift times of the peaks at 23.8, 32.7 and 37.2 ms correspond to reduced mobility values of $K_0 = 2.20 \text{ cm}^2/\text{Vs}$ for the RIP and $1.60 \text{ cm}^2/\text{Vs}$ for M^- . The peak at 37.2 ms which we have tentatively identified to be the dimer has $K_0 = 1.31 \text{ cm}^2/\text{Vs}$.

6.9 Investigating TNT

2,4,6 trinitrotoluene (TNT) is a yellow solid with the formula $\text{C}_6\text{H}_2(\text{NO}_2)_3\text{CH}_3$. Its mass is 227 amu. It is best known as a useful explosive material and its explosive yield is used as the standard measure of strength for bombs and other explosives.

The operating conditions during the experiment were:

$P = 990$ mbar, $t_{\text{GATE}} = 0.3$ ms, $V_{\text{HT}} = 4.0$ kV. Pure air was initially used for the carrier gas.

A sample of the headspace from the analyte was introduced into the forward flow of carrier gas for the IMS and a mass scan was then taken (shown in figure 6.9.1) where a peak at m/z 226 corresponding to $[\text{TNT-H}]^-$ is seen.

The peaks seen in figure 6.9.1 arise from the following ions:

- RIP assigned to m/z 32 to 94
- $[\text{TNB}]^-$ at m/z 213 (now regarded as an ‘impurity’ from a previous investigation)
- $[\text{TNT-H}]^-$ assigned to m/z 226, resulting from proton abstraction
- Unidentified ion at m/z 288

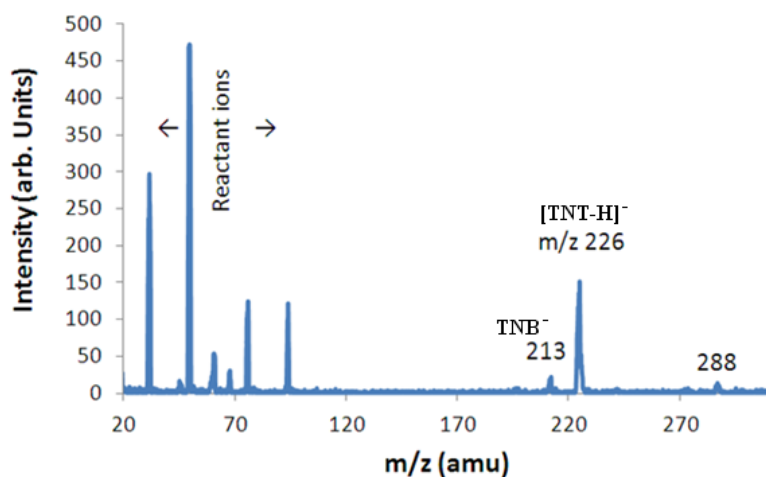


Figure 6.9.1 MS scan of 2,4,6 TNT in air

A TIMMS scan was then taken as seen in figure 6.9.2 where the major peak corresponds to the reactant (RIP) ions at 23 ms.

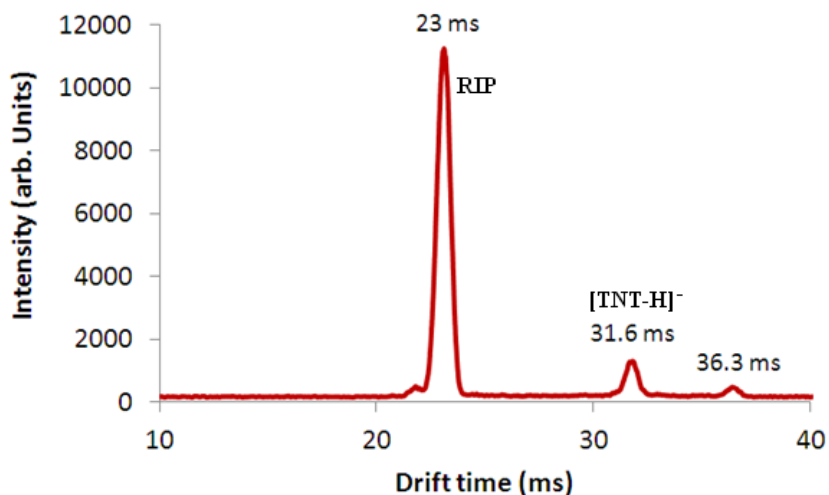


Figure 6.9.2 TIMMS scan of 2,4,6 TNT in air

A selected mobility scan done at m/z 226 amu confirmed that the peak at 31.6 ms was due to [TNT-H]⁻ ions as seen in figure 6.9.3. It also indicates that in figure 6.9.1, the higher mass peak around m/z 288 again seen at 36.3 ms is formed from some CID of a TNT⁻ cluster in the IMS-MS interface region.

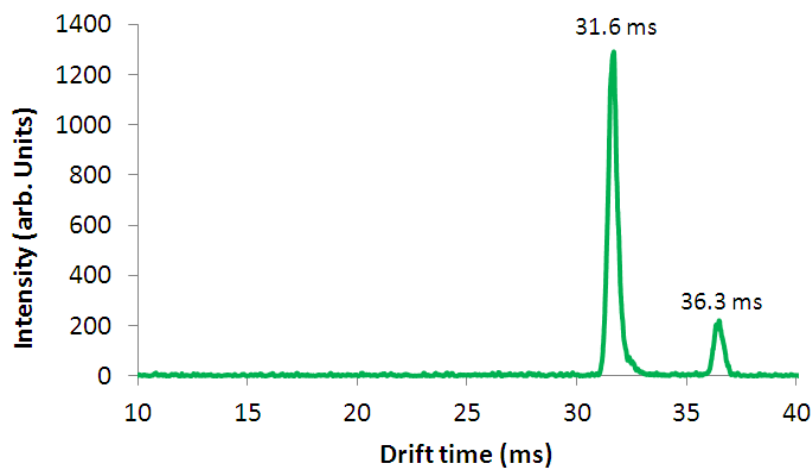


Figure 6.9.3 SIMMS scan at m/z 226 in air

From the drift time of 31.6 ms corresponding to the peak for $[\text{TNT-H}]^-$, the reduced ion mobility K_0 is $1.55 \text{ cm}^2/\text{Vs}$

The temperature was then increased to 70°C which caused (via the safety switch) V_{HT} to be reduced to about 3 kV with a corresponding increase in drift time. Figure 6.9.4 shows a mass scan taken at this temperature. Comparing the spectrum with that of figure 6.9.1 at 30°C , it is seen that the peak at m/z 226 shows increased volatility of the analyte and reduced water content in the source gas as evidenced by the peak at m/z 50 (corresponding to $(\text{H}_2\text{O})\text{O}_2^-$).

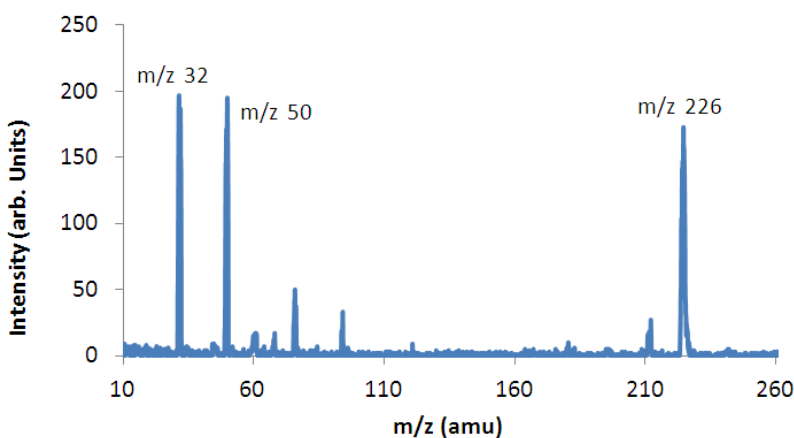


Figure 6.9.4 MS scan for 2,4,6, TNT in air at 70°C source gas temperature

A TIMMS scan was then taken with the temperature of the source gas increased to 86°C (figure 6.9.5) where a significant increase of analyte and reduction of RIP is seen.

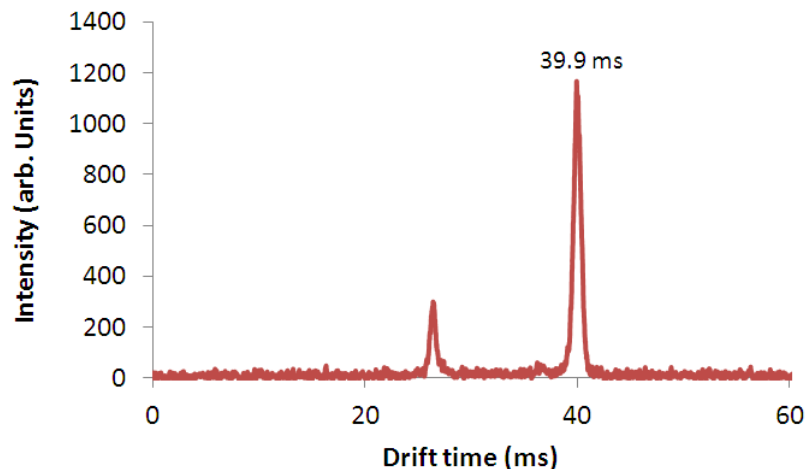


Figure 6.9.5 TIMMS scan for 2,4,6 TNT in air at 86°C

6.10 Investigating the use of the dopant hexachloroethane in nitrogen

In order to dope the system to get chloride ions so that the results could be compared with those from other workers, [135,136] hexachloroethane (C_2Cl_6) vapours were admitted into the forward flow of the drift tube with pure nitrogen being used in place of air for the carrier gas. When taking a high resolution mass scan, peaks corresponding to Cl^- (the dominant peak) and Cl_2^- were seen in addition to the small peak arising from residual $[TNT-H]^-$. Although it may seem unusual for Cl_2^- to be formed from C_2Cl_6 , it is often noticed that Cl_2^- is produced following electron attachment to polychlorinated compounds [134].

A TIMMS scan was then taken as seen in figure 6.10.1. The small peak immediately following that at 20.4 ms is probably due to the formation of Cl_2^- ions while that at 31.5 ms is from the residual TNT vapours in the system.

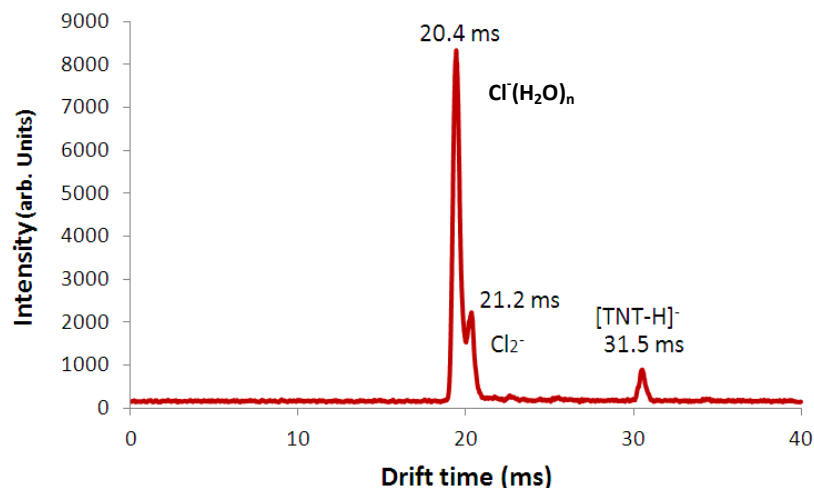


Figure 6.10.1 TIMMS scan for N₂ with C₂Cl₆ dopant

The reduced ion mobility K_0 for the peak at 31.5 ms in figure 6.10.1 which corresponds to [TNT-H]⁻ is 1.55 cm²/Vs. For the new chlorine based reactant ions, Cl⁻(H₂O)_n at 20.4 ms has $K_0 = 2.40$ cm²/Vs and Cl₂⁻ at 21.2 ms has $K_0 = 2.31$ cm²/Vs.

A low resolution mass scan was then taken as shown in figure 6.10.2. The peak at m/z 226 corresponds to [TNT - H]⁻ formed from the reaction Cl⁻ + TNT → [TNT - H]⁻ + HCl

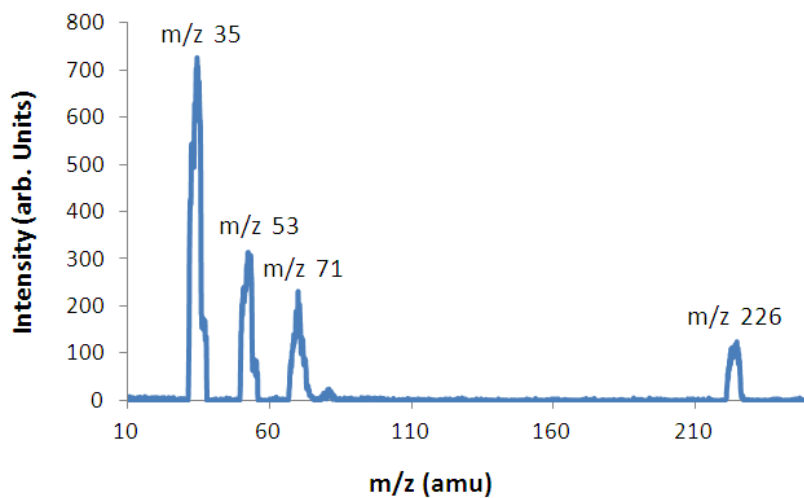


Figure 6.10.2 Low resolution MS scan for N₂ with C₂Cl₆ dopant

Considering the peaks seen comprising the new RIP, further high resolution mass scans at each peak were taken and these are shown in figures 6.10.3 to 6.10.5. Note, the product ion peak in nitrogen is still at m/z 226 being $[\text{TNT-H}]^-$.

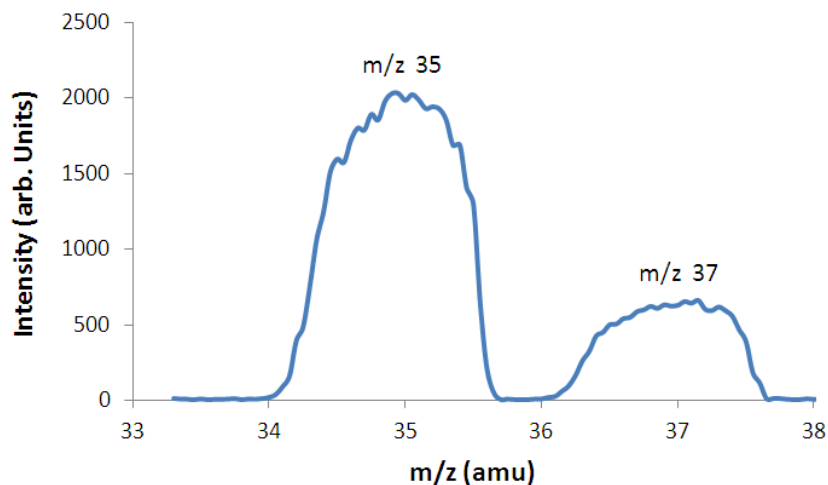


Figure 6.10.3 MS scan around m/z 35 for N_2 with C_2Cl_6 dopant

The peaks at m/z 35 and 37 seen in figure 6.10.3 correspond to the isotopes of Cl^- in the ratio 3:1 (correctly following the abundance of the isotopes of chlorine at m/z 35 and 37 being 75% and 25% respectively). In figure 6.10.4, the peaks at m/z 53 and 55 correspond to hydrated chlorine ions being $(\text{H}_2\text{O})\text{Cl}^-$ again in the isotopic ratio 3:1.

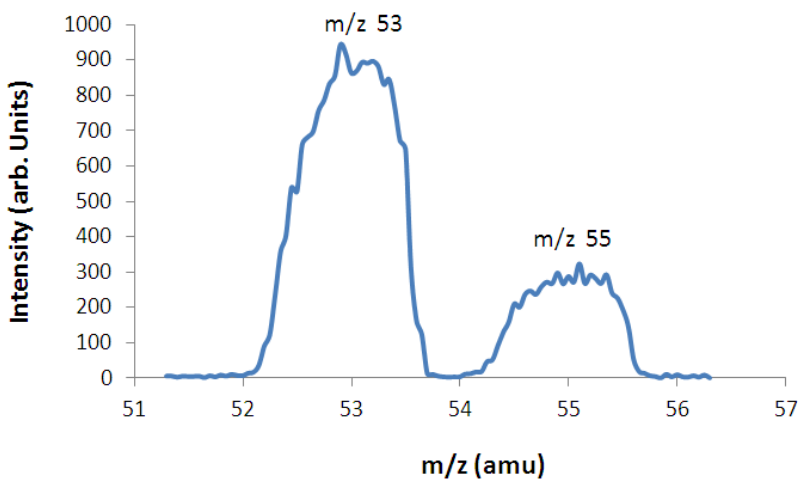


Figure 6.10.4 MS scan around m/z 53 for N_2 with C_2Cl_6 dopant

The peaks seen in figure 6.10.5 correspond to Cl^- , Cl_2^- and $\text{Cl}^-\cdot(\text{H}_2\text{O})_2$ as identified below in table 6.10.1.

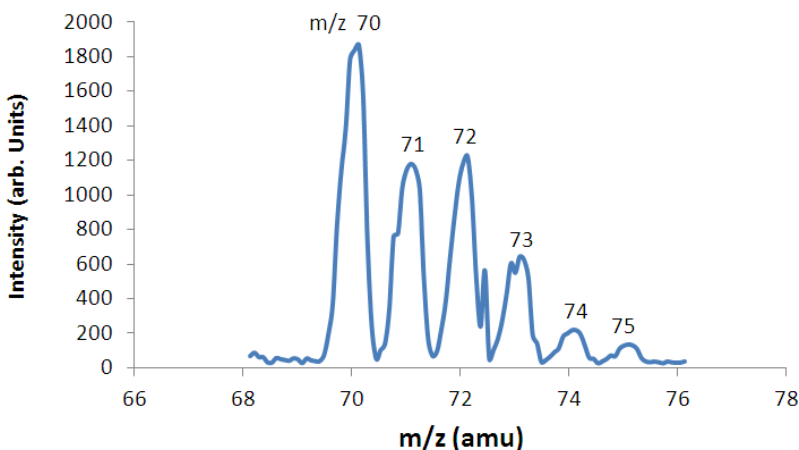


Figure 6.10.5 MS scan around m/z 72 for N_2 with C_2Cl_6 dopant

Table 6.10.1 Identification of m/z ions for N_2 with C_2Cl_6 dopant as seen in figure 6.10.6

m/z	70	71	72	73	74	75
ion	$^{35}\text{Cl}_2^-$	$^{35}\text{Cl}(\text{H}_2\text{O})_2^-$	$^{35}\text{Cl}\cdot^{37}\text{Cl}^-$	$^{37}\text{Cl}(\text{H}_2\text{O})_2^-$	$^{37}\text{Cl}_2^-$	$\text{H}\cdot^{37}\text{Cl}_2^-$

The values of K_0 calculated as $1.55 \text{ cm}^2/\text{Vs}$ for $[\text{TNT} - \text{H}]^-$ in both air and nitrogen compare favourably with that of $1.54 \text{ cm}^2/\text{Vs}$ reported by other workers, e.g. [135,136].

6.11 Investigating TNT in pure nitrogen with no dopant present

After removing the hexachloroethane dopant source, the temperature of the drift tube was raised to 86°C . The system was then left to bake out under nitrogen carrier gas for three hours. After cooling down back to 30°C a mass scan showed no presence of Cl^- ions. TNT vapours were then admitted into the system. Only free electrons were available now for reactions and just two peaks were seen in the mass scan at m/z 213 corresponding to a residue of TNB^- left over from a

previous investigation, and m/z 227 corresponding to the non-dissociative electron attachment to TNT, whereby $e^- + \text{TNT} \rightarrow \text{TNT}^-$. A low resolution mass scan was made over the range m/z 210 to 230 covering TNB^- and TNT^- as shown in figure 6.11.1.

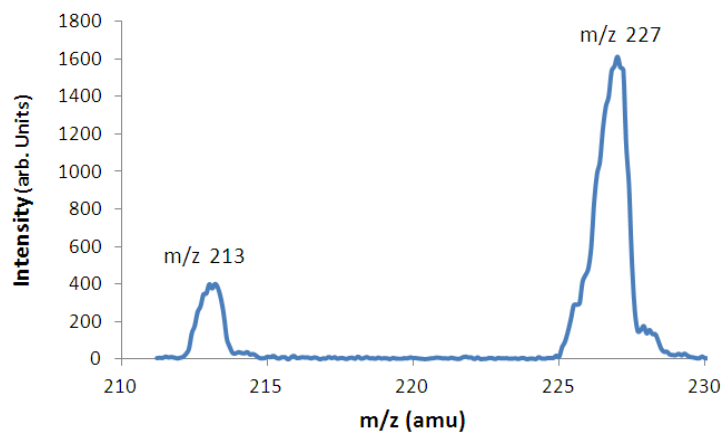


Figure 6.11.1 Mass scan around m/z 211 to 230 for N_2 (no dopant present)

A high resolution mass scan around m/z 224 to 229 gave the spectrum seen in figure 6.11.2. At this higher resolution, the dominant peak at m/z 227 is from TNT^- whereas that at m/z 226 is from $[\text{TNT-H}]^-$ (probably formed from a reaction involving some residual air present in the system).

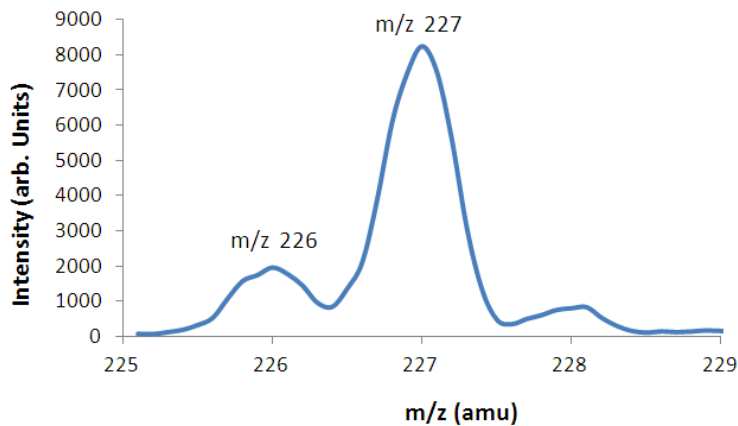


Figure 6.11.2 Mass scan around m/z 225 to 229 for N_2 (no dopant present)

The system was then again doped with hexachloroethane where it was seen (as shown in figure 6.11.3) that the dominant peak had shifted back to m/z 226 with the smaller peak now at m/z 227 due to the ^{13}C isotope.

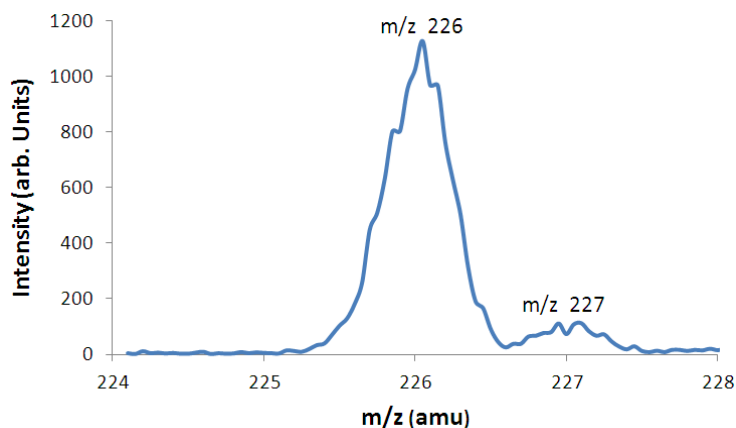


Figure 6.11.3 Mass scan around m/z 224 to 228 for N_2 with dopant

In the mass spectra, the peak seen at m/z 213 corresponding to TNB^- has arisen from a trace of TNB remaining from the previous experiments conducted.

6.12 Summary and review

For TNT the following were found:

- Attachment of free electrons only results in TNT^- .
- Reactions with $\text{O}_2^-(\text{H}_2\text{O})_n$ produce a single peak at $[\text{TNT-H}]^-$ through proton abstraction
- Reactions involving the Cl^- dopant producing Cl^- , Cl_2^- and $\text{Cl}^-\cdot\text{H}_2\text{O}$ reactant ions also produce a single peak at $[\text{TNT-H}]^-$, again through proton abstraction

Comparing results from investigations in both positive and negative ions mode, it is seen that:

- In both positive and negative ions mode, the RIP is of a similar mobility, probably due to the humidity of the carrier air producing a similar number of water clusters around the core H_3O^+ or O_2^- ion.
- In both modes, the amplitude (counts/s) of the ion signal from the channeltron is also of a similar magnitude, indicating that a similar amount of cations and anions are being produced in the ionising region.
- In the positive ions mode, the reaction pathway was observed to be through proton transfer.
- In the negative ions mode, reaction pathways were seen to be either from electron transfer, or from proton abstraction, as confirmed in section 1.2.11.

A review of the results from the experiments is given in table 6.12.1.

Table 6.12.1 Listing of analytes used in the negative ion mode with their results

Compound	Carrier	Product ions	Mass (m/z)	K_0 (cm^2/Vs)
Clean air	Air	RIP $\text{O}_2^-(\text{H}_2\text{O})_n$		2.10
Methyl salicylate (MS)	Air	$(\text{MS} - \text{H})^-$	151	1.55
1,3 Dinitrobenzene (1,3 DNB)	Air	DNB^-	168	1.68
2,4,Dinitrotoluene (2,4 DNT)	Air	$(\text{DNT} - \text{H})^-$	181	1.58
2,6 Dinitrotoluene (2,6 DNT)	Air	$(\text{DNT} - \text{H})^-$	181	1.61
1,3,5 Trinitrobenzene (1,3,5 TNB)	Air	TNB^-	213	1.61 Dimer 1.31
2,4,6 Trinitrotoluene (2,4,6 TNT)	Air	$(\text{TNT} - \text{H})^-$	226	1.55
	$\text{N}_2 + \text{C}_2\text{Cl}_6$	$(\text{TNT} - \text{H})^-$	226	1.55
	N_2	TNT^-	227	1.53
Hexachloroethane (C_2Cl_6)	N_2	$\text{Cl}^-(\text{H}_2\text{O})_n$	35, 53, 71	2.40
		Cl_2^-	70	2.31

Chapter 7 REVIEW AND DISCUSSION OF FUTURE WORK

7.1 Review of achievements made with the IMS-QMS system.

Use of opto-isolators:

In chapter 2 the design requirements and their implementation were discussed for improvements in flexibility of operation of the IMS and IMS-QMS system. One of the first considerations was to allow improvement in operation in terms of safety, by the use of opto-isolators for coupling of 5 V gate pulses to the ion gate (being at a high potential of several kV) rather than following the usual method of using a coupling capacitor (which poses the risk of dielectric breakdown, and also degradation of the square wave gate pulse).

Hardware intermediary for obtaining selected and total ion mass mobility spectra

Bearing in mind the requirements for obtaining total and selected ion mobility spectra using LabVIEW a special interface was designed (the pulse count to pseudo analogue converter) for incorporating into the system, along with a complete theoretical description of its operation.

Software development for acquiring spectra, using LabVIEW

Chapter 3 gave details of the software development using LabVIEW. Since this was implemented, a paper has been produced by others offering a program for operating an IMS system alone (also using LabVIEW) [118] that gives similar functionality to that already developed (but not being so user friendly as the version described here). However, to date, no software has been offered to operate an IMS-QMS system using LabVIEW and with the application of the count converter mentioned above, this aspect represents a unique contribution to knowledge/understanding in this area.

Experiments resulting in analyte spectra not previously obtained

In chapters 5 and 6, experiments are described that characterise the system, with some results providing a unique contribution to knowledge of the behaviour of particular analytes on an IMS-QMS system. These particular analytes are:

In positive ion mode: diacetone and dipropylene glycol methyl ether (DPGME)

In negative ion mode: methyl salicylate, 1,3,5-trinitrobenzine (1,3,5 TNB) and hexachloroethane

7.2 Factors that have arisen since the design and use of the system

The main outcome from an IMS system apart from a mobility spectrum, is the determination of the reduced mobility of our analyte. Questions relating to the validity of stated values of K_0 for particular analytes are discussed below.

Consideration of Reduced Mobility and Correction Factor in its calculation

At present, there are no standards laid down for IMS systems and so the literature values of K_0 are taken from a variety of sources where the operating conditions may be quite different in terms of drift tube design, humidity and operating temperature. When quoted, they are usually accompanied with the operating temperature and drift gas composition used at the time of measurement.

According to the theoretical mobility equation as given in section 1.2.6 of chapter 1,

assuming no clustering of the ions occurs, $K \propto \frac{1}{N\sqrt{T}}$. Since pressure $P \propto N$, then scaling

down to normalise for K_0 is appropriate for P but is clearly not for T where a reciprocal square root relationship exists. Thus, it can be seen that the actual value of K when measured under standard conditions would most likely be different to that of K_0 when calculated from a

mobility value obtained at a higher temperature, and so it is to be expected that the range of reduced mobility values quoted in literature would be wider for analytes having drift times that are more affected by operating temperature than others.

Therefore, simply stating that reducing the mobility K down to K_0 in proportion to give the equivalent mobility at standard conditions by multiplying K by $\frac{T_0 \times P}{P_0 \times T}$ may be an incorrect assumption, as the non linear effect of operating temperature on drift time and hence mobility is not considered. Thus an ion mobility value for an analyte measured at 30°C may be significantly different when measured at say, 150°C due to the increased number of collisions of ions with the more energetic buffer gas impeding the progress of the ions down the drift tube.

Some analytes exhibit only a small change in mobility over a certain temperature range, whereas ion clusters for example, will be affected significantly by temperature. This is seen for example, in Shumates table of reduced mobility values [137], where the degree of water clustering (which is strongly affected by operating temperature), causes a range in K_0 of 2.08 to 2.67 for the ion clusters $H^+(H_2O)_5$ to $H^+(H_2O)$.

Several suggestions for a reference analyte have been made in the literature, some being more suitable than others [138] but no firm decision has yet been forthcoming although the main criteria would clearly be insensitivity of mobility to operating temperature. [139].

Revised calculation of reduced mobility

Since completing the experiments described in chapters 5 and 6, a modification has been made to the system to remove unwanted variations in drift time (see appendix A4.13). This has resulted in the drift voltage being now half that of the applied voltage to the drift tube, resulting in the following modification to the equation for calculating K_0 :

In chapter 2, equation 2.1 gives $K_0 \sim \frac{0.09546 \times P}{V_d (t_d - t_{ms} - t_f)}$ with drift tube temperature at 30°C.

Where V_d = total voltage applied to the drift tube, t_d = drift time of the ions, t_{ms} = transit time of the ions through the mass spectrometer, and t_f = group delay time through the reconstruction filter.

With $V_d = V_{HT}/2$ the above equation becomes;

$$K_0 \sim \frac{0.191 \times P}{V_{HT} (t_d - t_{ms} - t_f)} \dots \text{equation 7.1}$$

(Generally we operate at $V_{HT} = 4$ kV)

7.3 Future improvements

Incorporation of a calibration factor

In military IMS equipment, a calibration factor is incorporated to take account of variations in calculated ion mobility due to mechanical differences caused by manufacturing tolerances affecting the operating conditions. This calibration factor is exclusive to that particular instrument and would be incorporated into the software for calculating the reduced mobility of the detected sample. In this thesis, the mobilities found over the experiments have mostly been in good agreement with literature values but to improve confidence, a calibration factor could similarly be incorporated into our system to allow an adjustment to be made to correct for system changes.

A way of determining the appropriate correction factor could be as follows:

$$\text{Fundamentally, drift velocity } v_d = KE = \frac{L}{t_d} \text{ (see section 1.2.7 in chapter 1)}$$

Hence $Kt_d = \frac{L}{E}$ which is a constant, thus $Kt_d = K_F t_{dF}$

where, K_F = mobility of reference analyte used for the calibrant and t_{dF} is its respective drift time found at a particular temperature and pressure.

If F is the calibration factor and putting $F = K_F t_{dF}$, then the corrected value of

mobility K is $\frac{F}{t_d}$ (at the same temperature and pressure)

Similarly, the equivalent reduced mobility value could be found using $K_0 = \frac{F_0}{t_d}$

where $F_0 = K_{0F} t_{dF}$ with K_{0F} being the literature reduced mobility of the reference analyte.

This is similar to the form seen in literature when discussing calibration [131].

Once the factor F has been found, it can be used to modify the calculation of K_0 such that

equation 7.1 now simply becomes $K_0 \sim \frac{F_0}{t}$ where $t = t_d - t_{ms} - t_f$

Note, F_0 is only applicable at the drift tube pressure when it was determined, and would need to be determined again if the pressure changes. The next section describes a way of taking pressure variations into account.

Direct display of K_0 on mobility spectra

In our system, the pressure is not regulated. Variations in ambient pressure of between 980 mbar to 1020 mbar have been observed on different days when conducting experiments. This range of 40 mbar covers a variation of minus 3.3% to plus 0.7% around the standard pressure of 1013 mbar, and may cause significant inaccuracy in the automatic determination of K_0 unless it is taken into account. Hence, since F_0 was found at a certain pressure, say, P_{test} , this

needs to be taken into account in subsequent experiments to avoid having to find a new value when the pressure changes. To do this, an output from the drift pressure gauge is required to be presented to the software so that any deviation from P_{test} can be taken into account. This facility also provides the capability of direct calculation of K_0 and its display on the x-axis instead of the less informative drift time shown at present. Let γ be the factor that takes into account P at the time of measurement.

For example, if the pressure gauge gives an output V_p of 0 to 10 V over the range 0 to 2000 mbar, then if $P_{test} =$ say 998 mbar, this would correspond to a voltage of 4.99 V. Since an increase in pressure produces a proportionate decrease in K_0 , then the calculation for reduced

$$\text{mobility would be } K_0 = \frac{F_0}{t} \times \frac{V_p}{4.99}$$

$$\text{Hence, } K_0 = \frac{\gamma}{t} \quad \text{where } \gamma = \frac{F_0 \times V_p}{4.99}$$

Using LabVIEW it therefore becomes a straightforward matter to include an arithmetic block within the graph plotting section in the v.i. to operate on t producing a direct readout of reduced mobility on the x-axis.

Generation of carrier gas (pure air)

The measurements described in chapters 5 and 6 were made using compressed pure air from gas cylinders. It would be more desirable to replace the use of cylinders with a ‘gas generator’ consisting of an oil-free air compressor with filtration. Apart from cheaper running costs, the system would always be in a state ready for immediate measurements to be taken.

(With cylinders, to conserve gas when not in use, the system is closed down and the drift tube is isolated from the gas supply and pumped down.)

Monitoring drift voltage

A factor affecting the accuracy in calculation of ion mobility from drift time is the value of the voltage across the drift region. It was seen in chapter 4, test 4.7, figure 4.11 that the drift time is proportional to the reciprocal of drift voltage. It is therefore desirable to ensure that the value of the drift voltage is correct in order to make a confident calculation of K_0 . The pressure and temperature in the drift tube are already monitored on our instrument, but it is proposed now that a display of the drift voltage would be beneficial in promoting confidence in the ion mobility values obtained from the system. It would also be useful as a system diagnostic in case of malfunction. The voltage monitor would need to be in the form of a very high input resistance (say 10 G Ω) EHT voltmeter to cause minimal change in drift voltage from the initial design value. (Recall from chapter 1 that the resistance across the drift region via the rings totals 80 M Ω .) A design for such an instrument is given in appendix 7.1.

Software implementation of the pulse converter using a microcontroller

This would allow optimisation of the operating parameters with the following advantages:

- Communication with the control computer for automatic control of gate pulse width and frequency setting according to the spectral length and analyte mass.
- Synchronisation of gate pulse and acquisition timing which may reduce the number of accumulations required and hence time for detection.

Improvements on pumping to eliminate the microphony effect manifest in the IMS spectra

In order to significantly reduce the pick-up from vibration caused by the turbo molecular pumps, they could be replaced with the new magnetic bearing type which produce much less vibration (but cost significantly more to buy), or diffusion pumps could be used which present no vibration at all. Diffusion pumps however, because of their nature, may possibly

introduce some oil contamination which would pose a serious problem since the whole IMS drift tube assembly would then have to be taken apart and meticulously cleaned.

Accurate incorporation of transit time of ions through the quadrupole

A useful study may be to investigate the transit time of ions from the Faraday plate to the channeltron as a function of their mass. A general value of 0.3 ms was used in the investigations since this was observed to be the time taken for the water RIP. It may vary though between ions over a mass range of say m/z 32 to 400 (covering the typical masses of analytes being investigated in our system) up to around 0.5 ms. Taking this into account would then enhance the accuracy of the calculation of K_0 .

Further signal processing of spectral data

It may be that fewer averages will be needed if some post filtering is made using a digital filter having say, a Bessel response (which combines a maximally flat step response in the time domain with good roll-off in the frequency domain). A v.i. to accomplish this is provided within the LabVIEW component library.

Simplified drift tube

A drift tube made using monolithic resistive glass such as that made by Photonis [140] would remove the need for drift rings. This would yield several improvements such as much reduced production cost, a superiorly homogenous drift field and absence of surface charging effects.

Alternative ionisation source

Although a radioactive source is highly convenient for ionisation purposes, it is deemed as hazardous and in order to circumvent the extensive safety procedures and certification involved, other methods have been implemented [141]. Photo ionisation by UV light has

been used [142] but this method yields a limited ionisation current and hence poorer sensitivity. Increasingly, the employment of a direct current (d.c.) corona discharge source is found [143] and the ionisation current is typically an order of magnitude higher than that provided by a ^{63}N radioactive source, but these eventually require replacement due to contamination from sputtering of the electrodes. Their lifetime may however be considerably extended by pulsing the electrodes [144].

7.4 Newly emerging applications

The advantages of the IMS-QMS system over SIFT and PTRMS systems were discussed in chapter 1, section 1.3. Other radically different approaches have been developed such as ‘electronic noses (e-noses)’ and even the use of bees but their application is restricted as they lack the selectivity and broadness of the methods already discussed.

There are ever increasing uses now being found for IMS systems, and in addition to the general areas mentioned in chapter 1, section 1.1, some of the more unusual approaches being found are for:

- Detection of diseases in wood [145]
- Monitoring the fermentation process in beer [146]
- Diagnosis of pathological conditions in animals [147]
- Determining cocaine contamination of banknotes from around the world [148]
- Monitoring the atmosphere on board the International Space Station [149]

7.5 Potential applications for the newly developed IMS-QMS system

The new science that can be developed from the use of the IMS-QMS system relates to an improvement in the understanding of the ion-molecule reactions occurring in atmospheric (high pressure) IMS systems, which can be fed back to develop the technology for it to

achieve its full potential. In pursuit of this, further work is planned for the immediate future to include:

- Supplementary investigations into explosive agents to include the compounds TNT, TNB, DNB and DNT.
- Study of the ion-molecule reactions of compounds used for anaesthetic purposes (enflurane C_2HCl_5 and isoflurane C_2Cl_6) in areas such as operating theatres.

Appendix 8 provides details of proposed papers arising from these and previous investigations using the system.

Apart from ongoing investigations for homeland security purposes, other potential areas offering possible investigation are in the monitoring of landfill gas emissions and also further investigations into the effects of dopants on selectivity.

7.6 Final comments

The development of the IMS-QMS system in the molecular physics laboratory has been a challenging and very interesting project. To see it being put to use for obtaining spectra is most satisfying and it is hoped that it proves to be a valuable addition to the facilities available in the department for continuing research into the applications of IMS.

APPENDICES

Appendix 1

A1.1 – Estimation of ion density and current

It is useful to have an idea of what ion signals can be expected when using a FP in an IMS system for the development of the data acquisition hardware and capture. To approximate this, we start with a calculation of the ion density within the ion source.

The radioactive source producing beta particles has a strength of 10 mCi ($= 37 \times 10^7$ Bq) hence a disintegration rate D of 37×10^7 /s . The mean energy of the β particles is 17 keV. [12] Thus the particles are ejected from the source with sufficient energy to ionise many molecules such as nitrogen which has an ionisation potential of 15.6 eV.

If I = amount of ionisation produced from a β particle then

$$I = \frac{\text{mean energy of } \beta \text{ particle}}{\text{ionisation potential of nitrogen}} = \frac{17 \times 10^3 \text{ eV}}{15.6 \text{ eV}} = 1.1 \times 10^3 \text{ ions per } \beta \text{ particle.}$$

The volume of the cylindrical ^{63}Ni ionisation source is $\sim 0.8 \text{ cm}^3$ and so in every second, the amount of cations ($n+$) produced per unit volume is

$$\frac{D \times I}{V} = \frac{37 \times 10^7 \times 1.1 \times 10^3}{0.8 \text{ cm}^3} = 5.1 \times 10^{11} \text{ cm}^{-3} \text{ s}^{-1}$$

Anions are also being produced through electron attachment. Although the net overall charge of the plasma is zero, there is a reservoir of cations and anions available to be extracted into ionisation region of the drift tube. The rate at which cations are being formed is balanced by the rate at which they are being lost by the processes of extraction by the electric field and recombination with the anions.

In order to estimate the average density of ions with time, the recombination rate must be considered.

If n_+ is the density of cations (ions/cm³) and n_- is the density of anions in the plasma source, then the rate at which cations are lost through recombination is given by the differential equation $\frac{d}{dt}(n_+)_{\text{lost}} = -k(n_+)(n_-)$ where k is the cation - anion recombination coefficient.

At equilibrium, $n_+ = n_-$

and so $\frac{d}{dt}(n_+)_{\text{lost}} = -k (n_+)^2$ where a typical value for k is $10^{-6} \text{ cm}^3 \text{ s}^{-1}$ [150]

In steady state the rates of ion production and recombination are balanced. The number of cations/cm³ is found from: $\frac{D \times I}{V} = k (n_+)^2$. Therefore $n_+ = \sqrt{\frac{D \times I}{V k}}$. Substituting in relevant numbers gives $n_+ = [5.1 \times 10^{17}]^{1/2} = 7.14 \times 10^8$ ions

The drift velocity of the ions as they are extracted from the radiation source by the electric field is around 500 cm/s and so in 1 s, the volume swept through is the cross-sectional area of the source ($=0.8 \text{ cm}^2$) \times 500 cm = 400 cm³. The number of ions in this volume flowing /s is therefore $7.14 \times 10^8 \text{ ions cm}^{-3} \text{ s}^{-1} \times 400 \text{ cm}^3 = 2.9 \times 10^{11} \text{ s}^{-1}$.

The ion current = $2.9 \times 10^{11} \times 1.6 \times 10^{-19} \sim 4.6 \times 10^{-8} \text{ A}$ (46 nA)

This simple calculation has not taken into account possible losses in the drift tube (e.g. at the gate and through diffusion). Further more, the calculation does not take into account extraction of the ions from the ion source. Nevertheless, we can expect at best tens of nA from the FP. Correspondingly all electronics were designed on the assumption that typically nA need to be detected. Experimentally, we recorded a current from the FP of approximately 1nA.

A1.2 – Calculation of E/N within the drift tube

The gas number density N of the drift gas can be related to its pressure and temperature as follows:

At STP, $T_0 = 273.15\text{ K}$, $P_0 = 1013\text{ mbar}$ and 1 *mole* of gas contains N_A molecules occupying 22.414 l where Avogadro's number $N_A = 6.022 \times 10^{23}$ molecules/mol.

If n = the number of moles of drift gas in a volume V and N = number density of the drift

gas, then $N = \frac{n}{V}$. Therefore at STP, $N_0 = \frac{N_A}{V_0} = \frac{6.022 \times 10^{23}}{22.414 \times 10^3\text{ cm}^3} = 2.687 \times 10^{19} / \text{cm}^3$

The gas law states that $PV = nRT$ and so substituting $n = NV$ produces $P = NRT$

Therefore the ratio $\frac{P_0}{P} = \frac{N_0 T_0}{NT}$ hence $N = \frac{N_0 T_0}{P_0} \times \frac{P}{T}$

But as stated above, $N_0 = \frac{N_A}{V_0}$ therefore $N = \frac{N_A T_0}{V_0 P_0} \times \frac{P}{T}$

Using a typical pressure and temperature of 1006 mbar and 303.15 K gives:

$$N = \frac{6.022 \times 10^{23} \times 273.15 \times 1006}{22.414 \times 1013 \times 303.15} = 2.404 \times 10^{19} / \text{cm}^3$$

The field strength $E = 212\text{ V/cm}$, therefore $\frac{E}{N} = \frac{212}{2.404 \times 10^{19}} = 8.82 \times 10^{-18}\text{ Vcm}^2$

$$= 0.882 T_d$$

A1.3 – Comparison between thermal and drift kinetic energies of an ion

Consider a hydronium ion H_3O^+ of $m/z = 19$. Assuming thermal equilibrium, the average thermal KE of the ion is $KE_{av} = \frac{3}{2} kT$ where $k =$ Boltzmanns constant ($= 8.167 \times 10^{-5}$ eV/K). When the temperature T is 303.15 K (30°C being the drift tube operating temperature) then:

$$KE_{av} = \frac{3}{2} \times 8.617 \times 10^{-5} \times 303.15 \text{ eV} = 0.039 \text{ eV}$$

The overall KE aquired from the electric field after reaching a steady state drift velocity v_d is given by $KE_{field} = \frac{1}{2} m v_d^2$ and from experiment, it was seen that $v_d = 5 \text{ m/s}$.

Virtually all of the hydronium ions will react with the water clusters and a typical cluster size of $m/z = 73$ (predominantly seen in the mass spectra discussed in chapter 5) can be considered.

$m/z = 73$ corresponds to a molecular mass of $73 \times 1.66 \times 10^{-27} \text{ Kg} = 12.18 \times 10^{-26} \text{ Kg}$.

Therefore:

$$KE_{field} = \frac{1}{2} \times 12.18 \times 10^{-26} \times 5^2 = 15.23 \times 10^{-25} \text{ Joules}$$

$$\text{But } 1 \text{ eV} = 1.602 \times 10^{-19} \text{ J and so } KE_{field} = \frac{15.23 \times 10^{-25}}{1.602 \times 10^{-19}} = 9.50 \times 10^{-6} \text{ eV}$$

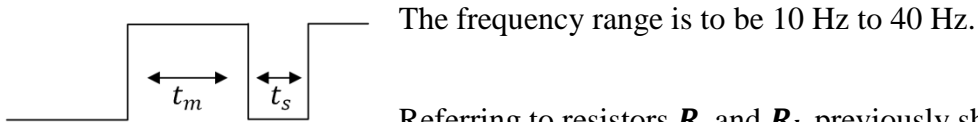
and the ratio of KE_{field} to KE_{av} is then $\frac{9.50 \times 10^{-6}}{0.039} \times 100\% = 0.024\%$.

i.e. the ions remain thermal

APPENDIX 2

A2.1 Determining the component values for the trigger and gate pulse generator

The astable section



Referring to resistors R_a and R_b previously shown in chapter 2, figure 2.3, then for the pulse waveform the timing formulae are:

$$t_m = 0.7(R_a + R_b)C \quad \text{and} \quad t_s = 0.7R_bC$$

Therefore the pulse repetition frequency, $f = \frac{1.44}{(R_a + 2R_b)C}$ (2A.1)

Choosing a value for $C = 0.47 \mu\text{F}$ and $t_s = 10 \text{ ms}$, then $R_b = \frac{t_s}{0.7C} = \frac{10 \times 10^{-3}}{0.7 \times 0.47 \times 10^{-6}} = 30.4 \text{ k}\Omega$.

Thus at a frequency of 10 Hz, $t_m + t_s = 100 \text{ ms} \therefore t_m = 90 \text{ ms}$

Transposing the above equation for t_m ,

$$R_a = \frac{t_m}{0.7C} - R_b = \frac{90 \times 10^{-3}}{0.7 \times 0.47 \times 10^{-6}} - 30.4 \text{ K} = 243 \text{ k}\Omega$$

At 40 Hz, $t_m + t_s = 25 \text{ ms} \therefore t_m = 15 \text{ ms}$

$$\therefore R_a = \frac{15 \times 10^{-3}}{0.7 \times 0.47 \times 10^{-6}} - 30.4 \text{ K} = 15.2 \text{ k}\Omega$$

Referring to figure 2.3 it is seen that $R_a = R_v + R_1$

Thus, with $R_v = 0$ (at $f = 40 \text{ Hz}$), $R_1 = R_a = 15.2 \text{ k}\Omega$ leaving $R_v = 243 - 15.2 = 227.8 \text{ k}\Omega$

Clearly this is not a standard value, so choosing R_v to be a 100 k Ω linear law potentiometer, the respective values of the other components need to be scaled accordingly.

If the resistor values are scaled down, then the capacitor value must be scaled up in proportion to keep the required times unchanged.

Thus, if R_a is halved, then C must be doubled.

Let $R_a = 243/2 = 121.5$ k Ω , then with $R_v = 100$ k Ω , $R_1 = 121.5 - 100 = 21.5$ k Ω

Similarly, $R_b = 30.4 / 2 = 15.2$ k Ω

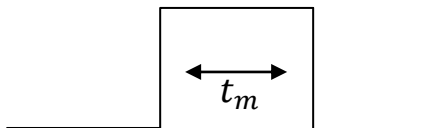
The final component values (to nearest preferred value) are therefore:

$R_v = 100$ K $R_1 = 22$ K $R_b = 15$ K $C = 0.94$ μ F (two 0.47 μ F capacitors in parallel)

A2.2 The monostable section

The gate pulse duration range is to be 0.2 ms to 4 ms.

Referring to R_a previously shown in Fig 2.4 then for the pulse shown below, $t_m = 1.1R_aC$



Choosing a value for $C = 0.47$ μ F, then with $t_m = 4$ ms, $R_a = \frac{t_m}{1.1C} = \frac{4 \times 10^{-3}}{1.1 \times 0.47 \times 10^{-6}}$

= 7.8 k Ω . When setting $C = 0.047$ μ F, R_a will be $10 \times 7.8 = 78$ k Ω

At $t_m = 0.2$ ms, $R_a = \frac{0.2 \times 10^{-3}}{1.1 \times 0.047 \times 10^{-6}} = 3.9$ k Ω

At $t_m = 4$ ms, (20×0.2) $R_a = 3.9$ k $\Omega \times 20 = 78$ k Ω

Thus, the range of variation in R_a is $(78 - 3.9) \text{ K} = 74.1 \text{ k}\Omega$

If again a $100 \text{ k}\Omega$ pot is used, then the scaling ratio will be $100/74.1 = 1.35$ for the resistors, and $1/1.35 = 0.74$ for the capacitor(s).

Thus, $R_1 = 3.9 \text{ k}\Omega \times 1.35 = 5.27 \text{ k}\Omega$ and $C = 0.47 \text{ }\mu\text{F} \times 0.74 = 0.35 \text{ }\mu\text{F}$

The final component values (to the nearest preferred value) are therefore:

$$R_v = 100 \text{ k}\Omega \quad R_1 = 5.2 \text{ k}\Omega$$

and $C = 330 \text{ nF}$ in parallel with 22 nF (making approximately $0.35 \text{ }\mu\text{F}$)

A2.3 Lens Power Supply Unit

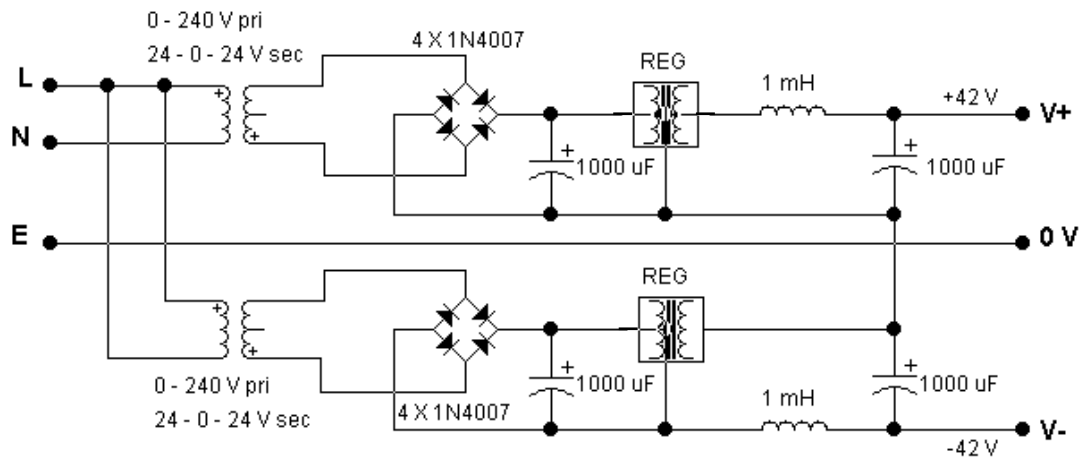


Figure A2.3.1 Schematic diagram of the lens PSU

In figure A2.3.1 the regulator REG is formed as shown in figure A2.3.2.

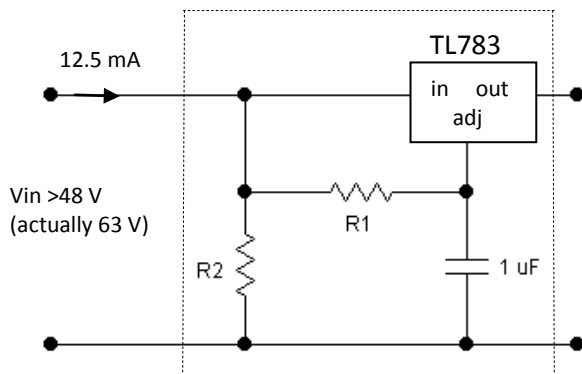


Figure A2.3.2 showing composition of REG

Referring to figure A2.3.2, the current into the adj terminal is $83 \mu\text{A}$, and $R2$ is suggested in the data sheet [35] to be 82Ω . From the data sheet, the output voltage is found from:

$$V_{\text{OUT}} = V_{\text{ref}}(1 + R2/R1) \text{ where } V_{\text{REF}} = 1.25 \text{ V, thus for } V_{\text{OUT}} = 40\text{V,}$$

$$40 = 1.25(1 + R2/82) \text{ giving } R2 = 2542 \Omega \text{ (2K7 to npv).}$$

Using a value of 2K7 gives $V_{OUT} = 1.25(1 + 2700/82) = 42.4$ V (which when measured was actually +42.1 V and -42.3 V). Note, $W_{R2} = 42.4^2/2700 = 0.67$ W so a 1 W rating resistor was used.

Lens voltage adjustment

The voltage can be adjusted from the positive and negatives extremes as shown in figure A2.3.3.

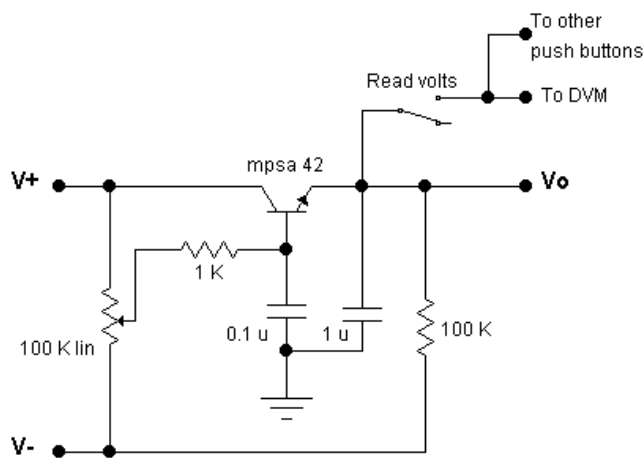


Figure A2.3.3. Circuit for lens voltage adjustment. The wire to the DVM is coloured purple.

A modification was made to boost the positive voltage to enable lens F2 to reach 65 V, as shown in figure A2.3.4.

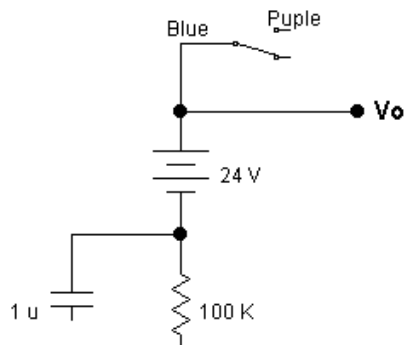


Figure A2.3.4 showing circuit for F2 boost

At the FP amplifier box, the screen grid supply is further filtered to remove 50 Hz noise picked up by the screened supply lead. Since the current drawn is negligible, a relatively high resistor value can be used, as shown in figure A2.3.5.

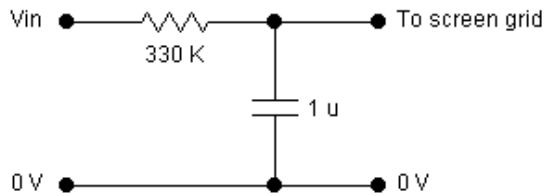


Figure A2.3.5 showing the 50 Hz noise filter to the screen grid

At 50 Hz, the reactance of the capacitor $X_c = 3 \text{ k}\Omega$ and so a 100:1 reduction in noise is made. When connecting an oscilloscope to the screen, a 1.5 mV p-p ripple was seen. This is equivalent to $1.5 \times 10^{-3} \times 10^{-7} \text{ A/V}$ ie 0.15 nA noise equivalent.

The front panel consists of five push buttons and voltage adjustment pots to select which lens output to view on the digital panel meter, as seen in figure A2.3.6.

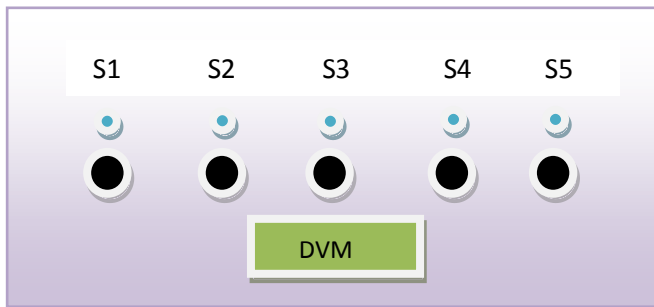


Figure A2.3.6 showing the layout of the front panel of the lens PSU

Internal wiring to the output socket on the lens PSU, and the plug connecting to the FP amplifier box and quadrupole lenses

The outputs from the PSU appear on a 9-way ‘D’ socket as shown in figure A2.3.7.

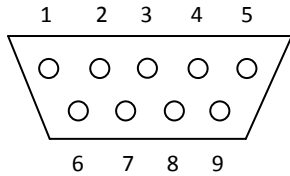


Figure A2.3.7 showing the pin arrangement (rear solder view) of the 9-way 'D' type output socket on the lens PSU

Table A2.3.1 lists the assignments of the pins for wiring from the internal supplies to the 9-way 'D' type socket at the rear of the lens.

Table A2.3.1

Pin	1	2	3	4	5	6	7	8	9
Button	S1	0V	S2	n/c	S3	S4	n/c	S5	n/c
Lens	Scn. Grid	Gnd	FP	-	Cone	Lens 1 Fc	-	Lens 2 F2	-
Wire	Brown	Black	Red	-	Yellow	Green	-	Blue	-

The lens voltages appear on the pins of the 9-way 'D' type plug at the end of the connecting cable going to the FP amplifier box as shown in figure A2.3.8.

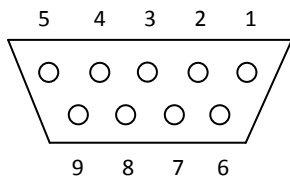


Figure A2.3.8 showing the pin arrangement (rear solder view) of the 9-way 'D' type output plug on the connecting lead (FP amplifier box end).

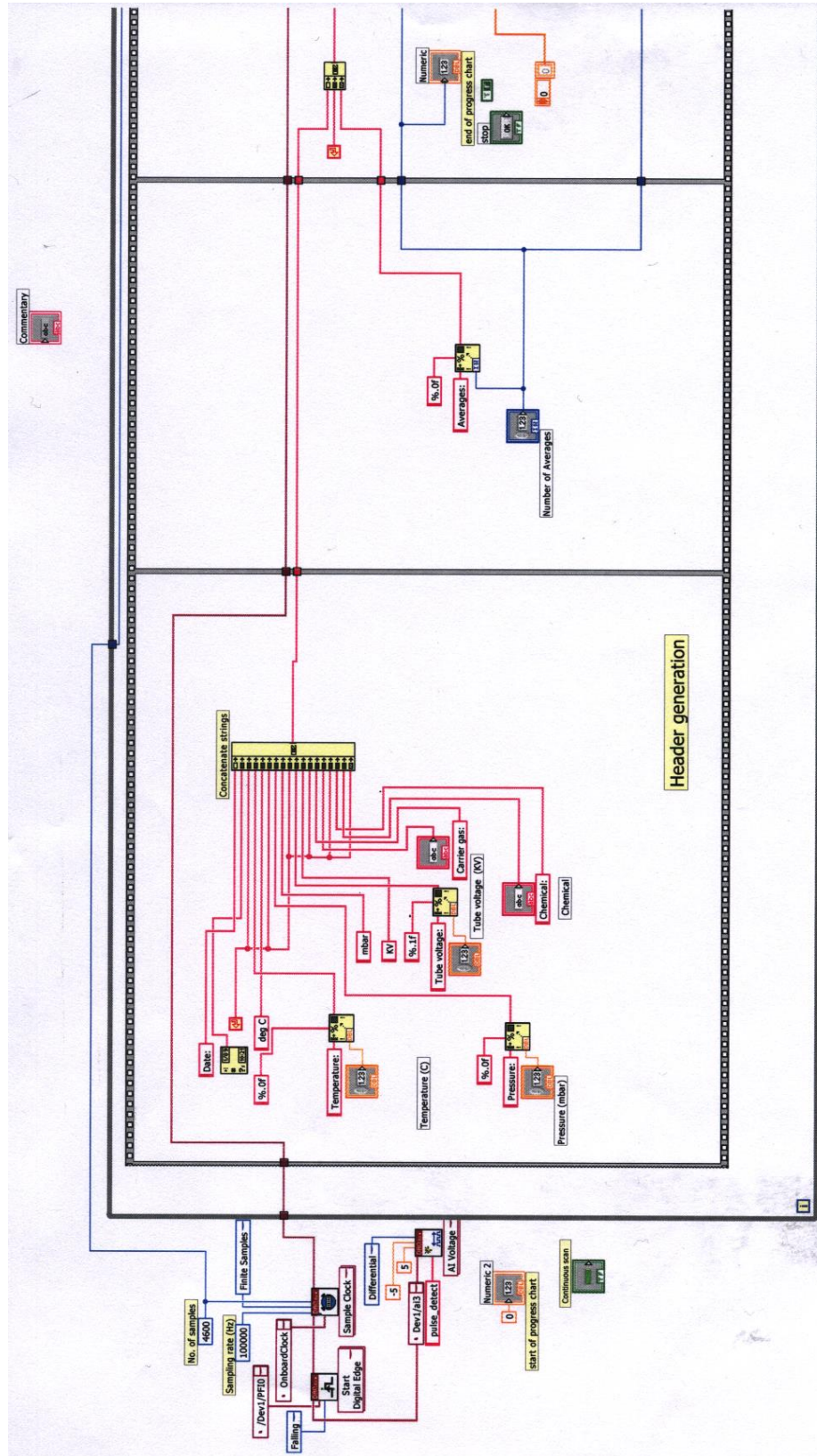
Table A2.3.2 lists the assignments of the pins in the 'D' type plug on the connecting cable connecting to the FP amplifier box.

Table A2.3.2

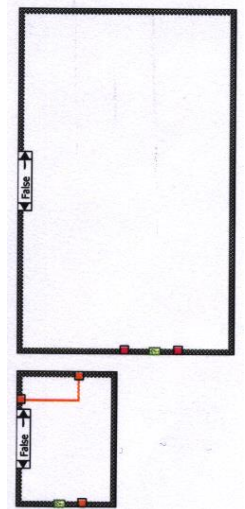
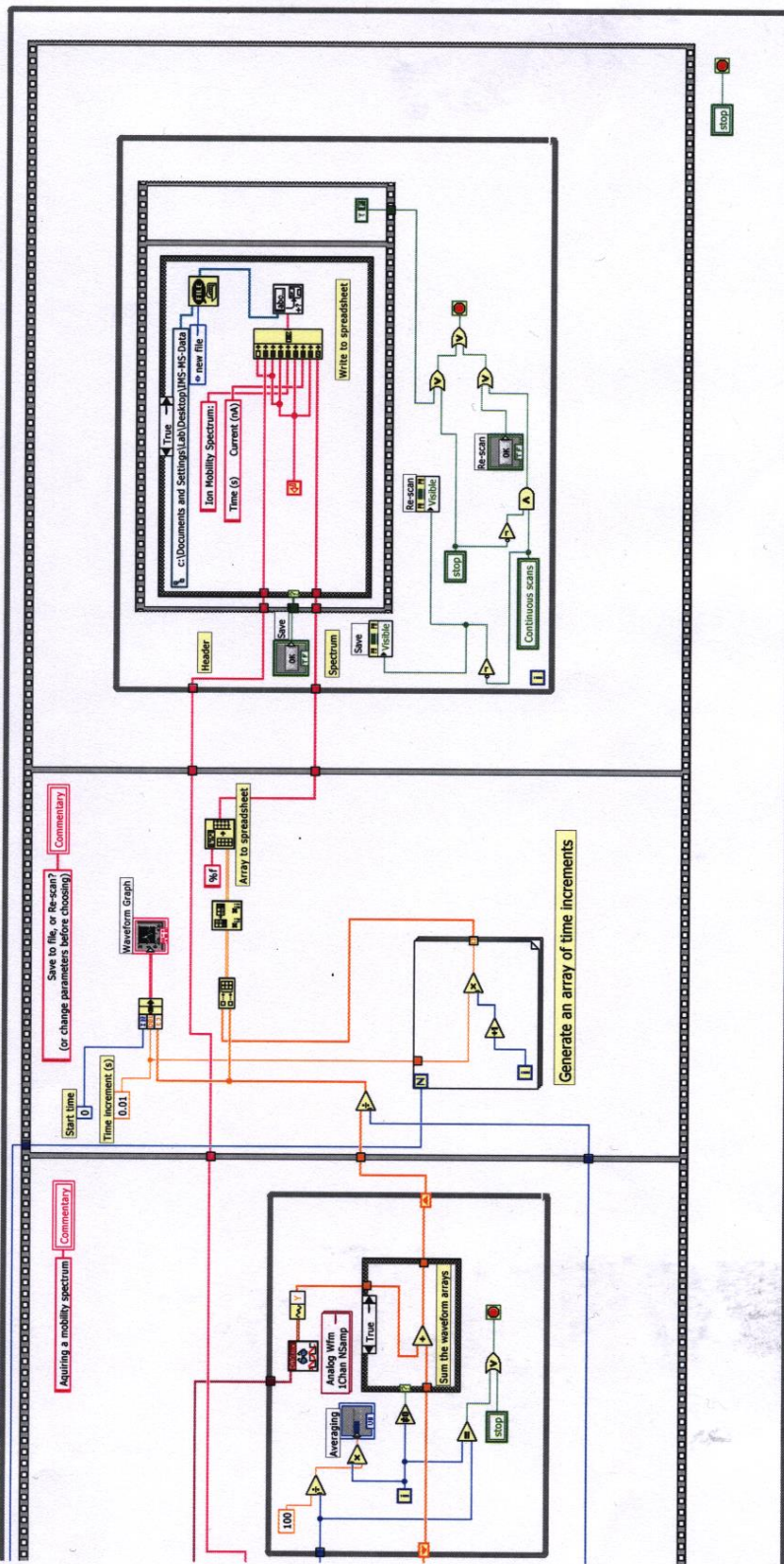
Pin	1	2	3	4	5	6	7	8	9
Button	S1	0V	S2	n/c	S3	S4	n/c	S5	n/c
Lens	Scn. Grid	Gnd	FP	-	Cone	Lens 1 Fc	-	Lens 2 F2	-
Wire	White	Screen of cable	Purple	-	Black	Blue	-	Brown	-

APPENDIX 3 (note, all the programs are on a cd included with the thesis)

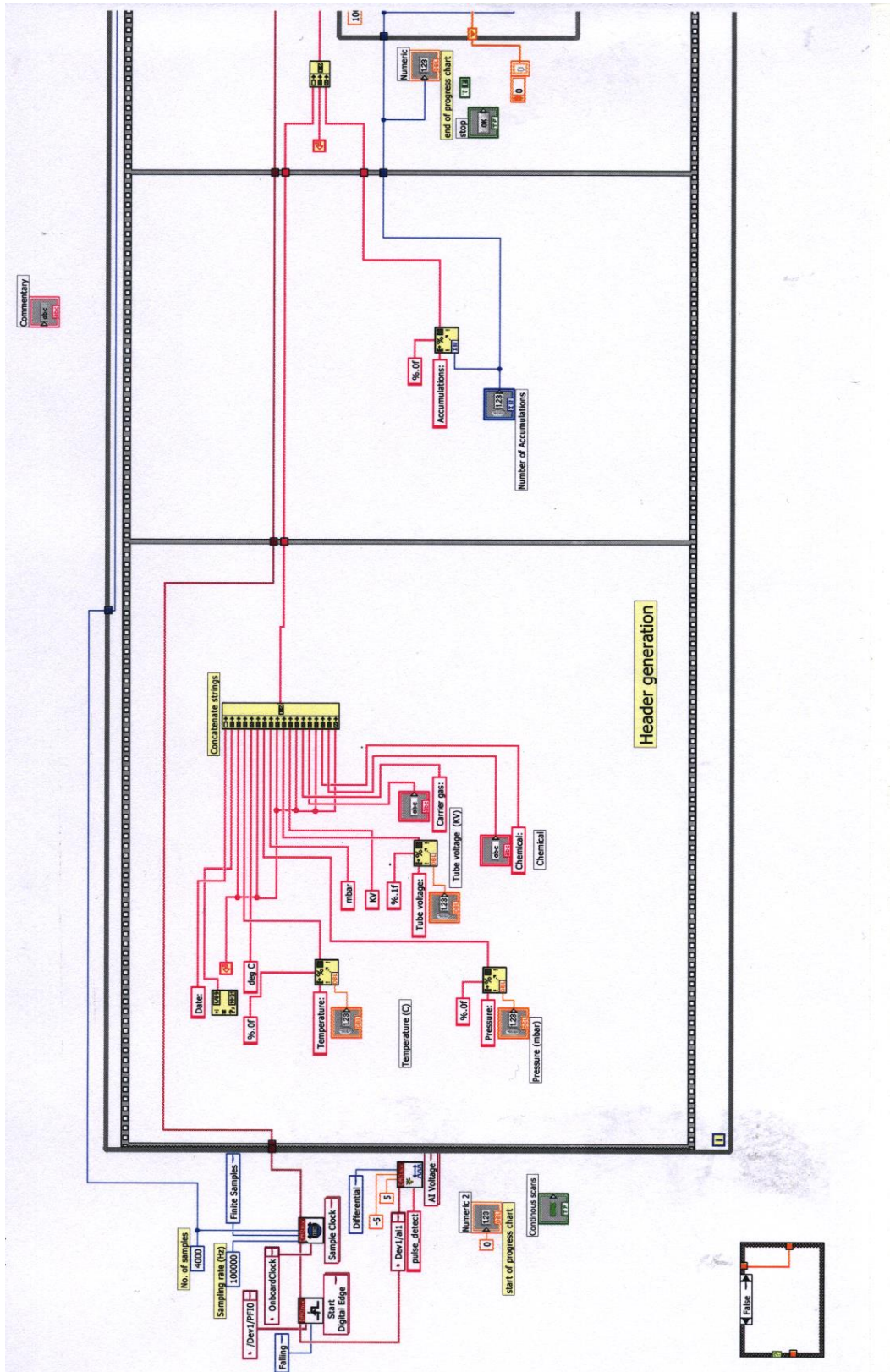
A3.1 LabVIEW program IMS.vi – first section



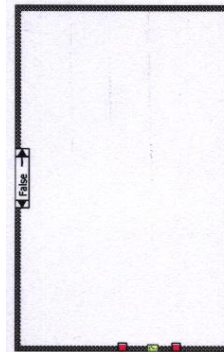
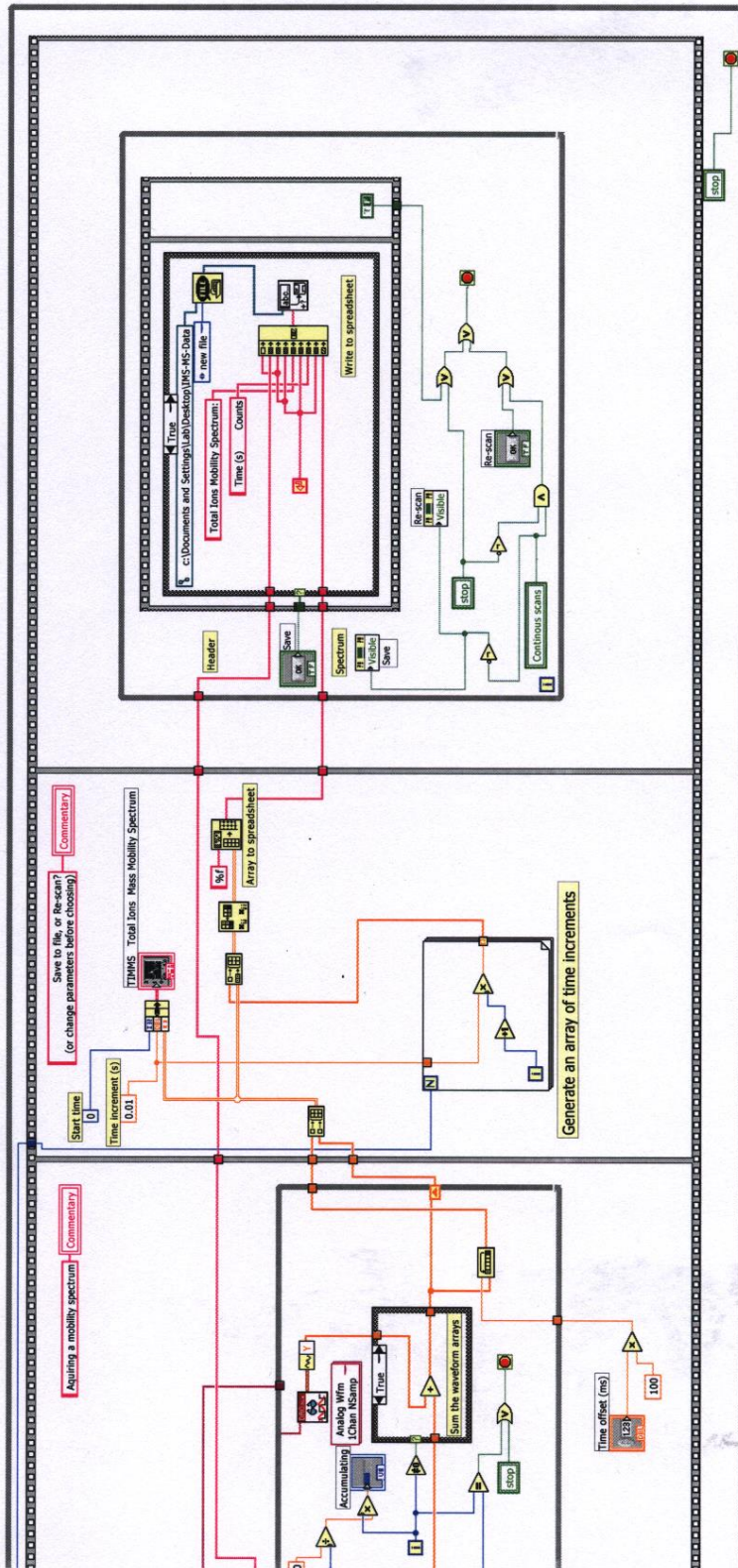
LabVIEW program IMS.vi – second section



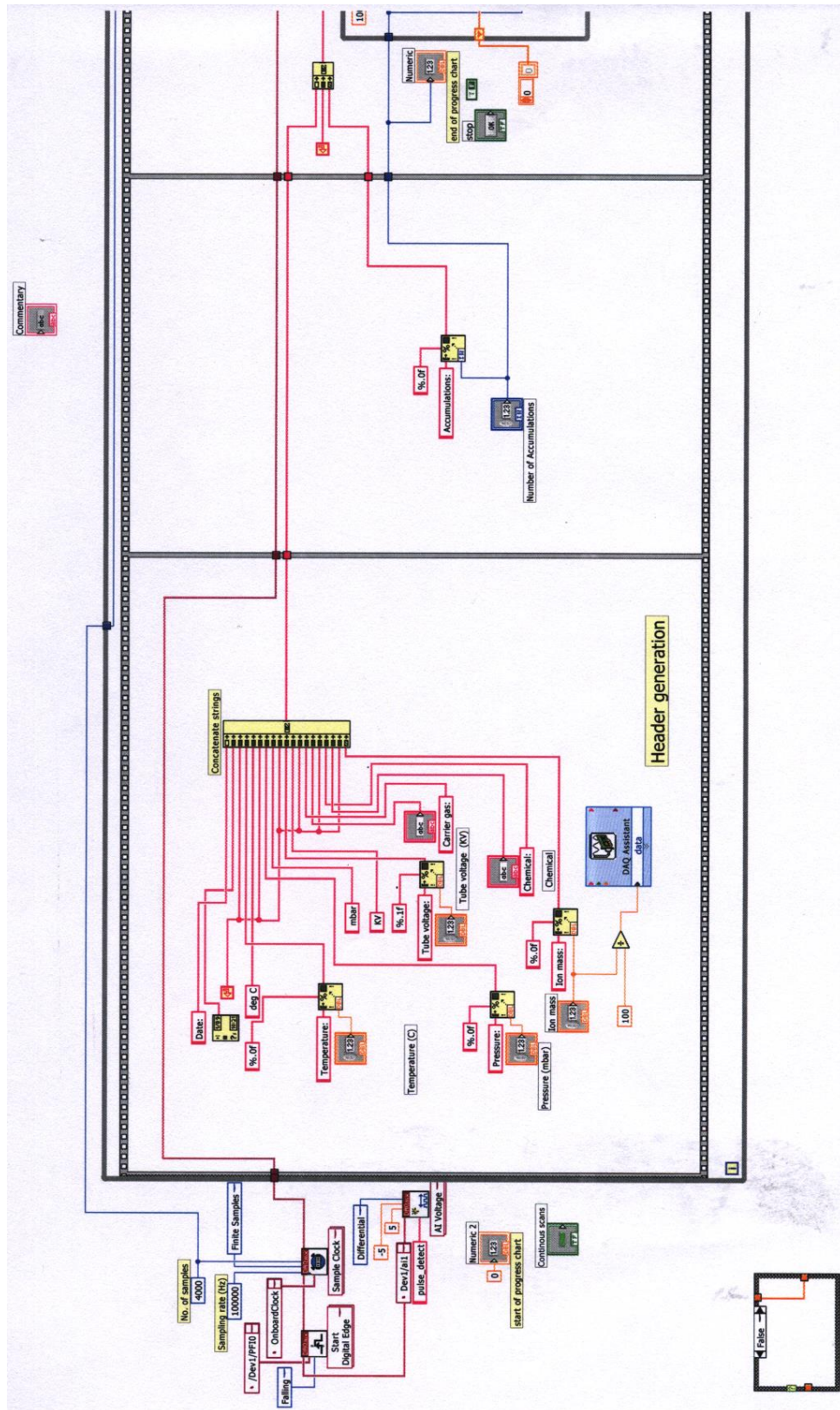
A3.2 LabVIEW program TIMMS.vi – first section



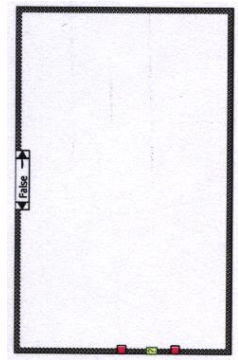
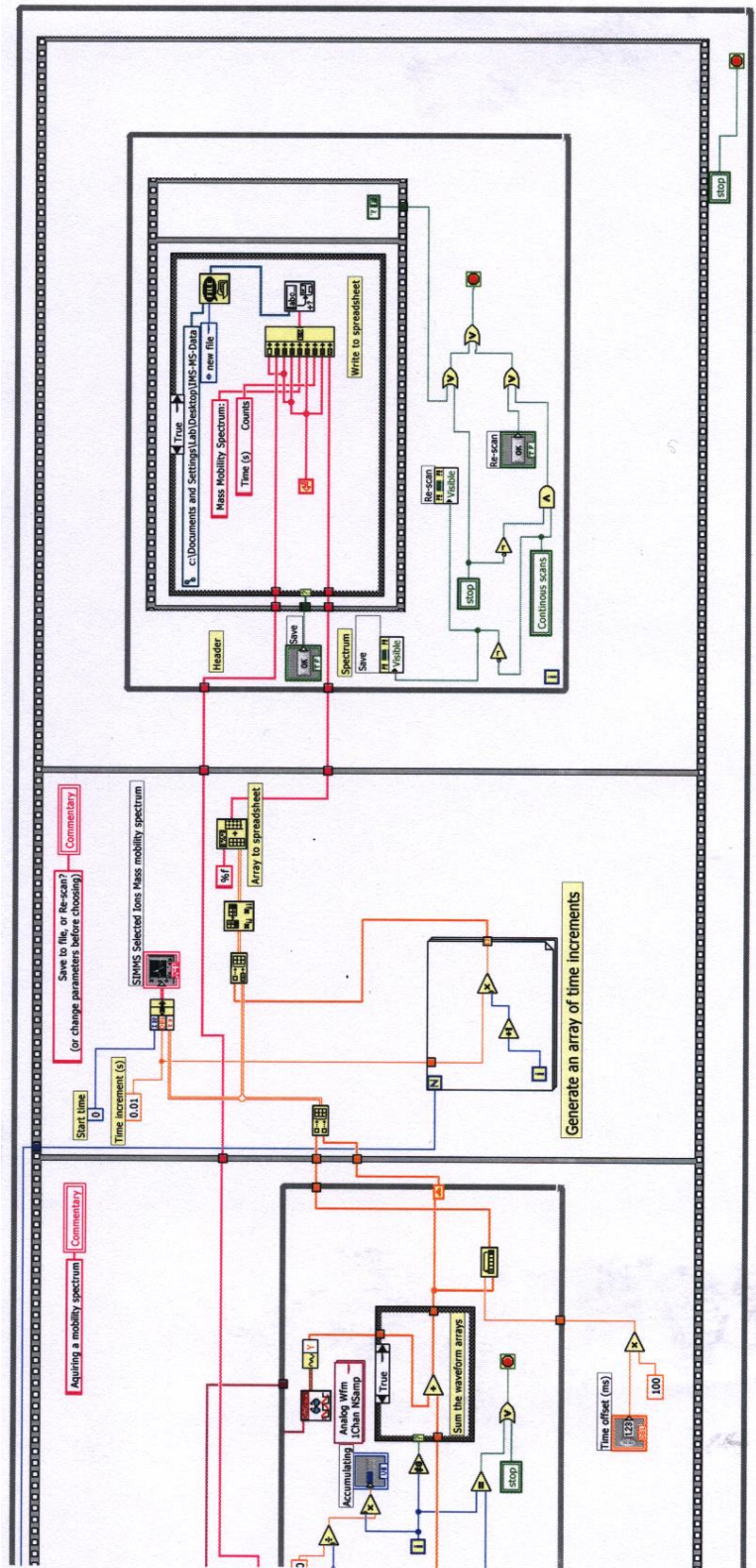
LabVIEW program TIMMS – second section



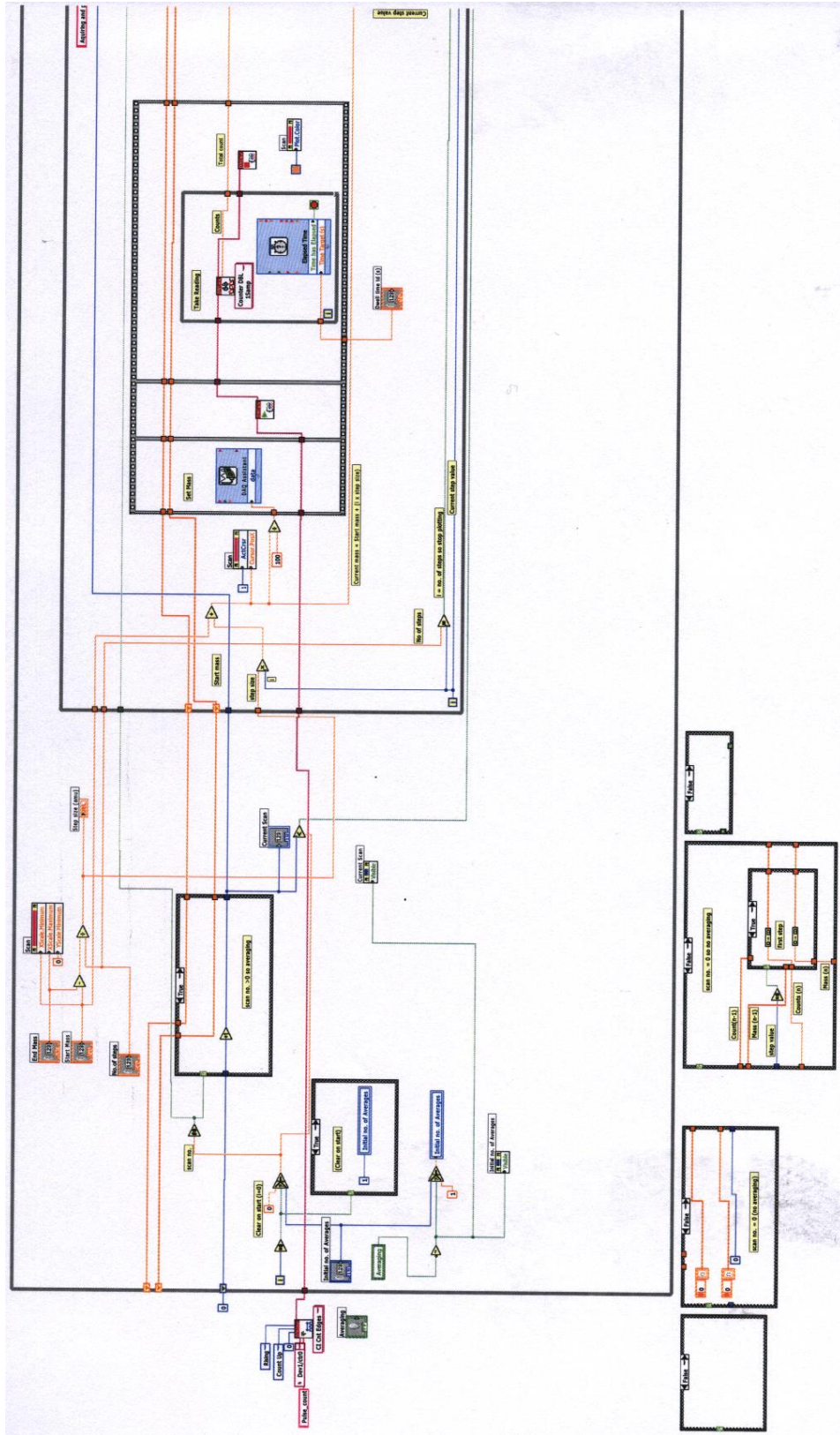
A3.3 LabVIEW program SIMMS.vi – first section



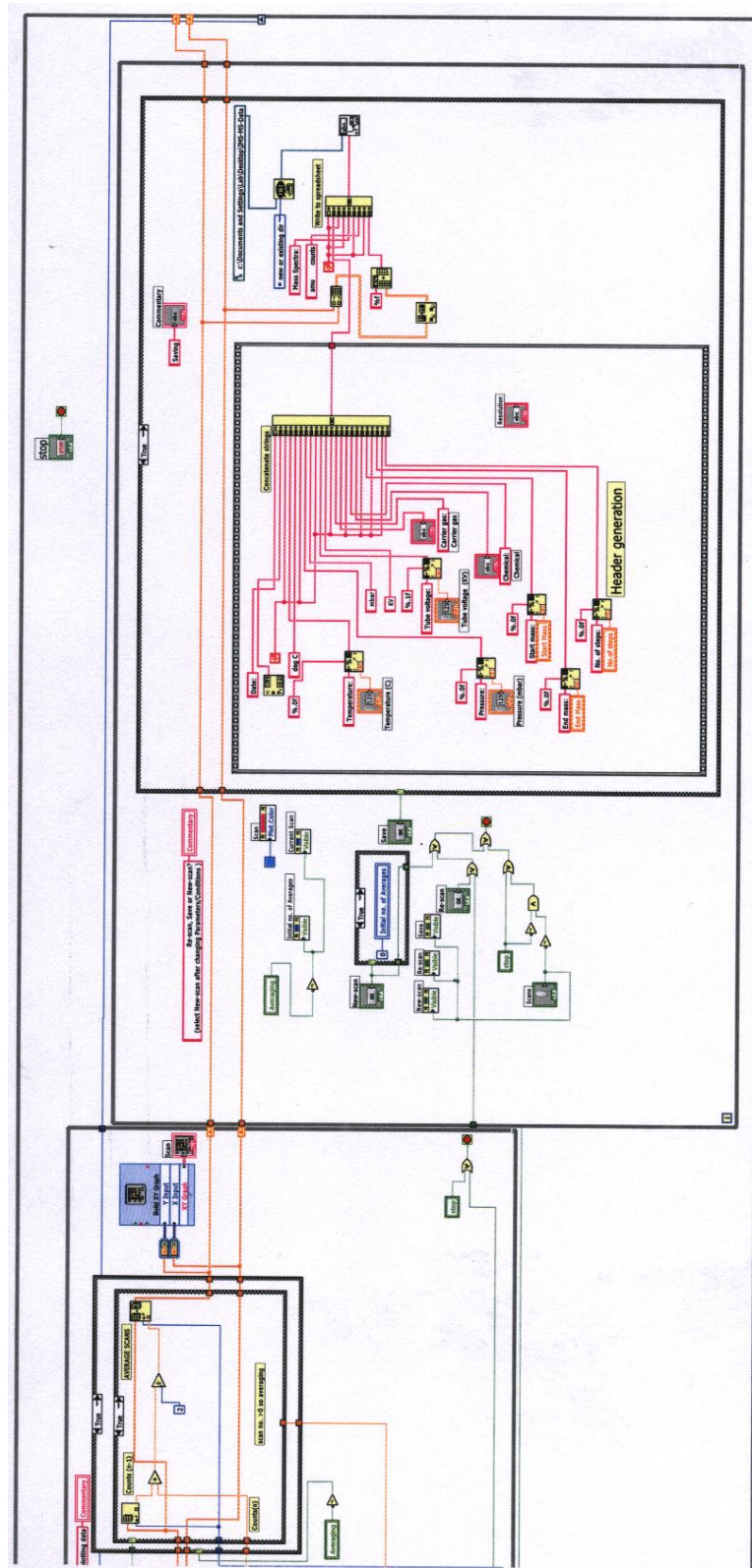
LabVIEW program SIMMS.vi – second section



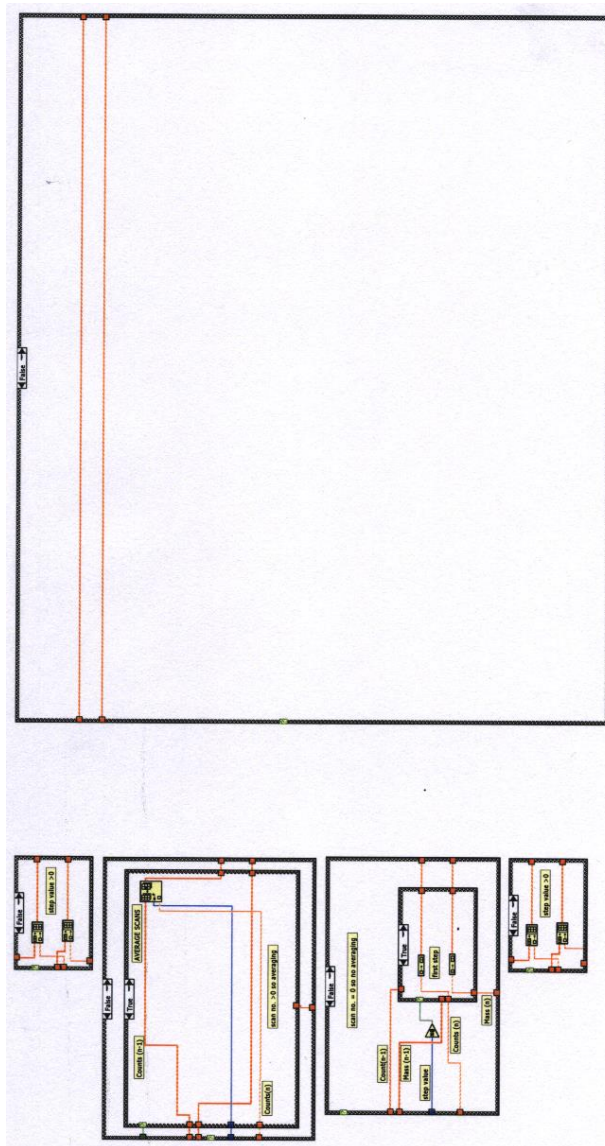
A3.4 LabVIEW program MS.vi – first section



LabVIEW program MS.vi – second section



LabVIEW program MS.vi – third section



A3.5 Averaging over several spectral scans with the MS program

- Select 'Single Scan' mode
- Switch 'Averaging' on
- Press the 'New Scan' button (this sets the initial average to zero and acquires the first scan)
- Set the required number of averages
- Press the 'Re Scan' button to average over the scans

APPENDIX 4

A4.1 Bringing the drift tube up to atmospheric pressure using lab air (with the drift tube pumped down, rotary and turbo pumps working.)

1. Initiate gas flows:

- a) Ensure forward/contra flow valves are shut off.
- b) Power up the mass flow controllers
- c) Open the compressed air valve.
- d) Slowly open the forward and contra flow valves and monitor the tube pressure.
- e) When the pressure reaches 1010 mbar open the green exhaust valve.
- f) Check the flow rates on the mass flow controllers

2. Switch on:

- a) Lens power supply (if not already on)
- b) 12V power supply
- c) Gate interface unit
- d) HV power supply (set to 4 kV)
- e) SXP unit
- f) RF controller
- g) Pulse pre-amplifier

3. Configure the SXP unit and set the Faraday Plate Switch as required.

(See appendix sections 5A.6 or 5A.7 for the SXP settings).

Shutting Down. (Tube evacuates via the orifice in the FP).

4. Switch off:

- a) Pulse pre-amplifier
- b) RF Controller
- c) SXP unit
- d) HV power supply
- e) Gate interface unit
- f) 12 V power supply
- g) Lens power supply (leave on to stabilise if using over a period of days)

5. Evacuate the drift tube.

- a) Close the green exhaust valve and immediately shut off the forward and contra flows.
- b) Remove the power to the mass flow controllers. (Otherwise with no flow through them their control valves will be permanently energised causing them to get hot.),

A4.2 Bringing the IMS-MS system up to atmosphere and shutting down

1. Bring the IMS drift tube up to atmospheric pressure (see appendix 5A.2)
2. Press STOP on Turbo 1 controller
3. Wait approx 1 minute
4. Press STOP on Turbos 2 and 3 controllers
5. Wait approx 1 minute
6. Close Rotary 1 valve
7. Wait approx 1 minute
8. Close Rotary 2 and rotary 3 valves
9. Turn off the rotary pumps
10. Open the air valve on Turbo 1
11. Switch off the turbo fans

The MS system will now gradually vent up to atmospheric pressure.

Turning on the system and pumping down

1. Switch the turbo fans on
2. Close the air valve on Turbo 3
3. Turn on rotary pumps 3,2 and 1
4. Slowly open the valves on rotary pumps 3 and 2
5. Wait 1 minute
6. Open the valve on rotary pump 1
7. Wait until the pressure is $< 10^{-1}$ mbar
8. Turn on Turbo 3
9. Turn on Turbo 2
10. Wait 1 minute
11. Turn on Turbo 1

Close the green valves on the IMS system to seal against carrier gas flows

A4.3 Changing the set point on the mass flow controllers

- Press **Main**, (*shows the totalised flow*), **Total**, **Control Set up**
- Press **Input** until the select symbol > points to **Local**
- Press select until **Set** is pointed to
- Use **Up** and **Down** to get the required set point
- To exit, press **Control Set up, Menu**

A4.4 Wiring changes for selecting the ion polarity

Positive ion mode

- Connect the bnc lead between the socket marked **M** at the rear of the **quadrupole** and the socket marked **MULTIPLIER** at the rear of the **rf controller**.
- On the **PCDU** box, connect the 0 Ω link (marked **LINK**) to the socket marked **EI/P**

Negative ion mode

- Connect the 22 M Ω link (marked **BIAS**) to the socket marked **M** at the rear of the quadrupole.
- On the **PCDU** box, connect the bnc lead between the socket marked **EI/P** and the socket marked **MULTIPLIER** at the rear of the **rf controller**.

A4.5 IMS-QMS Settings – Positive ion mode

$V_{\text{GATE}} = 100 \text{ V}$

Parameter combination	Keyboard combination	(Other Parameters)	Keyboard
Polarity = +	V (ions)		F1
Lens 2 = -26 V	V		F4
Ext mass ON	V		F5
	<i>(On for spectra display with LabVIEW, OFF for spectra display on SXP)</i>		
Focus = 0 V	Z (source)	F6	Scale B (spectrum) F5
Pole bias = 0 V	X (filter)	F1	Gain range C (detector) F3
Resolution	X	F2,F3	
Total ions OFF	X	F5	
SEM = 2500 V	C (detector)	F2	

On multi-power supply

Screen = 25 V (Nominal for IMS) *The best lens settings were found by tuning with the TIMMS program, using 500 accumulations (gave 40 ± 4 counts). (Using water chemistry.)*

FP = 20 V (Variable for MS)

Cone = 14 V

FC = -15 V

F2 = -25 V

To obtain total ions mass mobility spectra (using the TIMMS program):

Parameter	Keyboard combination
Ext mass OFF	V (ions) F5
Total ions ON	X (filter) F5
First mass = 10 amu	B (spectrum) F1 <i>(for total ion count of all with masses > 10 amu)</i>
Mass span = 0	B (spectrum) F2

A4.6 IMS-QMS Settings – Negative ion mode

$V_{\text{GATE}} = 30 \text{ V}$

Parameter combination	Keyboard combination	(Other Parameters)	Keyboard
Polarity = –	V (ions)		F1
Lens 2 = 6 V	V		F4
Ext mass ON	V		F5
	<i>(On for spectra display with LabVIEW, OFF for spectra display on SXP)</i>		
Focus = 12 V	Z (source)	F6	Scale B (spectrum) F5
Pole bias = 34 V	X (filter)	F1	Gain range C (detector) F3
Resolution	X	F2,F3	
SEM = 2800 V	C (detector)	F2	

On multi-power supply

Screen = -37 V (Nominal for IMS) *The best lens settings were found by tuning with the TIMS program, using 500 accumulations which gave 150counts. (Using water chemistry.)*

FP = -12V (Variable for MS)

Cone = 0 V

FC = 20 V

F2 = 65 V

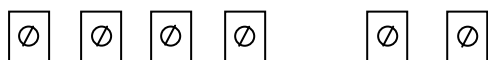
To obtain total ions mass mobility spectra (using the TIMMS program):

Parameter	Keyboard combination
Ext mass OFF	V (ions) F5
Total ions ON	X (filter) F5
First mass = 10 amu	B (spectrum) F1 <i>(for total ion count of all with masses > 10 amu)</i>
Mass span = 0	B (spectrum) F2

A4.7 Calibrating the SXP unit. (0 to 600 amu)

The 10 turn pots are located behind the front panel on the r.f. controller. Undo the two upper screws only and hinge the panel downwards.

Layout of the calibration control potentiometers



LR Mass Scale LM Δ M RES
Slope Offset

Operation:

LR Affects the peak width in the lower third of mass range. Adjust at around 28 amu.

Mass Slope Sets the position of the high mass peaks. Adjust at around 614 amu.

Scale Offset Sets the position of the low mass peaks.

LM Affects peak width (no further information available)

Δ M Adjusts peak width (0 – 100%) uniformly over the whole mass range.
Adjust on a central peak (around 264 amu)

RES Affects the peak width with progressively more effect at higher masses.
Adjust at around 502 amu.

Note: It may be required to re-adjust Δ M afterwards and to re-check the mass adjustments.

Taken from SXP Elite Operator Manual page IV-59.

A4.8 Removing the IMS drift tube from the system

Preparatory:

- Ensure that all voltage sources are turned off (including the heater).
- Ensure that the drift tube is at atmospheric pressure.
- To allow easier access to the drift tube, disconnect and remove the ± 12 V power supply and the gate pulse generator. Unplug all of the high voltage connectors from the connector box and ion voltage selector unit, and remove the gate interface unit.

Procedure:

1. Disconnect the contra flow at the pressure gauge T piece leaving the 6 cm long pipe attached to the drift tube flange.
2. Disconnect the forward flow at the sample inlet T piece leaving the 8 cm long pipe attached to the drift tube
3. Disconnect the exhaust at the drift tube flange
4. If required, remove the six 2.5 mm Allen bolts from the IMS flange and withdraw the ionisation source assembly.

Caution! RADIATION HAZARD - β rays are emitted from the open end of the radiation source, so position it accordingly on the bench to prevent exposure.

5. Unscrew the eight $\frac{1}{2}$ inch bolts on the flange (support the flange when removing the last (top) bolt and carefully withdraw the drift tube assembly).

Removing the screen grid

Wearing gloves to minimise contamination:

1. Remove the solder from the electrical connection tag.
2. Remove the three M2 mounting screws along with their insulators.
3. Withdraw the screen grid and insulating washer. (This may require holding the soldering iron on the joint to ensure that the wire is disconnected).

Attaching the screen grid

Attach in reverse order to the above, but ensure that the orifice in the Faraday plate is central with the hole in the screen grid so that ion flow is not impeded. To assist in location of the insulating washer, it may be found easier to fix the screen grid onto the Faraday plate by first passing the screw-insulators through the holes in the screen grid and then attaching the insulating washer to the grid via the screws. The assembly can then be placed against the Faraday plate in the alignment shown and screwed into position.

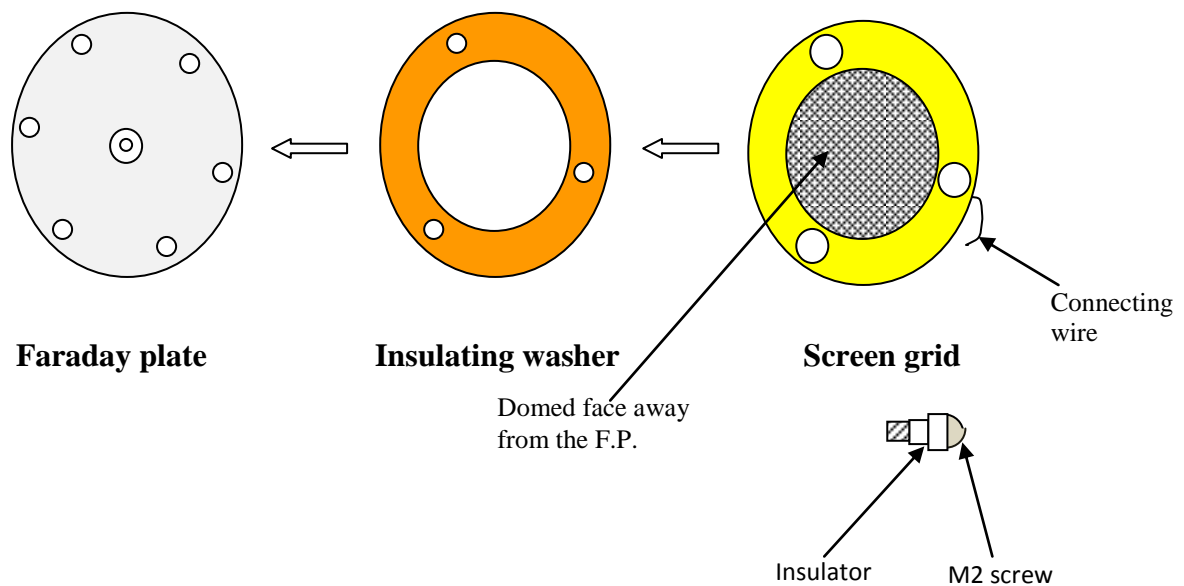
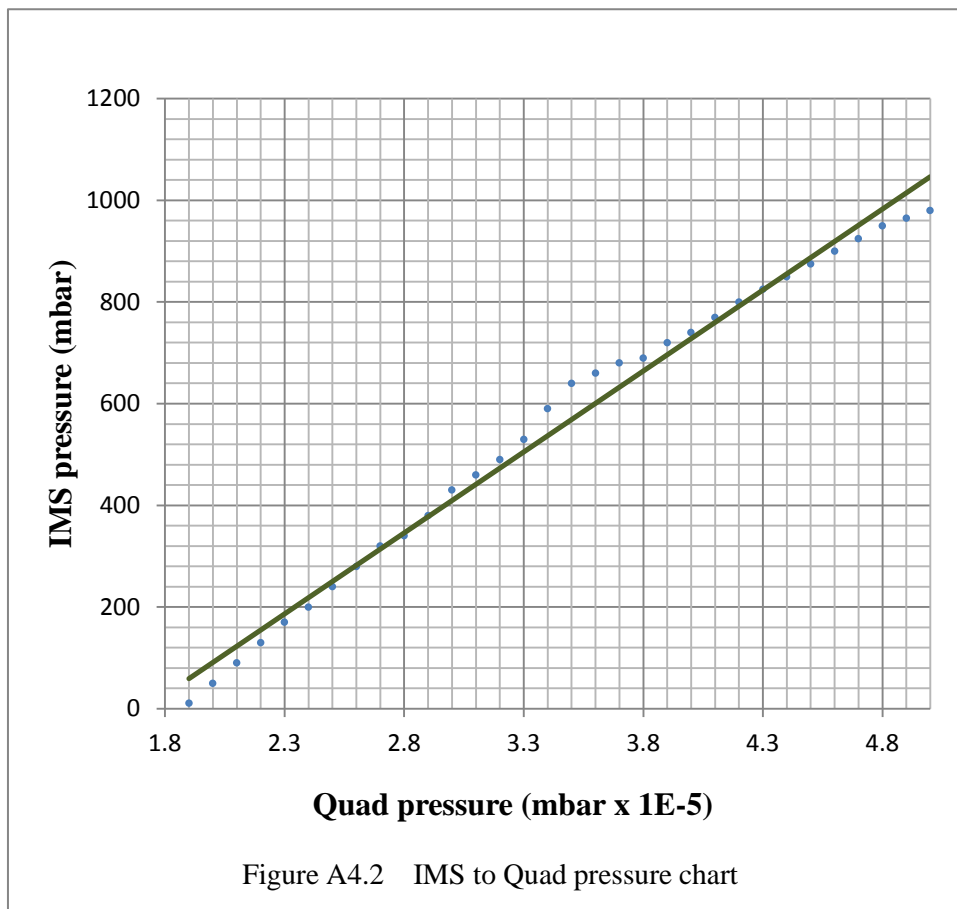


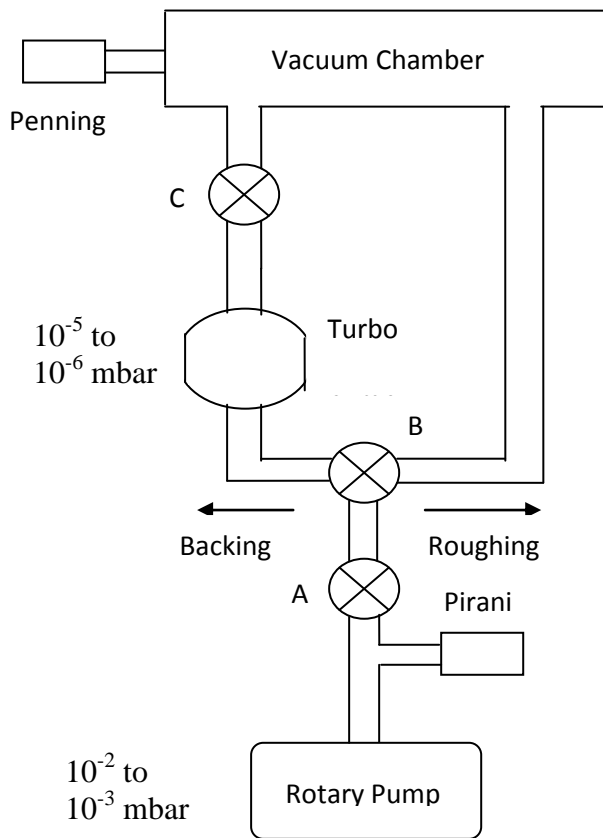
Figure A4.1 showing the screen grid to FP order of assembly

A4.9 IMS to Quad pressure chart

At one stage, when looking for a leak in the IMS system, it was necessary to be able to know what the pressure in the drift tube was when pumping down when a pressure gauge was not present. It was however still possible to monitor the pressure in the quadrupole region and so a look-up chart was prepared as shown in figure A4.2 below. It is interesting to see that the relationship follows a linear trend.



A4.10 Important points to observe when shutting the system down.



Initially Pumping Down from Atmosphere

- Ensure that valves A and C are closed, and that valve B is set to the ‘roughing’ position. All pressure gauges should be switched off.
- Switch on the rotary pump and slowly open valve A.
- Switch on the Pirani pressure gauge.
- Providing that the reading is less than 10^{-1} mbar, turn on the cooling water and turn valve B to the ‘backing’ position.
- Switch the turbo pump on.
- Open valve C
- Switch on the Penning gauge. If the pressure is $>10^{-4}$ mbar, check for leaks. A good pressure is $<10^{-5}$ mbar.

Precautions to take when shutting down.

Before switching the turbo pump off:

- Switch the Penning gauge off to prevent failure at higher pressures.
- Switch the turbo pump off and leave the cooling water on for 30 min before turning the water supply off.

If it is then required to switch the rotary pump off:

- First close valve C and wait until the turbo pump is cool, then close valve A to prevent oil from the rotary pump being sucked into the rest of the system by the vacuum.
- Switch off the Pirani gauge to prevent burnout of the filament at higher pressures.
- Switch the rotary pump off.

A4.11 IMS temperature comparison/calibration

The sealant for the interface between the thermocouple inside the drift tube to the temperature controller is silicon sealant which although providing an airtight seal, appeared to be continuously out gassing causing severe contamination inside the drift tube, probably most severely when baking out under vacuum. (An earlier unsuccessful attempt to use special low out gassing araldite failed since the araldite would not stick to the thermocouple cable, and so an airtight seal was not obtained.) It was also found shortly after that there had been an oil leak in the air compressor supplying the department severely contaminating the air lines with oil vapour and this was probably the source of the contamination all along. It was therefore decided to dispense with the compressor and use bottled compressed air of high purity instead.

By correlating the temperature of the outside of the heating jacket with that of the drift tube, the internal thermocouple can then be removed and the outside thermocouple fixed to the heating jacket can then be used instead. By using a suitable calibration curve, the controller can therefore be set at a value to give the required temperature. To obtain a calibration curve, the data shown in table A4.1 was taken. All the readings are in degrees centigrade. Readings are referenced to T_{2c} since this is the controlling variable. Δ represents the error in the reading given by the controller. It is seen from table 5A.12.1 that the error increases with rising temperature from around 2 °C to 5 °C.

Taking Δ into account, table A4.1 can be constructed to provide the calibration curve by plotting the controller reading T_j against T_2 (internal) where T_j is now the temperature of the heating jacket as given by the controller. Thus, $T_2 = T_j - \Delta$

Table A4.1 Controller temperature readings against actual drift tube and heating jacket temperatures

Dual electronic thermometer		Controller	
T1 (external)	T2 (internal)	T2c (controller)	T2c – T2(int) = Δ
24	26	28	2
25	27	30	3
27	28	31	3
28	30	32	2
30	32	35	3
35	37	40	3
42	46	50	4
44	51	55	4
47	56	60	4
49	62	65	3
54	66	70	4
61	76	80	4
68	85	90	5
72	95	100	5
78	104	110	6
84	115	120	5

A plot of [T1(external) + Δ] against [T2 (internal)] (+ Δ since T1 (external is now provided by the controller, which reads too high by an amount Δ) will then produce the calibration curve.

Renaming [T1 (external) + Δ] to $T_{\text{CONTROLLER}}$ and [T2 (internal)] to $T_{\text{DRIFT TUBE}}$ and will provide table A4.2:

Table A4.2 Variation of indicated temperature with actual drift tube temperature

$T_{\text{CONTROLLER}}$	$T_{\text{DRIFT TUBE}}$	$T_{\text{CONTROLLER}}$	$T_{\text{DRIFT TUBE}}$
26	26	51	56
28	27	52	62
30	28	58	66
30	30	65	76
33	32	73	85
38	37	77	95
46	46	84	104
47	51	89	115

Calibration curve

Exporting table A4.2 into excel produced the curve shown in figure A4.3

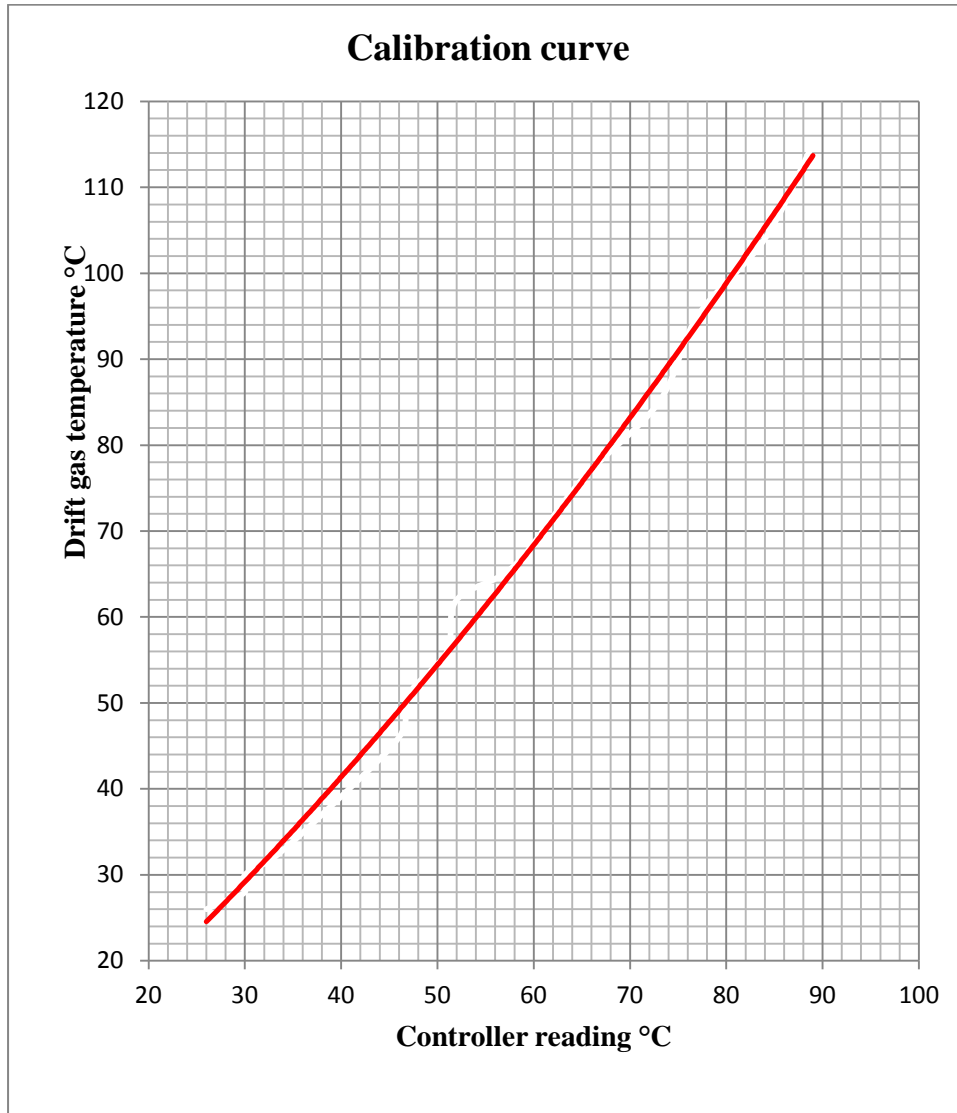


Figure A4.3 Relationship between indicated temperature on the controller and actual drift gas temperature

A4.12 Parameter values relative to a normally working system

In order to ensure at any time that the system is operating normally, the following nominal measurements are provided.

Pressure values:

Drift tube: 1010 mbar → Quad: 4.2×10^{-5} mbar
3 mbar → 1.7×10^{-5} mbar

V_{HT} set to 4.5 kV draws 0.057 mA from supply

With $t_{GATE} = 0.2$ ms and 500 accumulations/averages:

At 30 °C: (with 40:40 res.)

SIMMS mass mobility spectrum 1000 counts/s at $m/z = 73$, $t_d = 20.9$ ms

IMS ion mobility spectrum 0.1 nA peak, $t_d = 20.6$ ms.

A4.13 Modification to ring connections to eliminate the drift problem

The ring voltage was set by the chain of resistors connected across the rings to set up a homogenous electric field, in this case (the gate ring being half way along the chain) being effectively sourced from V_{HT} via $80\text{ M}\Omega$. In order to hold the ring voltage at a steady value, it is better to derive it from a relatively low resistance source. This was accomplished by bypassing the chain with a potential divider comprising two high stability $10\text{ M}\Omega$ resistors as shown in figure A4.4.

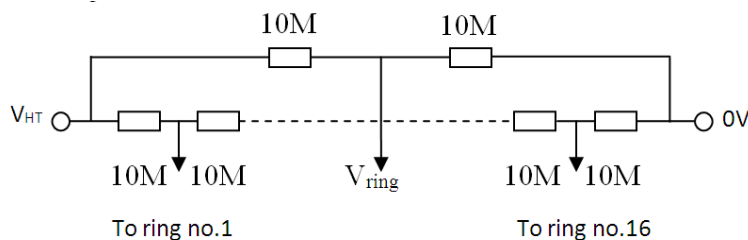


Figure A4.4 Modification to ring circuit

Total ring resistance = $160\text{ M}\Omega$, Voltage splitter = $20\text{ M}\Omega$ total so current through splitter is eight times that through the ring resistors, holding V_{ring} constant.

$$\text{Thus } V_{ring} = \frac{V_{HT}}{2}. \text{ If } V_{HT} = \text{say, } 5\text{ kV max, then power dissipated in } 10\text{ M}\Omega = \frac{(2.5 \times 10^3)^2}{10 \times 10^6}$$

= 0.63 W , so use a 2 W rating, e.g. Tyco HB03 series (element voltage up to 15 kV), RS stock number is 296-0702.

After completing the modification, it was found in subsequent investigations using analytes that the drift problem no longer existed.

APPENDIX 5

A5.1 Determining the syringe flow rate required to give a final concentration in the gas flow to the drift tube

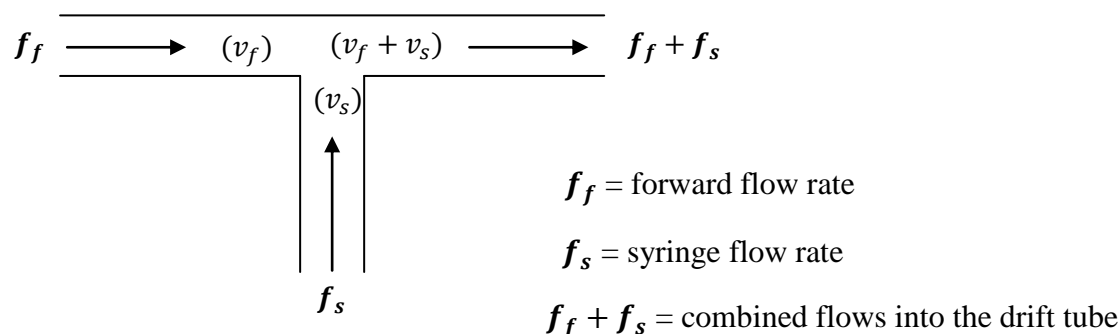


Figure A5.1 - Flows relating to concentration in the inlet system

Considering the layout shown in figure A5.1, in one second, the corresponding volumes swept through will be v_f , v_s and $v_f + v_s$ respectively. Volume v_f contains the purified air carrier gas and volume v_s contains the mixture of concentration C_a expelled from the syringe.

The concentration C_a is found from the volume that the analyte vapour takes up in the syringe

$$v_a \text{ divided by the syringe volume } v_s \text{ i.e. } C_a = \frac{v_a}{v_s}.$$

Hence, in the forward flow, the total volume flowing in one second will be $(v_f + v_s)$, and the final concentration C_f will therefore be $v_a/(v_f + v_s)$.

$$\text{Thus, } \frac{C_f}{C_a} = \frac{v_a}{v_f + v_s} \times \frac{v_s}{v_a} = \frac{v_s}{v_f + v_s} \text{ hence } C_f = C_a \times \frac{v_s}{v_f + v_s}$$

$$\text{but flow rate is swept volume per unit time, thus } C_f = C_a \times \frac{f_s}{f_f + f_s}$$

The syringe flow rate can be found by transposing the above equation to give:

$$f_s = f_f \times \frac{C_f}{C_a - C_f}$$

Using this formula, the corresponding computer program 'syringe.bas' for calculating the syringe flow rate for a required final concentration is given in Appendix 5.2.

A5.2 - Program to calculate syringe flow rate for a required sample concentration in the drift flow gas

'syringe.bas 'D C Howse

CLS

PRINT "program to calculate syringe drive flow rate for a required concentration"

PRINT "=====

PRINT

INPUT "Analyte concentration in the syringe (ppmv)"; Ca

'convert to ppbv

Ca = Ca * 1000

INPUT "Final concentration required in the forward flow (ppbv)"; Cf

INPUT "Forward flow (ml/minute)"; Ff

'convert forward flow to ml/hour

Ff = Ff * 60

'calculate syringe flow rate

Fs = Ff * Cf / (Ca - Cf)

PRINT "Set syringe flow rate to "; INT(Fs * 100) / 100; " ml/hour"

A5.3 Program to calculate reduced ion mobility

```
'K0.bas  D C Howse
CLS
'reduced mobility calculation
PRINT "Calculation of reduced mobility"
PRINT "=====
PRINT : PRINT "Assuming T = 30 deg C and Drift tube voltage = 4.5 kV"
PRINT
INPUT "Drift tube pressure (mbar) "; P
INPUT "drift time (ms) "; td
'convert td to seconds
td = td / 1000
'Voltage applied to drift tube (V) is 4.5 kV
'Hence drift voltage =4.5/2 = 2.25 kV
V = 2250
'Temperature = 30 + 273 = 303 deg Kelvin
T = 303
'Length of drift region L = 10.36 cm
L = 10.36
'calc field strength E
E = V / L
'calc mobility K
K = L / (E * td)
PRINT : PRINT "Mobility = "; INT(K * 100) / 100
'calc reduced mobility K0
K0 = K * 273 / T * P / 1013
PRINT "Reduced mobility K0 = "; INT(K0 * 100) / 100
```


A5.4 Sample Dilution using a Pressure Vessel

Figure A5.2 shows the layout of the apparatus used to obtain gas samples. The basic idea is to pump down the system to 0 mbar, then to fill with sample vapours to a pressure P_s where $P_s > 1$ atmosphere to facilitate filling of a syringe. Nitrogen is then introduced up to a total system pressure of P_t . The sample concentration in the system will then be P_s/P_t .

Operational sequence

To get an initial dilution after connecting in the sample vial assembly, the following steps are taken:

- Ensure that all valves **A - E** are closed
- Switch on the vacuum pump
- Open **A**, **C** and **E** to pump the system down to a reading of 0 mbar on the pressure gauge
- Close **A** to isolate the vacuum pump
- Close **C** and open **D**
- Open **C** and let the partial pressure due to the sample vapours in the system rise to a given value P_1
- Close **C** and **D**
- Open **B** to fill the system with nitrogen to a pressure P_2
- Close **B**
- Close **E**
- Open **A** and **C** and pump out the system up to the dilution chamber

The sample concentration in the dilution chamber based on partial pressures is therefore $\frac{P_1}{P_2}$

Important

- Before switching the vacuum pump off, to avoid oil being drawn into the system, disconnect the nitrogen connection and open valve **B** to vent the system (up to the dilution chamber) to atmosphere.
- Before disconnecting the sample vial assembly, ensure that valve **C** is closed to isolate the inlet.

To obtain a second dilution

The previous sequence will end with valves **B** and **E** closed and the system pumped down to 0 mbar.

- Open **A** to pump the system down (as the first chamber may have lost vacuum)
- Close **C** and then **A** to isolate the vacuum pump
- Open **E** to cause the chambers to share the gas from the dilution chamber
- Open **A** and pump down to required pressure P_3
- Close **A**
- Open **B** to fill the system up to the dilution chamber with N_2 to a pressure P_4
- Close **B**
- Close **E**
- Open **A** and pump out

The sample concentration based on partial pressures is given by: $C_2 = \frac{P_1}{P_2} \times \frac{P_3}{P_4}$

Explanation

The gas law states: $PV = nRT$ hence $P \propto \frac{n}{V}$ where n = number of moles of the gas, and so for a fixed volume, $P \propto n$ (1)

If the total pressure P_{tot} is made up of partial pressures, for example P_s for an acetone sample and P_{air} for the supporting air, then $P_{tot} = P_s + P_{air}$

The concentration of acetone C is therefore $\frac{n_s}{n_{tot}} = \frac{P_s}{P_{tot}}$ (from equation (1))

In the first dilution, let the initial sample pressure be P_1 and the total pressure P_{tot} be P_2 .

Then for the first dilution, the concentration $C_1 = \frac{P_1}{P_2}$

For a second dilution, the first chamber is pumped down to zero mbar and then the dilution chamber is used to fill the first chamber. The total pressure will now drop to P_3 and the partial pressure due to the sample = $P_3 \times C_1$ since the concentration is unchanged.

Nitrogen is then let in to increase the total pressure to P_4 and the concentration will now become:

$$C_2 = \frac{P_3 \times C_1}{P_4} = \frac{P_3}{P_4} \times \frac{P_1}{P_2}$$

Similarly, for a third dilution,

$$C_3 = \frac{P_5}{P_6} \times \frac{P_3}{P_4} \times \frac{P_1}{P_2} \text{ and so.}$$

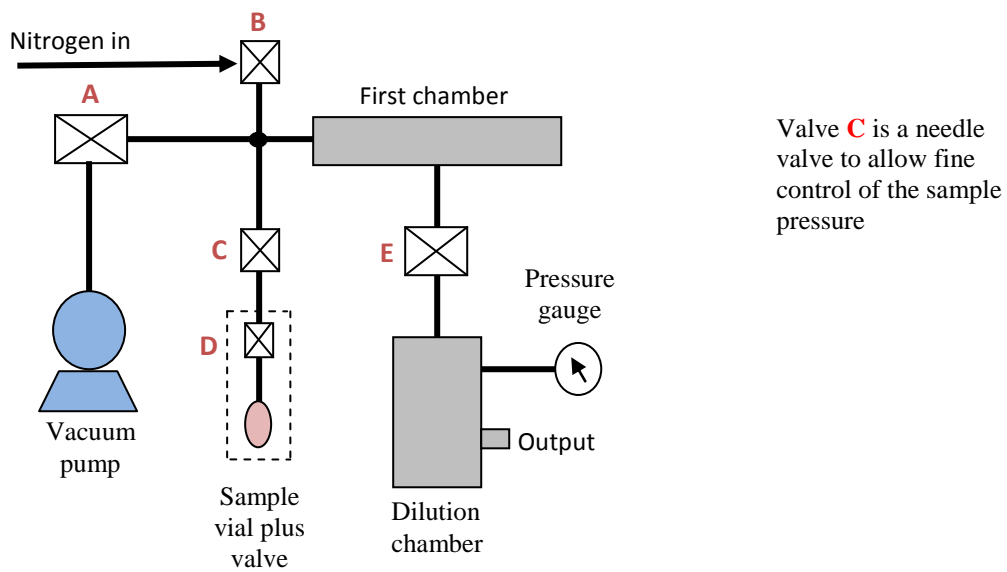


Figure A5.2 Layout of the dilution rig

A5.5 Sample Concentration using a Diffusion tube

If sample vapours diffuse out of the end of the tube at D g/min into a flow of F l/min, the

concentration can be said to be $\frac{D}{F}$ g/l(1).

However, the concentration is required as a volumetric ratio and so the sample rate D requires

conversion into litres of sample/min. The number of moles/min N of D g/min is $\frac{D}{R}$ where R

is the relative formula mass of the sample. Eg. For CO_2 , $R = 44$ g/mole.

N moles of any gas will take up a volume of $N \times 22.4$ l at STP. Therefore the volume taken

up in one minute by $\frac{D}{R}$ moles is $\frac{D}{R} \times 22.4$ litres

Thus, from equation (1), the volumetric concentration C is now $\frac{D}{R} \times \frac{22.41}{F}$ (2)

Where: D = sample diffusion rate out of the diffusion tube (g/min)

R = relative formula mass of the sample (g/mole)

F = flow rate of the carrier gas (l/min)

A5.6 Dilution Chart

Sample dilution using the dilution rig (pressure vessel technique)

Chemical

Date

First dilution

P1 =mbar

P2 =mbar

Concentration = $P1 / P2 \times 10^6$ ppmv

Thus C1 =ppmv

Second dilution

P3 =mbar

P4 =mbar

Concentration = $C1 \times P3 / P4$ ppmv

Thus C2 =ppmv

Third dilution

P5 =mbar

P6 =mbar

Concentration = $C2 \times P5 / P6$ ppmv

Thus C3 =ppmv

A5.7 Calculation of vapour pressure using the Antoine equation

This equation describes the relationship between vapour pressure and temperature for pure chemicals. Thus, the vapour pressure may be found from:

$$\log_{10} p = A - \frac{B}{C+T}$$

Where p is the vapour pressure in bar, T is the temperature in Kelvin and A , B and C are specific constants for the chemical. Vapour pressure is dependent only on temperature.

The equation gives a good approximation over a specific temperature range.

From the National Institute of Standards and Technology (NIST) Chemistry WebBook site (webbook.nist.gov/chemistry/) the constants may be found by selecting 'formula' and then typing in the chemical formula and then looking up under 'phase change' data.

Example

For acetone (C_3H_6O) the 'Antoine Equation Parameters' for temperatures between 259.16 and 507.6 Kelvin are given as;

$$A = 4.42448 \quad B = 1312.253 \quad C = -32.445$$

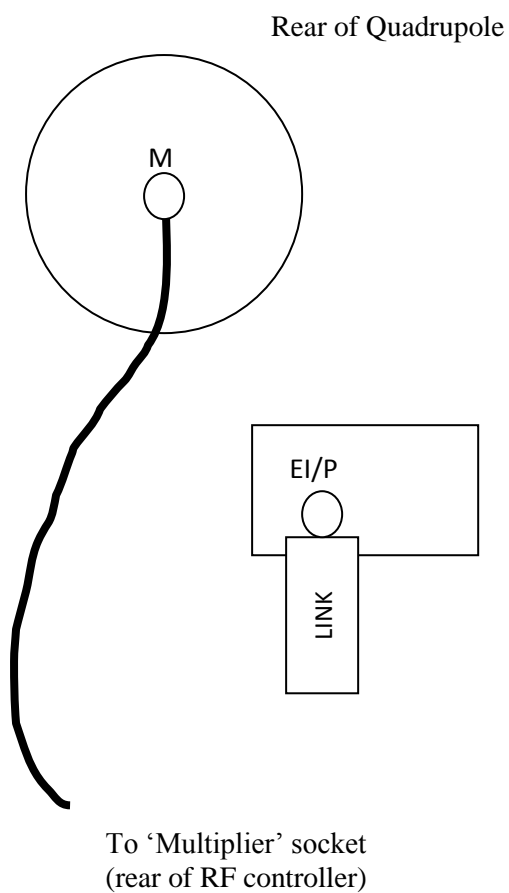
The operating temperature T is 295.15 K (22°C) and substituting these values into the formula gives $\log(P) = -0.571$

Anti-logging gives $p = 0.2687$ bar or **268.7 mbar**.

Appendix 6

A6.1 Quadrupole Connections for Ion Modes – A Pictorial Summary

Positive Ions Mode



Negative Ions Mode

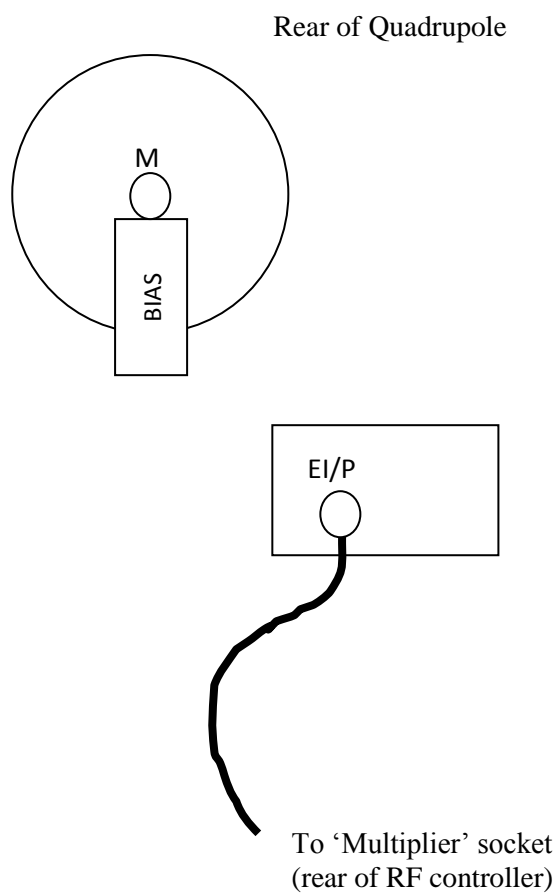


Figure A6.1 Quadrupole Connections for Ion Modes

Appendix 7

A7.1 High input impedance kilovoltmeter

A circuit to achieve this function is shown in figure A7.1 below. The input impedance is approximately 10 G Ω . The 1 M Ω variable resistor is a trimmer to adjust for a correct reading. With 4 kV in, the output voltage to the DVM will be 4 V.

Input current = 4kV/10G = 0.4 μ A.

The op-amp needs to be a low input bias current type, e.g. LF351 (50 pA i/p bias current).

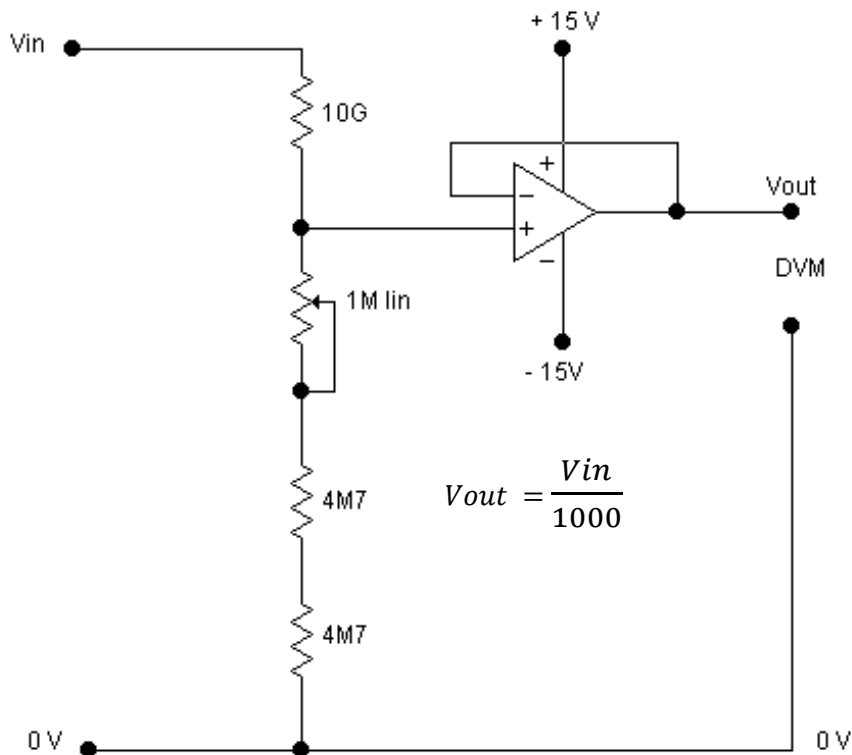


Figure A7.1 Circuit diagram for a high input impedance kilovoltmeter

Appendix 8

Publications in preparation

1. *Development of a sampled pulse count to analogue converter for display of ion mobility spectra using an Ion Mobility Spectrometer – Mass Spectrometer*

This paper culminates from the work done throughout this thesis. After an initial introduction and description of the system, focus is made mainly on the development of the novel pulse count to pseudo analogue converter that was designed for acquiring selected ions mass mobility spectra.

2. *Investigations into the detection of nitro aromatic explosives using an IMS – QMS system*

Concerning homeland security, a description is given in this paper of the results obtained from further investigations on the explosives TNT, TNB, DNT and DNB using the IMS-QMS system.

3. *An Investigation into anaesthetic compounds and the chlorinated ethanes, enflurane and isoflurane.*

Here, results are given from investigations made with the use of the IMS-QMS system on compounds found in the medical community.

4. *A software suite developed using LabVIEW for use with a tandem Ion Mobility Spectrometer – Mass Spectrometer system*

In this paper, a review of the programs used for data acquisition and display of spectra will be given that highlights the user friendliness of the human-machine interface obtained when using the graphical programming language LabVIEW to control an IMS-MS system.

REFERENCES

1. Mayhew, C.A. and Watts, P. *Fundamentals, Development and Applications of Ion Mobility Spectrometry (IMS) for Enhanced Detection of Threat Agents*. 2006. Research grant application.
2. Borsdorf, H.; Eiceman, G.A., *Ion mobility spectrometry: principles and applications*, Appl. Spectrosc. Rev. 2006,41, 323-375.
3. Borsdorf, H.; Mayer, T.; Zarejousheghani, M.; Eiceman, G.A., *Recent developments in ion mobility spectrometry*, Appl. Spectrosc. Rev. 2011,46(6), 472-521.
4. Eiceman G.A. *Ion-mobility spectrometry as a fast monitor of chemical composition*. Trends in analytical chemistry, vol. 27, no. 4, 2002
5. Makinen, M.A., Anttalainen, O.A. Sillanpaa, M.E.T., *Ion mobility spectrometry and its Applications in detection of chemical warfare agents*, Anal. Chem. 2010, 82,9594-9600.
6. Seto, Y; Kanamori-Kataoka, M; Tsuge, K.; Ohsawa, I.; Maruko, H.; Sekiguchi, H.; Sano, Y.; Yamashiro, S.; Matsushita, K.; Sekiguchi, H.; et al., *Development of an on-site detection method for chemical and biological warfare agents*, Toxin Rev. 2007,26, 299-312.
7. Hill, H.H.; Steiner, W.E., *Ion mobility spectrometry for monitoring the destruction of chemical warfare agents*, Edited by Kolodkin, V.M.; Ruck, W., *Ecological Risks Associated with the Destruction of Chemical Weapons*, Proceedings of the NATO Advanced Research Workshop on Ecological Risks Associated with the Destruction of Chemical Weapons, Lueneburg, Germany, October 22-26, 2003, 2006, pp. 157-166.
8. *Organisation for the Prohibition of Chemical Weapons (OPCW), Fact Sheet 4: What Is a Chemical Weapon?* The Hague, The Netherlands. 2000. <http://www.opcw.org/about-chemical-weapons/what-is-a-chemical-weapon/>
9. Steiner, W.E.; Glowers, B.H.; Matz, L.M.; Siems, W.F.; Hill, H.H., Jr., *Rapid screening of aqueous chemical warfare agent degradation products: ambient pressure ion mobility mass spectrometry*, Anal. Chem. 2002, 74, 4343-4352.

10. Wu, C.; Steiner, W.E.; Tornatore, P.S.; Matz, L.M.; Siems, W.F.; Atkinson, D.A.; Hill, H.H., Jr., *Construction and characterization of a high-flow, high-resolution ion mobility spectrometer for detection of explosives after personnel portal sampling*, *Talanta* 2002, 57, 123-134.
11. Fetterolf, D.D.; Clark, T.D., *Detection of trace explosive evidence by ion mobility spectrometry*, *J. Forensic Sci.* 1993, 38(1), 28-39.
12. Eiceman, G.A.; Stone, J.A., *Ion mobility spectrometry in homeland security*, *Anal. Chem.* 2004, 76(21), 390A-397A.
13. Karpas, Z., *Ion mobility spectrometry: a tool in the war against terror*, *Bull. Israel Chem. Soc.* 2009,24,26-30.
14. Eiceman, G.A.; Schmidt, H., *Advances in ion mobility spectrometry of explosives*, in *Aspects of Explosive Detection*, Editors Marshal, M.; Oxley, J., Elsevier, Amsterdam, 2009, pp. 171-202.
15. Babis J S, Sperline R P, Knight A K, Jones D A, Gresham C A, Denton M B, *Performance evaluation of a miniature ion mobility spectrometer drift cell for application in hand-held explosives detection ion mobility spectrometer* *Anal Bioanal CHEM* (2009) 395:411-419
16. Liang X, Wang X, et al. *Sensitive detection of black powder by stand-alone ion mobility spectrometer with chlorinated hydrocarbon modifiers in drift gas*. *Talanta* 121 (2004) 215-219
17. Smiths Detection Ltd., *The GID-3 chemical agent detector*. [2010: www.smithsdetection.com/GID-3.php].
18. Smiths Detection Ltd., *IONSCAN 500DT Simultaneous Explosives and Narcotics Trace Detector*. [2007: www.smithsdetection.com/eng/IONSCAN_500DT.php].
19. Armenia S, Garrigues S, Guardia M, Brassier J, Alcalá M, Blanco M, Perez-Alfonso C, Galipienso N. *Detection and characterization of emerging psychoactive substances by ion mobility spectrometry*. *Drug testing and analysis*. (2013)

20. Guddat,S.: Thevis,M.; Kapron.J.: Thomas.A.; Sehanzer.W., *Drug testing and analysis*, Adv. Sports Drug Testing. 2009, 1(11-12), 545-553.
21. Fytche, L.M.; Hupe, M.; Kovar, J.B.; Pilon, P., *Ion mobility spectrometry of drugs of abuse in customs scenarios: concentration and temperature study*, J. Forensic Sci. 1992, 37, 1550-1566.
22. Lawrence, A.H., *Detection of drug residues on the hands of subjects by surface sampling and ion mobility spectrometry*, Forensic Sci. Int. 1987, 34, 73-83.
23. Nanji, A.N.; Lawrence, A.H.; Mikhael, N.Z., *Use of skin sampling and ion mobility spectrometry as a preliminary screening method for drug detection in an emergency room*, J. Toxicol. Clin. Toxicol. 1987, 25, 501-515.
24. Armenia, S.; de la Guardia, M., *Analytical methods to determine cocaine contamination of banknotes from around the world*, Trends Anal. Chem. 2008, 27, 344-351.
25. Buryakov, I.A.; Baldin, M.N., *Comparison of negative and positive modes of ion-mobility increment spectrometry in the detection of heroin vapors*, J. Anal. Chem. 2008,63,787-791.
26. Verkouteren, J.R.; Staymates, J.L., *Reliability of ion mobility spectrometry for qualitative analysis of complex, multicomponent illicit drug samples*, Forensic Sci. Int. 2011, 206, 190-196.
27. Geraghty, E.; Wu, C.; McGann, W., *Effective screening for "club drugs" with dual mode ion trap mobility spectrometry*, Int. J. Ion Mobility Spectrom. 2002, 5, 41-44.
28. Dussy, F.E.; Berchtold, C.; Briellmann, T.A.; Lang, C.; Steiger, R.; Bovens, M., *Validation of an ion mobility spectrometry (IMS) method for the detection of heroin and cocaine on incriminated material*, Forensic Sci. Int. 2008, 177, 105-111.
29. Baumbach, J.I., *Process analysis using ion mobility spectrometry*, 2006, Anal Bioanal Chem 384:1059-1070

30. Budde, K.J., *Determination of organic contamination from polymeric construction materials for semiconductor technology*, Mater. Res. Soc. Symp., Proc. Ultraclean Semiconductor Processing Technology and Surface Chemical Cleaning and Passivation, 1995, 386, 165-176.
31. Budde, K.J.; Holzapfel, W.J.; Beyer, M.M., *Detection of volatile organic contaminants in semiconductor technology—a comparison of investigations by gas chromatography and by ion mobility*, Proc. 39th Annu. Tech. Meeting 1ES, Las Vegas, NV April 1993, p. 366.
32. Budde, K.J., *Organic surface analysis in semiconductor technology by ion mobility spectrometry*, Proc. Electrochem. Soc. 1995, 95-30, 281-296.
33. Budde, K.J.; Holzapfel, W.J.; Beyer, M.M., *Application of ion mobility spectrometry to semiconductor technology: outgassings of advanced polymers under thermal stress*, J. Electrochem. Soc. 1995, 142, 888-897.
34. Pilzecker, P.; Baumbach, J.I.; Kurte, R., *Detection of decomposition products in SF₆: a comparison of colorimetric detector tubes and ion mobility Spectrometry*, Proceedings of the Conference on Electrical Insulation and Dielectric Phenomena, 2002, 865-868; DOI 10.1109/CEIDP.2002.1048932.
35. Baumbach, J.I.; Pilzecker, P.; Trindade, E., *Monitoring of circuit breakers using ion mobility Spectrometry to detect SF₆-decomposition*, Int. J. Ion Mobil. Spectrom. 1999, 2, 35-39.
36. Soppart, O.; Pilzecker, P.; Baumbach, J.I.; Klockow, D.; Trindade, E., *Ion mobility spectrometry for on-site sensing of SF₆ decomposition*, IEEE Trans. Dielectr. Electr. Instil. 2000, 7, 229-233.
37. Dean, K.R.; Carpio, R.A., *Real-time detection of airborne contaminants in DUV lithographic processing environments*, Proc. IBS 1995, 41, 9-17.

38. Vigil, J.C.; Barrick, M.W.; Grafe, T.H., *Contamination control for processing DUV chemically amplified photoresists*, Proc. SPIE Int. Soc. Opt. Eng. 1995, 2438, 626-643, Adv. Resist Technol. Proc. XII, Editor Allen, R.D.
39. Karpas, Z.; Tilman, B.; Gdalevsky, R.; Lorber, A., *Determination of volatile biogenic amines in muscle food by ion mobility spectrometry (IMS)*, Anal. Chim. Acta 2002, 463, 155-163.
40. Bota, G.M.; Harrington, P.B., *Direct detection of trimethylamine in meat food products using ion mobility spectrometry*, Talanta 2006, 68, 629-635.
41. Ogden, I.D.; Strachan, N.J.C., *Enumeration of Escherichia coli in cooked and raw meats by ion mobility spectrometry*, J. Appl. Microbiol. 1993, 74, 402-405.
42. DeBono, R.; Grigoriev, A.; Jackson, R.; James, R.; Kuja, P.; Loveless, A.; Le, T.; Nacson, S.; Rudolph, A.; Yin, S., *Rapid analysis of pesticides on imported fruits by GC-IONSCAN*, Int. J. Ion Mobil. Spectrom. 2001, 4, 16-19.
43. Borsdorf, H.; Roetering, S.; Nazarov, E.G.; Weickhardt, C., *Rapid screening of pesticides from fruit surfaces: preliminary examinations using a laser desorption-differential mobility spectrometry coupling*, Int. J. Ion Mobil. Spectrom. 2009, 12, 15-22.
44. Jafari, M.T.; Azimi, M., *Analysis of sevin, amitraz, and metalaxyl pesticides using ion mobility spectrometry*, Anal. Lett. 2006, 39, 2061-2071.
45. Tuovinen, K.; Paakkanen, H.; Hanninen, O., *Detection of pesticides from liquid matrices by ion mobility spectrometry*, Anal. Chim. Acta 2000, 404, 7-17.
46. Jazan, E and Mirzaei, H. *Direct analysis of human breath ammonia using corona discharge ion mobility spectrometry*, 2014, J. Pharm Biomed Anal. 88: 315-320
47. Bunkovskii A, Maddula S, Davies A, Westhoff M, Litterst P, Bodeker B, Baumhach J I. *One-year time series of investigations of analytes within human breath using ion mobility spectrometry*. Int. J. Ion Mobil. Spec. (2010) 13:141-148 DOI

48. Klein CC, Wietstock S, Hoffmann M. *Breath analysis using Ion Mobility Spectrometry (IMS) as diagnostic tool in equine reproduction medicine* Biomed Tech 201 (2013)3; 58
49. Ulanowska A, Ligor M, Amann A, Buszewski B. *Determination of Volatile Organic Compounds in Exhaled Breath by Ion Mobility Spectrometry*. Chem. Anal. (Warsaw), 53, 953 (2008)
50. Westho M, Litter, PD, Frertag L, Urfer W, Bader S, Baumbach JI. *Ion mobility spectrometry for the detection of volatile organic compounds in exhaled breath of lung cancer patients - Results of a pilot study*. Thorax Online (2009) 10.1136/thx.2008.099465
51. Westhoff, M.; Litterst, P; Freitag, L.; Urfer, W.; Bader, S.; Baumbach, J.L, *Ion mobility spectrometry for the detection of volatile organic compounds in exhaled breath of patients with lung cancer: results of a pilot study*, Thorax 2009, 64, 744-748.
52. Baumbach, J.L. *Ion mobility spectrometry coupled with multi-capillary columns for metabolic profiling of human breath*, J. Breath Res. 2009, 3, 034001.
53. Snyder A P, Shoff D B. *Detection of Bacteria by Ion Mobility Spectrometry*. Anal. Cham. 1991, 83, 526-529
54. Strachan NJ.C, Nicholson F.J., Ogden I.D. *An automated sampling system using ion mobility spectrometry for the rapid detection of bacteria*. Analytica Chimica Acta 313 (1995) 63-67
55. Strege, M.A.; Kozerski, J.; Juarbe, N.; Mahoney, P, *At-line quantitative ion mobility spectrometry for direct analysis of swabs for pharmaceutical manufacturing equipment cleaning verification*. Anal. Chem. 2008, 80, 3040-3044.
56. Qin, C.; Granger, A.; Papov, V.; McCaffrey, J.; Norwood, D.J., *Quantitative determination of residual active pharmaceutical ingredients and intermediates on equipment surfaces by ion mobility spectrometry*, J. Pharin. Biomed. Anal. 2010, 51, 107-113.

57. Walia, G.; Davis, M.; Stefanou, S.; Debono, R., *Using ion mobility spectrometry for cleaning verification in pharmaceutical manufacturing*, Pharm. Technol. April 2003, 72-78.
58. Strege, M. A., *Total residue analysis of swabs by ion mobility spectrometry*, Anal. Chem. 2009,81,4576-4580.
59. Marquez-Sillero, I.; Aguilera-Herrador, E.; Cardenas, S.; Valcarcel, M., *Ion-mobility spectrometry for environmental analysis*, Trends Anal. Chem. 2011, 30, 677-690.
60. Eiceman, G.A.; Snyder, A.P.; Blyth, D.A., *Monitoring of airborne organic vapors using ion mobility spectrometry*, Int. J. Environ. Anal. Chem. 1990, 38, 415-425.
61. Eiceman, G.A.; Nazarov, E.G.; Tadjikov, B.; Miller, R.A., *Monitoring volatile organic compounds in ambient air inside and outside buildings with the use of a radio-frequency-based ion-mobility analyzer with a micromachined drift tube*, Field Anal. Chem. Tech. 2000,4, 297-308.
62. Simpson, G.; Klasmeier, M.; Hill, H.; Atkinson, D.; Radolovich, G.; Lopez Avila, V.; Jones, T.L., *Evaluation of gas chromatography coupled with ion mobility spectrometry for monitoring vinyl chloride and other chlorinated and aromatic compounds in air samples*, J. HighResolut. Chromatogr. 1996, 19, 301-312.
63. Walls, C.J.; Swenson, O.F.; Gillispie, G.D., *Real-time monitoring of chlorinated aliphatic compounds in air using ion mobility spectrometry with photoemissive electron sources*, Pmc. S PIE Int. Soc. Optical Eng. 1999, 3534, 290-298.
64. Smiths Detection Ltd., *CAM Chemical Agent Monitor*.
[2007: www.smithsdetection.com/CAM.php]
65. Turner, R.B. and Brokenshire, J.L., *Hand-held ion mobility spectrometers. Trends in Analytical Chemistry*. Vol 13, no. 7. 1994
66. Eiceman, G.A.; Karpas, Z., *Ion Mobility Spectrometry, 2nd edition*, CRC Press, Boca : Raton, FL, 2005.

67. Hill, H.H. Dwivedi, P. and Kanu, A.B., *Reduction in false positive responses for explosives detection using ion mobility mass spectrometry (IMMS)*. Bulletin of Laser and Spectrometry Society of India, 2006. 14:p. 92-103
68. Puton, J. Nousiainen, M. and Sillanpaa, M., *Ion mobility spectrometers with doped gases*. Talanta, 2008. 76(5):p. 978-987.
69. *LabVIEW* © National Instruments Corporation (U.K.) Ltd. Berkshire. RG14 2PS
70. Collins. D,C., Lee. M,L.,*Developments in ion mobility spectrometry-mass spectrometry*. 2002. Anal Bioanal Chem 372:66-73
71. Hunka, D.E. and Austin, D.E., *Ion Mobility Spectrometer/Mass Spectrometer (IMS-MS)*. 2006, Sandia National Laboratories.
72. Adams N.G., Smith D. *The selected ion flow tube (SIFT): a technique for studying ion – neutral reactions*. Int. J. Mass Spectrom. Ion Phys., 1976, 21, 349.
73. Feguson, E.E., Fesenfeld, F.C., Schmeltkopf, A.L. (1966). *Flowing afterglow measurements of ion – neutral reactions*. Adv. At. Mol. Phys. 5,1
74. Peterkops, R *Theory of ionization of atoms by electron impact*. Boulder, Colo: (1977) Colorado Associated University Press.
75. Lagg, A., Taucher, J.,Hansel, A., Lindinger, W. (1994). *Application of proton transfer reactions to gas analysis*. Int J. Mass Spectrom. Ion Processes 134,55
76. Williams, J.P.; Bugarcic, T.; Habtemariam, A.; Giles, K.; Campuzano, I.; Rodger, P.M.; Sadler, P.J., *Isomer separation and gas-phase configurations of organoruthenium anti-cancer complexes: ion mobility mass spectrometry and modeling*, J. Am. Soc. Mass Spectrom. 2009, 20, 1119-1122.
77. Kim, S.H.; Spangler, G.E., *Ion-mobility spectrometry-mass spectrometry of two structurally different ions having identical ion mass*, Anal. Chem. 1985, 57, 567-569.

78. Li, H.; Giles, K.; Bendiak, B.; Kaplan, K.; Siems, W.F.; Hill, H.H., *Resolving structural isomers of monosaccharide methyl glycosides using drift tube and traveling wave ion mobility mass spectrometry*, Anal. Chem. 2012, 84, 3231-3239.
79. Albritton, D.L., et al. *Mobilities of Mass-Identified H_3^+ and H^+ Ions in Hydrogen*. Physical Review. Vol 171, no.1. 1968
80. Giles, K., Grimsrud, E.P., *The Kinetic Ion Mobility Mass Spectrometer: Measurements of Ion-Molecule Reaction Rate Constants at Atmospheric Pressure*. J. Phys. Chem. 1992, 96, 6680-6687
81. Kanu, A.B.; Dwivedi, P.; Tam, M.; Matz, L.; Hill, H.H., Jr., *Ion mobility-mass spectrometry*, J. Mass Spectrom. 2008, 43, 1-22.
82. Sysoev, A. et al. *Development of an ion mobility spectrometer for use in an atmospheric pressure ionization ion mobility spectrometer/mass spectrometer instrument for fast screening analysis*. Rapid Commun. Mass Spectrom. 2004: 18: 3131-3139
83. Ringer, J.; Ross, S.K.; West, D.J., *An IMS/MS investigation of lewisite and lewisite/mustard mixtures*, Int. J. Ion Mobil. Spectrom. 2002, 5, 107-111.
84. Kozole J, Stairs I, Clio I, Harper J D, Lukow S R, Lareau R T, DeBono R, Kuja F. *Interfacing an Ion Mobility Spectrometry Based Explosive Trace Detector to a Triple Quadrupole Mass Spectrometer*. Anal. Chem. 2011, 83, 8596-8603
85. Lawrence, A.H., *Ion mobility spectrometry/mass spectrometry of some prescription and illicit drugs*, Anal. Chem. 1986, 58, 1269-1272.
86. Brosi, A.R.; Borkowski, C.T.; Conn, E.E.; Griess, I.C., Jr. *Characteristics of Ni^{59} and Ni^{63}* , Phys. Rev 1951, 81, 391-395.

87. Salleras, M.; Kalmsa, A.; Krenkow, A.; Kessler, M.; Goebel, J.; Meuller, G.; Marcoal, S., *Electrostatic shutter design for a miniaturized ion mobility spectrometer*, Sens. Actuators B Chem. 2006, 118, 338-342.
88. Zuleta, L.A.; Barbula, G.K.; Robbins, M.D.; Yoon, O.K.; Zare, R.N., *Micromachined Bradbury-Nielsen gates*, Anal. Chem. 2007, 79(23), 9160-9165.
89. Tadjimukhamedov, F.K.; Puton, J.; Stone, J.A.; Eiceman, G.A., *A study of the performance of an ion shutter for drift tubes in atmospheric pressure ion mobility spectrometry: computer models and experimental findings*, Rev. Sci. Instrum. 2009, 80, 103103-103110.
90. Puton, I., *Static and dynamic properties of the shutter grid for the ion mobility spectrometer*, Sci. Instrum. (Nauch. Apparat.) 1989, 4(1), 29-41.
91. Tolmachev, A.V.; Clowers, B.H.; Belov, M.E.; Smith, R.D., *Coulombic effects in ion mobility spectrometry*, Anal. Chem., 2009, 81(12), 4778-4787.
92. Seims, W.F. et al., *Measuring the Resolving Power of Ion Mobility Spectrometers*. Analytical Chemistry. 1994. 66, p. 4195-4201
93. Eiceman, G.A.; Nazarov, E.G.; Stone, J.A.; Rodriguez, J.E., *Analysis of a drift tube at ambient pressure: models and precise measurements in ion mobility spectrometry*, Rev. Sci. Instrum. 2001, 72, 3630-3621.
94. Eiceman, G.A.; Vandiver, V.J.; Chen, T; Rico-Martinez, G., *Electrical parameters in drift tubes for ion mobility spectrometry*, Anal. Instrum. 1989, 18(3-4), 227-242.
95. Mayhew, C.A., et al., *Measurements of thermal electron attachment rate coefficients to molecules using an electron swarm technique*. European Physical Journal D, 2005. 35(2): p. 307-312.
96. *NI PCI-6014 Data sheet*: www.sine.ni.com/nips/cds/view/p/lang/en/nid/11442

97. Baim, A. and Hill, H.H., *Resolution Measurement for Ion Mobility Spectrometry*. Anal. Chem. 1985, 57, 1902 - 1907
98. Kanu, A.B. Gribb, M.M. and Hill, H.H., *Predicting optimal resolving power for ambient pressure ion mobility spectrometry*. Analytical Chemistry, 2008. 80(17): p. 6610-6619
99. Revercomb, H.E. and E.A. Mason, *Theory of Plasma Chromatography Gaseous Electrophoresis - Review*. Analytical Chemistry, 1975. 47(7): p. 970-983.
100. McDaniel, E.W.; Mason, E.A.. *The Mobility and Diffusion of Ions in Gases*, Wiley Interscience, New York, 1973.
101. Vautz, W., et al., *An implementable approach to obtain reproducible reduced ion mobility*. Int. J. Ion Mobil. Spec. (2009) 12: p, 47-57
102. <http://webbook.nist.gov/chemistry/>
103. Kebarle, P; Searles, S.K.; Zolla, A.; Scarborough, J.; Arshadi, M., *The solvation of the hydrogen ion by water molecules in the gas phase. Heat and entropies of solvation of individual reaction: $H^+(H_2O)_{n-1} + H_2O = H^+(H_2O)_n$* . J. Am. Chem. Soc. 1967, 89(25), 6393-6399.
104. Kim, S.H.; Betty K.R.; Karasek, F.W., *Mobility behavior and composition of hydrated positive reactant ions in plasma chromatography with nitrogen carrier gas*, Anal. Chem. 1978, 50(14), 2006-2016.
105. Cheng, H.P, *Water Clusters: Fascinating Hydrogen-Bonding Networks*. Journ Phy Chem A (1998) Vol 102, No 31
106. Kebarle, P.; Chowdhury, S., *Electron affinities and electron-transfer reactions*, Chem.Rev., 1987, 87(3), 513-534.
107. Tou, J.C.; Ramstad, T.; Nestricks, T.J., *Electron mobility in a plasma chromatograph*, Anal. Chem. 1979, 51, 780-782.

108. Sabo, M. Et al. *Atmospheric Pressure Corona Discharge Ionisation and Ion Mobility Spectrometry/Mass Spectrometry study of negative corona discharge in high purity oxygen and oxygen/nitrogen mixtures*. Int. Journ. Mass Spectrom. 293 (2010) 23-27
109. Spangler, G.E.; Collins, C.L., *Reactant ions in negative ion plasma chromatography*, Anal. Chem. 1975, 47, 393-402.
110. Carr, T.W., *Negative ions in plasma chromatography-mass spectrometry*, Anal. Chem. 1977, 49, 828-831.
111. Jarvis, G.K., Kennedy, R.A. Mayhew, C. A. *Investigations of low energy electron attachment to ground state group 6B hexafluorides (SF₆, SeF₆, and TeF₆) using an electron-swarm mass spectrometric technique*. Int. J. Mass Spectrom. 205 (2001) 253-270
112. *EasiDew Portable Hygrometer* – Michell Instruments Ltd. Ely, U.K.
113. *A Guide to the Measurement of Humidity*. © Michell Instruments. 2009
114. *Data sheet SLFS022C*. (2002). Texas Instruments. PO Box 655303, Dallas, Texas.75265
115. RS Components Ltd. Birchington Road, Corby, Northants. NN17 9RS. UK
116. Travis, J and Kring, J. *LabVIEW for Everyone*, Third Edition. Prentice Hall 2009
117. Wojciech, D. et al. *Processing of the Signal from Detectors Used in Ion Mobility Spectrometry*.Anal. Sciencenes. Vol 26,983-988, 2010
118. Davis, E.J., Clowers, B.H., Siems, W.F. Hill, H.H. Jr. *Comprehensive software suite for the operation, maintenance, and eveluation of an ion mobility spectrometer*. Int.J. Ion Mobil. Spec. (2011) 14:117-124
119. Private discussion with Dr. Peter Watts

120. Watts, P. Wilders, A. *On the resolution obtainable in practical ion mobility systems. Int. Journ. Mass Spectrom and Ion Processes*, 112 (1992) 179-190
121. Hassan, U. Anwar, M.S., *Reducing noise by repetition: introduction to signal averaging. Eur. J. Phys.* 31 (2010) 453-465
122. Private communication with Dr. Kevin Giles
123. Siems, W. F., Wu, C., Tarver, E. E., et al. *Measuring the Resolving Power of Ion Mobility Spectrometers. Anal. Chem.* (1994), 66, 4195
124. Lee, Y. J. et al. *Collision-Induced Dissociation of Mobility-Separated Ions Using an Orifice-Skimmer Cone at the back of a Drift Tube. Anal. Chem.* 2001, 73, 3549-3555
125. Harris, N.S. *Modern Vacuum Practice*, McGraw-Hill. 1997. p28
126. Arce, L. et al., *Sample-introduction systems coupled to ion-mobility spectrometry equipment for determining compounds present in gaseous, liquid and solid samples. Trends in Ana. Chem.* (2008), Vol 27, No 2
127. Bell, A. J. et al *Studies on gas-phase ion-molecule reactions of 2-methyl-2-propanol (t-butyl alcohol) with protonated water clusters. Int. Journ. Mass Spectrom. and Ion Processes* 173 (1998) 65-70
128. <http://antoine.frostburg.edu/chem/senese/101/liquids/faq/antoine-vapor-pressure.shtml>.
What is the Antoine Equation?
129. http://www1.diccism.unipi.it/Nicolella_Cristiano/chimica_applicata/materiale/dati/dati_pdf/Costanti_Antoine.pdf
130. Watts, P., *Use of Ion Mobility Spectrometry for the Detection and Analysis of Vapours. Ana. Proc.* (1991), vol 28

131. Fernandez-Maestre, R., Hill, H.H. Jnr. *Ion mobility spectrometry for rapid analysis of over-the-counter drugs and beverages*. Int. J. Ion. Mobil. Spec. (2009), 12:91-102
132. Kanu, A., Hill, H. H. Jnr. *Identity confirmation of drugs and explosives in ion mobility spectrometry using a secondary drift gas*. Talanta 73 (2007), 692-699
133. Spangler, G., Lawless, P., *Ionization of Nitrotoluene Compounds in Negative Ion Plasma Chromatography*. Anal. Chem. (1978), Vol. 50, No. 7, p 884
134. Jarvis, G.K. et al. *An investigation of electron attachment to CHCl_2F , CHClF_2 and CHF_3 using an electron-swarm mass spectrometric technique*. Int. Nat. Journal of Mass Spectrometry and Ion Processes 164 (1997) 207-223
135. Astbury, G., et.al. *Analysis of explosives using electrospray ionization/ion mobility spectrometry (ESI/IMS)*. Talanta 50 (2000) 1291-1298
136. Ewing, R. D., et.al. *A critical review of ion mobility spectrometry for the detection of explosives and explosive related compounds*. Talanta 54 (2001) 515-529
137. Shumate, C., et al. *Table of reduced mobility values from ambient pressure ion mobility spectrometry*. Journal of Chromatography, 373 (1986) 141-173
138. Atwal, G. K., et al., *Chemical standards for ion mobility spectrometry: a review*. Int. J. Ion Mobil. Spec. (2009) 12:1-14
139. Viitanen, A., et al., *Adjusting mobility scales of ion mobility spectrometers using 2,6-DtBP as a reference compound*. Talanta 76 (2008) 1218-1223
140. Kwasnik, M., Gonin, M., Fuhrer, K., Barbeau, K., Fernandez, F.M., *Performance, resolving power and radial ion distributions of a prototype nanoelectrospray ionisation resistive glass atmospheric pressure ion mobility spectrometer*, Anal. Chem. 2007, 79, 7782-7791

141. Sielemann, S.; Baumbach, J.I.; Schmidt, H., *IMS with non radioactive ionization sources suitable to detect chemical warfare agent simulation substances*, Int. J. Ion Mobil. Spectrom. 2002, 5, 143-148.
142. Sielemann, S.; Baumbach, J.I.; Pilzecker, P.; Walendzik, G., *Detection of trans-1,2-dichloroethene, trichloroethene and tetrachloroethene using multi-capillary columns coupled to ion mobility spectrometers with UV-ionisation sources*, Int. J. Ion Mobil. Spectrom. 1999,2,15-21.
143. Tabrizchi, M., Khayamian, T., Taj, N., *Design and optimisation of a corona discharge ionisation source for ion mobility spectrometry*, Rev. Sci. Instrum. 2000, 7,2321-2328
144. Hill, C.A., Thomas, C.L.P., *A pulsed corona discharge switchable high resolution ion mobility spectrometer – mass spectrometer*, Analyst 2003, 128, 55-60
145. Hubert, T., Tiebe, C., Stephan, I., *Detection of fungal infestations of wood by ion mobility spectrometry* Int. Biodeterior. Biodegradation 2011, 65(5), 675-681
146. Vautz, W., Baumbach, J.L., Jung, J., *Beer fermentation control using ion mobility spectrometry – results of a pilot study*, J. Institute Brewing, 2006, 112(2), 157-164
147. Karpas, Z.; Marcus. S.; Golan. M.. *Method for the Diagnosis of Pathological Conditions in Animals*, filing date June 18, 2009; application number 12/456,591; publication number U.S. 2009/0325191 A1.
148. Armenia, S.; de la Guardia, M., *Analytical methods to determine cocaine contamination of banknotes from around the world*, Trends Anal. Chem. 2008, 27, 344-351.
149. Limero, T; James, J.; Reese, E.; Trowbridge, J.; Hohmann, R., *The Volatile Organic Analyzer (VOA) Aboard the International Space Station*, SAE Technical Paper
150. Kay and Laby. *Tables of Physical and Chemical constants*. NPL. (2014), 4.4.3